

# From microscale to macroscale modeling of drying porous media

**Dissertation**

zur Erlangung des akademischen Grades

**Doktoringenieur**

**Dr.-Ing.**

von **MSc. Xiang Lu**

geb. am 15.06.1992 in Anhui, China

genehmigt durch die Fakultät für Verfahrens- und Systemtechnik  
der Otto-von-Guericke-Universität Magdeburg

Promotionskommission: Jun.-Prof. Dr.-Ing. Alba Dieguez Alonso (Vorsitz)  
PD Dr.-Ing. habil. Abdolreza Kharaghani (Gutachter)  
Prof. Dr.-Ing. habil. Evangelos Tsotsas (Gutachter)  
Dr. Christoph Kirsch (Gutachter)

eingereicht am: June 29, 2021

Promotionskolloquium am: December 17, 2021

# Declaration

I hereby declare that I prepared the dissertation with the title:

**From microscale to macroscale modeling of drying porous media**

submitted without inadmissible assistance and without the use of any aids other than those indicated. Facts or ideas taken from other sources, either directly or indirectly, have been marked as such.

In particular, I did not use the services of a commercial graduation consultation. Further, I have not made payments to third parties either directly or indirectly for any work connected with the contents of the submitted dissertation.

The work has not so far been submitted either in Germany or abroad in same or similar form as a dissertation and has also not yet been published as a whole.

Magdeburg, June 29, 2021

MSc. Xiang Lu

# Abstract

In this thesis, the volume-averaged transport parameters of the one-dimensional macroscopic continuum model (CM) for drying are determined from three-dimensional microscopic discrete pore network models (PNMs). Then these macroscopic parameters are fed into the CM for quick predictions. The discrete model called throat-pore model (TPM) is presented and compared with a throat-node model (TNM) by performing simulations under identical initial and boundary conditions.

The CM used in this work is an isothermal version of the broadly accepted macroscopic CM of drying. The CM is treated with different boundary conditions. The first treatment is to impose the evaporation rate at the drying front (or surface). The second is to impose flux boundary conditions at two interfaces, i.e., at the interface between the (gas-side) boundary layer and the (medium-side) dry region, as well as at the interface between the dry and unsaturated regions which evolves freely during drying. The latter approach is named as three-transport-zone CM, which includes three sectionally applicable transport equations to reproduce the drying characteristics of capillary porous media.

Parameters included in these models are the moisture transport coefficient in the wet zone within the porous medium, the vapor transport coefficient in the dry zone within the porous medium, the vapor transport coefficient in the gas-side diffusion layer, the vapor pressure-saturation relationship at the surface, as well as the vapor pressure-saturation relationship at the drying front. Those macroscopic parameters are extracted from the PNM datasets.

Operation of the CM is very sensitive upon the moisture transport coefficient in the totally or partially saturated zone of the porous medium. A hybrid method is introduced to control the effect of the sensitivity of the CM on the macroscopic parameters. By punctually adjusting the dataset in the high saturation period, the CM provides a stronger agreement with pore network simulations, which shows that the underlying transport phenomena are better preserved in the scattered dataset that the new hybrid method provides.

Moreover, the surface vapor transport coefficient-surface vapor concentration relationship is assessed from PNM simulations, which can be used in the frame of a CM to couple the porous medium with the boundary layer. Besides, emendation factors are introduced to

link the normalized evaporation rate from the wet part of the porous medium surface with the surface wetness or surface saturation. Their evaluation shows that the normalized evaporation rate contributed from wet patches tends to surface saturation with increasing intensity of drying, whereas a similar but weaker trend can be observed with surface wetness. This correlation provides, especially in case of enhanced and non-isothermal drying processes, a simple method for coupling the wet surface region with the gas-side boundary layer in a two-equation CM. The evaporation rate from the wet surface region has also been evaluated by inserting PNM data into a modified version of Schlünder's model. The results are not encouraging the derivation of CM boundary conditions according to Schlünder, neither for the whole medium surface nor for its wet part.

Furthermore, correlations of macroscopic parameters with pore structures are discussed with respect to the mean and standard deviation of monomodal throat radius distribution as well as for bimodal pore size distribution.

Finally, the Brooks and Corey capillary pressure model is revisited from the microscopic aspect. The parameters in this model, the wetting phase residual saturation, entry capillary pressure, and the size distribution index, are assessed and their correlations with microstructural features are discussed.

# Kurzzusammenfassung

In dieser Arbeit werden die volumengemittelten Transportparameter des eindimensionalen makroskopischen Kontinuumsmodells (CM) für die Trocknung aus dreidimensionalen, mikroskopischen und diskreten Porennetzwerkmodellen (PNMs) bestimmt. Dann werden diese makroskopischen Parameter für schnelle Vorhersagen in das CM eingespeist. Das diskrete Modell, das als Halse-Poren-Modell (TPM) bezeichnet wird, wird vorgestellt und mit dem Halse-Knoten-Modell (TNM) verglichen, indem Simulationen unter identischen Anfangs- und Randbedingungen durchgeführt werden.

Das verwendete CM ist eine isotherme Version des für die Trocknung allgemein akzeptierten makroskopischen CM. Das CM wird mit unterschiedlichen Randbedingungen gelöst. Die erste Variante besteht darin, das CM mit der Verdampfungsgeschwindigkeit an der Trocknungsfront (oder Oberfläche) anzusetzen. Die zweite besteht darin, Massendichten an zwei Grenzflächen zu definieren, d.h. an der Grenzfläche zwischen der (gasseitigen) Grenzschicht und dem (mittelseitigen) trockenen Bereich sowie der Grenzfläche zwischen dem trockenen und dem teilgesättigten Bereich, die sich frei entwickelt während des Trocknens. Der letztere Ansatz wird als CM mit drei Transportzonen bezeichnet, das drei abschnittsweise anwendbare Transportgleichungen enthält, um die Trocknungseigenschaften von kapillaren porösen Medien zu reproduzieren.

In diesen Modellen enthaltene Parameter sind der Feuchtigkeitstransportkoeffizient in der Nasszone innerhalb des porösen Mediums, der Dampftransportkoeffizient in der Trockenzone innerhalb des porösen Mediums, der Dampftransportkoeffizient in der gasseitigen Diffusionsschicht, die Beziehung zwischen Dampfdruck und Sättigung an der Oberfläche sowie die Dampfdruck-Sättigung-Beziehung an der Trocknungsfront. Diese makroskopischen Parameter werden aus den PNM-Datensätzen extrahiert.

Der Betrieb des CM ist sehr empfindlich gegenüber dem Feuchtigkeitstransportkoeffizienten in der vollständig oder teilweise gesättigten Zone des porösen Mediums. Eine Hybridmethode wird eingeführt, um den Einfluss der Empfindlichkeit des CM auf die makroskopischen Parameter zu steuern. Durch punktuelle Anpassung des Datensatzes in der Hochsättigungsperiode ermöglicht das CM eine bessere Übereinstimmung mit Porennetzwerksimulationen, was zeigt, dass die zugrunde liegenden Transportphänomene in dem von der neuen Hybridmethode bereitgestellten Streudatensatz besser erhalten bleiben.

Darüber hinaus wird die Beziehung zwischen Transportkoeffizienten und Konzentration des Dampfes an der Körperoberfläche anhand von PNM-Simulationen bewertet, die im Rahmen eines CM verwendet werden kann, um das poröse Medium mit der Grenzschicht zu koppeln. Außerdem werden Emendationsfaktoren eingeführt, um die normierte Verdunstungsgeschwindigkeit vom feuchten Teil der Oberfläche des porösen Mediums mit der Oberflächenfeuchte oder Oberflächensättigung zu verknüpfen. Ihre Bewertung zeigt, dass die normierte Verdunstungsgeschwindigkeit, die von feuchten Stellen getragen wird, mit zunehmender Trocknungsintensität zur Oberflächensättigung neigt, während ein ähnlicher, aber schwächerer Trend auch bei der Oberflächenfeuchte beobachtet werden kann. Diese Korrelation liefert insbesondere im Fall von schnellen und nicht isothermen Trocknungsprozessen ein einfaches Verfahren zum Koppeln des feuchten Oberflächenbereichs mit der gasseitigen Grenzschicht in einem CM mit zwei Gleichungen. Die Verdunstungsgeschwindigkeit aus dem feuchten Oberflächenbereich wird durch Einfügen von PNM-Daten in eine modifizierte Version des Schlünder-Modells bewertet. Die Ergebnisse legen die Ableitung von CM-Randbedingungen nach Schlünder weder für die gesamte Oberfläche noch für ihren feuchten Teil nahe.

Weiterhin werden Korrelationen makroskopischer Parameter mit der Porenstruktur für unterschiedliche Mittelwerte und Standardabweichungen einer monomodalen Verteilung des Radius von Knotenhälsen sowie für eine entsprechende bimodale Verteilung diskutiert.

Schließlich wird das Kapillardruckmodell von Brooks und Corey unter mikroskopischen Gesichtspunkten überarbeitet. Die Parameter in diesem Modell, (Restsättigung der benetzenden Phase, Eintrittskapillardruck, Größenverteilungsindex) werden bewertet und ihre Korrelationen mit Merkmalen der Mikrostruktur diskutiert.

# Contents

<b>1</b>	<b>Introduction and overview</b>	<b>1</b>
1.1	Background . . . . .	1
1.1.1	Description of porous media . . . . .	1
1.1.2	Drying process . . . . .	5
1.1.3	Drying models . . . . .	9
1.1.4	Surface of porous media . . . . .	11
1.1.5	Pore structure . . . . .	14
1.1.6	Parameters in capillary pressure function . . . . .	15
1.2	Aim . . . . .	17
1.2.1	Pore geometry in PNM . . . . .	18
1.2.2	Issues of the current continuum model and its parameterization . . . . .	18
1.2.3	Macroscopic parameters . . . . .	19
1.2.4	Pore structure effects on macroscopic parameters . . . . .	20
1.3	Scope of the work . . . . .	20
<b>2</b>	<b>Pore network modeling</b>	<b>22</b>
2.1	Introduction . . . . .	22
2.2	Model description . . . . .	23
2.2.1	Labeling of pores and throats . . . . .	23
2.2.2	Generation of pores and throats . . . . .	26
2.2.3	Drying algorithm in the capillary-viscous regime . . . . .	28
2.2.4	Numerical algorithm . . . . .	38
<b>3</b>	<b>Pore network simulations of drying: Throat-node model vs. throat-pore model</b>	<b>42</b>
3.1	The pore space of porous medium approximated by PNM . . . . .	42
3.2	Vapor transport conductance . . . . .	45
3.3	Liquid transport conductance . . . . .	48
3.4	Drying kinetics . . . . .	51
<b>4</b>	<b>One-equation continuum model for drying capillary porous media</b>	<b>59</b>
4.1	Assumptions . . . . .	59

4.2	Component mass balance for liquid water . . . . .	60
4.3	Component mass balance for water vapor . . . . .	61
4.4	Mass balance for moisture transport . . . . .	62
4.5	Initial and boundary conditions . . . . .	63
<b>5</b>	<b>Two versions of the one-equation continuum model for drying</b>	<b>65</b>
5.1	Moving front boundary condition . . . . .	65
5.1.1	Wet surface . . . . .	66
5.1.2	Dry surface . . . . .	66
5.2	Boundary conditions defined for three transport zones . . . . .	67
5.2.1	Wet surface . . . . .	68
5.2.2	Dry surface . . . . .	69
5.3	Numerical method used to solve the CM . . . . .	70
<b>6</b>	<b>Determination of the macroscopic parameters of the one-equation continuum model from pore network simulations</b>	<b>73</b>
6.1	Moisture transport coefficient . . . . .	74
6.1.1	Computation for extracting the moisture transport coefficient . . .	74
6.1.2	The moisture transport coefficient . . . . .	75
6.2	Relative humidity . . . . .	80
6.2.1	Computation of the relative humidity . . . . .	80
6.2.2	Relative humidity profile . . . . .	81
6.3	Vapor transport coefficients . . . . .	83
6.3.1	Computation of the vapor transport parameters . . . . .	85
6.3.2	Profiles of vapor transport parameters . . . . .	87
<b>7</b>	<b>Feeding the macroscopic parameters into the one-equation continuum model</b>	<b>90</b>
7.1	Influence of averaging intervals on the CM solution . . . . .	91
7.2	Influence of different treatment methods on the CM solution . . . . .	92
7.3	Assessment of the CM by PNM simulations . . . . .	94
7.4	Hybrid method . . . . .	97
7.5	Comparison between the two versions of the continuum model . . . . .	102
<b>8</b>	<b>Evaporation from the surface of capillary porous media</b>	<b>106</b>
8.1	Pore network setting and surface parameter estimation . . . . .	108
8.2	Surface parameters from pore network data . . . . .	109
8.3	Wet surface region evaporation rates . . . . .	112
8.4	Schlünder's formula for the wet surface region . . . . .	117
<b>9</b>	<b>Macroscopic parameters dependence on the pore network heterogeneity</b>	<b>124</b>
9.1	Influence of mean throat radius . . . . .	125

9.2	Influence of the standard deviation of throat radius . . . . .	129
9.3	Bimodal pore size distribution . . . . .	133
<b>10</b>	<b>Parameters in the Brooks and Corey capillary pressure model</b>	<b>140</b>
10.1	Model description . . . . .	140
10.1.1	Network structure . . . . .	141
10.1.2	Static PNM algorithm . . . . .	142
10.2	Wetting phase residual saturation . . . . .	145
10.3	Entry pressure . . . . .	149
10.4	Capillary pressure-effective saturation . . . . .	150
10.5	Pore size distribution index . . . . .	152
<b>11</b>	<b>Summary and Outlook</b>	<b>157</b>
11.1	Summary . . . . .	157
11.2	Outlook . . . . .	161
11.2.1	Pore network modeling . . . . .	161
11.2.2	Two-equations continuum model . . . . .	162
11.2.3	Macroscopic parameters . . . . .	163

# Nomenclature

---

$a_s$	interfacial area	$\text{m}^2$
$A$	cross-sectional area of medium	$\text{m}^2$
$A_s$	cross-sectional area of meniscus	$\text{m}^2$
$A_{tot}$	total cross-sectional area of menisci throats	$\text{m}^2$
$\mathbf{A}_v$	matrix of water vapor conductances	$\text{kg}/(\text{Pa} \cdot \text{s})$
$\mathbf{A}_w$	matrix of liquid water conductances	$\text{kg}/(\text{Pa} \cdot \text{s})$
$\mathbf{b}_v$	matrix of water vapor boundary conditions	$\text{kg}/\text{s}$
$\mathbf{b}_w$	matrix of liquid water boundary conditions	$\text{kg}/\text{s}$
$D$	moisture transport coefficient	$\text{m}^2/\text{s}$
$D_v$	moisture transport coefficient for vapor phase	$\text{m}^2/\text{s}$
$D_{va}$	diffusion coefficient of vapor in air	$\text{m}^2/\text{s}$
$D_{v,b}$	vapor diffusion coefficient in gas-side boundary layer	$\text{m}^2/\text{s}$
$D_{v,e}$	vapor diffusion coefficient in the dry zone	$\text{m}^2/\text{s}$
$D_w$	moisture transport coefficient for liquid phase	$\text{m}^2/\text{s}$
$g_v$	vapor conductances	$\text{kg}/(\text{Pa} \cdot \text{s})$
$g_w$	water conductances	$\text{kg}/(\text{Pa} \cdot \text{s})$
$h$	center distance between two pores/nodes	$\text{m}$
$\Delta h$	distance from drying front to surface	$\text{m}$
$H$	network height	$\text{m}$
$j$	mass flux	$\text{kg}/(\text{m}^2 \cdot \text{s})$
$J_v$	vapor flow rate	$\text{kg}/\text{s}$
$k$	effective permeability	$\text{m}^2$
$k_v$	vapor phase permeability	$\text{m}^2$
$k_w$	water phase permeability	$\text{m}^2$
$L$	height of porous medium	$\text{m}^2$
$L_t$	length of throat	$\text{m}$
$\bar{L}_t$	mean length of throat in network	$\text{m}$
$\dot{m}_v$	vapor flux or drying rate	$\text{kg}/(\text{m}^2 \cdot \text{s})$
$\tilde{M}_v$	molar mass of water vapor	$\text{kg}/\text{kmol}$
$\dot{M}_v$	vapor flow rate at meniscus	$\text{kg}/\text{s}$

$\dot{M}_w$	water flow rate in throat	kg/s
$N$	number of pores/nodes	-
$P$	atmospheric pressure	Pa
$P_m$	liquid pressure at meniscus	Pa
$P_v$	vapor pressure	Pa
$P_v^*$	saturated vapor pressure	Pa
$P_w$	water pressure	Pa
$\dot{q}$	volume flux	$\text{m}^3/(\text{m}^2 \cdot \text{s})$
$\dot{Q}$	volume flow rate	$\text{m}^3/\text{s}$
$R$	radius	m
$\bar{R}$	mean radius	m
$\tilde{R}$	universal gas constant	J/kmol · K
$S$	saturation	-
$S_{a_s, max}$	saturation when interfacial area is maximum	-
$S_e$	effective saturation	-
$S_T$	saturation of turning point	-
$t$	time	s
$\Delta t$	time step	s
$T$	temperature	K or °C
$v$	fluid velocity	m/s
$V$	volume	$\text{m}^3$
$X$	moisture content	-
$\mathbf{X}_v$	matrix which contains vapor pressure	Pa
$\mathbf{X}_w$	matrix which contains water pressure	Pa
$Z$	connectivity	-

---

### ***Greek symbols***

$\delta$	boundary layer thickness	m
$\varepsilon$	network porosity	-
$\zeta$	ratio of liquid flow rate over total flow rate	-
$\theta$	liquid-solid contact angle	-
$\lambda$	size distribution index	-
$\mu$	dynamic viscosity	Pa · s
$\rho_w$	water density	$\text{kg}/\text{m}^3$
$\sigma$	surface tension	N/m
$\sigma_0$	standard deviation	m
$\sigma_m$	standard deviation of meniscus size	m
$\tau$	relative interfacial area	-

$\varphi$	relative humidity	-
$\Phi$	parameters in Schlünder's model	-
$\Psi$	surface wetness	-

---

### ***Subscripts and superscripts***

$DF$	drying front
$DZ$	dry zone
$ev$	evaporation
$g$	gas phase
$irr$	irreducible
$i, j$	indices of pore
$k, n, z$	indices of slice
$l$	liquid
$net$	network
$p$	pore
$req$	required
$single$	single of slice
$s$	solid
$surf$	surface
$t$	throat
$tot$	total

---

### ***Abbreviations***

CM	continuum model
CV	control volume
FVM	finite volume method
IDP	initial drying period
LTDR	liquid transport dominated region
NLE	non-local equilibrium effect
PNM	pore network model
PNP	pore neighbor pore
PNT	pore neighbor throat
REV	representative elementary volume
SEM	scanning electron microscopic
TPTR	two-phase transport region
TNM	throat-node model
TNP	throat neighbor pore

TNT	throat neighbor throat
TP	transition period
TPM	throat-pore model
TS	top slice
VTDR	vapor transport dominated region

---

# Chapter 1

## Introduction and overview

Drying of porous materials is central to many environmental and engineering applications, including the evaporation of water from soils, the drying of food and building materials, the drying of porous electrodes, etc. Regardless of the application field, mathematical models for drying of porous materials are generally developed at two model hierarchies: At the macroscale, a partially saturated porous medium is described as a continuum, and the distribution of state variables is computed by means of functions in space and time. The corresponding set of equations is referred to as a continuum model (CM) (Whitaker, 1977). Discrete pore network models (PNMs) are, in contrast, developed to describe transport phenomena in partially saturated porous media at the pore scale (microscale). A PNM approximates the void space within a porous medium as a network of pores and nodes. Simple physical laws applied to each pore result in a large system of ordinary differential equations with degrees of freedom at each node of the pore network. Although both approaches may be useful for applications, each method also suffers from drawbacks.

Thus, this chapter first provides the necessary background about porous media and the drying process. Afterward, we explain the mathematical approaches to describe the drying process, i.e. continuum models and pore network models. In fact, the combination of these two modeling approaches (i.e. CM & PNM) offers new opportunities for simulating the drying process. In the following section, we will present the motivation for current work. In the end, the scope of this dissertation is specified.

### 1.1 Background

#### 1.1.1 Description of porous media

Porous materials are common in the surroundings (Fig. 1.1), but also in engineering applications, for example as processed foods or solid pharmaceutical dosage forms. In general, a porous medium consists of a solid or collection of solid bodies (which is called matrix or frame), with sufficient open space in or around the solids to enable fluids to pass through (Fig. 1.2). The void space in the porous medium can be mapped by an

interconnected network of pores. Pores filled or partially filled with fluids can express the distribution of fluids in the porous medium. This approach is adopted in discrete pore network modeling (Chapter 2).

Porous media can be classified upon physical properties of the solid matrix and its interplay with fluid transport. For example, the water (liquid) molecules can be physically bound on the interior solid free surface by molecular forces (i.e., van der Waals force) or chemically bound (water of crystallization). Classification of the porous media can stand on the percentage of bound water over the free water during the transport process. If the portion of bound water is significant, the porous medium is called hygroscopic. Hygroscopic materials have in common pore sizes reported to be smaller than about 100  $nm$ , such as cement paste, apple, potato.

In contrast, when free water plays a dominant role in liquid transport, we name these materials as capillary porous media (or non-hygroscopic porous media). The capillary porous media are typically composed of pores with sizes in the order of 100  $\mu m$  (Geoffroy and Prat, 2014). Typical examples are bricks or a packed bed of relatively large glass particles. In this work, we only focus on transport properties of capillary porous media. That is to say, the pore size of porous media is assumed in the micrometer range.



Figure 1.1: Examples of natural materials (a) sandy soils (taken on a beach in Barcelona, Spain) (b) sandstones (taken in Lanzarote, Spain) as well as of (c) building materials (taken in Prague, Czech Republic).

To facilitate the quantification of transport properties of capillary porous media, we need to characterize their morphology. Porosity  $\varepsilon$  is one major property of the porous

medium, defined as:

$$\varepsilon = \frac{V_g + V_l}{V_g + V_l + V_s} = \frac{V_{void}}{V_{tot}}. \quad (1.1)$$

Here,  $V_{void}$  ( $m^3$ ) represents the void volume in the porous medium, which consists of the volume of the gas phase  $V_g$  ( $m^3$ ) and liquid phase  $V_l$  ( $m^3$ ).  $V_s$  ( $m^3$ ) denotes the solid volume.

Since the porous medium can be filled or partially filled with liquid, local or global (network) saturation (or moisture content),  $S$  or  $S_{net}$ , describes its degree of wetness:

$$S = \frac{V_l}{V_g + V_l}; S_{net} = \frac{V_{l,net}}{V_{g,net} + V_{l,net}}. \quad (1.2)$$

Local saturation refers to some control volume which is relevant from the macroscale perspective (or a slice that makes sense for the discrete model), global saturation represents the saturation in the entire porous medium.

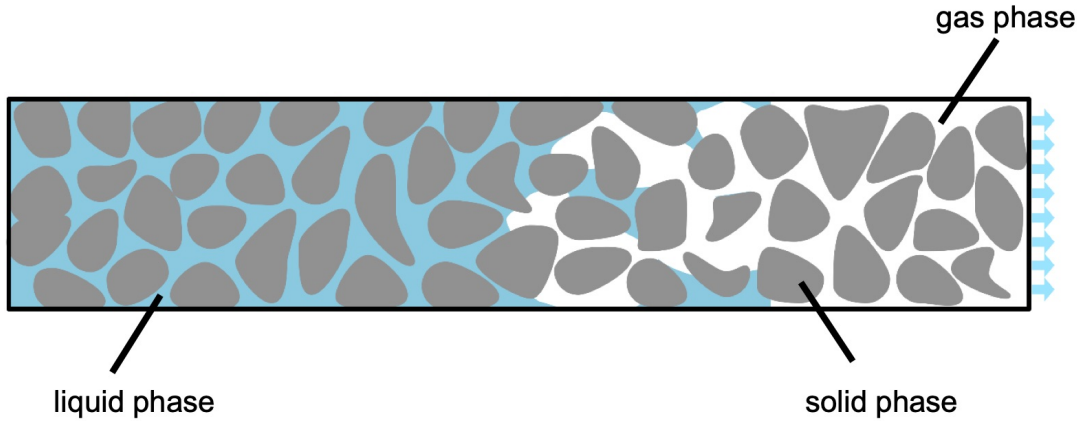


Figure 1.2: Schematic representation of a multiphase porous medium during the drying process.

Nevertheless, the major mechanism of liquid transport in the capillary porous medium is the capillary force. The Young-Laplace equation is most commonly used to express the capillary pressure,  $P_c$  (Pa), under equilibrium (static):

$$P_c = \frac{2\sigma\cos\theta}{r}. \quad (1.3)$$

Here,  $r$  (m) denotes the radius of the capillary tube,  $\sigma$  ( $N/m$ ) is the surface tension, and  $\theta$  ( $^\circ$ ) is the contact angle of the liquid on the wall of the capillary tube (Fig. 1.3). The Young-Laplace equation can be understood as a balance of the force at the meniscus surface (capillary force) with the surface forces of fluids, i.e. the water and gas, acting along the perimeter of the capillary tube. Once this condition is fulfilled, a stable meniscus as in Fig. 1.3 can be observed.

The dynamic fluid flow in porous media is conventionally quantified via Darcy's law.

This relates the instantaneous volume flux  $\dot{q}$  ( $m^3/(m^2 \cdot s)$ ) through the porous medium (superficial velocity), the permeability  $k$  ( $m^2$ ), the dynamic viscosity of the fluid  $\mu$  ( $Pa \cdot s$ ) and the pressure gradient (as the driving force for fluid flow) in the form:

$$\dot{q} = -\frac{k}{\mu} \frac{\partial P}{\partial z}. \quad (1.4)$$

Here,  $z$  is the direction of the capillary pressure, and the equation can be integrated over distance  $L$  ( $m$ ) from pressure  $P_a$  (Pa) to pressure  $P_b$  (Pa) (Fig. 1.4) to obtain the integral form of the Darcy's law:

$$\dot{q} = -\frac{k}{L\mu} \Delta P, \quad \Delta P = P_b - P_a. \quad (1.5)$$

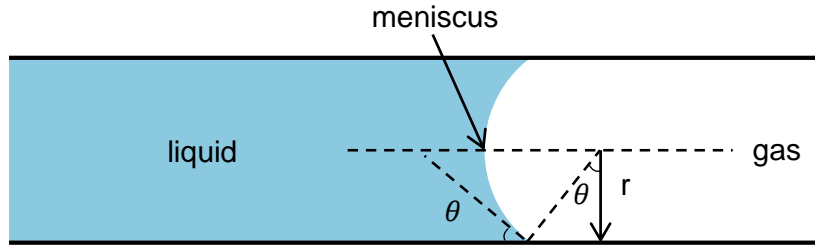


Figure 1.3: Liquid-gas interface confined in a capillary tube with a hydrophilic solid surface.

In a capillary tube (Fig. 1.3), the pressure difference  $\Delta P$  between the gas phase,  $P_g$  (Pa), and the liquid phase,  $P_w$  (Pa), can be expressed by:

$$\Delta P = P_g - P_w = P_c = \frac{2\sigma \cos\theta}{r}. \quad (1.6)$$

The fluid velocity  $\nu$  (interstitial velocity,  $m/s$ ) is related to the volume flux  $\dot{q}$  by the porosity  $\varepsilon$ :

$$\nu = \frac{\dot{q}}{\varepsilon}. \quad (1.7)$$

Key parameter in Darcy's law is the permeability,  $k$ , which represents the ability of the porous medium to allow the fluid to pass through. The permeability of a porous medium is related to its porosity, pore size, etc.

Fick's law can be used to describe diffusion in porous media. It relates the diffusion mass flux,  $j$  ( $kg/(m^2 \cdot s)$ ), to the mass concentration of the diffusing gas species ( $w_x$ ):

$$j = -D \frac{\partial w_x}{\partial z}. \quad (1.8)$$

Here,  $D$  ( $m^2/s$ ) denotes the diffusion coefficient. It is equal to the molecular diffusivity of the gas species in an empty space. In a porous medium it depends on the volume element considered (void or total). Defined on total volume (or on the empty cross-sectional area),

$D$  becomes an effective diffusion coefficient that depends on obstruction (elements of the solid phase are obstacles for gas diffusion) and tortuosity.

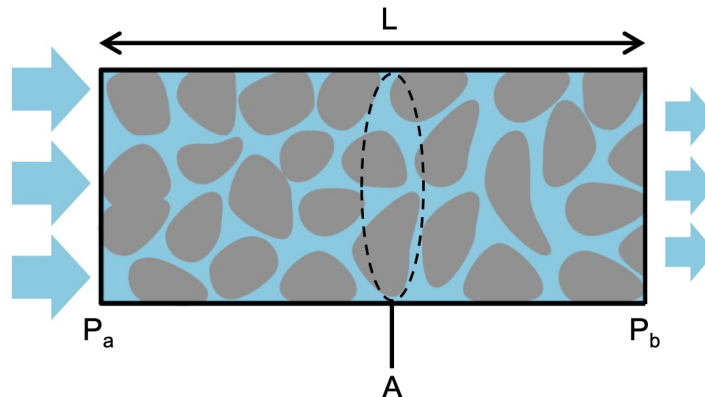


Figure 1.4: Schematic of the definition of Darcy's law.

In this end, the transport properties of fluids in porous media are governed by several parameters such as permeability, capillary pressure, diffusion coefficient. All these parameters are associated with the microscale properties of the porous media. In this work, we focus on the transport phenomena in drying porous media, which involves the transport for the liquid phase and the gas phase. In the following section, we will introduce the basics of the drying process of capillary porous media.

### 1.1.2 Drying process

Drying is a mass and heat transfer process resulting in the gradual removal of water or another solvent by evaporation from a porous material. This process can be strongly affected by boundary conditions. For example, heat supply from air (gas) flow over the porous medium or indirect heat supply into the material may be of importance, especially in case of non-isothermal drying. Moreover, the behavior of drying reflects not only the interplay between mass and heat transfer in the adjacent gas-side boundary layer (which could be affected by the temperature, relative humidity, and flow velocity of the surrounding air) but also the properties of fluid flow within the porous medium.

Nevertheless, global drying kinetics is used to describe the characteristics of the drying process. This is done in the form of a relationship between the drying rate ( $dS/dt$  or  $dX/dt$ ) and the overall saturation ( $S$ ) or the moisture content ( $X$ ). Most of the porous media undergo a 1<sup>st</sup> drying period and a 2<sup>nd</sup> drying period (Fig. 1.5). The 1<sup>st</sup> drying period is defined by constant drying rate, i.e. by values of  $dS/dt$  or  $dX/dt$  that vary little with liquid content. This phenomenon is frequently and easily observed with non-hygroscopic porous media. However, an initial drying period (IDP), in which drying rate demonstrates a sharp drop, is found for some porous media with high obstacles to liquid transport (Srikiatden and Roberts, 2007). This very first period may be overseen or overlaid by

the inaccuracy of classical experimental measurements of the moisture content of porous media, such as gravimetric drying experiments, especially since the mass of the liquid evaporated during this period is very much smaller compared to the liquid trapped in the porous medium. Contrary, this drop of the drying rate could be clearly indicated through improved technical tools for the measurement of the liquid content of the sample, such as X-ray microtomography or nuclear magnetic resonance (Gupta et al., 2014).

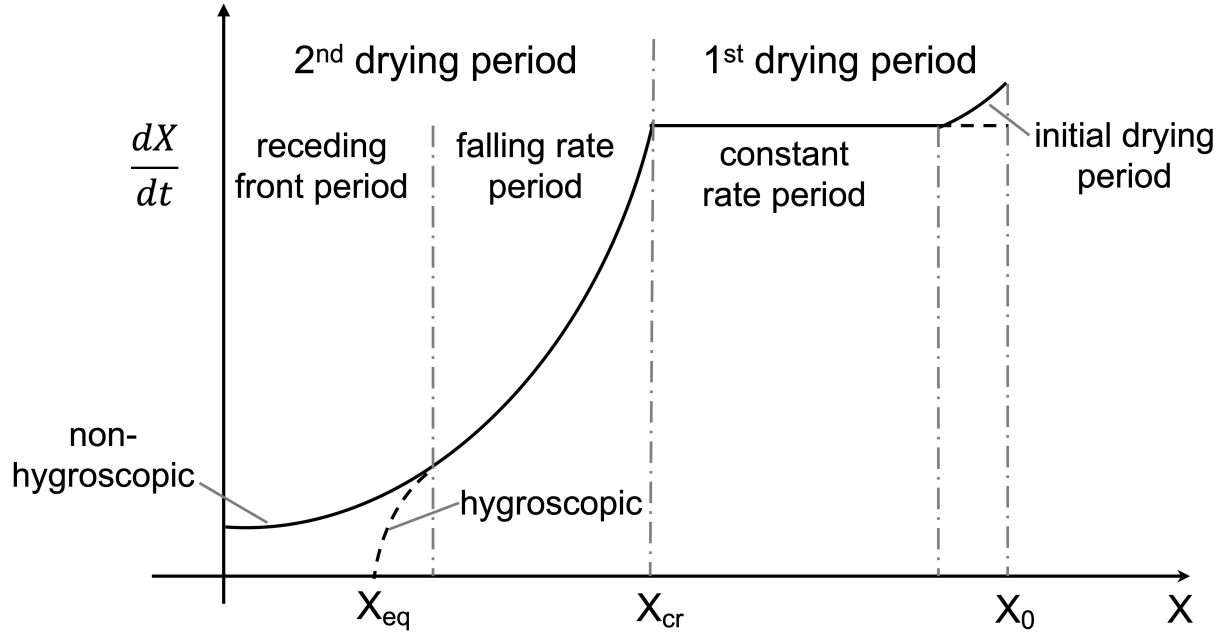


Figure 1.5: Scheme of drying rate curves for hygroscopic and non-hygroscopic (capillary) porous medium.  $X_0$  is initial liquid content,  $X_{cr}$  critical liquid content, and  $X_{eq}$  equilibrium liquid content. Four periods are presented: Initial drying period, constant rate period, falling rate period and receding front period.

Constant drying rate is the typical behavior in the 1<sup>st</sup> drying period. In this period, the capillary pumping and the internal film flow maintain the liquid content at the surface at a level that enables the liquid flux from the porous medium to meet the demand of evaporation rate (Prat, 2002). As a result, the drying rate remains constant and the surrounding gas is saturated with vapor at the surface of the porous medium. Therefore, the drying rate in this period is controlled by external conditions, i.e., external free diffusion length, temperature, and flow velocity of surrounding air.

The second drying period appears after the 1<sup>st</sup> drying period at the critical moisture content. The second drying period contains the falling rate period and the receding front period. During the second drying period, the capillary forces can no longer bring enough liquid from the depth of the porous medium to the medium surface, leading to a decline in the evaporation rate. The starting saturation of the second drying period is defined as the critical saturation or irreducible saturation. The value of the irreducible saturation is a transport property that results from the competition of capillary forces, viscous forces, gravity forces. This value also associates with drying conditions, dimension of the porous

medium and its inner pore structure. A full discussion of the irreducible saturation against heterogeneity of the capillary porous media is presented in Chapter 10.

The phenomenon behind the falling drying rate is the shrinkage of surface liquid coverage, which leads to the drop of vapor pressure adjacent to the surface below the saturation pressure. The vapor pressure at the surface directly controls the performance of evaporation. Thus, the relative humidity is defined to indicate the actual vapor pressure,  $P_v$  (Pa) over the saturated vapor pressure,  $P_v^*$  (Pa), at a given temperature,  $T$  (K):

$$\varphi = \frac{P_v}{P_v^*(T)}. \quad (1.9)$$

For hygroscopic materials, the correlation of the residual saturation (or moisture content) in the porous medium with relative humidity at equilibrium is named sorption isotherm. Brunauer (1944) observed five typical types of sorption isotherms. They all show that the liquid content reaches zero at zero relative humidity. If the relative humidity of the gas is though larger than zero and the material is hygroscopic, an equilibrium liquid content is reached after the drying process (Fig. 1.5). The remaining liquid in hygroscopic materials cannot be removed by the drying process unless the state variables of this process (gas humidity, temperature, pressure) are changed favorably.

Additionally, internal transport resistance increases during the falling rate period, when the liquid cannot be directly transported to the outer surface. Instead, the liquid is locally transformed into vapor and then transported by vapor diffusion towards the surface. Liquid transport is prevented because the connected liquid phase is broken into dispersed isolated liquid clusters, the number of which increases in the falling rate period.

The consequence of continuous growth of internal resistance is to reduce the surface saturation, form a dry region near the surface, and push the liquid-vapor region away from the surface. These phenomena occur in the receding front period. The evaporation rate in this period drops dramatically.

In addition to drying curves, the saturation (moisture) profiles provide details of the drying process. Saturation profiles record the local distribution of the liquid along the major direction of mass transfer during drying. Figure 1.6 shows schematically classical profiles for a capillary porous medium at two instants during drying. The saturation is evenly distributed during the constant drying period (Fig. 1.6a). In contrast, the liquid has been completely removed from the vicinity of the open surface, whereas saturation at the bottom may remain constant in the falling rate and in the receding front period (Fig. 1.6b).

The drying front is the interface at which evaporation takes place. It may be curved and distributed over a certain length of the porous medium. This length is the width of the drying front. The width of the drying front can be indicated on the saturation profile, see Fig. 1.6, and depends on the transport mechanism. For example, a sharp drying front is

observed during the drying of some building materials, such as gypsum (Pel and Landman, 2004). Pore network drying simulations with liquids of high viscosity resulted in drying fronts with limited width (Metzger et al., 2007b).

To favorably manipulate the drying process, reliable models that can describe the basic physical mechanisms are needed. Such models could be used for optimizing the drying process in order to reduce the drying time and thus lower the energy supply. In the following section, we introduce two approaches for modeling of the drying process.

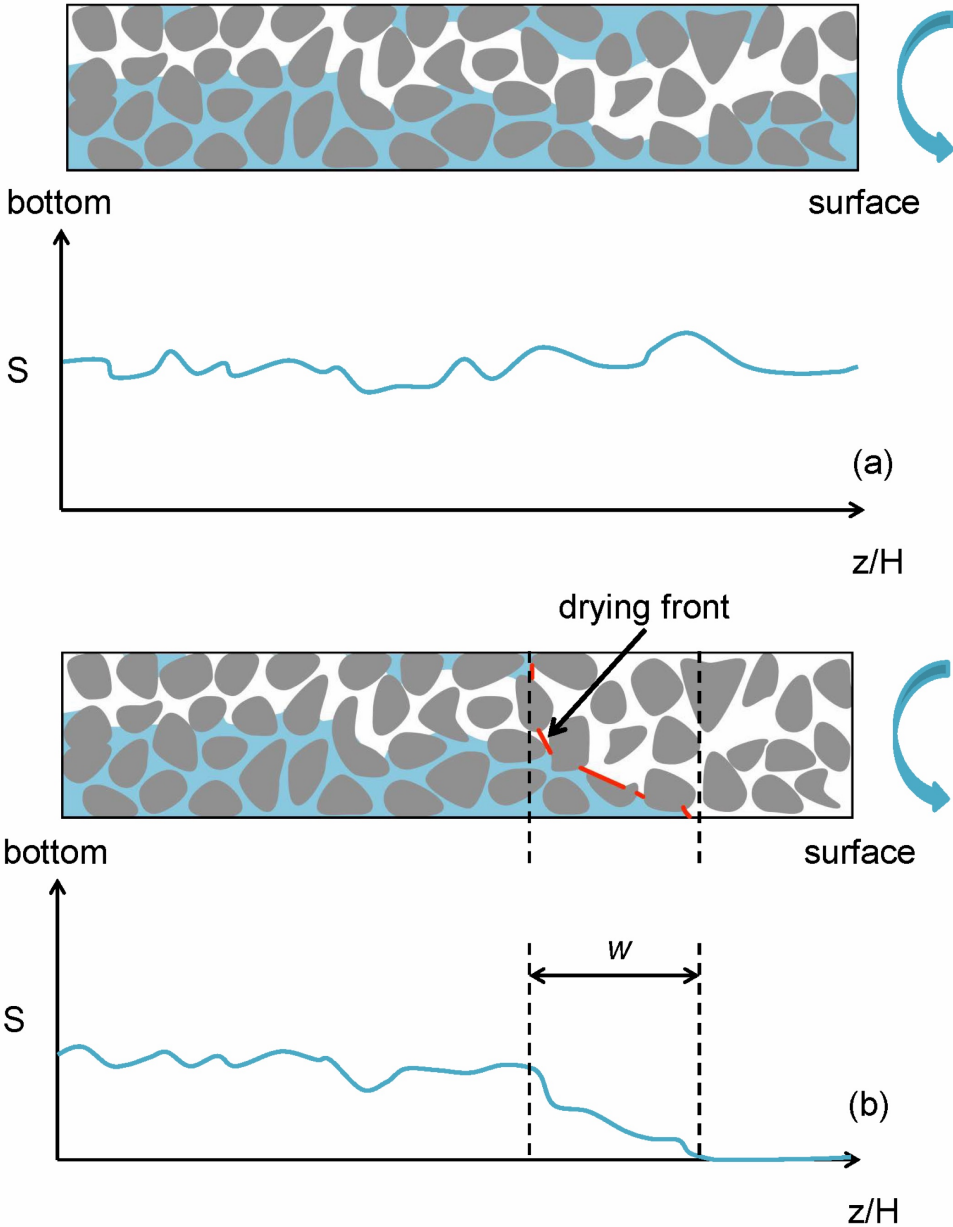


Figure 1.6: Scheme of saturation profiles characteristic of (a) 1<sup>st</sup> drying period and (b) 2<sup>nd</sup> drying period.

### 1.1.3 Drying models

Regardless of the application field, mathematical models are generally developed at two levels of model hierarchy: At the macroscale, a partially saturated porous medium is described as a continuum and the state variables are computed as smooth functions of space and time. The corresponding set of equations is referred to CM (Whitaker, 1977). On the other hand, PNMs are developed to describe transport phenomena in partially saturated porous media at the pore scale. A PNM approximates the void space within a porous medium as a network of pores and nodes. Simple physical laws applied to each pore result in large systems of algebraic equations with degrees of freedom at each node of the pore network. Details of these two approaches will be discussed in the following.

#### 1.1.3.1 Continuum model

The most advanced CMs are developed within the framework of the volume averaging technique. The underlying transport phenomena are described by gradients in spatially-averaged quantities and controlled by nonlinear parameters (Philip and de Vries, 1957; Whitaker, 1977) (Fig. 1.7). While the CMs are readily competent on the application side, they require macroscopic parameters and suffer from significant shortcomings in theoretical aspects. Macroscopic transport parameters are usually acquired by experiments. For example, Pel et al. (1993, 1996) and Marchand and Kumaran (1994) measured moisture concentration profiles and then derived the moisture diffusivity ( $D$ ), by adding liquid ( $D_w$ ) and vapor ( $D_v$ ) phase diffusivities, as a function of moisture content for building materials. Pel et al. (1993) distinguished the variation of moisture diffusivity with moisture content into three regimes. At high saturation, moisture transport is dominated by liquid transport. With decreasing moisture the large pores are drained by gas and no longer contribute to liquid transport, so that moisture diffusivity decreases. When the liquid within the sample no longer forms a continuous phase, moisture transport is governed by vapor pressure. Gómez et al. (2007) calculated permeability for the liquid phase ( $k_w$ ) and the vapor phase ( $k_v$ ) by recording the capillary pressure profile with global saturation along the drying process, to then obtain by conversion the moisture diffusivity ( $D$ ).

In general, the determination of macroscopic parameters is key to the CM, but not easy. One major issue is to, without destroying the samples, observe the liquid distribution inside the porous medium in three-dimensions along the drying process. Although X-ray tomograms are readily used to extract the structure of porous media, recording the liquid distribution is still demanding (Wang et al., 2012). It is easier to capture images of the drying process for pseudo-two-dimensional transparent micromodels, such as a single layer of packed beads confined between transparent glass plates (Sun et al., 2016; Kharaghani, 2020).

Macroscopic parameters are typically reported as nonlinear functions against saturation.

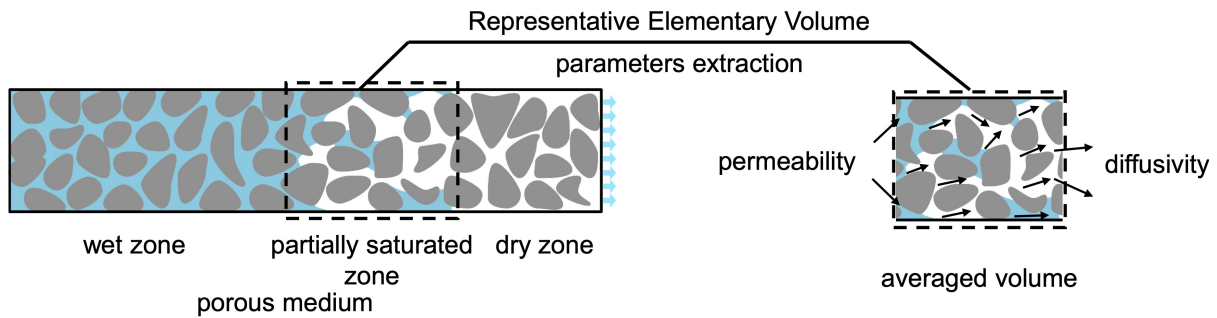


Figure 1.7: Schematic of the averaging volume of the porous medium for the continuum model.

For example, the relationship between capillary entry pressure and saturation can be described as a power law (Brooks, 1966). Pel et al. (1996) determined the moisture transport coefficient from measured moisture concentration profiles, showing that the moisture diffusivity does not decrease continuously with progressing drying process, but is enhanced again at small moisture content by vapor transport. Moreover, macroscopic properties are highly associated with pore structure, i.e. mean radius, standard deviation, etc. Brace (1980) reported the range of permeability to span more than 13 orders of magnitude for various natural porous materials because of significant variation in pore structure.

Apart from macroscopic transport parameters, the CM also needs surface parameters. Critical, here, is the relative humidity. The surface is classically assumed to be at saturation vapor pressure (relative humidity equal to unity) during the 1<sup>st</sup> drying period (Carmeliet et al., 2004; Gómez et al., 2007; Haghghi et al., 2013). Lockington et al. (2003) used the boundary condition of constant velocity of a drying front moving into the material during the second stage of drying. Pel et al. (2002) applied at the surface the relative humidity which is determined by the desorption isotherm for hygroscopic material. In contrast, for the non-hygroscopic material, as we discussed, the relative humidity at the surface of the capillary porous medium demands a better explanation. Additionally, the surface diffusion coefficient also appears in the CM. In Chapter 8, we revisit the surface of the porous medium from the microscale approach, then evaluate macroscopic parameters. The derivation of CMs from the basic mass balance equations and the implementation of suitable parameters are explained in Chapter 4 and Chapter 5.

### 1.1.3.2 Pore network modeling

While CMs are easily applicable, predicting the transition between the 1<sup>st</sup> drying period (with nearly constant drying rate) and the 2<sup>nd</sup> drying period (with a significant decrease in drying rate) remains a challenge. Moreover, it is clear that the drying characteristics are the manifestation of interactions that take place with fluid at a microscopic level

within the porous matrix. Thus, PNMs were introduced as a tool to provide details about the interplay of microstructure with transport mechanisms, having been successful in describing problems that involved two- or multi-phase flow. In early PNMs of drying by Prat (1993) the drying process is treated as an invasion percolation phenomenon (Wilkinson and Willemsen, 1983) driven by evaporation. Later on, more versatile PNMs were developed by several research groups (Yiotis et al., 2001; Metzger and Tsotsas, 2008).

For example, Prat (1993) and his group included the effect of gravity and later Metzger and Tsotsas (2008) considered liquid viscosity while extending the models from two to three dimensions. By incorporating these two critical effects, PNMs were able to provide realistic fluid distributions with liquid clusters and single menisci. Although such simulations enabled to express the essential characteristics of drying kinetics, the time predictions for reaching a given saturation level during the 2<sup>nd</sup> drying period did not correspond well with experiments, even for the simple case of slow isothermal drying of packing of particles. One possible explanation is that an essential fluid transport mechanism, referred to as the film effect, was still neglected in the PNMs. The film effect, which has been observed to have a substantial impact during the drying process in packings of spherical particles (Yiotis et al., 2012), was first included in two-dimensional PNMs (Prat, 2007).

It should be noted that computational cost sets limits to the application of PNMs. For example, Le et al. (2016) only worked on a  $50 \times 44$  two-dimensional pore network to study the heat transfer in drying. While, for the slow drying process, the network size was  $25 \times 25 \times 51$  in Attari Moghaddam et al. (2017a). Through all literature, the simulated size of the network could hardly ever reach the size of real materials subjected to drying in industrial applications.

In summary, PNMs like those which are developed and described in Chapter 2 can offer a detailed solution of the transport process that can pinpoint every pore of the porous medium. However, the current computation power sets limits to their application. Therefore, it needs a method to couple properties from the microscale (PNM) to the practical approaches at the macroscale (CM).

#### **1.1.4 Surface of porous media**

The drying of a capillary porous medium often includes a long constant rate period (CRP) in which the evaporation rate slightly varies with liquid content. Under the capillary dominated regime, the capillary pumping and the internal film flow maintain the liquid content at the surface at a level that enables the liquid flux from the porous medium to meet the demand of evaporation rate (Prat, 2002). The capillary dominated regime is identified that the characteristic width under controlled by the capillary force is longer than the length of sample. The isothermal slow drying process (drying under the room temperature) is a simple limiting case, for which equimolar diffusion can be assumed as the mechanism of mass transfer in the gas-side boundary layer. Schlünder made an attempt to

explain the experimentally often observed existence of a long CRP by an idealized model for the conditions that prevail at the surface of the porous medium (Schlünder, 1988). He assumed an even distribution of squares of size  $(2l \times 2l)$  on the surface, with a hemispherical droplet placed in the center of each of them (Fig. 1.8). When the diameter of the wet patch ( $2r$ ) is much smaller than the thickness of the external diffusion layer ( $\delta$ ), Schlünder obtained following correlation of actual evaporation rate ( $\dot{M}_{ev}$ ) to the evaporation rate of a completely wet surface ( $\dot{M}_{ev,I}$ ):

$$\frac{\dot{M}_{ev}}{\dot{M}_{ev,I}} = \frac{1}{1 + \frac{2r}{\pi\varepsilon} \sqrt{\frac{\pi}{4\Psi_{surf}}} \left( \sqrt{\frac{\pi}{4\Psi_{surf}}} - 1 \right)}. \quad (1.10)$$

Here,  $\Psi_{surf}$  is the relative wetted surface area (surface wetness), calculated as:

$$\Psi_{surf} = \frac{\pi r^2}{(2l)^2}. \quad (1.11)$$

The effect behind Eq. 1.10 is that when lateral diffusion is fast enough, the whole square appears (seen from the upper end of the boundary layer) to be at (nearly) saturation pressure. When this is fulfilled, nearly CRP conditions are obtained. If it is not (or not anymore) fulfilled,  $\dot{M}_v$  falls significantly below CRP evaporation rate  $\dot{M}_{ev,I}$ .

While very illustrative in explaining how CRPs with maximal evaporation rate can possibly exist, Schlünder's model is far less adequate for capturing the complexity of the drying process in accurate computations. For example, the heterogeneous nature of the porous medium surface may have an influence on drying rate. Talbi and Prat (2019) discussed how the shape of droplets at the surface may affect the evaporation rate, whereby the distribution of wet patches at the surface can also play a role. A transition period where the drying rate exhibits a distinct and sudden drop from the initial drying rate appears in many experimental as well as simulation works (Metzger et al., 2007a; Shahraeeni et al., 2012; Attari Moghaddam et al., 2017b).

Recently, the opportunities offered by PNM to view surface behavior during the drying process have started being used. Assuming liquid transport in the capillary regime and external mass transfer by diffusion, Attari Moghaddam et al. (2018) observed that two types of pores (dry and wet) contribute to the mass transfer from the surface. This result contrasts with the Schlünder assumption of the whole surface being covered with wet patches. Attari Moghaddam et al. (2018) also tested Schlünder's model from the PNM side. Applying Eq. 1.10 with the radii of specific surface throats and then averaging over the surface, evaporation rates have been evaluated which did not match well with the results obtained directly from the PNM. Talbi and Prat (2019) have also reported that the Schlünder formula leads to a poor prediction when upscaling from a single wet patch

to a heterogeneous surface, especially in case of low wetted surface area.

Nevertheless, it is important to focus the interest on the surface of drying porous materials, primarily because the surface couples the internal and the external mass transfer. Lehmann and Or (2013) used the Schlünder relationship to link these two mass transport regions for wet pore clusters that reach the drying surface. However, it has also been pointed out that the Schlünder formula fails to estimate the evaporation rate when the surface contains no liquid (Or et al., 2013).

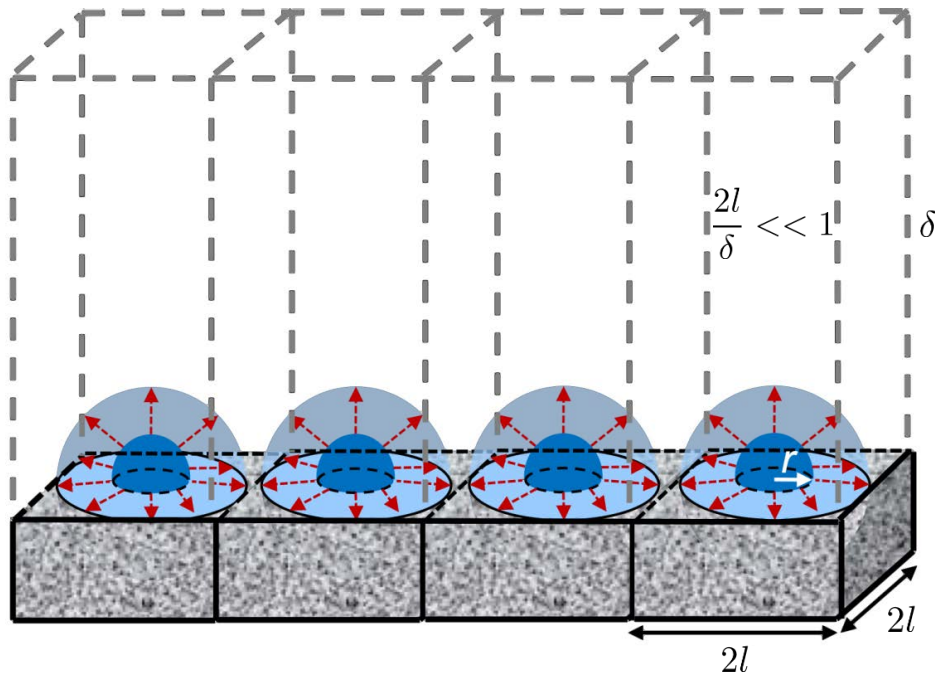


Figure 1.8: Scheme of Schlünder’s model: When vapor pressure can be equilibrated by diffusion in regions (light blue) that surround small wet spots (dark blue) at the bottom of a thick gas-side boundary layer, a partially wetted surface is expected to show approximately the same evaporation rate as the fully wetted surface.

The difficulty in defining boundary conditions for drying porous media by means of, e.g., the Schlünder formula for calculating the evaporation rate does not even arise when using the discrete pore network model, because such a model directly couples the internal with the external mass transfer by applying mass balances and momentum balances at the microscale. However, pore scale resolution in the description of internal transport phenomena makes the simulation algorithm time-consuming, and the computational cost becomes even higher if the external flow field has to be additionally computed by solving the Navier-Stokes equations (Weishaupt et al., 2019). Therefore, and though PNM simulations are valuable for analysis at the microscopic level, easily solvable CM must typically be used in order to describe the drying process for industrial applications at the macroscale.

However, as soon as coarsening to CMs becomes an issue, appropriate boundary conditions are, again, necessary. For example, the one-equation CM requires the external mass

transfer rate as a boundary condition. The external mass transfer can be described by Fick's law,

$$\dot{m}_v = \frac{D_{v,a} \tilde{M}_v}{\tilde{R}T} \frac{P_{v,surf} - P_{v,\infty}}{\delta}, \quad (1.12)$$

where  $P_{v,\infty}$  (Pa) denotes the vapor pressure in the bulk air,  $P_{v,surf}$  (Pa) the vapor pressure at the surface,  $\delta$  (m) the boundary layer thickness located between the network surface and the bulk air.  $\tilde{M}_v$  (kg/kmol) is the molar mass of vapor and  $T$  (K) is the temperature.  $\tilde{R}$  (J/(kmol · K)) is the universal gas constant.

The vapor pressure at the surface is typically assumed to be equal to the saturation pressure when the surface contains liquid (the drying process is assumed to be in the first drying period) (Shokri et al., 2008; Haghghi et al., 2013; Mosthaf et al., 2014). When the drying front recedes (in the FRP), the surface vapor pressure is determined by the desorption isotherm (Pel et al., 2002; Pel and Landman, 2004). It is though inaccurate to assume CRP drying rate even when the surface contains only a small amount of liquid and consider the FRP to occur only after a drying front has started to recede from the surface into the interior of the material. In fact, the drying curve for the viscous case typically demonstrates a short CRP or no CRP at all, that is to say, the falling rate period appears when the surface still contains liquid, as has been shown in many works (Defraeye et al., 2012; Attari Moghaddam et al., 2017a). Therefore, the previously described approach is too coarse and needs refinement. The new method to treat the surface is presented in Chapter 8.

### 1.1.5 Pore structure

The drying process of porous media is based on the interplay of fluid transport with the solid matrix. The role of pore structure in the drying process has been revealed by Metzger et al. (2007b). To this purpose, an isothermal model that included capillary and liquid viscous effects was applied to drying networks of different structures. It has been reported that the drying rate decreases from the beginning for monomodal pore size distribution, neglecting the film effect. However, a network with bimodal pore size distribution, featuring large pores in the vertical direction to the surface, demonstrated an extended first drying period. The longer first drying period improved the drying rate. Later, more complicated bimodal networks, i.e. long channels in both space directions and regular distribution of small clusters, were discussed in term of drying rate and phase distribution (Metzger et al., 2007c). It was found that the drying rate increases when the long macro-channels are placed perpendicularly to the network surface. The reason is that viscous forces have little effect, even for smaller pore dimensions, because the capillary pressure difference between micro- and macro-pores is usually sufficiently large (Metzger et al., 2007b). Note that as the drying process is related to pore structure, macroscopic parameters should be correlated to it. In this work, we will discuss the behavior of macroscopic parameters for

networks of different pore structure (Chapter 9).

### 1.1.6 Parameters in capillary pressure function

Invasion percolation (IP) introduced by Wilkinson and Willemsen (1983) provides a realistic description of the slow biphasic fluid displacement processes in porous materials. IP is relevant to various applications (such as secondary oil recovery) and was generally used to model a drainage process during which a wetting fluid is displaced by a nonwetting fluid (Chandler et al., 1982). IP was also used to model imbibition where a wetting fluid invades a porous medium originally saturated by a nonwetting fluid (Mason and Mellor, 1995). Moreover, the IP algorithm was adapted to describe immiscible displacement in drying porous media (Prat, 1993).

Invasion percolation is driven by the capillary pressure  $P_c$  which can be modeled with the normalized or effective wetting-phase saturation as proposed by Brooks (1966):

$$S_e = 1 \quad (P_c \leq P_e), \quad (1.13)$$

$$S_e = \left(\frac{P_c}{P_e}\right)^\lambda \quad (P_c \geq P_e). \quad (1.14)$$

where  $P_e$  (Pa) and  $S_e$  denote the entry pressure and effective saturation, respectively. The scaling parameter  $\lambda$  denotes the pore size distribution index which must be determined experimentally for each porous medium.  $P_e$  describes the minimum air pressure that needs to act on the liquid phase prevailing in the medium to allow the air to invade the porous medium.  $S_e$  is a linear function of saturation  $S$  and related to the irreducible saturation  $S_{irr}$ , defined as:

$$S_e = \frac{S - S_{irr}}{1 - S_{irr}}. \quad (1.15)$$

The irreducible saturation  $S_{irr}$  defines the amount of liquid that the medium with a given pore structure can retain. This liquid is held in the medium by capillary forces and cannot be removed by the capillary pressure.

To investigate whether and how irreducible saturation is correlated with the microstructure of porous media, it may be worth to make an analogy between irreducible saturation in the capillary-controlled invasion process and mercury entrapment in porosimetry, as these processes share common principles. In porosimetry mercury cannot be retracted from a large pore unless a meniscus appears at one end of that pore so that mercury can penetrate to the surface. Thus, if a large pore is embedded in a network of fine pores, it remains full unless some fine pores evacuate at some lower extrusion pressure - this effect is referred to as shielding effect (Conner and Lane, 1984; Conner et al., 1987). Portsmouth and Gladden (1991) remarked that there is a characteristic entrapment of mercury in a network of pores with Gaussian pore size distribution (PSD), which depends on the

ratio of the standard deviation of the distribution to the mean pore radius - this ratio is called coefficient of variation and defines the width of the PSD. Further, Conner and Lane (1984) performed analyses and have concluded that higher connectivity can yield lower entrapment of mercury. Other researchers have also disclosed the fact that topology of the medium and spatial correlations between pores and throats can influence porosimetry results (Portsmouth and Gladden, 1991; Tsakiroglou and Payatakes, 1991; Knackstedt et al., 2001).

Nevertheless, the irreducible saturation does not have the same correlations with microstructural features as the mercury entrapment. Isolated mercury from the bulk of the network is forced to move if the Laplace equation is fulfilled when continuously decreasing the nonwetting phase pressure. That is to say, the mercury in sites surrounded by narrow void spaces is trapped in the medium when the Laplace equation is not satisfied. However, this situation is different in capillary-controlled invasion processes. For instance, in slow, isothermal drying an isolated liquid cluster is considered as stationary when the liquid in this cluster cannot move into neighbor clusters by increasing the capillary pressure that acts on the network, but the liquid can continuously be reduced by evaporation so that the moisture is transported through the vapor phase. Neglecting evaporation at the isolated clusters would mean that the liquid in the isolated clusters is not reducible because these clusters are surrounded by gas phase saturated with vapor. In such situation, the residual saturation in the network represents the saturation for which liquid can be transferred by the capillary pressure out of the porous medium. Thus, mercury porosimetry can provide information on the geometry and topology within the porous medium, but the irreducible saturation indicates a transport property.

Besides the irreducible saturation, the Brooks and Corey capillary pressure model also requires the entry pressure  $P_e$  (or bubbling pressure). The entry pressure, as defined by White et al. (1970), is the capillary pressure at the inflection point on the capillary pressure-saturation ( $P_c$ - $S$ ) curve, where the value of  $dP_c/dS$  is a minimum at high saturation. Early numerical studies conducted at the pore scale show that the entry pressure depends on the interplay of the pore geometry and wettability of the porous medium (see, e.g., Rabbani et al., 2016 and references therein). Further, on the basis of pore scale simulations, Raeini et al. (2012) suggested that the entry pressure increases as the pore body to pore throat contraction ratio increases. Ferrari and Lunati (2013) assumed perfect water-wet conditions, similar to Raeini et al. (2012) but contrary to Rabbani et al. (2016) and conducted two-phase flow numerical simulations. The results of which indicate that the entry pressure is marginally dependent on the viscosity ratio and capillary number.

The pore size distribution index of the network is also an essential parameter of the Brooks and Corey capillary pressure model, which represents the heterogeneity of the porous medium. The heterogeneity can be characterized using a fractal model, which reflects the relationship between the number of pores and pore radii. Kewen (2004) reported

that the pore size distribution index increases with a decrease in the fractal dimension of the porous medium. Overall, many researchers reported the pore size distribution index as a specific value to express the fractal nature of pores in a porous medium under the Brooks and Corey capillary pressure model (Moseley and Dhir, 1996; Kewen, 2004). However, the heterogeneity of the porous medium is poorly captured in this parameter. As can be seen from the Brooks and Corey capillary pressure model, the pore size distribution index correlates the capillary pressure with the saturation. By contrast, the capillary pressure depends on the meniscus size distribution in the liquid cluster. Thus, it is worth to reconsider whether the pore size distribution index (as an index for network heterogeneity) can estimate the capillary pressure.

The Brooks and Corey capillary pressure model (Eqs. 1.13 to 1.15) has widely been utilized for several decades in petroleum and other industries (Kjosavik et al., 2002). And, the fact that this model can be put on a solid theoretical base has already been proven by using the fractal approach to porous media (Kewen, 2004). However, this model stands at the macroscopic level and thus neglects microscale morphological and topological information of a porous medium such as the heterogeneity of the pore size distribution and randomness in pore connectivity. Therefore, it is interesting to revisit the macroscopic parameters in the Brooks and Corey capillary pressure model and reveal the internal correlation of these parameters with the heterogeneity of porous media.

Experimental identification of relations between the macroscopic parameters (i.e.  $S_{irr}$ ,  $P_e$  and  $\lambda$ ) and the pore structure is, though, not straightforward due to the difficulty in accessing the geometrical features of porous media. Another possibility is to utilize the opportunities offered by PNMs.

## 1.2 Aim

The aim of this thesis is to create pore scale resolved data for drying porous media by PNMs, and then derive from such data parameters that can be used in the frame of CMs for quick computations at the macroscale. Nontrivial upgraded CMs that can otherwise not be derived and parameterized are the target.

To reach this aim, we have to fulfill the following conditions: First, the PNM should be able to produce a reliable relationship between drying process characteristics and saturation. Second, we should be able to derive usable macroscopic parameters from the dataset generated by the PNM. Additionally, an upgraded CM should be able, by means of appropriate parameters, to reproduce the drying process at the macroscale. In short, we have to handle three issues, at least, in the current thesis: a reliable PNM, proper macroscopic parameters, and a sophisticated parameterized CM.

### 1.2.1 Pore geometry in PNM

As discussed, PNMs become more sophisticated by more comprehensive consideration of the underlying transport mechanisms in order to improve the prediction of the drying characteristics. Another aspect that might influence the performance of PNM is the way that the structure of voids within the drying porous materials is modeled: Yiotis et al. (2001, 2015) treated the entire void space as pore bodies, leaving throats as conductors and capillary barriers. This approach is suitable for materials with large pore volumes, such as granular materials. Prat (1998) and Metzger et al. (2007a) approximated the void space using hydraulic pore throats and numerical pore nodes. This model is referred to as the throat-node model (TNM) (Fig. 1.9a). Although this approach extended the application range of PNMs, it has the drawback that the void space may be overestimated. In the TNM, the void space is calculated by summing all throat volumes, which are considered as cylinders with a fixed length. Based on the assumption that throats are connected with numerical nodes, there is a region of overlap at each node. If one adds all throat volumes in TNM to yield the void space of a porous medium while ignoring the overlap region, then the void space is overestimated (Fig. 1.9b). This problem was recognized by Attari Moghaddam et al. (2018) when they applied TNM to study the surface phenomena that occur during drying of non-hygroscopic porous media. They obtained a high value for the irreducible saturation  $S_{irr}$  (i.e., the saturation at which liquid stops being transported via capillary effects from bottom to top of the drying porous medium) at network porosity  $\varepsilon = 0.594$  (higher than the average porosity of beds packed with mono-sized spherical particles,  $\varepsilon \approx 0.4$ ).

In contrast, the throat-pore model (TPM), in which both cylindrical throats and spherical pores contain liquid and contribute to moisture transport is used in the present work (see Fig. 1.9c). This network geometry would solve the overlap region dilemma in the TNM. We focus on a slow, isothermal drying process based on invasion percolation of the gas phase and viscous flow of the liquid. This kind of TPM has been used by Moebius and Or (2014) to study the dynamics of displacement fronts in drainage and by Le et al. (2017) for superheated steam drying, though in two-dimensional space. However, there is no detailed comparison between TNM and TPM in previous literature, not even for the slow, isothermal drying process. This gap is closed in the present work. Such comparison will clarify the reason for the overestimation of the irreducible saturation by the TNM (see Chapter 3). Thus, we would expect the TPM to provide a reliable description of the change in drying characteristics with the saturation.

### 1.2.2 Issues of the current continuum model and its parameterization

Let us briefly discuss the parameterization of CMs. Recently, Attari Moghaddam et al. (2017b) evaluated the classical CM using parameters obtained from a PNM. The evaluation

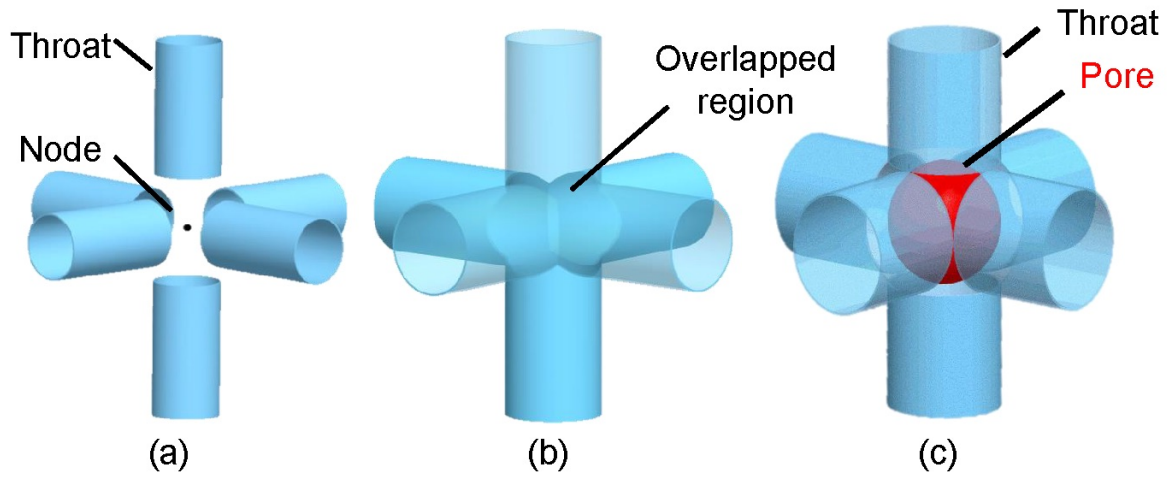


Figure 1.9: Approximation of the pore space by a) the throat-node model with distances of the ends of the throats from the node, b) the throat node model with volume overlap at the node and c) the throat-pore model.

resulted in fair but not perfect agreement when comparing saturation profiles from PNM and CM for the drying process. Attari Moghaddam et al. ignored the significant scatter in moisture transport coefficients obtained from the PNM, especially in the high local saturation region, and fitted their data by three smooth curves. This approach can destroy certain transport information contained in the primary dataset. This may be a reason why they could not match saturation profiles at the surface of the porous medium, particularly in the beginning of the drying process. Besides, they realized that fitted moisture transport coefficient profiles could not capture the transport process in the empty region (i.e. when  $S < 2 \times 10^{-4}$ ) of the porous medium. They tackled this issue by recalculating parameters in their CM based on the identified evaporation rate from the PNM. However, this treatment of the empty region by Attari Moghaddam et al. (2017b) limits the applicability of the CM, because the evaporation rate is one expected outcome from the CM. To improve the performance of the CM, modified versions of this model will be presented in this thesis.

### 1.2.3 Macroscopic parameters

As discussed, Attari Moghaddam et al. (2017b) treated the PNM dataset very coarsely, which destroys certain transport information contained in the primary dataset. For example, Attari Moghaddam et al. (2017b) showed three non-linear curves  $D(S)$  over the whole drying process. Each curve could be separated into two parts: values scattered when the local saturation was larger than 0.68 but became clear for local saturations smaller than 0.68. However, possible reasons behind the scatter of data have not been discussed in their work. Thus, one possible method to improve the performance of CM could be to more precisely consider the local variation of saturation in different states of the evolving drying process in the determination of macroscopic parameters. This could

prevent omitting the critical transport information that prevailed in such datasets.

Additionally, some macroscopic parameters have not been extracted from the dataset by Attari Moghaddam et al. (2017b). So they recalculated the missing information on vapor diffusivity for local saturation smaller than  $2 \times 10^{-4}$ . Rather than re-determination of this parameter, which is associated with the loss of some predictive ability of the CM, we could define additional parameters for that region during the drying process.

In summary, macroscopic parameters are key in reproducing the drying characteristics by CM to reveal the transport information at the pore scale. To this end, this thesis will present which parameters are needed, how to extract these macroscopic parameters, and how to understand these macroscopic parameters.

#### **1.2.4 Pore structure effects on macroscopic parameters**

Closing the gap between microscopic datasets and the macroscopic CM stresses that macroscopic parameters can vary very much with pore structure. To understand the correlation of pore structure with macroscopic parameters, we will focus on aspects such as the mean pore radius, the standard deviation of pore radius, and the presence of bimodal pore size distributions.

Regarding the drying process, Metzger and Tsotsas (2008) investigated how vital is the role of pore structure (with monomodal pore size distribution, i.e. different width of normal radius distribution, and coordination number) in intraparticle heat and mass transfer and thus drying kinetics. They reported that connectivity and spatial correlations of pore size (i.e. macro-channels placed vertically in a network with bimodal pore size distribution) are important for drying behavior (Metzger et al., 2007a). Different drying behaviors could be represented by different macroscopic parameter functions. Therefore, this work will present correlations of macroscopic parameters with pore structure.

### **1.3 Scope of the work**

This thesis aims at bridging the gap between PNM at the microscale and CM at the macroscale. For this purpose, mathematical models at both the microscopic and the macroscopic level are employed. In Chapter 2, we review the existing PNM and modify the most adaptable throat-node model into the throat-pore model. The algorithm of the throat-pore model is introduced.

In Chapter 3, we compare the transport properties of TNM and TPM. We demonstrate how the void space of porous media is represented in those two configurations. The vapor conductance and the liquid conductance are compared, and the dependence of respective ratios between TPM and TNM on the ratio of pore radius to throat radius is also presented. Finally, drying characteristics of the two configurations are compared.

Classical CM is introduced in Chapter 4 and put, in terms of parameters, into the

diffusion-based format. The boundary conditions are also discussed here. However, the existing treatment of boundary conditions sets limitations to applications. Therefore, two modifications of CM are resented in Chapter 5, namely moving front CM and the three-transport-zone CM. The numerical method (finite volume method) to solve the CM is also introduced there.

In Chapter 6, we evaluate the macroscopic parameters needed in the CMs based on PNM datasets. CMs need the moisture transport coefficient, relative humidity in the two-phase zone and at the surface, as well as the parameter of vapor transport in the dry zone and the gas-side diffusion layer. Values and behavior of those macroscopic parameters are discussed.

In Chapter 7, we feed the macroscopic parameters into the CMs. In this process, we have to face the issue of treating PNM datasets. Macroscopic parameters are usually highly dependent on the stage of the drying process (network saturation  $S_{net}$ ) and the local saturation  $S$ . Two essential aspects in treating PNM datasets, averaging over different ranges of network saturation and treatment of local saturation, are discussed in regard of their role in CM performance. A new hybrid method is introduced to capture the interplay of macroscopic parameters extracted from PNM with CMs.

Chapter 8 studies the surface of the porous media from a PNM standpoint. The surface is viewed as empty pores and liquid pores. The surface parameters, i.e., the surface vapor pressure-surface saturation relationship and the surface vapor transport coefficient-surface vapor concentration relationship, are accessed from PNM datasets. Additionally, emendation factors are introduced to link the normalized evaporation rate from the wet part of the porous medium surface with the surface wetness or surface saturation. Besides, the evaporation rate from the wet surface region is evaluated by inserting PNM data into a modified version of Schlünder's model.

In Chapter 9, links between macroscopic parameters and pore structures are explored. For this purpose, the mean radius and the standard deviation of the throat size distribution are systematically altered. Additionally, a bimodal pore size distribution in which macro-channels are vertically and evenly placed in a matrix of micro-channels is investigated.

Another macroscopic parameter, the capillary pressure, is computed based on results obtained from the static PNM in Chapter 10. The classical empirical equation, Brooks and Corey capillary pressure model, is revisited based on the PNM simulations. Parameters required in the Brooks and Corey capillary pressure model (i.e., the irreducible saturation, pore size index and entry pressure) are directly recorded from the PNM, and also their correlation with pore structure is discussed.

Chapter 11 summarizes the main results presented in this thesis and also highlights recommendations for future work.

# Chapter 2

## Pore network modeling

This chapter provides a comprehensive presentation of the pore network model (PNM) with throat-pore configuration (TPM), developed for a capillary porous medium that dries in the capillary-viscous regime.

### 2.1 Introduction

Pore network modeling is a versatile tool to describe transport phenomena in porous media. The PNM that only considers capillary forces (e.g. Prat, 1993; Yiotis et al., 2001) is named as static PNM. The static PNM is straightforward because it avoids the need for pressure computation, and in each invasion step, the invaded throat/pore is the one which has the largest radius according to the Young-Laplace equation (Eq. 1.3). When the liquid viscosity is introduced into PNM (e.g. Metzger et al., 2006), the invasion process cannot be distinguished only based on the size of throat/pore radius. We call this model as dynamic PNM. The dynamic PNM does not rely only on the capillary forces (Eq. 2.1), but also on the viscous forces. The invasion positions in dynamic PNM should be balanced as a whole. For each invasion step, the number of invasion sites and invasion positions is uncertain, which depends on the competition between the capillary pressure and the liquid viscosity. For the development of our present dynamic PNM, several assumptions are made, listed as follows.

Isothermal conditions are assumed, similarly as in many PNM for drying of porous media (Prat, 1998; Yiotis et al., 2001; Metzger and Tsotsas, 2008). Although the isothermal condition is a reasonable assumption only for moderate drying conditions, it allows for a systematic analysis of the involved transport phenomena without the additional complexity of the interplay with the temperature gradient in the porous medium. Nonisothermal pore network models have been proposed by Surasani et al. (2008) and Le et al. (2017), but they were of relatively small size.

Constant gas pressure is considered throughout this work. The vapor transfer in the gas-filled part of the porous medium and the gas-side boundary layer is described by the

logarithmic law for non-equimolar diffusion next to an evaporating liquid-gas interface (Stefan’s law). Since total pressure is constant and there is no net flow of the gas phase, there is no viscous effect considered in the gas. Additionally, both the Kelvin effect (the situation of capillary condensation that is caused by the reduction of equilibrium vapor pressure over the meniscus) and the Knudsen effect (that plays a significant role for diffusion with pore sizes smaller than the mean free path of the gas molecules) are disregarded. These simplifications are justifiable if the mean throat/pore radius is larger than  $100 \mu m$  and drying takes place at room temperature ( $20 \text{ }^\circ\text{C}$ ).

The liquid is assumed as free water occupying fully or partly filled pores/throats. The porous medium is treated as a capillary porous medium, thus any adsorption phenomena are neglected. Liquid film flows are not taken into account in the current model.

## 2.2 Model description

In Prat (1998) and Metzger et al. (2007a), network pore structure consists of cylindrical pore throats and numerical pore nodes. This pore network is called throat-node model (TNM) in this thesis. This network geometry overestimates the void volume at each node. In the present work, a different PNM is also defined on a regular three-dimensional lattice of spherical pores and cylindrical throats, namely a throat-pore model (TPM) (Fig. 2.1).

The drying algorithm is composed of three main parts: The labeling of throats/pores, generation of pores and throats, and the drying algorithm.

### 2.2.1 Labeling of pores and throats

First, we have to label throats and pores comprising a three dimensional network. The numbers of pore layers in  $x$ ,  $y$ , and  $z$  directions are  $N_i$ ,  $N_j$ , and  $N_k$ , respectively. The top layer of the network (network surface in Fig. 2.1), denoted by  $N_k$ , is coupled with the gas-side boundary layer, which contains  $N_{BL}$  layers of pores (including the surface layer). The central distance between two adjacent pores is uniform,  $h = 1000 \mu m$ .

The labeling algorithm depends on the spatial configuration of the network. For example, in a cubic network, a pore is intersected with six throats resulting in coordination number 6. In an octahedron network, a pore is connected with eight throats resulting in coordination number 8. Although details of labeling of the network are different between those two configurations, the principle of labeling is similar, which is to find correlations between pores and throats (pore neighboring throat), between throats and pores (throat neighboring pore), and between pores and pores (pore neighboring pore). The following part shows an example of the labeling process for a cubic network.

Labeling of pores starts along the x-direction from the bottom layer to the top layer. Labeling of throats is swept first along the x-direction (green throats), followed by the y-direction (yellow throats) and finally along the z-direction (blue throats) (Fig. 2.1). The

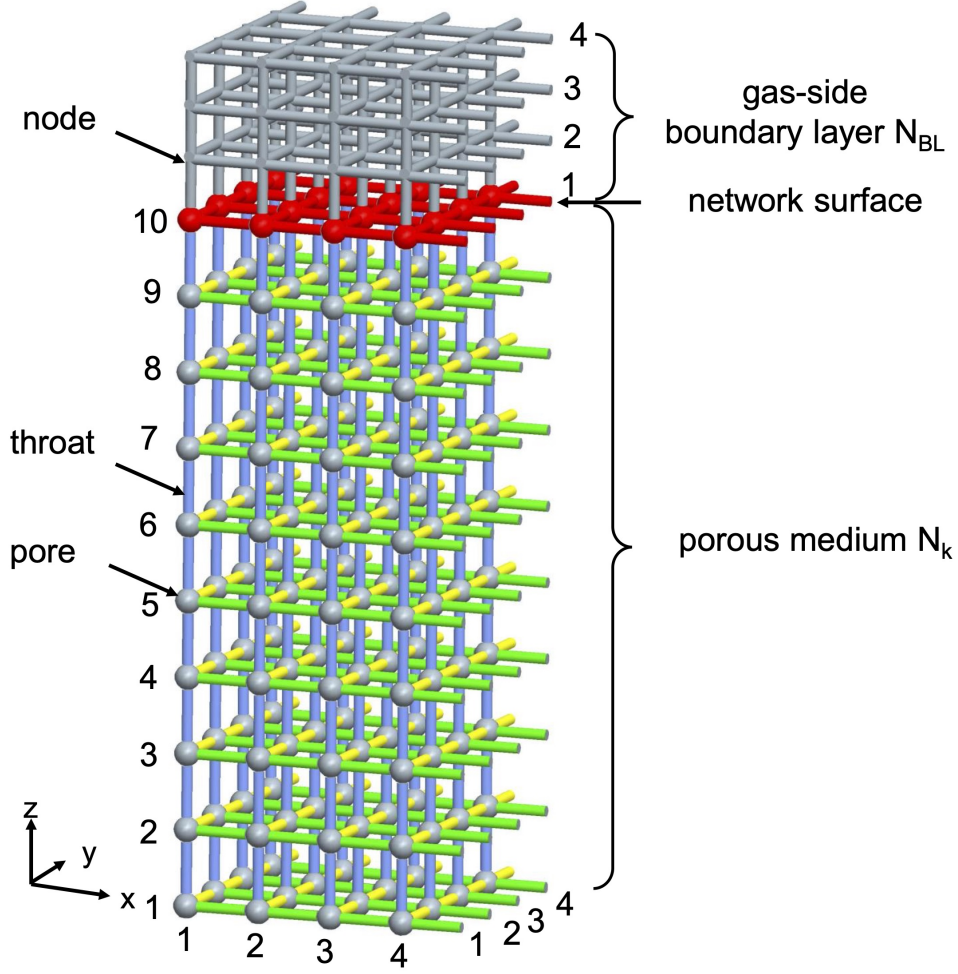


Figure 2.1: Sketch of a 3D cubic pore network ( $4 \times 4 \times 10$ ) with the gas-side diffusion boundary layer ( $4 \times 4 \times 4$ ) on top. Periodic boundary conditions are applied on the lateral faces of the network. The green throats are in x-direction, yellow throats are in y-direction, and blue throats are in z-direction.

labeling of throats in the boundary layer is conducted in the same order after all throats in the network have been labeled. The number of pores in the network is

$$N_p = N_i N_j N_k, \quad (2.1)$$

and the total number of pores (including boundary layer) is

$$NP = N_i N_j (N_k + N_{BL} - 1). \quad (2.2)$$

The number of surface pores is

$$N_{surf} = N_i N_j. \quad (2.3)$$

The number of throats in the network is

$$N_t = 3N_i N_j (N_k - 1). \quad (2.4)$$

It should be noted that in Eq. 2.4 one additional row of throats is counted in x- and in y-direction, because of periodic boundary conditions being used in these directions. The total number of throats in the network (including the gas-side boundary layer) is

$$NT = N_t + (3(N_{BL} - 1) + 2) N_{surf}. \quad (2.5)$$

Following this labeling method, we generate the throat neighbor pore (TNP) and pore neighbor pore (PNP) matrices.

The TNP array ( $2 \times NT$ ) stores the information of neighboring pores for each throat. For the configuration shown in Fig. 2.2 one obtains

$$TNP = \begin{bmatrix} 1 & 2 \\ 2 & 3 \\ 3 & 4 \\ 4 & 1 \\ \vdots & \vdots \end{bmatrix},$$

which is a small part of the array based on Fig. 2.1. Periodic boundary conditions are applied on the lateral faces of the network, which means that, for example, the 4<sup>th</sup> pore is connected with the 1<sup>st</sup> pore through the 4<sup>th</sup> throat. Neighboring pores of each pore are stored in the pore neighboring pore (PNP) matrix. The matrix dimension of PNP depends on the given coordination number. For example, for the geometry of Fig. 2.2, the PNP matrix has a size of  $6 \times NP$ , where 6 means that one pore is connected with six other pores. Figure 2.2 is an example that shows the assignment of neighboring pores (dark blue pores) to the 1<sup>st</sup> pore (the red pore) based on the above labeling method. The 1<sup>st</sup> pore is directly connected to the 2<sup>nd</sup> pore, the 5<sup>th</sup> pore and the 17<sup>th</sup> pore. By applying the periodic boundary conditions on the sides of the network, the 1<sup>st</sup> pore is also linked with the 4<sup>th</sup> pore and the 13<sup>th</sup> pore. The pores neighboring pore 1 are  $PNP[1] = [17 \ 13 \ 5 \ 4 \ 2 \ 0]$ , for example. The PNP matrix for the pores shown in Fig. 2.2 reads:

$$PNP = \begin{bmatrix} 17 & 13 & 5 & 4 & 2 & 0 \\ 18 & 14 & 6 & 3 & 1 & 0 \\ 19 & 15 & 7 & 4 & 2 & 0 \\ 20 & 16 & 8 & 3 & 1 & 0 \\ \vdots & \vdots & \vdots & \vdots & \vdots & \vdots \end{bmatrix}.$$

Thus, a pore is connected with six pores, except pores which are in the top layer and the bottom layer (connected with five pores).

After having generated the matrices TNP and PNP, the matrix pore neighbor throat (PNT) can be calculated by identifying the correlation of pores with throats. For example,

in the 1<sup>st</sup> row of PNP, pore 1 is connected with pore 2. The next step is to find in which row in TNP pores 1 and 2 exist. Thus, we can ensure that throat 1 appears in the 1<sup>st</sup> row of PNT. Applying this algorithm to every element in PNP, the matrix PNT is obtained

$$PNT = \begin{bmatrix} 289 & 157 & 145 & 4 & 1 & 0 \\ 290 & 158 & 146 & 2 & 1 & 0 \\ 291 & 159 & 147 & 3 & 2 & 0 \\ 292 & 160 & 148 & 3 & 4 & 0 \\ \vdots & \vdots & \vdots & \vdots & \vdots & \vdots \end{bmatrix}.$$

The matrix of throat neighbor throat (TNT) is required for the PNM with volumeless nodes. However, for the PNM with spherical pores it is unnecessary to compute the TNT matrix. Additionally, a matrix that records the number of pores neighboring to a throat (NPT) should be generated. For example, NPT[1] is 5 since pore 1 is connected to 5 pores and has 5 throats attached to it.

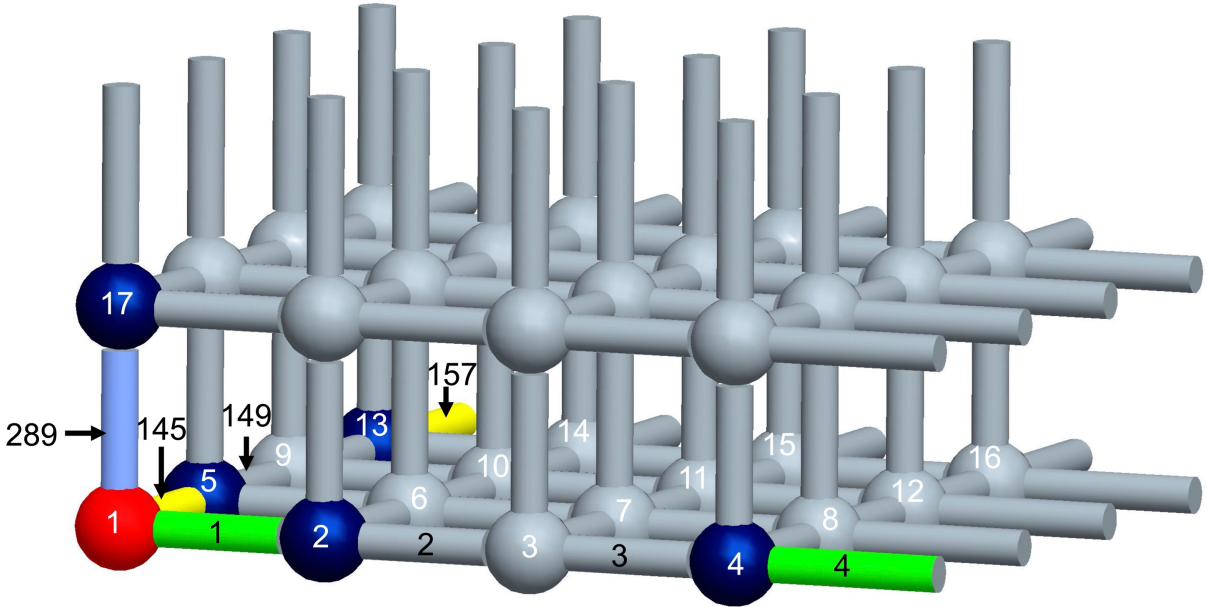


Figure 2.2: An example for the labeling of pores and throats in a network with size of  $4 \times 4 \times 10$  and gas-side diffusion boundary layer ( $4 \times 4 \times 4$ ) on top, as shown in Fig. 2.1.

### 2.2.2 Generation of pores and throats

Throat radii ( $R_t$ ) are sampled randomly from a normal size distribution with a mean of  $\bar{R}_t = 250 \mu\text{m}$  and standard deviation of  $\sigma_{0,t} = 25 \mu\text{m}$ . Using this size distribution and assuming that the pore radius ( $R_{p,i}$  or  $R_{p,j}$ ) is greater than or equal to the largest radius of neighbor throats ( $R_{t,ij}$ ), the pore radius distribution with a mean of  $\bar{R}_p = 283 \mu\text{m}$  and

standard deviation of  $\sigma_{0,p} = 16 \mu\text{m}$  is obtained. Throat-pore networks in Chapters 3, 6, 7 and 8 are generated according to these two size distributions as shown in Fig. 2.4a. However, since the mean and standard deviation of throat/pore radii are systematically varied in Chapters 9 and 10, a check is necessary so as to avoid unreasonable values of throat/pore radii. First, the radii of throats and pores are sampled from the respective size distributions. It is then checked for each throat: If its radius is smaller than zero, it is replaced with a new value calculated as:

$$R_{t,ij} = \Omega \bar{R}_t, \quad (2.6)$$

where  $\Omega$  is a random number between 0 and 1. Thus, we ensure that the throat radius is larger than zero and the pore radius is greater than or equal to the largest radius of neighbor throats.

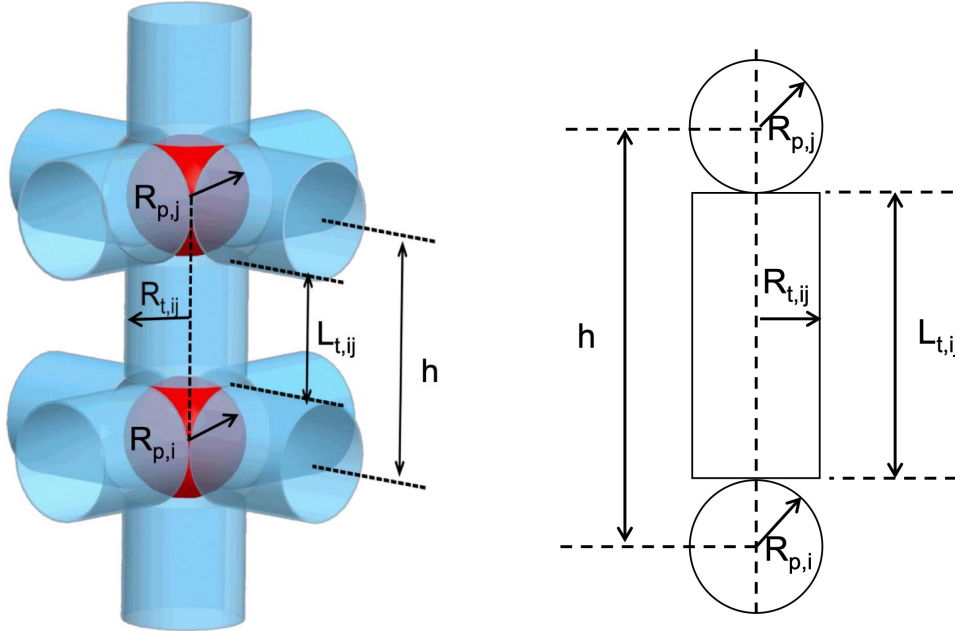


Figure 2.3: Schematic of the throat-pore model (TPM).

To calculate the throat length, the radii of two pores located at the throat ends are subtracted from the center distance between these two pores ( $h = 1000 \mu\text{m}$ ), i.e.  $L_{t,ij} = h - R_{p,i} - R_{p,j}$ . While doing so, it is ensured that  $h > (R_{p,i} + R_{p,j})$ . Figure 2.4b shows the throat length distribution used in Chapters 3, 6, 7 and 8.

After assigning radii to all pores and throats, the array  $(A_{t/p})$  is generated to store the cross-sectional area of pores and throats needed to calculate the flow conductance. The flow conductance of a throat depends on its cross-sectional area ( $A_{t,ij} = \pi R_{t,ij}^2$ ) and the flow conductance of a pore relies on its cross-sectional area ( $A_{p,i} = \pi R_{p,i}^2$ ). The cross-sectional area for vapor transfer along the network surface ( $A_{t,surf,x}$  and  $A_{t,surf,y}$ ) is  $0.5h^2$ . The cross-sectional area between the network surface and the gas-side boundary layer ( $A_{t,surf,z}$ )

and in the boundary layer ( $A_{t,BL,x}$ ,  $A_{t,BL,y}$  and  $A_{t,BL,z}$ ) is  $h^2$  (see Fig. 2.5).

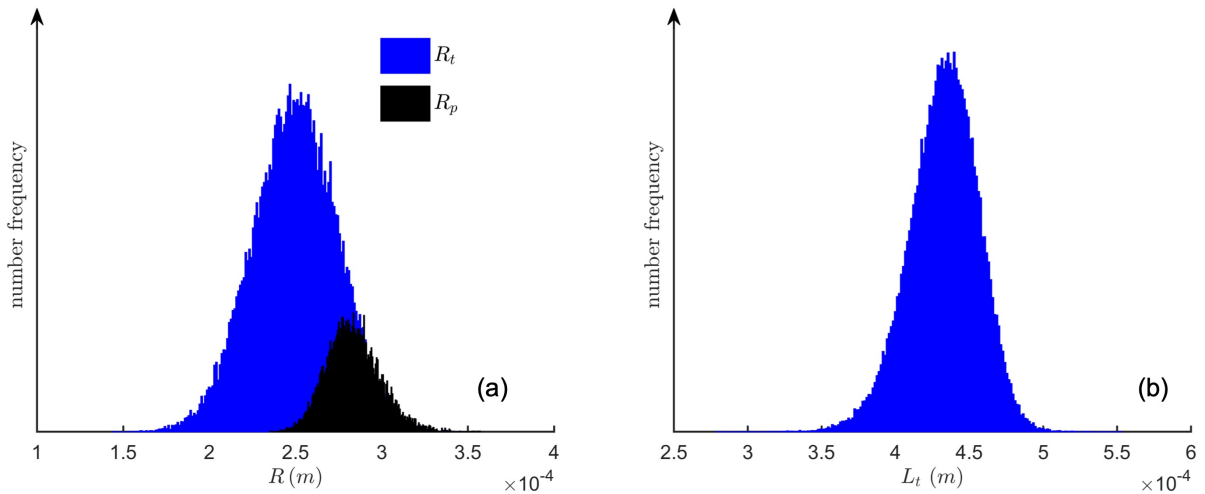


Figure 2.4: Distributions of pore radius and throat radius with mean throat radius  $250 \mu m$  and the standard deviation of throat radii  $25 \mu m$  (a) and the throat length distribution  $L_t$  (b). The pore radii are larger than or at least equal to the largest radius of neighbor throats.

### 2.2.3 Drying algorithm in the capillary-viscous regime

We present details of the PNM algorithm that can describe the liquid and vapor transport in the limit of capillary-viscous regime at isothermal conditions.

#### 2.2.3.1 Saturation of throats and pores

The algorithm begins with pores and throats completely saturated with liquid. Vapor pressure distribution in the boundary layer is calculated based on the condition that surface pores (red pores in Fig. 2.1) contain saturation vapor pressure and the pores adjacent to the bulk air are assumed to have zero vapor pressure. During the drying process, the liquid-vapor interface (meniscus) moves into the pore network and the saturation decreases. The change of local saturation is stored in two arrays, the throat saturation  $S_{t,i}$  and the pore saturation  $S_{p,i}$ , which can take values from 1 (completely filled with free water) to 0 (completely empty). Thus, three kinds of pores and three types of throats are identified: Empty pores ( $S_{p,i} = 0$ ) and empty throats ( $S_{t,i} = 0$ ), those fully occupied by vapor phase; full pores ( $S_{p,i} = 1$ ) and full throats ( $S_{t,i} = 1$ ), those fully occupied by liquid phase; and partially filled pores ( $0 < S_{p,i} < 1$ ) and partially filled throats ( $0 < S_{t,i} < 1$ ), those at the liquid-gas interface.

#### 2.2.3.2 Vapor pressure in pores

Once the menisci move into the network, empty pores form. The vapor pressure in these pores is defined as follows:

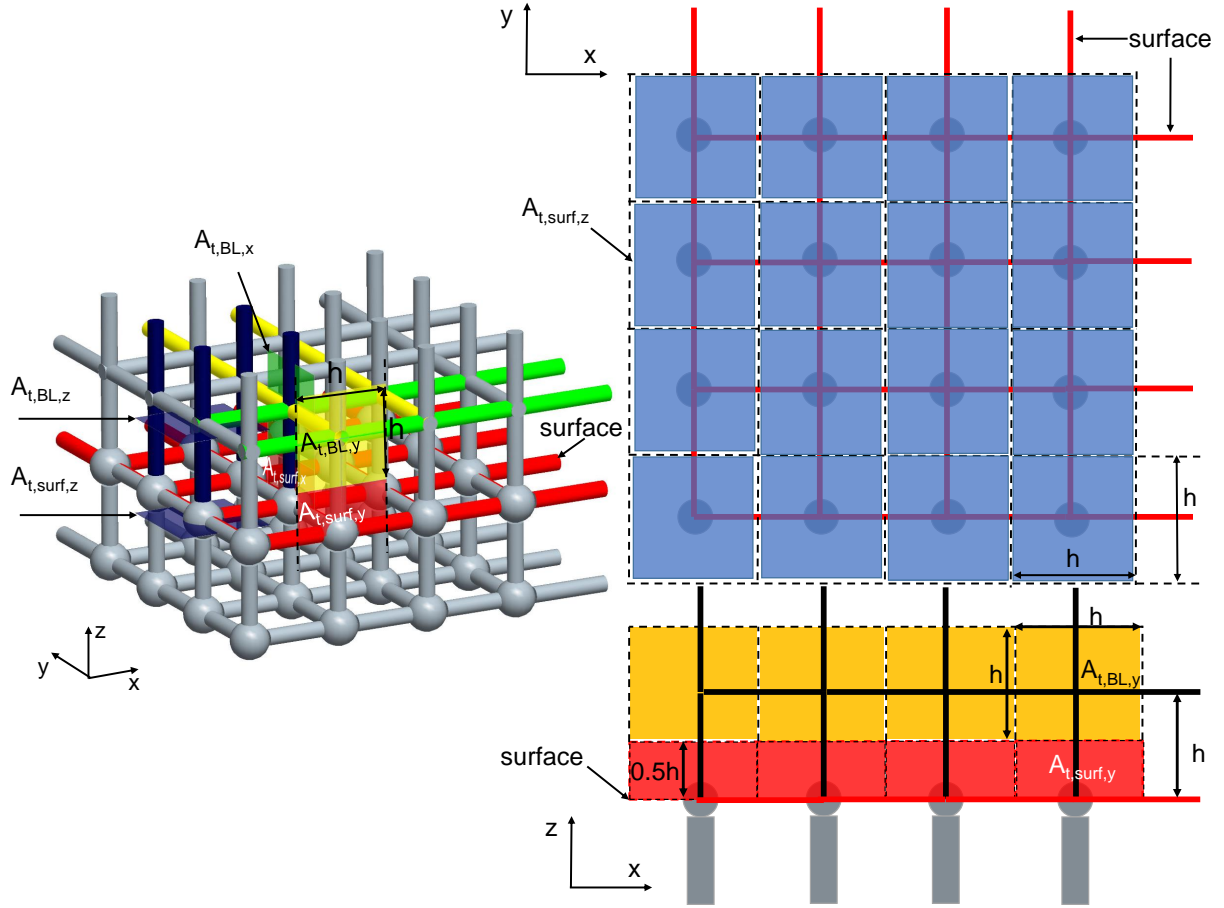


Figure 2.5: Different cases of cross-sectional area for vapor diffusion in the boundary layer and at the network surface. Surface throats and respective cross-sectional areas in the horizontal direction are in red. The cross-sectional area of surface pores to the boundary layer in the vertical direction are in dark blue. The throats in the gas-side boundary layer are in green (x-direction), yellow (y-direction), and dark blue (z-direction), corresponding to its cross-sectional area.

1. An empty pore connected to only empty neighbor throats is at unknown vapor pressure  $P_v$ , which can be calculated by a vapor balance equation;
2. An empty pore connected to at least one full or partially filled neighbor throat is assumed to be at saturation vapor pressure,  $P_v^*$ ;
3. The vapor pressure in a partially filled pore is at saturation vapor pressure,  $P_v^*$ .

The saturation vapor pressure  $P_v^*$  is 2339 Pa at a uniform temperature of 20 °C. The vapor pressure values of empty pores are stored.

### 2.2.3.3 Vapor transport

Stefan's law is used to describe the vapor transport in the gas-filled region of the network and in the gas-side boundary layer. The vapor phase is considered as a continuous phase.

Vapor flow rate ( $\dot{M}_{v,ij}$ ) between two pores is calculated by:

$$\dot{M}_{v,ij} = g_{v,ij} P \ln \left( \frac{P - P_{v,j}}{P - P_{v,i}} \right), \quad g_{v,ij} = \frac{D_{va} \tilde{M}_v}{\tilde{R}T \left( \frac{R_{p,i}}{A_{p,i}} + \frac{L_t}{A_t} + \frac{R_{p,j}}{A_{p,j}} \right)}, \quad (2.7)$$

where  $A_{p,i}$ ,  $A_{p,j}$ , and  $A_t$  ( $m^2$ ) denote the cross-sectional area of pore  $i$  ( $\pi R_{p,i}^2$ ), pore  $j$  and throat ( $\pi R_t^2$ ), respectively.  $D_{va}$  ( $m^2/s$ ) denotes the diffusion coefficient of vapor in the air.  $P_{v,i}$  and  $P_{v,j}$  are the vapor pressure in pore  $i$  and pore  $j$ , respectively.  $P$  ( $Pa$ ) is the total (atmospheric) pressure. The derivation of this equation can be found in Chapter 3.

The vapor pressure in empty pores with neighbor throats containing liquid and in partially filled pores is considered to be equal to the saturation vapor pressure. The mass balance equation for the vapor phase is then written for all gas pores of unknown vapor pressure as:

$$\sum_j \dot{M}_{v,ij} = 0. \quad (2.8)$$

The sum is over all neighboring gas pores which are connected by an empty throat. The boundary conditions are as follows: Saturation vapor pressure for gas pores with neighbor throats containing liquid and for partially filled pores; vapor pressure of the drying air for pores located at the far end of the boundary layer.

Figure 2.6 illustrates the vapor mass balance at vapor pore 1 surrounded by liquid pores (pores 3, 5, and 7 in dark blue) and by vapor pores (pores 2, 4, and 6 in light blue). The vapor mass balance for pore 1 can be written as:

$$\begin{aligned} & g_{v,8} P \ln \left( \frac{P - P_{v,1}}{P - P_{v,2}} \right) + g_{v,9} P \ln \left( \frac{P - P_{v,1}}{P - P_{v,3}} \right) + g_{v,10} P \ln \left( \frac{P - P_{v,1}}{P - P_{v,4}} \right) \\ & + g_{v,11} P \ln \left( \frac{P - P_{v,1}}{P - P_{v,5}} \right) + g_{v,12} P \ln \left( \frac{P - P_{v,1}}{P - P_{v,6}} \right) + g_{v,13} P \ln \left( \frac{P - P_{v,1}}{P - P_{v,7}} \right) = 0. \end{aligned} \quad (2.9)$$

Hereby  $P_{v,3} = P_{v,5} = P_{v,7}$  is  $P_v^*$ .

Then, the mass balance for pore 1 can be rearranged as:

$$\begin{aligned} & \ln \left( 1 - \frac{P_{v,1}}{P} \right) (g_{v,8} + g_{v,9} + g_{v,10} + g_{v,11} + g_{v,12} + g_{v,13}) \\ & - g_{v,8} \ln \left( 1 - \frac{P_{v,2}}{P} \right) - g_{v,10} \ln \left( 1 - \frac{P_{v,4}}{P} \right) - g_{v,12} \ln \left( 1 - \frac{P_{v,6}}{P} \right) = \\ & g_{v,9} \ln \left( 1 - \frac{P_{v,3}}{P} \right) + g_{v,11} \ln \left( 1 - \frac{P_{v,5}}{P} \right) + g_{v,13} \ln \left( 1 - \frac{P_{v,7}}{P} \right). \end{aligned} \quad (2.10)$$

Applying Eq. 2.8 to all gas pores results in a set of equations. Assuming the saturated vapor pressure for saturated pores and invoking known vapor conductances of all gas pores  $g_v$ , the set of equations can be transformed into a linear system by replacing the unknown

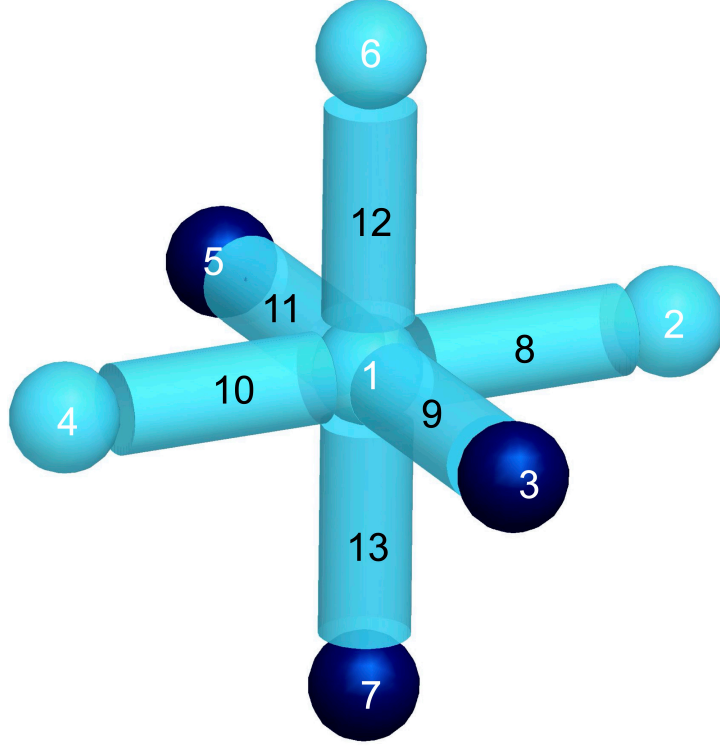


Figure 2.6: Illustration of a vapor mass balance with possible boundary conditions. The dark blue color represents water, and the light blue color represents vapor.

vapor pressure  $\mathbf{P}_{v,i}$  with the variable

$$\mathbf{X}_{v,i} = \ln \left( 1 - \frac{\mathbf{P}_{v,i}}{P} \right). \quad (2.11)$$

In mathematical terms:

$$\mathbf{A}_v \times \mathbf{X}_v = \mathbf{b}_v, \quad (2.12)$$

where  $\mathbf{A}_v$  is the matrix of vapor conductances,  $\mathbf{X}_v$  the vector of unknown  $\mathbf{X}_{v,i}$  and  $\mathbf{b}_v$  is the vector of boundary conditions. The matrix of vapor conductances is of size  $NP \times NP$  (including the nodes in boundary layer) and can be filled as:

$$\mathbf{A}_v = \begin{bmatrix} \sum_{i=PNT[1,i]}^{1:NPT[1]} g_{v,i} & -g_{v,PNT[1,1]} & 0 & \cdots & 0 \\ -g_{v,PNT[2,1]} & \sum_{i=PNT[2,i]}^{1:NPT[2]} g_{v,i} & 0 & & \vdots \\ 0 & 0 & \ddots & & \\ \vdots & & & \ddots & \\ 0 & \cdots & & & \sum_{i=PNT[NP,i]}^{1:NPT[NP]} g_{v,i} \end{bmatrix}. \quad (2.13)$$

The diagonal of matrix  $\mathbf{A}_v$  is calculated by the sum of the vapor conductances of throats

in each row of PNT. The nonzero values in each row,  $i$ , are negative vapor conductances to neighboring pores (unknown vapor pressure) of each row of PNP[ $i$ ]. For example,  $\mathbf{A}_v$  for the situation shown in Fig. 2.5 is rearranged from the left-hand side of Eq. 2.10:

$$\mathbf{A}_v = \begin{bmatrix} g_{v,8} + g_{v,9} + g_{v,10} + g_{v,11} + g_{v,12} + g_{v,13} & -g_{v,8} & 0 & -g_{v,10} & 0 & -g_{v,12} & 0 \end{bmatrix}. \quad (2.14)$$

The vector of vapor pressure boundary conditions, which has size NP, is denoted by  $\mathbf{b}_v$ . Each row of  $\mathbf{b}_v$  is made of the sum of the evaporation rates from saturation pores:

$$\mathbf{b}_v = \begin{bmatrix} \vdots \\ \mathbf{P}_v[\text{PNP}[i] \equiv P_v^*] \\ \sum_{i=\text{PNT}[i]} g_{v,i} \ln \left( 1 - \frac{P_v^*}{P} \right) \\ \vdots \end{bmatrix}. \quad (2.15)$$

One example of  $\mathbf{b}_v$  for the simple network model of Fig. 2.6 can be rearranged from the right-hand side of Eq. 2.10:

$$\mathbf{b}_v = \left[ g_{v,9} \ln \left( 1 - \frac{P_{v,3}}{P} \right) + g_{v,11} \ln \left( 1 - \frac{P_{v,5}}{P} \right) + g_{v,13} \ln \left( 1 - \frac{P_{v,7}}{P} \right) \right]. \quad (2.16)$$

Similarly to the boundary condition vector (or  $\text{NP} \times 1$  matrix), we also generate a matrix to store the known vapor pressures in the network for each step. Matrix  $\mathbf{P}_v$  has, again, the size of NP by 1. It contains the equilibrium vapor pressure ( $P_v^* = 2339$  Pa) for liquid pores and partially filled pores, as well as empty pores connected to at least one throat that contains liquid.

After having calculated the two matrices, namely  $\mathbf{A}_v$  and  $\mathbf{b}_v$  the preconditioned conjugate gradients method (Barrett et al., 1994) is used to tackle Eq. 2.12 for all pores in the network to obtain the matrix  $\mathbf{X}_v$ . The vapor pressure for each pore is, finally, solved as:

$$\mathbf{P}_v = P (1 - \exp(\mathbf{X}_v)). \quad (2.17)$$

#### 2.2.3.4 Phase change at the liquid-vapor interface

The vapor diffusion rate ( $\dot{M}_{v,ij}$ ) between two empty pores as well as between one liquid pore and one empty pore (Fig. 2.7) can be calculated based on Eq. 2.7.

Once the vapor pressure has been calculated in each pore, the vapor diffusion flow rate from pore  $i$  (i.e. pore 1 in Fig. 2.8) to each of its  $k$  empty neighbor pores (pores 2, 3 and 6 in Fig. 2.8) is  $\sum_k \dot{M}_{v,ik}$ . Assuming that this flow is contributed from several partially wet throats to pore  $i$ , then the evaporation rate in one of them (denoted as  $s$ ) can be obtained, as:

$$\dot{M}_{ev,s} = \frac{A_s}{A_{tot,i}} \sum_k \dot{M}_{v,ik}, \quad (2.18)$$

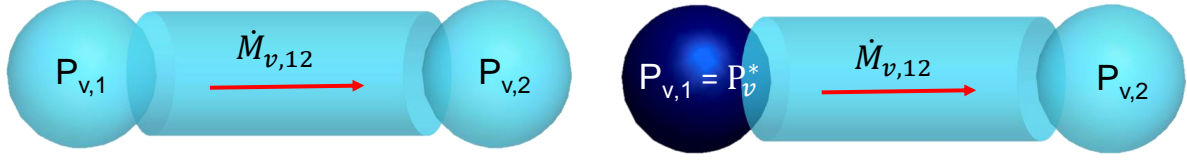


Figure 2.7: Vapor diffusion rate in empty throats. Dark blue represents the water, and light blue denotes the vapor.  $P_v^*$  is the saturated vapor pressure and  $P_{v,1}$  and  $P_{v,2}$  are unknown vapor pressures that are determined from the vapor mass balance.

where  $A_s$  is the cross-sectional area of the considered meniscus throat (red in Fig. 2.8) and  $A_{tot,i}$  is the total cross-sectional area of all throats with a meniscus neighbor to pore  $i$ . Justified by slow isothermal drying, condensation of vapor is neglected.

### 2.2.3.5 Liquid transport

The liquid transport mechanism at the pore scale can be described by Poiseuille's law. The liquid flow rate ( $\dot{M}_{w,ij}$ ) is motivated by the difference of water pressure between filled pore  $i$  and filled pore  $j$  as:

$$\dot{M}_{w,ij} = g_{w,ij} (P_{w,i} - P_{w,j}), \quad g_{w,ij} = \frac{\pi \rho_w}{8\mu} \frac{1}{\left( \frac{R_{p,i}}{R_t^4} + \frac{L_t}{R_t^4} + \frac{R_{p,j}}{R_t^4} \right)}, \quad (2.19)$$

where  $\rho_w$  ( $\text{kg}/\text{m}^3$ ) denotes the liquid density,  $\mu$  ( $\text{m}^2/\text{s}$ ) the liquid viscosity,  $P_{w,i}$  (Pa) and  $P_{w,j}$  (Pa) the liquid pressure in the pores  $i$  and  $j$ . Geometrical quantities are explained in Fig. 2.3. Derivation of Eq. 2.19 can be found in Chapter 3. The liquid pressure at each pore that is filled with water can be determined by the balance equations,

$$\sum_j \dot{M}_{w,ij} = 0, \quad (2.20)$$

meaning that the incoming flow rate equals the outflow rate at each pore. The sum is over all neighboring liquid pores which are connected by filled throats or partially filled throats. Based on the boundary conditions, stationary menisci and moving menisci are identified. Stationary menisci are characterized by the fact that evaporation exists at the interface, but the saturation is not reduced, which means that the liquid conductance for the stationary menisci is zero. In contrast, the interface of moving menisci moves (refilling or emptying) with evaporation. Thus, the balance condition at each throat/pore meniscus can be described by the Young-Laplace equation. This condition is used to determine the

associated liquid pressure ( $P_{m,t/p}$ ):

$$P_{m,t/p} = P - P_c, P_c = \frac{2\sigma \cos \theta}{R_{t/p}}, \quad (2.21)$$

where  $\sigma$  (N/m) and  $\theta$  ( $^\circ$ ) denote the surface tension and the equilibrium contact angle, respectively.  $P_c$  (Pa) and  $R_{t/p}$  (m) denote the capillary pressure and the radius of the meniscus of throat/pore. In this work, we assume that the liquid is perfectly wetting the solid matrix, meaning  $\theta = 0^\circ$ .

Applying Eq. 2.19 to liquid pores results in a set of equations which is transformed into a linear system as:

$$\mathbf{A}_w \times \mathbf{X}_w = \mathbf{b}_w, \quad (2.22)$$

where  $\mathbf{A}_w$  is the matrix of liquid conductances,  $\mathbf{X}_w$  is the vector of unknown pressure of liquid pores  $\mathbf{P}_w$  and  $\mathbf{b}_w$  is the vector of boundary conditions.

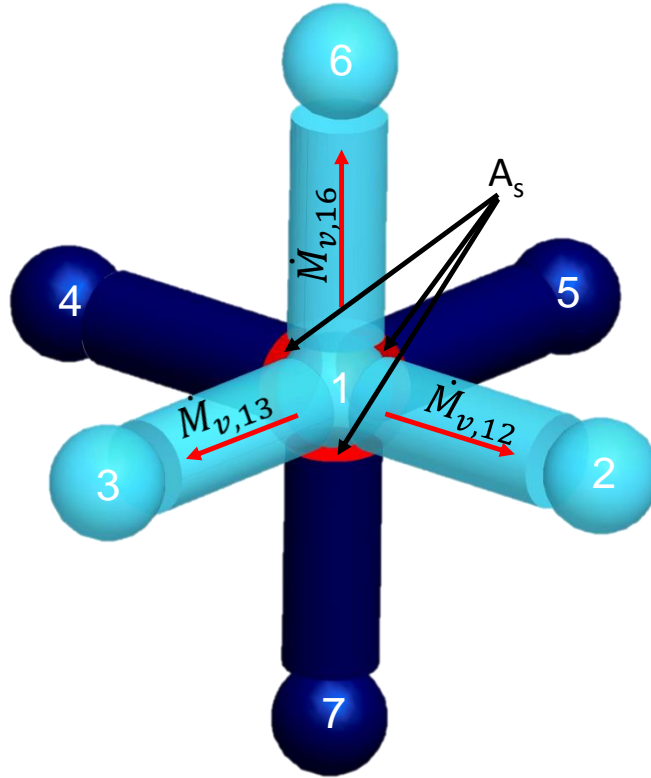


Figure 2.8: Phase change at an empty pore. Dark blue represents the water, and light blue denotes the vapor.

Figure 2.9 shows a small network of pores and throats as an example to explain the liquid transport calculation. The mass balance is written for liquid pore 1 and the following boundary conditions are considered: Vapor pores 2, 4 and 6 have the evaporation rates  $\dot{M}_{v,2}$ ,  $\dot{M}_{v,4}$ ,  $\dot{M}_{v,6}$ , respectively. Liquid pore 7 has unknown pressure  $P_{w,7}$ . Partially liquid filled pores 5 and 3 have the meniscus pressures  $P_{m,p,5}$  and  $P_{m,p,3}$ , respectively. Liquid

throat 10 contains a stationary meniscus, and liquid throats 9, 11 and 13 contain moving menisci (as one assumption of the situation for menisci). The detailed algorithm in treating menisci in model are presented in the following section. The assumption here is served to illustrate how to solve the mass balance for liquid transport.

Thus, the liquid mass balance for pore 1 can be written as:

$$g_{w,9}(P_{w,1} - P_{m,p,3}) + g_{w,11}(P_{w,1} - P_{m,p,5}) + g_{w,13}(P_{w,1} - P_{m,p,7}) + \dot{M}_{v,2} + \dot{M}_{v,4} + \dot{M}_{v,6} = 0. \quad (2.23)$$

Equation 2.23 is rearranged as:

$$(g_{w,9} + g_{w,11} + g_{w,13})P_{w,1} - g_{w,13}P_{w,7} = g_{w,9}P_{m,p,3} + g_{w,11}P_{m,p,5} - \dot{M}_{v,2} - \dot{M}_{v,4} - \dot{M}_{v,6}. \quad (2.24)$$

The left-hand side of Eq. 2.24 is rearranged for the liquid conductance of pore 1, as:

$$\mathbf{A}_w = [g_{w,9} + g_{w,11} + g_{w,13} \quad 0 \quad 0 \quad 0 \quad 0 \quad 0 \quad -g_{w,13} \quad 0]. \quad (2.25)$$

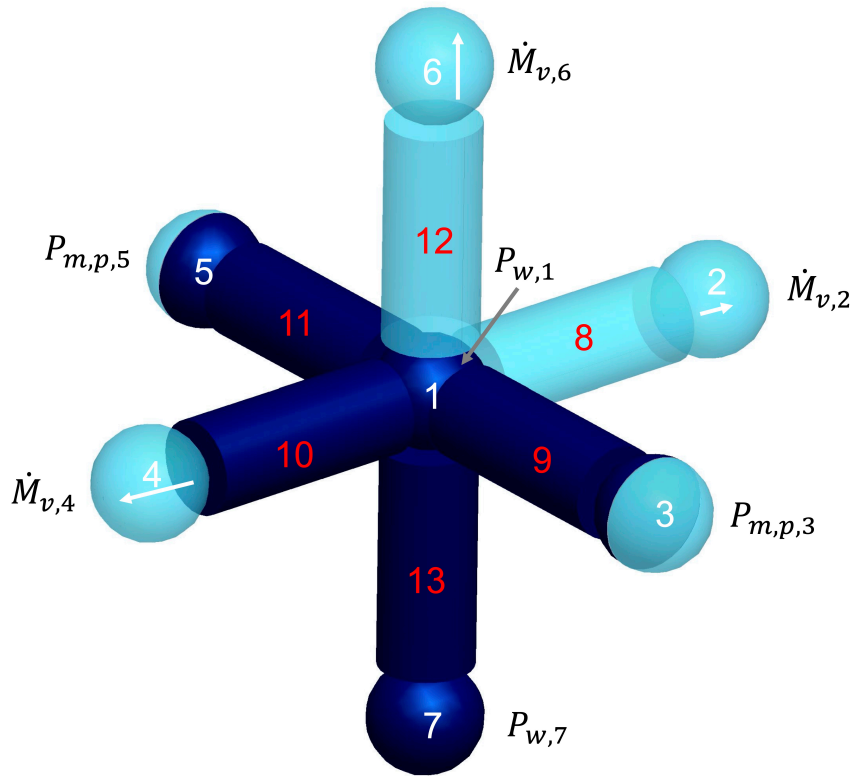


Figure 2.9: Illustration of pore 1 with associated boundary conditions. The free liquid water and the water vapor are shown in dark blue and light blue, respectively.

Thus, the vector for the unknown liquid pressures appears as:

$$\mathbf{X}_{\mathbf{w}} = \begin{bmatrix} P_{w,1} \\ 0 \\ 0 \\ 0 \\ 0 \\ 0 \\ P_{w,7} \\ 0 \end{bmatrix}. \quad (2.26)$$

The right-hand side of Eq. 2.24 is the boundary condition which can be written as:

$$\mathbf{b}_{\mathbf{w}} = \left[ g_{w,9}P_{m,p,3} + g_{w,11}P_{m,p,5} - \dot{M}_{v,2} - \dot{M}_{v,4} - \dot{M}_{v,6} \right]. \quad (2.27)$$

More generally, applying the mass balance to each liquid pore in the network, we form a set of equations that can be transformed into a linear system. Therefore, the matrix  $\mathbf{A}_{\mathbf{w}}$  is the size of  $N_p \times N_p$  (which only contains pores in the network of the porous medium):

$$\mathbf{A}_{\mathbf{w}} = \begin{bmatrix} \sum_{PNT[1,j]}^{PNT[1,j] \neq \text{stationary}} g_{w,PNT[1,j]} & \cdots & -g_{w,PNT[1,k]} & \cdots \\ \vdots & \sum_{PNT[2,j]}^{PNT[2,j] \neq \text{stationary}} g_{w,PNT[2,j]} & -g_{w,PNT[2,k]} & \vdots \\ \vdots & -g_{w,PNT[i,k]} & \sum_{PNT[i,j]}^{PNT[i,j] \neq \text{stationary}} g_{w,PNT[i,j]} & \vdots \end{bmatrix}. \quad (2.28)$$

Here  $j$  are the pore neighboring throats which contain moving menisci and filled throats connected to pores with unknown liquid pressure, and the sum of the liquid conductances of  $PNT[i, k]$  is placed in  $\mathbf{A}_{\mathbf{w},ii}$ ;  $k$  is the throat connected with another liquid pore of unknown liquid pressure, placed at position  $\mathbf{A}_{\mathbf{w},ik}$ .

The vector  $\mathbf{X}_{\mathbf{w}}$  can be seen as a matrix with size  $N_p \times 1$ , which is filled with the unknown values of liquid pore pressure  $P_w$  and 0 for the gas pores. The matrix of boundary conditions  $\mathbf{b}_{\mathbf{w}}$  has size  $N_p \times 1$ . The element of the boundary condition matrix which corresponds to a specific pore has to be derived by combination of the following cases:

- Once the pore is connected with an empty throat, we have to subtract the vapor mass flow rate  $\dot{M}_v$  from the value of the element of the boundary condition matrix.
- Once the pore is connected with a stationary meniscus throat, we also have to subtract the vapor mass flow rate at the stationary meniscus  $\dot{M}_v$ .

- Once the pore is connected with a moving meniscus throat with saturation  $S_t$ , we have to add the value of  $S_t g_w P_{m,t}$  to the value of the element of the boundary condition matrix.
- Once the pore is connected with a partially filled pore, we have to add the value of  $g_w P_{m,p}$ .

When  $\mathbf{A}_w$  and  $\mathbf{b}_w$  are set up, the preconditioned conjugate gradient method is used to compute the liquid pressure of pores, i.e.,  $\mathbf{X}_w$ .

### 2.2.3.6 Stability of menisci

The moving or stationary status of menisci should be distinguished before each invasion step. The invasion process is controlled by capillary pressure, suggesting that the throat with the largest radius is easiest to invade. In the network, we ensure that each pore radius is larger than or at least equal to the largest radius of neighbor throat. This makes menisci pores to be either refilling or emptying.

To deal with the situation of invasion in throats, we assumed the meniscus in the largest throat filled with liquid as the moving meniscus, other menisci in filled throats are stationary menisci. The partially filled throats are all assumed to have moving menisci. Based on this assumption, we calculate the conductance matrix  $\mathbf{A}_w$ , and the boundary condition matrix  $\mathbf{b}_w$ . Thus, we can solve the linear Eq. 2.22 to obtain the liquid pressure distribution of the liquid pores in the network.

After obtaining the liquid pressure distribution under the above assumption, we have to check whether the so-derived stationary menisci meet the demand of stability. Therefore, the required liquid pressure  $P_{w,req}$ , which is necessary in order to sustain evaporation, should be larger than the meniscus pressure calculated by Eq. 2.21. Thus the discrepancy of pressure:

$$\Delta P = P_{m,t/p} - P_{w,req}, \quad (2.29)$$

should be smaller than zero. Here the required water pressure,  $P_{w,req}$ , is according to Fig. 2.10 defined at the stationary meniscus:

$$P_{w,req,i} = P_{w,i} - \frac{\dot{M}_v}{g_{w,ij}}. \quad (2.30)$$

The requirement expressed by Eq. 2.29 should be satisfied by each stationary meniscus. Otherwise, we have to modify the previous assumption about stationary menisci. We change the largest meniscus among previously assumed to be stationary menisci into a moving meniscus. That is to say, a new moving meniscus is created. Thus, matrices  $\mathbf{A}_w$  and  $\mathbf{b}_w$  have to be altered correspondingly. The balance equations for liquid pores (Eq. 2.22) must be solved again. These loops have to be calculated until the balance conditions

are reached for all menisci (shown in Fig. 2.11).



Figure 2.10: Liquid pressure demand of stationary meniscus. The dark blue color represents the liquid, and the light blue color represents the vapor.

When gas invades the network, the liquid phase splits up into several regions with different sizes, the so-called liquid clusters. The liquid clusters consist of at least one nonempty throat connected to one nonempty pore. The liquid mass balance must be satisfied not only at each meniscus but also for each liquid cluster. The same procedure is applied to all liquid clusters.

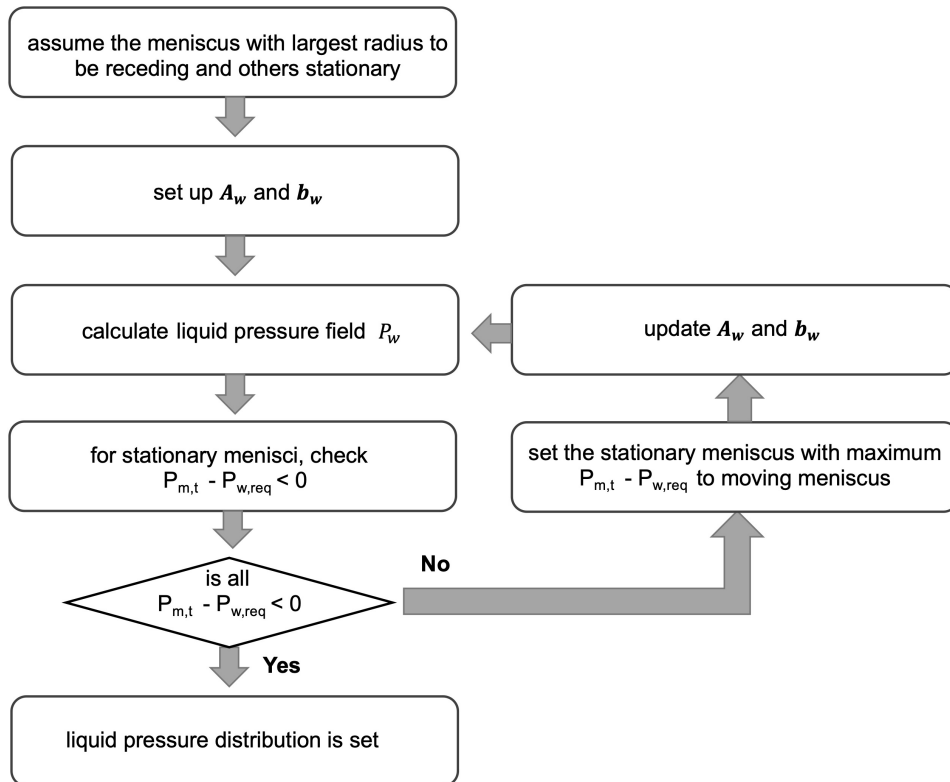


Figure 2.11: Flow chart of the algorithm to determine the liquid pressure in the network.

## 2.2.4 Numerical algorithm

After the water pressure in each liquid pore has been determined and all moving menisci (in the throats or pores) have been found, the time for each invasion step is calculated. The

mass flow rate for each throat with moving meniscus (emptying or refilling)  $\dot{M}_t$  corresponds to the liquid flow rate (Eq. 2.19) and the diffusion flow rate (Eq. 2.7). The mass flow rate for each pore with moving meniscus (emptying or refilling)  $\dot{M}_p$  has to consider the liquid flow from neighbor throats/pores, the neighbor menisci diffusion flow, and the diffusion flow in this pore. The time steps for the emptying and refilling events of meniscus throats or pores are computed by:

$$\Delta t_{emptying,t/p} = \frac{V_{t/p}\rho_w S_{t/p}}{\dot{M}_{t/p}}, \quad (2.31)$$

and

$$\Delta t_{refilling,t/p} = \frac{V_{t/p}\rho_w (1 - S_{t/p})}{\dot{M}_{t/p}}, \quad (2.32)$$

where  $V_{t/p}$  is the moving meniscus throat/pore volume and  $S_{t/p}$  is the respective saturation. Evaporation times for single throat menisci and single pore menisci ( $\Delta t_{single,t/p}$ ) are calculated from the volume, density, saturation, and evaporation rate as:

$$\Delta t_{single,t/p} = \frac{V_{single,t/p}\rho_w S_{single,t/p}}{\dot{M}_{ev, single,t/p}}. \quad (2.33)$$

Each time step ( $\Delta t$ ) of the simulation is decided as the minimum among  $\Delta t_{emptying,t/p}$ ,  $\Delta t_{refilling,t/p}$  and  $\Delta t_{single,t/p}$ .

Next, we have to update all saturations for each throat/pore with moving meniscus. When one throat empties, it creates one meniscus pore, and the connection of the liquid phase is not affected. Once the meniscus pore dries, it produces meniscus throats and is likely to break the cluster into small clusters. The number of liquid clusters in the network has to be counted. A variant of the Hoshen-Kopelman algorithm is used to label liquid clusters (Metzger et al., 2006).

The main steps of the TPM drying algorithm are as follows (see Fig. 2.12):

1. Generate a cubic network and input the network geometry data (throat/pore radii, length of throats), as well as the initial (e.g., temperature, liquid viscosity) and boundary conditions.
2. Calculate the vapor pressure distribution in the boundary layer and evaporation rate ( $\dot{M}_{ev}$ ) by the sum of all diffusion flows in the top slice of the network (TS) as:

$$\dot{M}_{ev} = \sum_{TS} \dot{M}_{v,TS}. \quad (2.34)$$

3. Find the meniscus throats/pores and calculate their mass flow rates. The number of liquid clusters and single meniscus throats/pores also has to be identified.
4. Determine the liquid pressure distribution. Calculate the flow rates (emptying/refilling) of throat/pore menisci. Get the emptying/refilling time of each throat/pore and the

times of single throats/pores to be emptied or refilled. The time of one invasion step ( $\Delta t$ ) is decided as the minimum time among these calculated times.

5. Update all parameters in the network, e.g., the liquid distribution and meniscus throats/pores.
6. Cluster labeling is active only when the previous step resulted in an emptied/refilled pore.
7. Calculate the vapor pressure distribution again, and the evaporation rate.

The network simulation is repeated from step 3 to step 7 until all the liquid has been evaporated ( $S_{net} = 0$ ).

Note that the simulation cost is high for the above algorithm. For example, a PC with processor Intel i7 CPU 4.00 GHz needs 30h to simulate the network with  $25 \times 25$  pores considered in every of in total 51 cross-sections of the network and 10 cross-sections of the gas-side boundary layer. Here, we identify some costly steps in the algorithm.

In every loop of the algorithm, much computational time is attributed to setting up and solving the linear system for liquid pressure at liquid pores for each cluster. The algorithm in Fig. 2.11 shows a loop to determine the liquid pressure. The scale of this loop depends on the number of active menisci throats. However, this number is augmented with ongoing invasion steps. The relative simulation cost for this part is amplified over every loop.

Additionally, the task of updating labels of liquid throats/pores also takes some time. In this work, we used the Hoshen-Kopelman algorithm, which is a serial method. The TPM algorithm only activates the Hoshen-Kopelman algorithm when a meniscus throat has been invaded. The algorithm of cluster labeling could also be optimized.

When standing at the global perspective, the loop in Fig. 2.12 is a major concern. The loop scale is extremely large. For example, for the above network size it has around  $10^6$  steps. The loop scale depends on the time step for one invasion. This time is selected among the drying times of each liquid cluster and the drying times of single menisci throats/pores. We used the minimum drying time to update the saturation. Thus, the minimum drying time is the effective time that is modeled in every step. However, it is possible that the time of one invasion step is from the drying of a single throat or pore that contained a liquid-gas meniscus. Under this circumstance, the liquid pressure distribution in the network remains identical to the previous step. It is then unnecessary to calculate the most expensive step by determining the liquid pressure again. Therefore, the algorithm is especially effective in the receding front period which is characterized by the existence of many single menisci, compare Fig. 3.9.

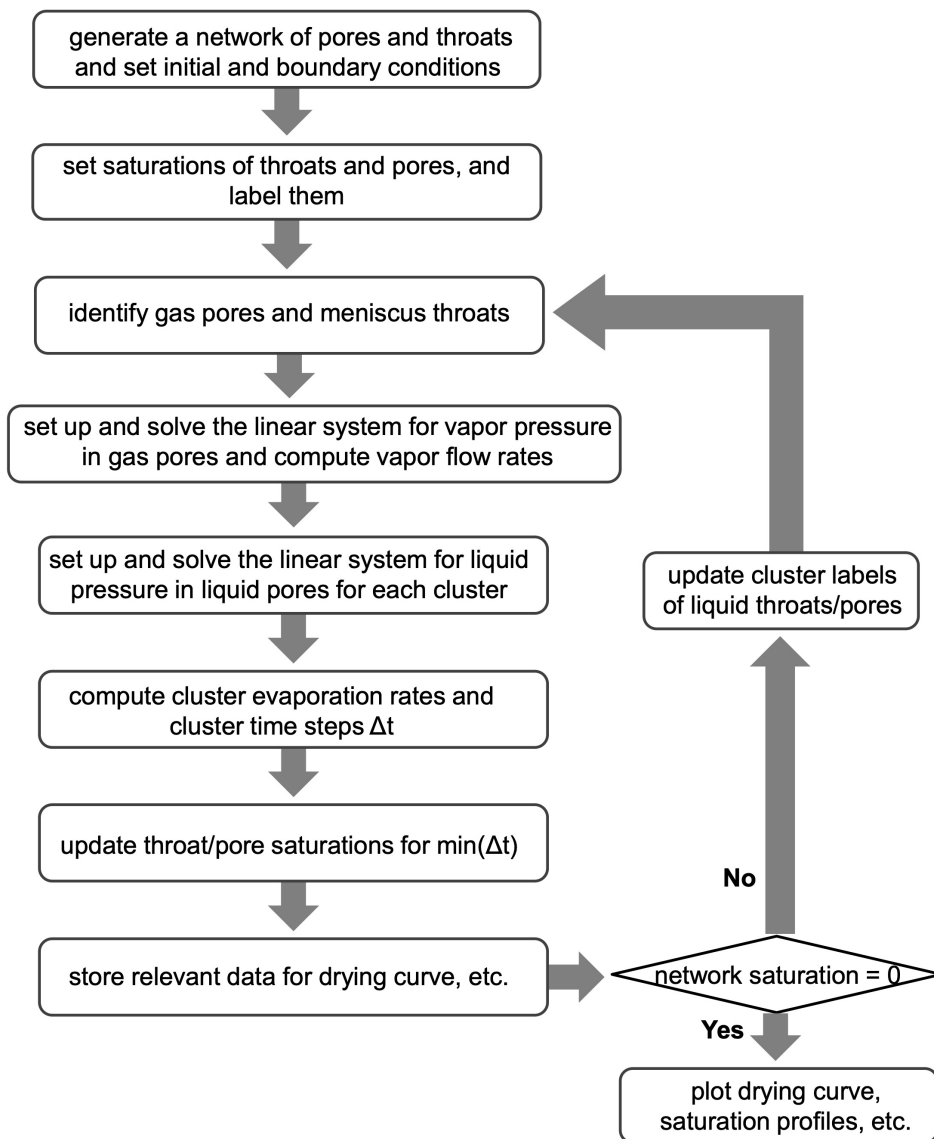


Figure 2.12: Flow chart of the algorithm of the throat-pore network model.

# Chapter 3

## Pore network simulations of drying: Throat-node model vs. throat-pore model

*This chapter is partly taken from “Lu, X., Kharaghani, A., Tsotsas, E., (2020), Transport parameters of macroscopic continuum model determined from discrete pore network simulations of drying porous media: Throat-node vs. throat-pore configurations. Chemical Engineering Science 223, 115723”.*

The present chapter compares the transport properties of the throat-node model (TNM) with those of the throat-pore model (TPM). First, we demonstrate how the void space of a capillary porous medium is approximated by these two configurations. Then, we evaluate the vapor and liquid conductances in these networks. For each phase, we quantify the discrepancy in conductances between TPM and TNM. Finally, we present drying predictions of both models.

### 3.1 The pore space of porous medium approximated by PNM

The network void space is calculated as the sum of all volumes of throats in TNM or of throats and pores in TPM. Once the distance between nodes is fixed ( $h = 1000 \mu\text{m}$ ), the mean radius decides about the void space. Figure 3.1 shows the porosity ( $\varepsilon$ ) of TNM and TPM networks with same size of  $25 \times 25 \times 51$  (width, depth, height) and with the same radius setting for throats and pores,  $R = R_p = R_t$ . In other words, for only the network porosity calculation, the radii of all throats and pores set to the same value. The plot indicates that the void space is overestimated by the TNM when the mean radius of throats and pores is larger than  $100 \mu\text{m}$ . When the mean radius reaches  $300 \mu\text{m}$ , the TNM fails to represent the network, as the calculated value of porosity is larger than 1.

In previous pore network drying simulations, the radius was usually set smaller than  $100 \mu\text{m}$  to avoid excessive overlap of throat ends (Metzger et al., 2007b). These networks only

represent the drying process at low porosity ( $\varepsilon < 0.1$ ), not in porous media such as bead packings. In Attari Moghaddam et al. (2017a), the drying process was studied based on the TNM by setting the radius to  $250 \mu\text{m}$ , resulting in a porosity of 0.594, which is beyond the porosity of a packed bed ( $\varepsilon = 0.4$ ). However, if we use the TPM to represent the void space, the calculated porosity of  $\varepsilon = 0.35$  is close to packed bed porosity. Therefore, the TPM seems to be more realistic for porous media which are similar to assemblies of spheres.

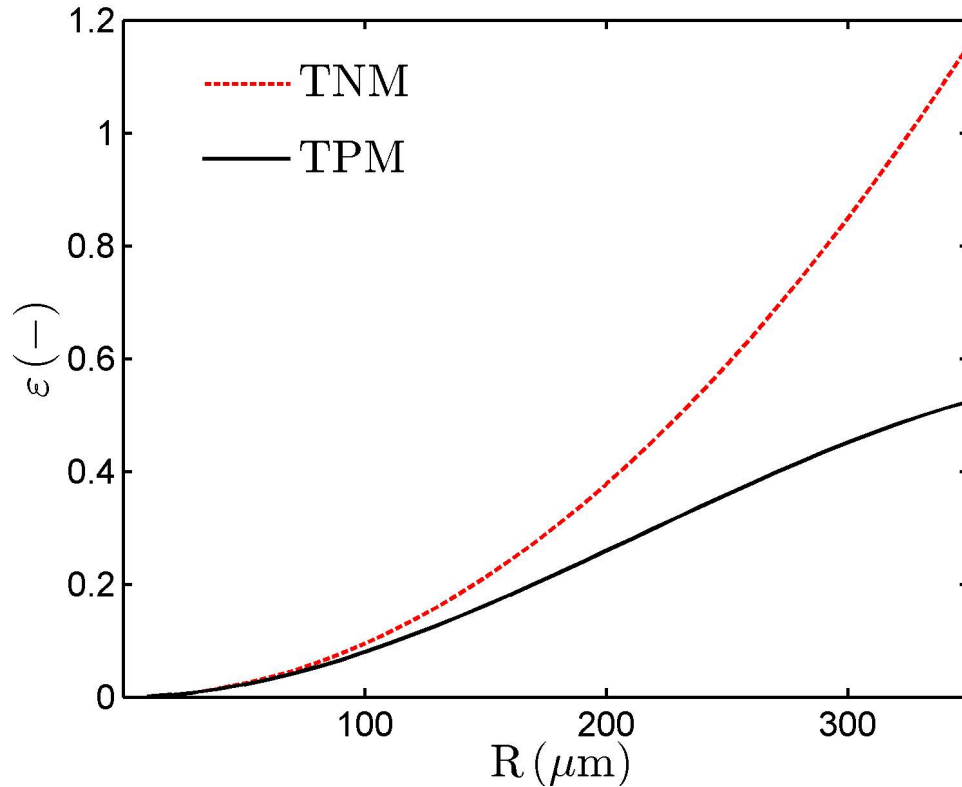


Figure 3.1: Network porosity as a function of the radius of throats and pores ( $R = R_p = R_t$ ) for two different model geometries with a fixed distance between nodes,  $h = 1000 \mu\text{m}$ .

The potential overestimation of void volume by the PNM would play a role in the drying simulation. However, the impact on the prediction of simulations has not been discussed, although the existence of overestimated volume in the TNM has been recognized (Attari Moghaddam et al., 2018). In this chapter, TPM and TNM simulations are systematically compared for the throat radii sampled from a normal size distribution with a mean of  $\bar{R}_t = 250 \mu\text{m}$  and standard deviation of  $\sigma_{0,t} = 25 \mu\text{m}$ . The procedure for the generation of the network geometry is presented in Chapter 2. Simulations were carried out for a relatively small network with Gaussian distributed radii. To reduce the level of uncertainty on parameters estimation, ten parallel realizations of the pore network have been considered. PNM simulation results are strongly influenced by the specific PNM geometry setting, which varies stochastically from one to the other network realization and

leads to different simulation results. Adding simulation results and then dividing them by the number of simulations makes no sense as the macroscopic parameters (or variables) depend on the saturation. The value of which is influenced by the previous state, which leads to unique vector correlations between macroscopic parameters with local saturation and network saturation. The normal averaging method treats the correlation among values as a scalar. To average the PNM dataset as a vector, we place the dataset into a  $100 \times 100$  matrix, in which the row represents intervals of local saturation from  $S = 0.01$  to  $1.00$  defined equidistantly with  $\Delta S = 0.01$ , and the column denotes the range of network saturation from  $S = 0.99$  to  $0.01$  with an even subdivision in steps  $\Delta S_{net} = 0.01$ . Then we average the values of the considered parameter for every element in this matrix. This method is adopted for averaging all macroscopic parameters.

The structural characteristics of pore network and the physical constants for the simulations are given in Tables 3.1 and 3.2. To observe the viscous effect in a small network, we assumed an unrealistic value of liquid viscosity in the simulations (Attari Moghaddam et al., 2017b). Before the comparison of drying characteristics between the two configurations, transport conductances ( $g_v$  and  $g_w$ ) are discussed. The spherical pores introduced into the PNM can influence the transport processes. Therefore, we will formulate the vapor transport conductance and the liquid transport conductance in PNM in the following sections, and then compare values between the TNM and the TPM. Finally, drying characteristics obtained from TNM and TPM will be compared.

Table 3.1: Characteristics used for dynamic drying simulations of TNM and TPM.

parameters	TNM	TPM
Network size	$25 \times 25 \times 51$	$25 \times 25 \times 51$
Boundary layer size	$25 \times 25 \times 10$	$25 \times 25 \times 10$
Mean pore radius ( $\mu\text{m}$ )	-	283
Mean throat radius ( $\mu\text{m}$ )	250	250
Standard deviation of throat radii ( $\mu\text{m}$ )	25	25
Standard deviation of pore radii ( $\mu\text{m}$ )	-	16
Center distance between two pores/nodes (mm)	1.0	1.0
Liquid volume ( $\text{m}^3$ )	$1.86 \times 10^{-5}$	$1.1 \times 10^{-5}$
Network porosity	0.59	0.35

Table 3.2: Physical parameters used for drying simulations.

Physical parameters	Value
Temperature (K)	293.15
Liquid viscosity ( $\text{Pa} \cdot \text{s}$ )	0.0028
Binary diffusion coefficient ( $\text{m}^2/\text{s}$ )	$2.5685 \times 10^{-5}$
Total pressure (Pa)	$10^5$
Surface tension (N/m)	0.07274
Saturation vapor pressure at 20 °C (Pa)	2339

### 3.2 Vapor transport conductance

One-side diffusion, resulting in Stefan's law is assumed for the vapor transport. That is to say, the diffusion of air molecules is balanced by the convective flow of air with the total gas, suggesting the immobility of air molecules. Derivation of vapor transport kinetics is as follows:

1. Equal diffusion flow rate between vapor and air:

$$\dot{N}_a^{diff} = -\dot{N}_v^{diff}. \quad (3.1)$$

2. Total molar flow rate of vapor:

$$\dot{N}_v = \dot{N}_v^{diff} + \tilde{y}\dot{N}^{conv}. \quad (3.2)$$

3. Molar flow rate of air:

$$\dot{N}_a = \dot{N}_v^{diff} + (1 - \tilde{y})\dot{N}^{conv} = 0. \quad (3.3)$$

Here,  $\dot{N}_a^{diff}$  is the molar flow rate of air transported by diffusion;  $\dot{N}_v^{diff}$  is the molar flow rate of vapor transported by diffusion;  $\dot{N}_v$  is total molar flow rate of vapor;  $\dot{N}_a$  is total molar flow rate of the air. The molar vapor fraction is

$$\tilde{y} = \frac{P_v}{P}. \quad (3.4)$$

with  $P_v$  as the vapor pressure, and  $P$  as the total gas pressure.

Fick's law is applied to describe the diffusive part of vapor flow:

$$\dot{N}_v^{diff} = -nAD_{va} \frac{d\tilde{y}}{dz}. \quad (3.5)$$

Combining Eqs. 3.1 to 3.5 we can get the total molar flow rate of vapor:

$$\dot{N}_v = -\frac{nAD_{va}}{1 - \tilde{y}} \frac{d\tilde{y}}{dz}. \quad (3.6)$$

Thus, the vapor mass flow rate between two nodes in TNM (Fig. 3.2) can be calculated by integrating over the length  $h$  with

$$n = \frac{P}{\tilde{R}T}, \quad (3.7)$$

and

$$\dot{M}_{ev,TNM} = \dot{N}_v \tilde{M}_v, \quad (3.8)$$

resulting in

$$\dot{M}_{ev,TNM} = \frac{PA_t D_{va} \tilde{M}_v}{\tilde{R}Th} \ln \left( \frac{P - P_{v,2}}{P - P_{v,1}} \right). \quad (3.9)$$

Here,  $A_t$  is the cross-sectional area of the throat, i.e.  $\pi R_t^2$ ,  $h$  is the length of the throat (the distance between two nodes),  $D_{va}$  is the diffusion coefficient of vapor in the air,  $\tilde{R}$  denotes the universal gas constant, and  $T$  is temperature.

Vapor mass flow rate in TPM (Fig. 3.2) is calculated between the centers of two pores by rearranging Eq. 3.6:

$$\frac{\dot{N}_v}{A} dz = -\frac{nD_{va}}{1-\tilde{y}} d\tilde{y}. \quad (3.10)$$

Thus,

$$\dot{N}_v \left( \int_0^{R_{p1}} \frac{1}{A_{p1}} dz + \int_{R_{p1}}^{h-R_{p2}} \frac{1}{A_t} dz + \int_{h-R_{p2}}^h \frac{1}{A_{p2}} dz \right) = -nD_{va} \left( \int_{\frac{P_{v,1}}{P}}^{\frac{P_{v,2}}{P}} \frac{\partial \tilde{y}}{(1-\tilde{y})} \right). \quad (3.11)$$

Finally, the vapor mass flow rate from the TPM is calculated as:

$$\dot{M}_{ev,TPM} = \frac{PD_{va} \tilde{M}_v}{\tilde{R}T \left( \frac{R_{p,1}}{A_{p,1}} + \frac{L_t}{A_t} + \frac{R_{p,2}}{A_{p,2}} \right)} \ln \left( \frac{P - P_{v,2}}{P - P_{v,1}} \right). \quad (3.12)$$

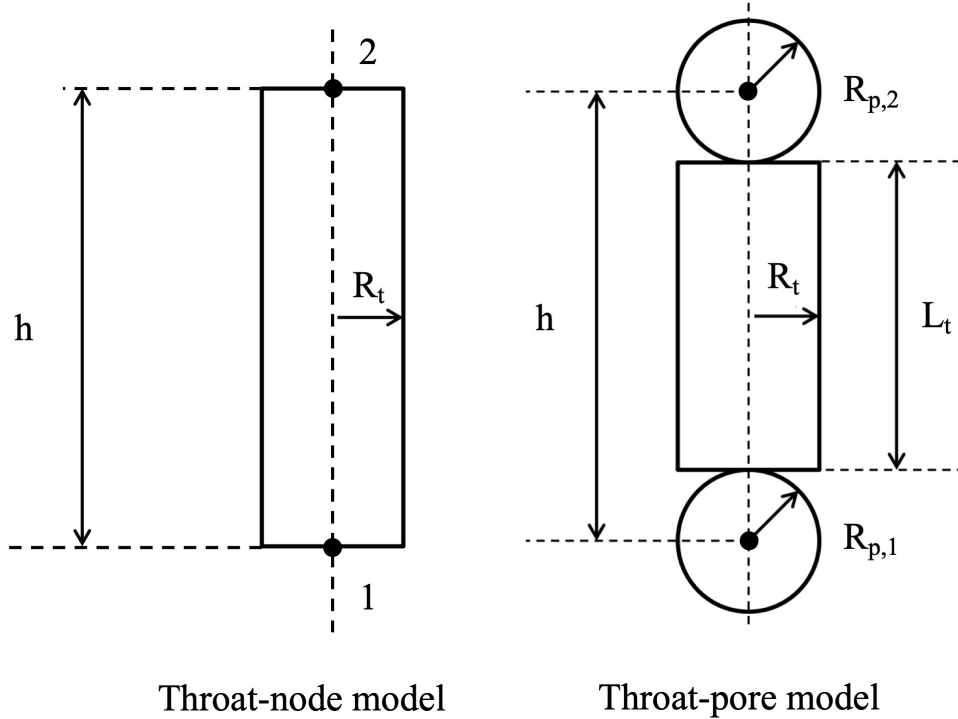


Figure 3.2: Schematic for the vapor transport conductance in the throat-node and the throat-pore model.

By use of expressions for the vapor mass flow rate in TNM (Eq. 3.9) and TPM (Eq.

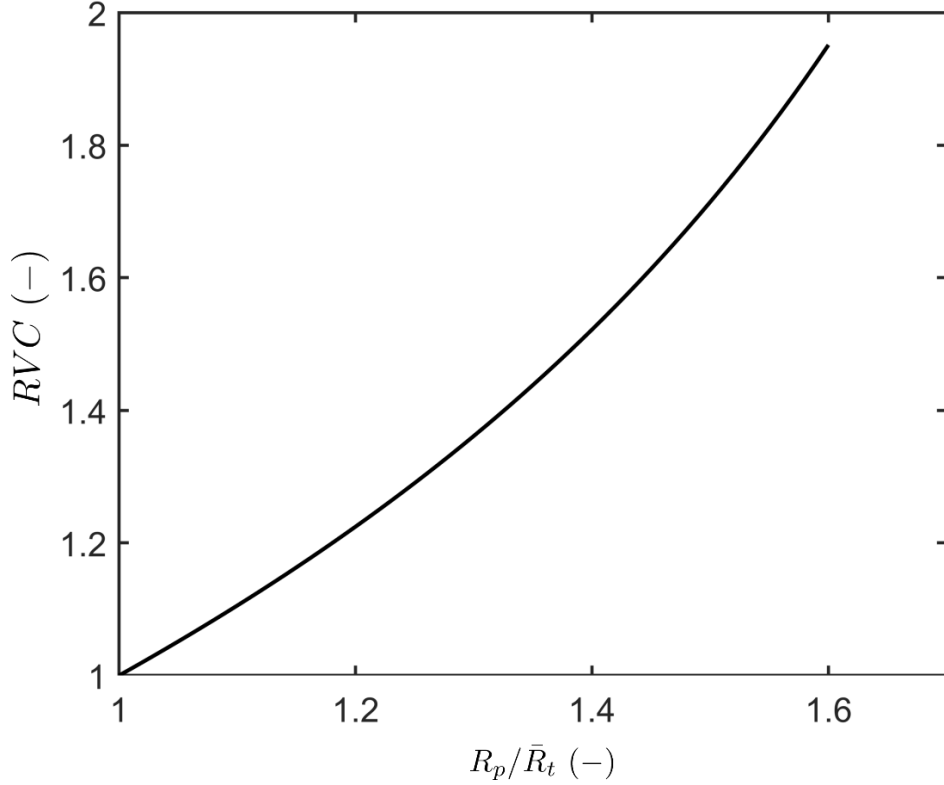


Figure 3.3: Ratio of vapor conductance for the TPM over TNM for  $h = 1000 \mu\text{m}$ ,  $R_t = 250 \mu\text{m}$ , and (in TPM)  $R_{p,1} = R_{p,2}$ .

3.12), the vapor transport conductance can be specified as, respectively:

$$g_{v,TNM} = \frac{A_t D_{va} \tilde{M}_v}{\tilde{R} T h}, \quad (3.13)$$

and

$$g_{v,TPM} = \frac{D_{va} \tilde{M}_v}{\tilde{R} T \left( \frac{R_{p,1}}{A_{p,1}} + \frac{L_t}{A_t} + \frac{R_{p,2}}{A_{p,2}} \right)}. \quad (3.14)$$

Here,  $L_t$  denotes the throat length that is determined by grid space and the pore radii at throat's ends, as  $L_t = h - R_{p,1} - R_{p,2}$ .

The ratio of vapor conductance in TPM over that in TNM indicates the effect of pore radius on vapor conductance, defined as relative vapor conductance (RVC):

$$RVC = \frac{g_{v,TPM}}{g_{v,TNM}}. \quad (3.15)$$

Figure 3.3 shows the ratio of vapor conductances for these two configurations for an identical throat radius of  $250 \mu\text{m}$  and the same length between two nodes or pores,  $h = 1000 \mu\text{m}$ . The spherical pores at the throat's ends, assumed here to have the same radius, improve the vapor conductance. The RVC increases nonlinearly with the ratio of pore

radius to throat radius, suggesting that the role of pores cannot be neglected when the pore radius is significantly larger than the throat radius.

Figure 3.4 shows the relative ratio of the vapor conductance against the ratio of pore radius to throat radius for different values of throat radius. The pores play a small role in the vapor conductance with narrow throats of fixed length. For example, the pore radius does not change significantly the vapor conductance when the throat radius is  $50 \mu\text{m}$ . Contrary, the pores enhance the vapor conductance in a network with the throat radius of  $250 \mu\text{m}$ .

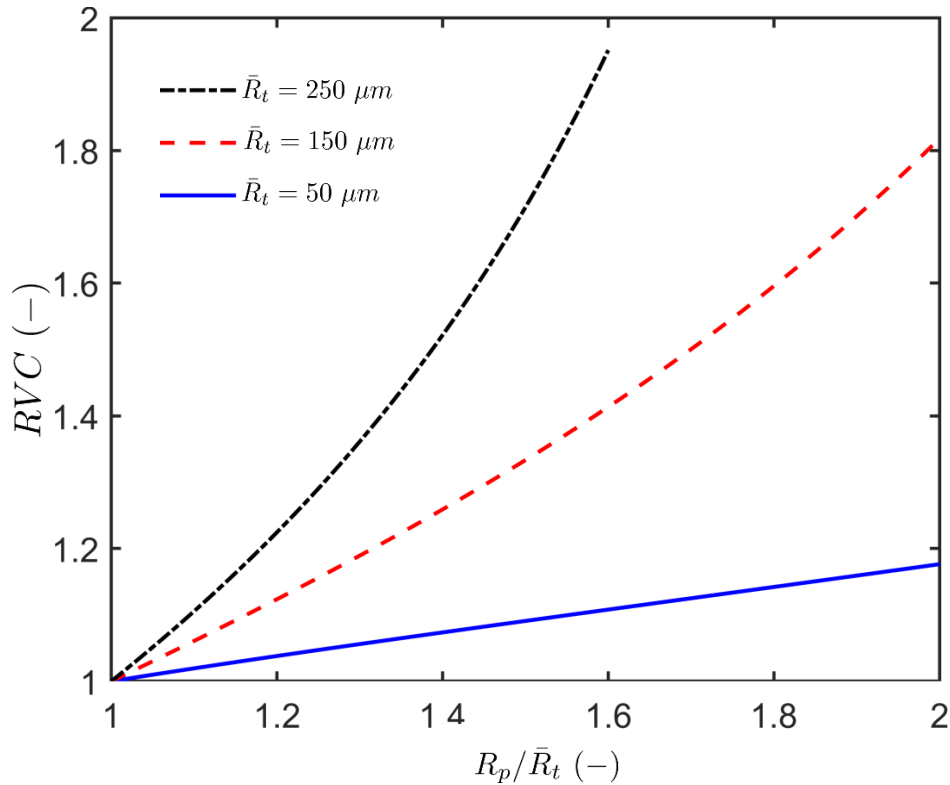


Figure 3.4: Relative vapor conductance (TPM over TNM) against the ratio of pore radius to throat radius for different values of mean throat radius. The pores at the ends of the throat have the same size, and the center distance is  $h = 1000 \mu\text{m}$ .

### 3.3 Liquid transport conductance

The momentum transport equation (Navier-Stokes equations) can be used to describe the transport of liquid between two nodes or pores (Fig. 3.5). Assuming steady-state, incompressible, unidirectional and laminar flow, the Navier-Stokes equations can be simplified, resulting in the Hagen-Poiseuille equation.

Applying these conditions the momentum transport equation for laminar viscous flow

in a cylindrical throat (Fig. 3.5) is obtained to:

$$0 = -\frac{dP}{dz} + \mu \left[ \frac{1}{r} \frac{d}{dr} \left( r \frac{dv_z}{dr} \right) \right]. \quad (3.16)$$

With the boundary conditions

$$\frac{dv_z}{dr} = 0 \text{ at } r = 0, \quad v_z = 0 \text{ at } r = R, \quad (3.17)$$

we get the velocity distribution profile  $v_z$  across the radius as:

$$v_z = -\frac{1}{4\mu} \frac{dP}{dz} (R^2 - r^2). \quad (3.18)$$

Equation 3.18 indicates that in a pipe of given length  $h$  and radius  $R$ , a velocity profile will be achieved, which is only a function of the ratio  $\Delta P/\mu$ .

The volumetric flow rate can be determined by integration to

$$\dot{Q} = \int_0^R v_z dA. \quad (3.19)$$

Finally, we combine Eqs. 3.18 and 3.19 to get the volumetric flow rate as:

$$\dot{Q} = -\frac{\pi}{8\mu} R^4 \frac{dP}{dz}. \quad (3.20)$$

In the TNM, the volumetric flow rate in a throat can be determined by integration over the length  $h$ ,

$$\int_0^h \frac{\dot{Q}}{R^4} dz = \frac{\pi}{8\mu} \int_{P_1}^{P_2} dP, \quad (3.21)$$

Introducing the liquid mass flow rate

$$\dot{M}_w = \dot{Q} \rho_w, \quad (3.22)$$

the liquid mass flow rate of the TNM can be obtained as:

$$\dot{M}_{w,TNM} = \frac{\pi \rho_w R_t^4}{8\mu h} (P_1 - P_2). \quad (3.23)$$

Regarding the liquid flow in the TPM, the transition process between throat and pore is neglected, suggesting identical fluid velocity profile in throats and pores (Fig. 3.5). This treatment can be accepted for the slow isothermal drying process. The liquid mass flow

rate can then be calculated by integrating Eq. 3.2 over the length  $h$ :

$$\dot{M}_{w,TPM} = \frac{\pi \rho_w}{8\mu} \frac{1}{\left(\frac{R_{p,1}}{R_{p,1}^4} + \frac{L_t}{R_t^4} + \frac{R_{p,2}}{R_{p,2}^4}\right)} (P_1 - P_2). \quad (3.24)$$

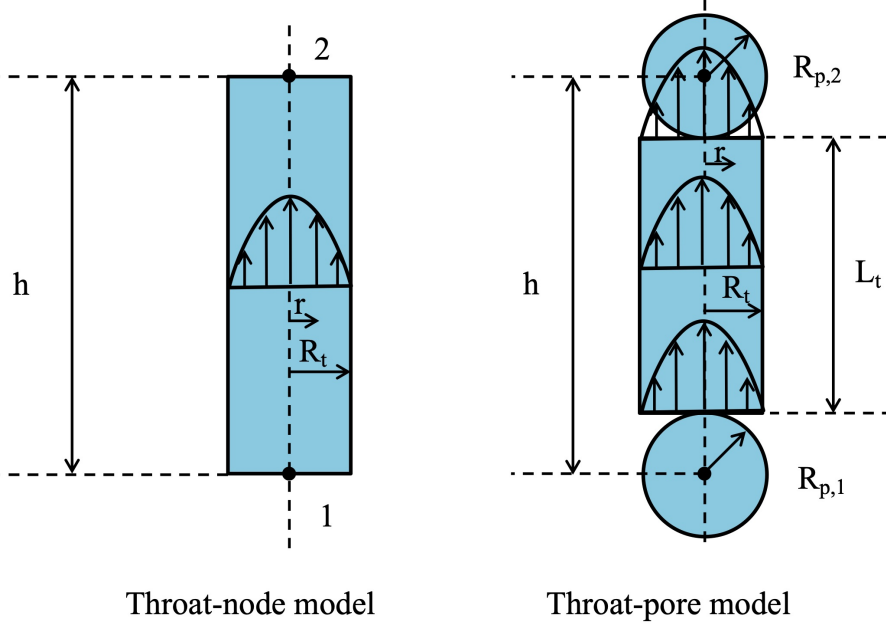


Figure 3.5: Velocity profile across cylindrical throats and spherical pores featuring laminar viscous flow.

The liquid transport conductances in the TNM and the TPM can be specified according to Eqs 3.23 and 3.24:

$$g_{w,TNM} = \frac{\pi \rho_w R_t^4}{8\mu h}, \quad (3.25)$$

$$g_{w,TPM} = \frac{\pi \rho_w}{8\mu} \frac{1}{\left(\frac{R_{p,1}}{R_{p,1}^4} + \frac{L_t}{R_t^4} + \frac{R_{p,2}}{R_{p,2}^4}\right)}. \quad (3.26)$$

The ratio of the liquid conductance of TPM over that of TNM can be evaluated as relative liquid conductance,

$$RLC = \frac{g_{w,TPM}}{g_{w,TNM}}. \quad (3.27)$$

Figure 3.6 shows RLC against the ratio of pore radius (assumed same for both pores of the TPM) to throat radius ( $250 \mu\text{m}$ ) with throat length or center distance of the pores of  $h = 1000 \mu\text{m}$ . The RLC increases strongly with the ratio of  $R_p/R_t$ . Once the throat radius is specified, the liquid conductance depends strongly on the pore radius (Fig. 3.6). The liquid conductance will be doubled for the network setting with  $R_p = 350 \mu\text{m}$  and  $R_t = 250 \mu\text{m}$ . Figure 3.7 shows that the sensitivity of RLC upon pore radius decreases with shrinking throat radius. The liquid conductance is much more sensitive to the pore radius

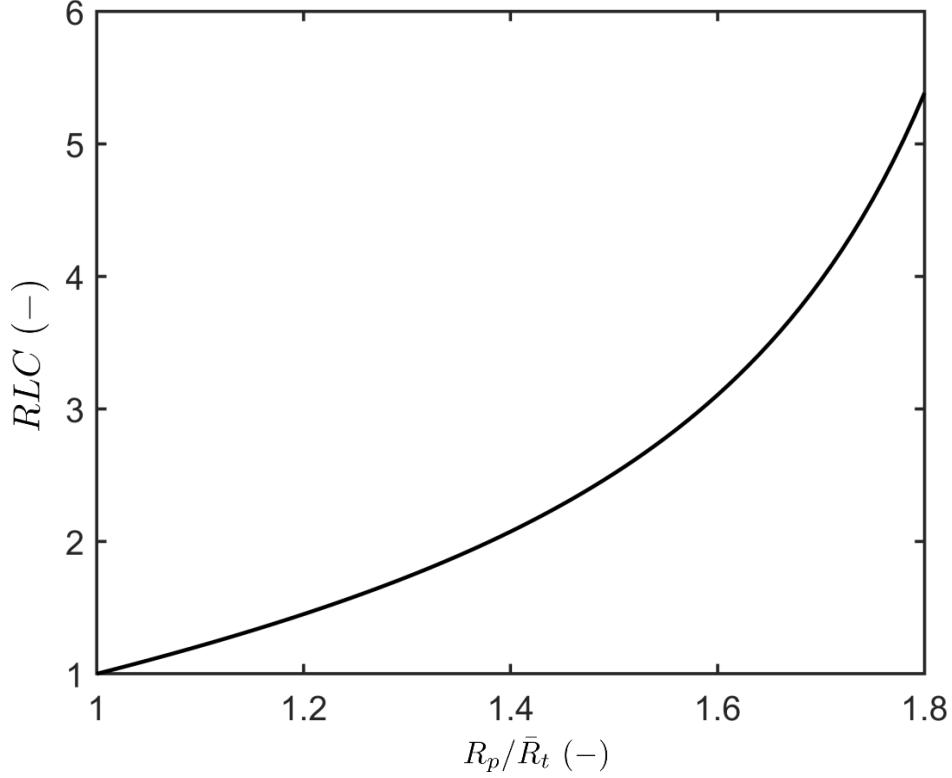


Figure 3.6: Relative liquid conductance of the TPM over TNM for same center distance,  $h = 1000 \mu\text{m}$ , and mean throat radius,  $\bar{R}_t = 250 \mu\text{m}$ . The two pores at the ends of the throat are assumed to have the same radius,  $R_p$ .

than the vapor conductance. Figure 3.3 indicates that the vapor conductance in TPM is 50% larger than in TNM with the network setting of  $350 \mu\text{m}$  for the pores and  $250 \mu\text{m}$  for the throat. In contrast, the liquid conductance is doubled between these two systems (Fig. 3.7). This is due to the fact that the liquid conductance depends on the fourth power of the radius in Eq. 3.26.

### 3.4 Drying kinetics

To enable the investigation of drying characteristics for the two different geometries, we introduce the evaluated vapor and liquid conductances into the TNM and TPM, respectively. Figure 3.8 shows the evolution of network saturation over time during the entire drying process and the corresponding normalized drying rate as a function of network saturation for the TNM and the TPM. Those profiles are achieved by averaging ten parallel simulations. The averaging method among the parallel simulations is introduced in Chapter 6.

The drying time of the TPM is less than half of the drying time obtained for the TNM. Such difference is not only caused by overestimated volume in the TNM but also affected by the spherical pores altering the invasion mechanism in the TPM. The two network

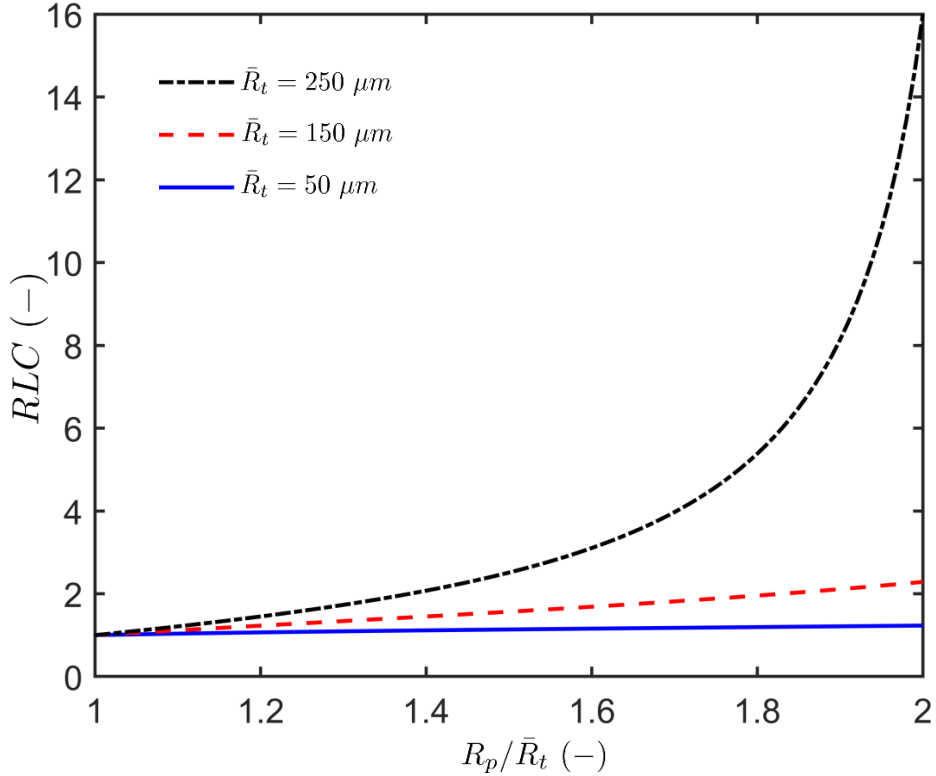


Figure 3.7: RLC for different throat radii with otherwise same conditions as in Fig. 3.6.

geometries share the same evaporation rate until a network saturation of 0.96. At high saturation ( $S > 0.96$ ), the two models produce the same number of single menisci and clusters (Fig. 3.9), and they have the same evaporation rate (Fig. 3.8). The evaporation rate decreases sharply during this period, which is oftentimes called initial transition period (TP). The TP is due to the invasion of surface pores, altering the surface vapor pressure distribution. It is not affected by network geometry. From that point on, the evaporation rate is higher for the TPM than for the TNM.

The drying kinetics of the TPM demonstrates a constant drying period until  $S_{net} = 0.75$ , whereas the evaporation rate of the TNM falls continually. The surface saturation is critical to the drying kinetics. During this constant evaporation rate period, the surface saturation is sustained since the liquid pumped from the depth of the network is sufficient to replenish the surface. The surface saturation lasts longer in the TPM than in the TNM. With periodic boundary conditions on the lateral sides, three throats correspond to one pore in the TPM, so that the TPM has  $4N$  structural elements ( $N$  is the number of pores) in comparison to  $3N$  structural elements in the TNM. As a result, more options are available in the TPM, suggesting a higher probability of radius difference between menisci. Therefore the capillary pumping is enhanced in the TPM, which can transport more liquid from bottom to surface of the porous medium. Meanwhile, liquid transport suffers less internal resistances in TPM (Fig. 3.9).

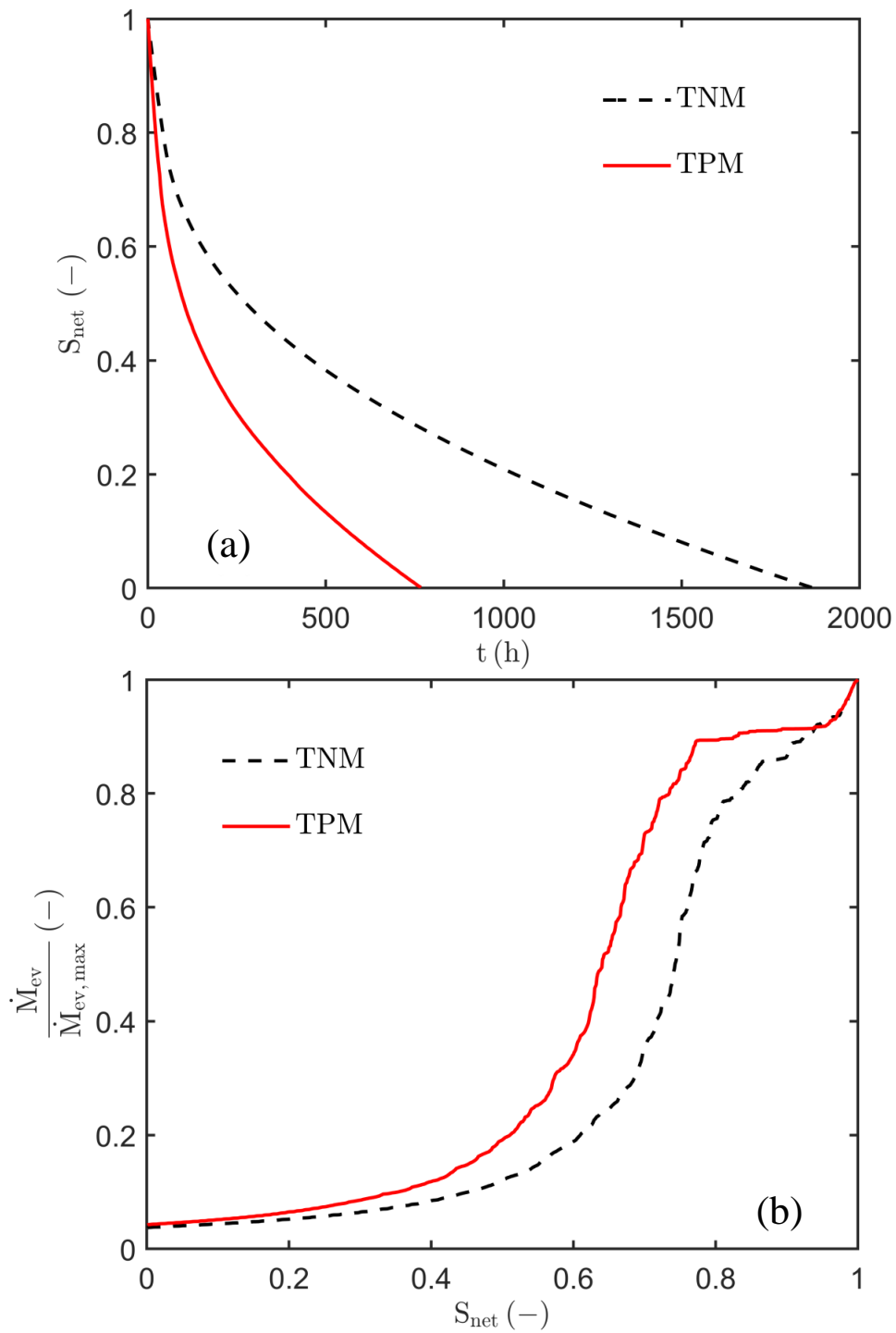


Figure 3.8: (a) Network saturation and (b) normalized drying rate obtained for TNM and TPM network geometries. The values are averaged over ten realizations for small saturation intervals.

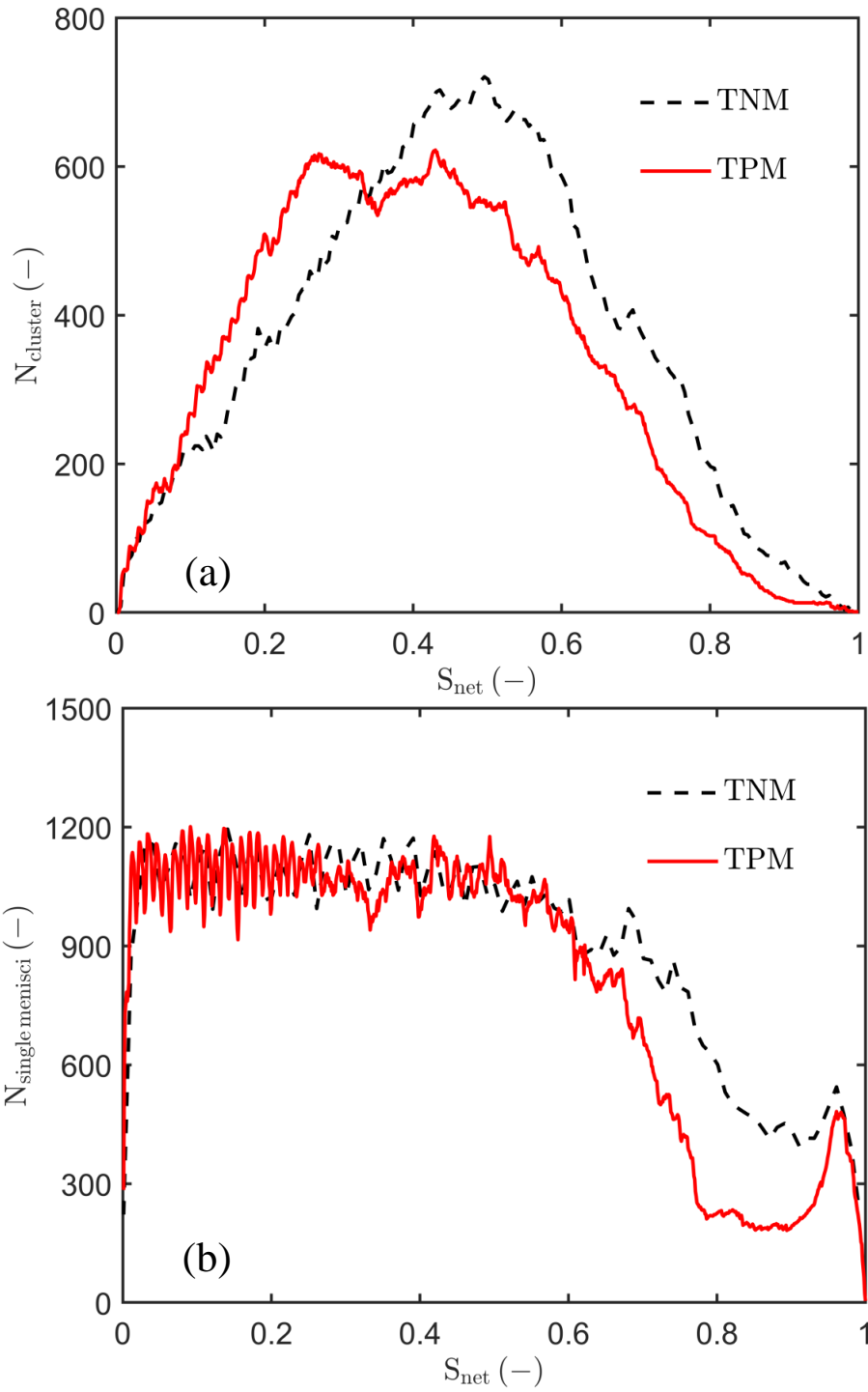


Figure 3.9: Numbers of (a) liquid clusters and (b) single menisci obtained for TNM and TPM network geometries. The values are averaged over ten realizations for small saturation intervals.

During the drying process, the internal resistance becomes larger than the external resistance (resistance of vapor transport in the boundary layer). The internal resistance is produced by, for example, single menisci and dispersed isolated liquid clusters. Once various single menisci and liquid clusters have been formed in the pore network, they break down paths for water transport from the depth of the network to the drying front. When it comes to the constant drying period, the number of single menisci in the TPM is significantly smaller than that in the TNM (Fig. 3.9). More local capillary pumping exists in the TPM. Therefore the internal resistance for this network geometry is lower. After the constant drying rate period, the evaporation rate is larger than the moisture transport rate within the network. The evaporation rate begins to drop. The internal resistance is increased by the air invasion forming numerous liquid clusters and single menisci (Fig. 3.9). The moisture transport resistance increases along with the drying history, but remains lower for the TPM than for the TNM.

When the evaporation front recedes, the evaporation rate becomes similar in the two models. During this period, liquid viscosity plays the dominant role in liquid transport. The number of single menisci reaches a maximum, which means that the internal resistance dramatically prevents moisture transport. With some fluctuation, the maximal number of single menisci is the same for both models. This result shows that pore volume plays a minor role in reducing the number of single menisci during this period. The moisture transport is dominated by the vapor phase during this period.

Figure 3.10 shows the saturation profiles for two the network geometries ( $z/H = 0$  is the bottom slice and  $z/H = 1$  is the top slice). The residence time of liquid in the top slice is longer in the TPM because of more capillary pumping and less internal resistance. Irreducible saturation  $S_{irr}$ , at which the liquid disconnects, is lower for the TPM than for the TNM. To further illustrate the differences between the different network geometries, we introduce the invasion profile. Invasion is defined by the ratio of the number of pores/nodes containing water ( $N_{l,slice}$ ) to the total number of pores/nodes in each slice ( $N_{tot,slice}$ ):

$$I = \frac{N_{l,slice}}{N_{tot,slice}} \quad (3.28)$$

Figure 3.11 shows the invasion ratio for the two models. In the receding rate period (e.g., for  $S_{net} = 0.3$ ), the two models have similar invasion profiles in bottom layers ( $z/H \approx 0.2 - 0$ ). However, these layers have a different value of saturation (Fig. 3.10). The overestimated volume in TNM leads to relatively high saturations. Therefore the irreducible saturation ( $S_{irr}$ ) declines when altering pore network geometry from TNM to TPM.

At this end, it should be noted that the TPM underestimates to a certain extent the liquid volume in the corners of throat and pore conjunctions (Fig. 3.12). This neglected volume in the current work would play no role in the invasion mechanism since the liquid

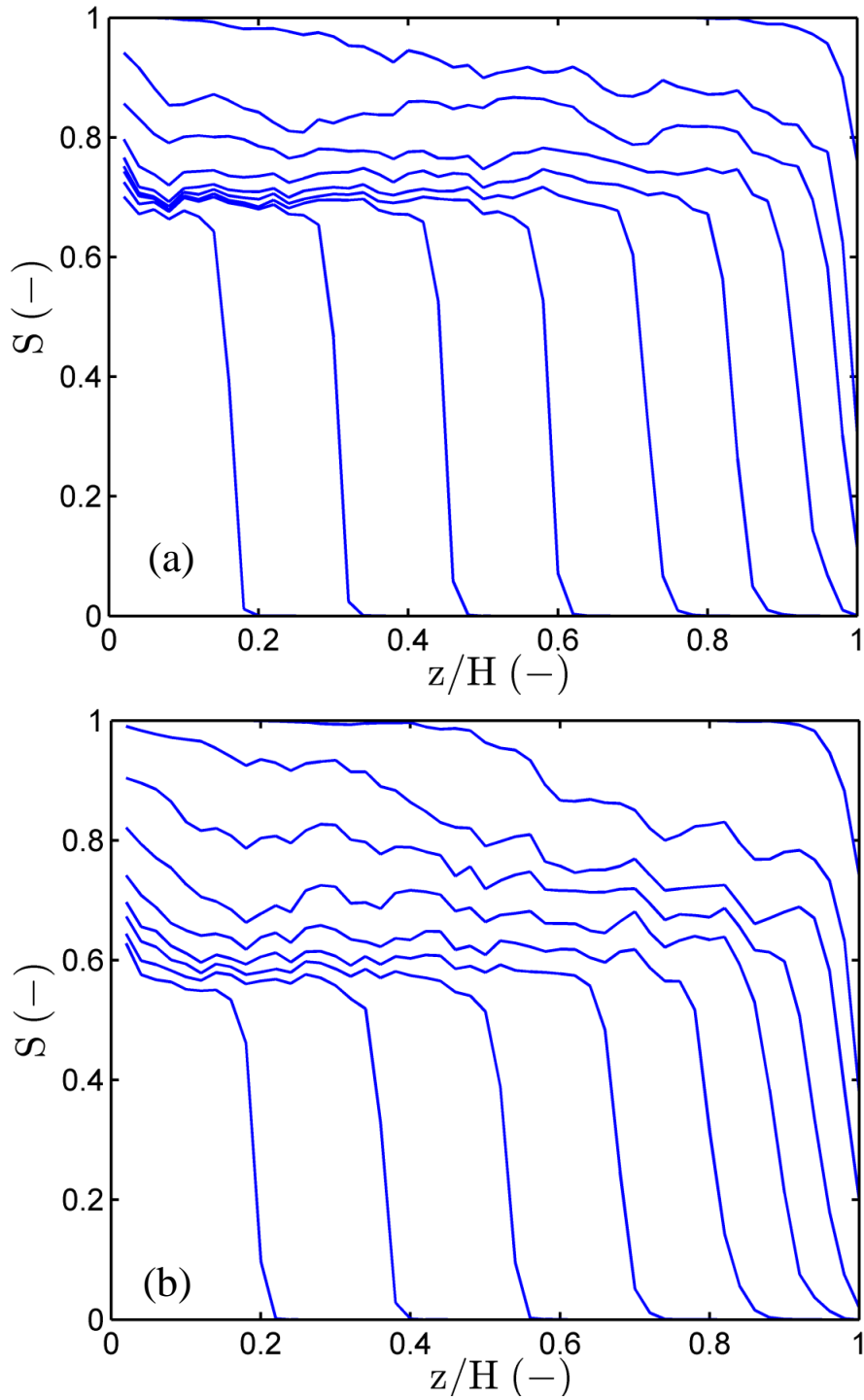


Figure 3.10: Saturation profiles (averages over ten realizations) obtained from PNM for two network geometries (a) TNM and (b) TPM. From top the profiles belong to network saturations of 0.99, 0.9, 0.8, 0.7, 0.6, 0.5, 0.4, 0.3, 0.2, and 0.1, respectively.

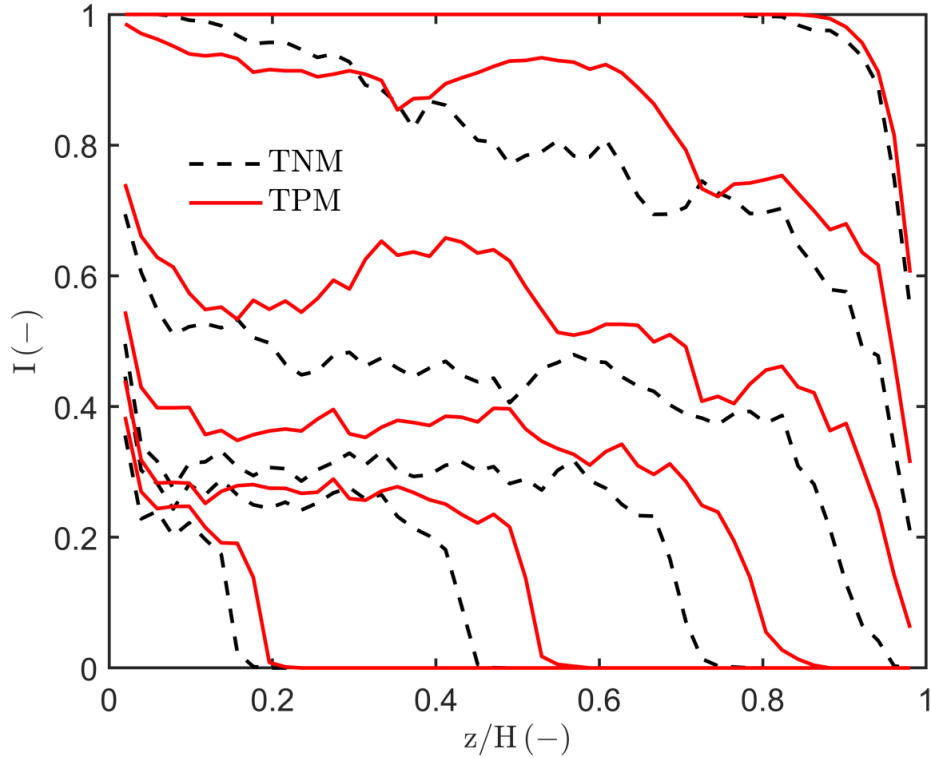


Figure 3.11: Ratio of liquid pores/nodes to total pores/nodes in each slice during drying obtained for the two models. From the top, profiles correspond to network saturations of 0.99, 0.9, 0.7, 0.5, 0.3, and 0.1, respectively (values are averaged over ten realizations).

is assumed to be free water and perfectly wetting. That is to say, the effect of geometry at the corners, leading to the reshaping of the liquid-vapor interface is not discussed in the current work. Based on these assumptions, this neglected volume in the corners can be compensated by assuming that the pore radius is larger or at least comparable with the largest radius of neighbor throats. This treatment could avoid the drawback of the TPM at the conjunctions on the void volume description.

The liquid flow at the corners of throats with non-circular cross section can play a significant role during the drying process. In this sense, the neglected volume at the conjunction (Fig. 3.12) may be considered further in the TPM. For example, a secondary capillary invasion process might be assumed. Vapor pressure of pores neighbor to these throats would then be assumed to remain at saturated vapor pressure even after complete invasion of the neighbor throats if liquid is still left behind in the corners. The pores would become unsaturated only after all liquid in the corner has been evaporated in the course of secondary capillary invasions. This treatment would correspond to the formation of liquid films that can enhance the liquid hydraulic connectivity, although a large volume of liquid has been removed by evaporation. Vorhauer et al. (2015) observed secondary capillary structures in experiments and modeled their influence on the drying process using a 2D TNM, where throats are cylinders with non-circular cross section.

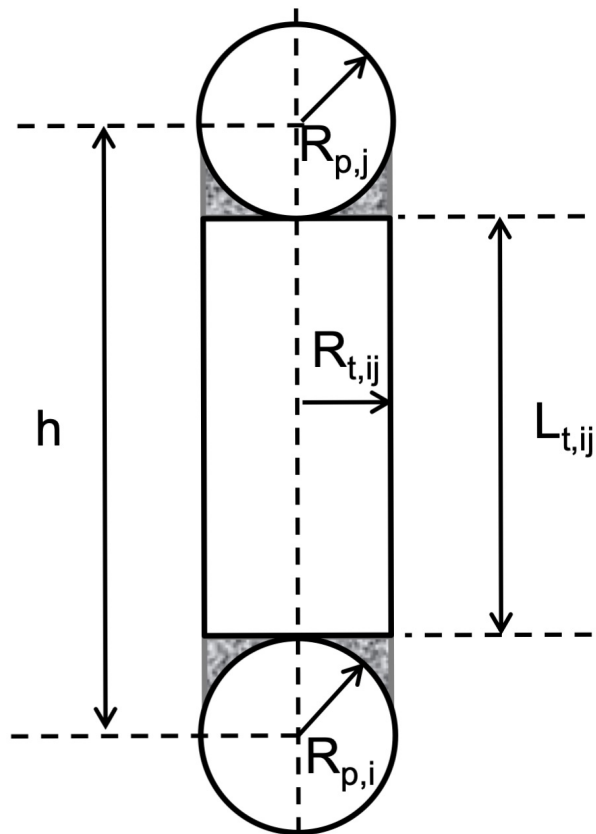


Figure 3.12: Schematic for the underestimation of the volume at the conjunctions between a throat and the two pores with which this throat is connected.

# Chapter 4

## One-equation continuum model for drying capillary porous media

*This chapter is partly taken from “Lu, X., Kharaghani, A., Tsotsas, E., (2020). Transport parameters of macroscopic continuum model determined from discrete pore network simulations of drying porous media: Throat-node vs. throat-pore configurations. Chemical Engineering Science 223, 115723”.*

In this chapter, we derive the one-equation continuum model and introduce its transport parameters. This continuum model (CM) can be used to describe a drying process in which the underlying transport phenomena are driven by gradients in spatially averaged quantities and controlled by nonlinear parameters. Such a description is based on the hypothesis of local equilibrium within a small volume element of the drying medium, although the entire medium has not reached the equilibrium state.

### 4.1 Assumptions

In order to derive the one-equation continuum model, the mass balance equations are written locally. For each control volume (Fig. 4.1), the following assumptions are made:

- No storage of kinetic energy (which cannot be absorbed by the fluid to alter the properties of fluid) in the mass of the flowing phases considered, i.e. no inertial forces and no free convection. The physical properties, density and viscosity, are independent of time.
- Time-constant reference volume with arbitrary size and shape (representative element volume, REV).
- Constant mass of the gas phase in a given volume.

In general, a balance equation can be expressed based on the status of the observer: standing stationary to describe the variables locally (most cases) or moving with a reference velocity.

To provide an easier pathway to derive equations, we build the following balance equations on the local format.

Assuming isothermal conditions at low temperature and constant gas pressure during the entire drying process, we can approximate the process by mass transport only in one spatial dimension (the direction perpendicular to the evaporative surface). In this frame, mass balances can be expressed separately for the liquid and for the vapor phase, but they can also be combined into one equation for the moisture transport.

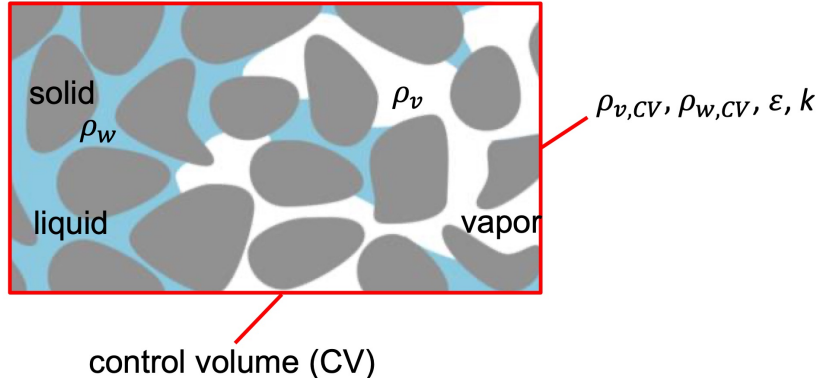


Figure 4.1: Schematic of the control volume of the porous medium for the continuum model.

## 4.2 Component mass balance for liquid water

Because of air invasion, the liquid phase is divided into liquid clusters (dispersed phase), which means that governing equations may not be suitable for every control volume at every time. Therefore, it is essential to assume that the liquid phase remains continuous during drying history.

Then, the general mass balance for liquid water in local formulation reads:

$$\frac{\partial \rho_{w,CV}}{\partial t} = -\frac{\partial}{\partial z}(\rho_{w,CV}v + j_{w,CV}) - \chi, \quad (4.1)$$

where the accumulation of liquid water in the control volume with time ( $\partial \rho_{w,CV} / \partial t$ ) is contributed by the convection flow ( $\rho_{w,CV}v$ ) and the diffusion flow ( $j_{w,CV}$ ) as well as the sink term ( $\chi$ ) in general. The diffusion term can be neglected because the liquid phase contains only water; the sink term  $\chi$  is caused by evaporation in the drying process;  $\rho_{w,CV}$  is the liquid component density in the control volume, which can be calculated by:

$$\rho_{w,CV} = \frac{m_{w,CV}}{V}. \quad (4.2)$$

Herein  $m_{w,CV}$  is the mass of liquid water in the control volume, and  $V$  is the total volume.

The total volume can be expressed by:

$$V = \frac{V_{void}}{\varepsilon}, \quad (4.3)$$

where  $V_{void}$  is the void part of the control volume and  $\varepsilon$  is the porosity of the porous medium. The mass of liquid water in the control volume can be expressed by:

$$m_{w,CV} = \rho_w V_{w,CV}, \quad (4.4)$$

where  $\rho_w$  is the density of liquid water and  $V_{w,CV}$  is the volume of liquid water in the control volume, which can be calculated by:

$$V_{w,CV} = S V_{void}. \quad (4.5)$$

Here,  $S$  is saturation ( $0 < S \leq 1$ ). By combining Eqs. 4.2 to 4.5,  $\rho_{w,CV}$  can be determined by:

$$\rho_{w,CV} = \varepsilon \rho_w S. \quad (4.6)$$

The velocity of liquid ( $v$ ) can be calculated by Darcy's law (neglecting gravity):

$$v = \frac{-\frac{k}{\mu} \frac{\partial P_w}{\partial z}}{\varepsilon S}. \quad (4.7)$$

By introducing Eqs. 4.6 and 4.7 into Eq. 4.1, the mass balance can be rearranged into:

$$\frac{\partial(\varepsilon \rho_w S)}{\partial t} = -\frac{\partial}{\partial z} \left( -\rho_w \frac{k \partial P_w}{\mu \partial z} \right) - \chi, \quad (4.8)$$

where  $k$  is the permeability.

### 4.3 Component mass balance for water vapor

The local vapor balance can be formulated in general as:

$$\frac{\partial \rho_{v,CV}}{\partial t} = -\frac{\partial}{\partial z} (-\rho_{v,CV} v + j_{v,CV}) + \chi. \quad (4.9)$$

The accumulation of the vapor in the control volume ( $\partial \rho_{v,CV} / \partial t$ ) can be determined by the convection term ( $\rho_{v,CV} v$ ) and by the diffusion term of vapor in air ( $j_{v,CV}$ );  $\chi$  is the source term which is equal to the sink term of liquid water at the slow isothermal drying and  $\rho_{v,CV}$  is the density of vapor in the control volume. This work assumes that drying takes place at room temperature and that total pressure within the drying material remains constant and equal to the total ambient pressure. This means that there is no flow of the gas phase in the drying material and the convection term can be neglected in Eq. 4.9.

Stefan's law is used to express the one-sided diffusion of vapor in the gas phase. Thus, the vapor mass flux can be calculated from Eq. 3.9 as:

$$j_v = \frac{\widetilde{M}_v \dot{N}_v}{A} = -\frac{D_{va} \widetilde{M}_v}{\widetilde{R}T} \left( \frac{P}{P - P_v} \right) \frac{\partial P_v}{\partial z}. \quad (4.10)$$

Using the total cross-sectional area in place of  $A$  in Eq. 4.10 means that

$$j_{v,CV} = j_v. \quad (4.11)$$

The density of vapor in the control volume ( $\rho_{v,CV}$ ) can be determined by:

$$\rho_{v,CV} = \frac{m_{v,CV}}{V} = \frac{\rho_v V_{v,CV}}{V}, \quad (4.12)$$

with

$$V_{v,CV} = V_{void} - V_{w,CV}. \quad (4.13)$$

The density of the vapor in the control volume results in:

$$\rho_{v,CV} = \varepsilon \rho_v (1 - S). \quad (4.14)$$

Finally, the mass balance for the vapor in local formulation becomes:

$$\frac{\partial(\varepsilon \rho_v (1 - S))}{\partial t} = -\frac{\partial}{\partial z} \left( -\frac{D_{va} \widetilde{M}_v}{\widetilde{R}T} \left( \frac{P}{P - P_v} \right) \frac{\partial P_v}{\partial z} \right) + \chi. \quad (4.15)$$

#### 4.4 Mass balance for moisture transport

The moisture transport mass balance for the drying process arises by summation of the mass balances for liquid water (Eq. 4.8) and for water vapor (Eq. 4.15):

$$\varepsilon \rho_w \frac{\partial S}{\partial t} = -\frac{\partial}{\partial z} \left( -\rho_w \frac{k}{\mu} \frac{\partial P_w}{\partial z} - \frac{D_{va} \widetilde{M}_v}{\widetilde{R}T} \left( \frac{P}{P - P_v} \right) \frac{\partial P_v}{\partial z} \right), \quad (4.16)$$

assuming that the drying process is quasi-steady in regard of the vapor (i.e., accumulation of vapor can be neglected).

Equation 4.16 is the one-equation CM, which can be written in the form of a diffusion model by introducing the vapor pressure-saturation pressure ratio (relative humidity)  $\varphi$ :

$$\varphi = \frac{P_v}{P^*}. \quad (4.17)$$

Considering Eq. 4.17 and  $\frac{\partial P_w}{\partial S} \frac{\partial S}{\partial z}$ , Eq. 4.16 is finally simplified as:

$$\varepsilon \frac{\partial S}{\partial t} = \frac{\partial}{\partial z} \left( D(S) \frac{\partial S}{\partial z} \right), \quad (4.18)$$

where  $D(S)(m^2/s)$  is represented by:

$$D(S) = \frac{k}{\mu} \frac{\partial P_w}{\partial S} + \frac{P_v^* D_{va} \widetilde{M}_v}{\rho_w \widetilde{R} T} \left( \frac{P}{P - \varphi P_v^*} \right) \frac{\partial \varphi}{\partial S}. \quad (4.19)$$

Therefore, major parameter in the one-equation CM (Eq. 4.18) is the moisture transport coefficient.

#### 4.5 Initial and boundary conditions

To solve Eq. 4.18, initial and boundary conditions need to be defined. The initial condition is straightforward, namely that the network is initially filled with free water:

$$S(z = 0 \rightarrow L, t = 0) = 1. \quad (4.20)$$

Two boundary conditions must be set: One is defined at the bottom of the porous medium (Fig. 4.2) as:

$$\rho_w D(S) \frac{\partial S}{\partial z} \Big|_{z=0,t} = 0. \quad (4.21)$$

The second boundary condition can be set at the medium surface or at the drying front. Classically, the surface is assumed to be at the saturated vapor pressure during the 1<sup>st</sup> drying period or at vapor pressure which is corrected using the desorption isotherm. The vapor mass flow from the surface to the ambient can be considered to be one-dimensional and described by the Stefan law. Thus, the boundary condition at the surface can be defined with the evaporation flux:

$$- \rho_w D(S) \frac{\partial S}{\partial z} \Big|_{z=L,t} = \dot{m}_v, \quad \dot{m}_v = - \frac{D_{va} \widetilde{M}_v P}{\widetilde{R} T \delta} \ln \left( \frac{P - P_{v,\infty}}{P - \varphi_{surf} P_v^*} \right), \quad (4.22)$$

where  $P_{v,\infty}$  (Pa) denotes the vapor pressure in the bulk air,  $P$  (Pa) the atmospheric pressure,  $\delta$  (m) the boundary layer thickness located between the network surface and the bulk air.  $\varphi_{surf} P_v^*$  represents the vapor pressure at the surface. Here, the relative humidity at the surface,  $\varphi_{surf}$ , in Eq. 4.22 is an additional macroscopic parameter.

Alternatively, the boundary condition at the liquid-vapor interface can be set depending on the progress of the drying process. For the first drying period, Eq. 4.22 can be selected. In contrast, Lockington et al. (2003) and Keita et al. (2013) assumed a constant moving velocity of the drying front in the second drying period.

Instead of observing the movement of the drying front, an evaporation flux boundary

condition at the drying front can directly be derived from the recorded profile of the drying rate obtained from experimental measurements (Pel et al., 1993). Alternatively, as can be seen in Attari Moghaddam et al. (2017b), the normalized drying rate profile obtained from pore network simulations, which can be seen as numerical experiments is used to reproduce the saturation profiles. However, this treatment to the boundary condition at the liquid-vapor interface limits the applicability of the CM for predictions.

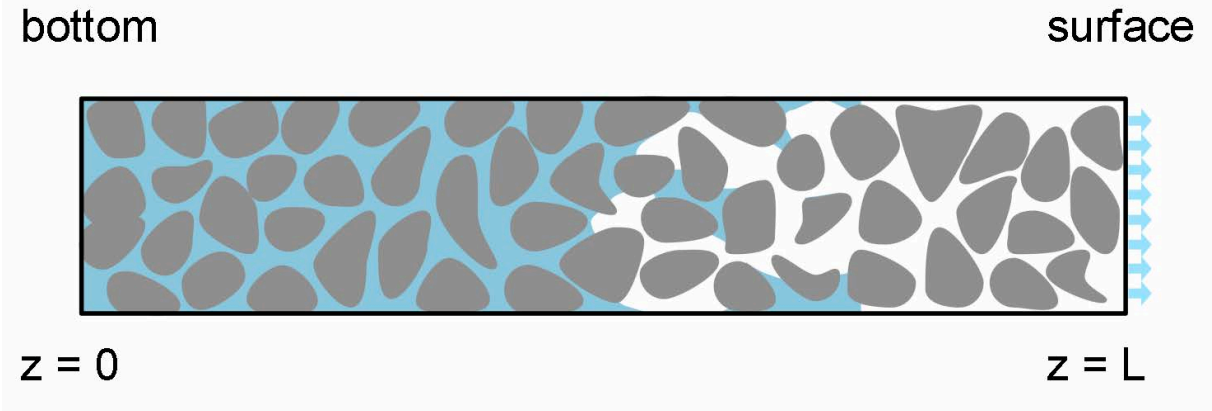


Figure 4.2: Schematic of the application domain of the CM with flux boundary condition on the surface.

# Chapter 5

## Two versions of the one-equation continuum model for drying

*This chapter is partly taken from “Lu, X., Kharaghani, A., Tsotsas, E., (2020). Transport parameters of macroscopic continuum model determined from discrete pore network simulations of drying porous media: Throat-node vs. throat-pore configurations. Chemical Engineering Science 223, 115723”. Another part is taken from “Lu, X., Tsotsas, E., Kharaghani, A., (2021). Drying of capillary porous media simulated by coupling of continuum-scale and microscale models. International Journal of Multiphase Flow 140, 103654”.*

The one-equation continuum model in the form that has been presented in Chapter 4 has difficulties in offering reliable predictions, especially when the drying front has receded into the porous medium. An issue is that the one-equation continuum model cannot truly describe the drying process for the receding front period during which the liquid is first transferred to the gas phase in the voids of the porous medium and then diffuses to the surface.

This chapter provides two methods to tackle this issue. One method is to use the one-equation CM with a moving front boundary condition. Another, somewhat more complex method distinguishes different transport regions in the porous medium, i.e., the wet region, the dry zone and the gas-side boundary layer. This is denoted by the three-transport-zone CM.

### 5.1 Moving front boundary condition

To implement the dynamic boundary condition into the CM, we have to combine an additional region, the gas-side boundary layer, with the porous medium of length  $L$  ( $m$ ) (Fig. 5.1). The thickness of the gas-side boundary layer is  $\delta$  ( $m$ ). The vapor pressure at the bulk air is  $P_{v,\infty}$  ( $Pa$ ). This version of the CM considers two periods of the process: Until the surface is still partially wetted, and after a drying front has started to recede.

### 5.1.1 Wet surface

Initially, the porous medium is filled with free water. Thus, the initial condition is considered as follows:

$$S(z = 0 \rightarrow L, t = 0) = 1, \varphi(z = L, t = 0) = 1, \varphi(z = L + \delta, t = 0) = \frac{P_{v,\infty}}{P_v^*}. \quad (5.1)$$

The mass balance for moisture transport reads as:

$$\varepsilon \frac{\partial S}{\partial t} = \frac{\partial}{\partial z} \left( D(S) \frac{\partial S}{\partial z} \right). \quad (5.2)$$

The boundary condition is set at the surface of the porous medium, according to:

$$D(S) \frac{\partial S}{\partial z} \Big|_{z=L,t} = -\frac{\dot{m}_v}{\rho_w}. \quad (5.3)$$

Here  $\dot{m}_v$  is the drying rate which can be calculated by Eq. 4.22. Equation 4.22 needs the vapor pressure at the surface. As mentioned, many works simply consider that the surface is at saturated vapor pressure when it is still wetted. However, this assumption will be questioned in this work. In fact, the surface vapor pressure has to be determined from experimental measurements or simulations. The adiabatic boundary condition at the bottom of the porous medium is given by Eq. 4.21.

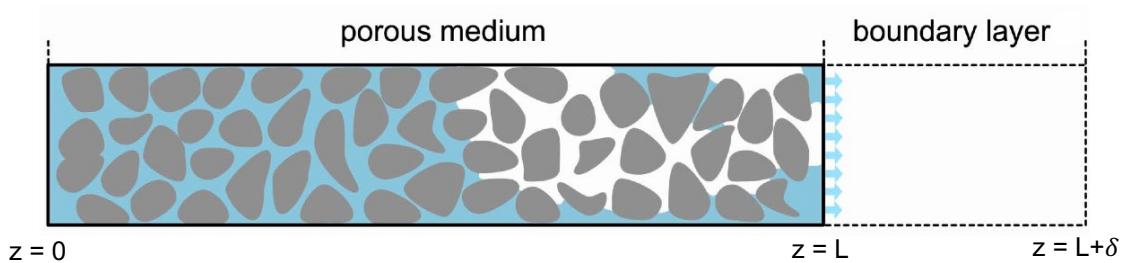


Figure 5.1: Schematic of the transport regions when the medium surface is still wet during drying.

### 5.1.2 Dry surface

After a certain time, the liquid on the surface has been evaporated. Then a drying front starts receding into the porous medium. As a result, a dry zone is formed between the drying front and the network surface (Fig. 5.2). The drying front can be locally determined when solving the moisture transport equation for the receding front drying period. The interface between the foremost position of the liquid and the empty region in the porous medium is defined as drying front (DF). The drying front moves into the depth of the network in the course of the drying process. The drying front in this work is defined

between two control volumes, where one is filled with saturation larger than 0.0001, and the next has saturation smaller than 0.0001. At saturation smaller than 0.0001, the control volume is assumed as empty. Thus, the position of the drying front is a function of drying time,  $0 < DF(t) < L$ .

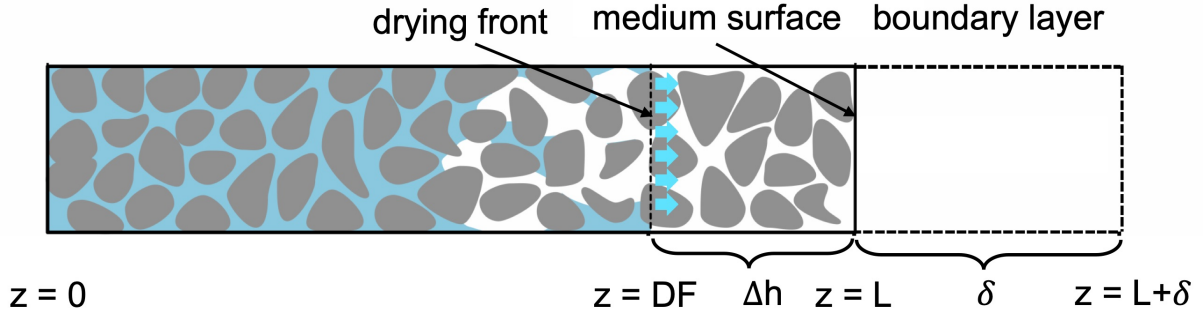


Figure 5.2: Schematic of transport regions when the drying front retreats into the porous medium during drying.

When the DF recedes into the medium, the evaporation rate from the DF is

$$\dot{m}_{v,DF} = \frac{D_{va} \tilde{M}_v P}{\tilde{R}T (\delta + \Delta h)} \ln \left( \frac{P - P_\infty}{P - \varphi_{DF} P_v^*} \right). \quad (5.4)$$

Here the distance between the DF and the bulk air is  $\delta + \Delta h$ , which increases further in the course of the drying process.  $\varphi_{DF}$  denotes the relative humidity at the drying front. Thus, the boundary condition at the drying front becomes:

$$D(S) \left. \frac{\partial S}{\partial z} \right|_{z=DF,t} = - \frac{\dot{m}_{v,DF}}{\rho_w}. \quad (5.5)$$

To solve Eq. 5.4, we have to calculate the relative humidity at the drying front, which is another macroscopic parameter that we have to determine from the PNM.

In summary, the moving front boundary condition is implemented after the drying front has started to recede from the surface. Based on this boundary condition, we solve the one-equation CM using the following macroscopic parameters: The moisture transport coefficient,  $D$ , the relative humidity at the surface,  $\varphi_{surf}$ , and the relative humidity at the drying front,  $\varphi_{DF}$ . The performance of this treatment of the CM will be presented in Chapter 7.

## 5.2 Boundary conditions defined for three transport zones

During the course of the drying process, three mass transport zones can be identified, namely: A wet zone (saturated or two-phase flow zone) in the porous medium, a dry zone in the porous medium (formed after the liquid phase has receded from the free surface),

and the external boundary layer in the gas side (Fig. 5.3). To integrate these three zones in one CM, we impose flux boundary conditions at two interfaces: The interface between the (gas-side) boundary layer and the (medium-side) dry region, as well as the interface between the dry region and the partially saturated part of the wet region which evolves freely during drying. This model is named the three-transport-zone continuum model.

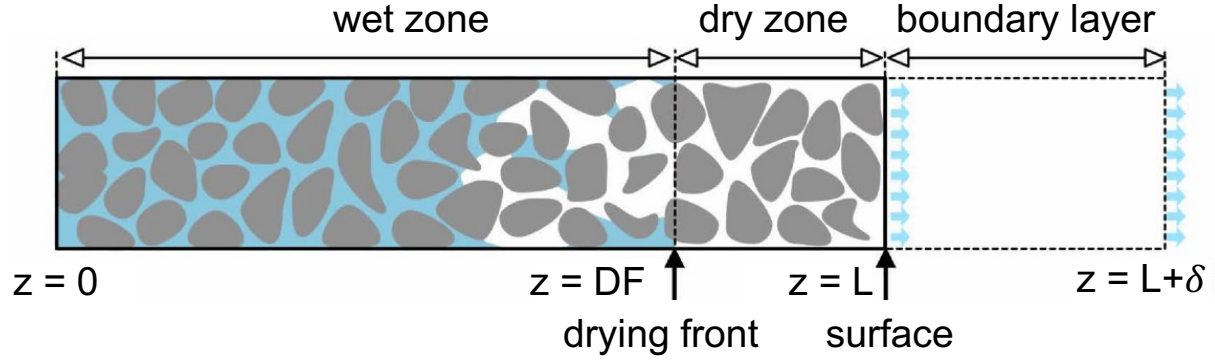


Figure 5.3: Three transport regions during the drying process.

### 5.2.1 Wet surface

In the first drying period, the whole porous medium belongs to the wet zone (saturated and partially saturated zone,  $z = 0$  to  $L$ ). Apart from moisture transport in this zone, only the vapor diffusion in the gas-side boundary layer ( $z = L$  to  $L + \delta$ ) needs to be considered during this period. The governing equation for moisture transport in the wet medium ( $z = 0$  to  $L$ ) reads:

$$\varepsilon \frac{\partial S}{\partial t} = \frac{\partial}{\partial z} \left( D(S) \frac{\partial S}{\partial z} \right). \quad (5.6)$$

The vapor diffusion in the gas-side boundary layer can be expressed by:

$$\frac{\partial \varphi}{\partial t} = \frac{\partial}{\partial z} \left( D_{v,b}(\varphi) \frac{\partial \varphi}{\partial z} \right), \quad (5.7)$$

where  $D_{v,b}$  ( $m^2/s$ ) is the vapor diffusion coefficient in the gas-side boundary layer and  $\varphi$  is the relative humidity:

$$\varphi = \frac{P_v}{P_v^*}. \quad (5.8)$$

To solve Eqs. 5.6 and 5.7, we have to specify initial and boundary conditions. The initial condition for Eq. 5.6 is that of full saturation of the porous medium:

$$S(z = 0 \rightarrow L, t = 0) = 1. \quad (5.9)$$

The initial condition for Eq. 5.7,  $\varphi(z = L \rightarrow L + \delta, t = 0)$ , should correspond to the steady state of relative humidity in the boundary layer. It can be calculated based on Eq. 5.7 by inserting the initial guess, as well as the boundary conditions  $\varphi(z = L, t) = 1$  and  $\varphi(z = L + \delta, t) = P_{v,\infty}/P_v^* = \varphi_\infty$ .

The boundary condition at the surface is:

$$\rho_w D(S_{surf}) \left. \frac{\partial S}{\partial z} \right|_{z=L,t} = \frac{P_v^* \tilde{M}_v}{\tilde{R}T} D_{v,b}(\varphi_{surf}) \left. \frac{\partial \varphi}{\partial z} \right|_{z=L,t}, \quad (5.10)$$

where  $\rho_w$  ( $kg/m^3$ ) is the water density,  $\tilde{M}_v$  ( $kg/kmol$ ) is the molar mass of vapor and  $T$  (K) is the temperature. The boundary conditions at the bottom of the porous medium and at the border of the boundary layer to bulk of air are, respectively:

$$\rho_w D(S) \left. \frac{\partial S}{\partial z} \right|_{z=0,t} = 0, \quad (5.11)$$

and

$$\varphi(z = L + \delta, t) = \varphi_\infty. \quad (5.12)$$

### 5.2.2 Dry surface

After a drying front has been built and started to recede into the porous medium, a dry zone is formed between the drying front and medium's surface. The governing equation reads in local formulation for vapor transport in this zone:

$$\varepsilon \frac{\partial \varphi}{\partial t} = \frac{\partial}{\partial z} \left( D_{v,e}(\varphi) \frac{\partial \varphi}{\partial z} \right). \quad (5.13)$$

where  $D_{v,e}(\varphi)$  ( $m^2/s$ ) is the vapor diffusion coefficient in this zone. In this way, mass transport takes place in three regions: The wet zone in the porous medium, the dry zone of the porous medium, and the gas-side diffusion layer. The drying front (DF) is determined in the same way as in Sec. 5.1.2, namely, based on the saturation (changing in the course of the drying process) of neighboring control volumes in the porous medium. Moisture transport in the wet zone ( $0 \leq z \leq DF(t)$ ) can be described by Eq. 5.6. Equation 5.13 applies to the dry zone of the porous medium ( $DF(t) \leq z \leq L$ ), whereas the vapor transport in the gas-side boundary layer ( $L \leq z \leq L + \delta$ ) can be expressed by Eq. 5.7.

To couple the dry zone with the wet zone in the porous medium and the gas-side boundary layer, two boundary conditions need to be specified. One boundary condition is at the drying front (DF):

$$\rho_w D(S) \left. \frac{\partial S}{\partial z} \right|_{z=DF,t} = \frac{P_v^* \tilde{M}_v}{\tilde{R}T} D_{v,e}(\varphi) \left. \frac{\partial \varphi}{\partial z} \right|_{z=DF,t}, \quad (5.14)$$

and another is set at the surface of the porous medium:

$$\frac{P_v^* \widetilde{M}_v}{\widetilde{R}T} D_{v,e}(\varphi) \frac{\partial \varphi}{\partial z} \Big|_{z=L,t} = \frac{P_v^* \widetilde{M}_v}{\widetilde{R}T} D_{v,b}(\varphi) \frac{\partial \varphi}{\partial z} \Big|_{z=L,t}. \quad (5.15)$$

Thus, three parameters are required in form of profiles with the state variables that express humidity,  $D(S)$ ,  $D_{e,v}(\varphi)$  and  $D_{e,b}(\varphi)$ , to solve Eqs. 5.6, 5.7, and 5.13. Additionally, relationships between saturation ( $S$ ) and relative humidity ( $\varphi$ ) at the drying front and at the surface are necessary to solve the boundary conditions for the CM (Eqs. 5.10, 5.14, and 5.15). The performance of this CM will be presented in Chapter 7.

### 5.3 Numerical method used to solve the CM

Both presented versions of the CM are based on partial differential equations, which, in this work, are solved using the finite volume method (FVM) by dividing the porous medium along its height coordinate into  $n$  finite volume elements. The discretization scheme is illustrated in Fig. 5.4. The lengths of volume elements are the same ( $\Delta z$ ), and  $S_i$  denotes saturation at the center of each volume element. Based on the CM version of Sec. 5.1, an example for the numerical solution is given in the following.

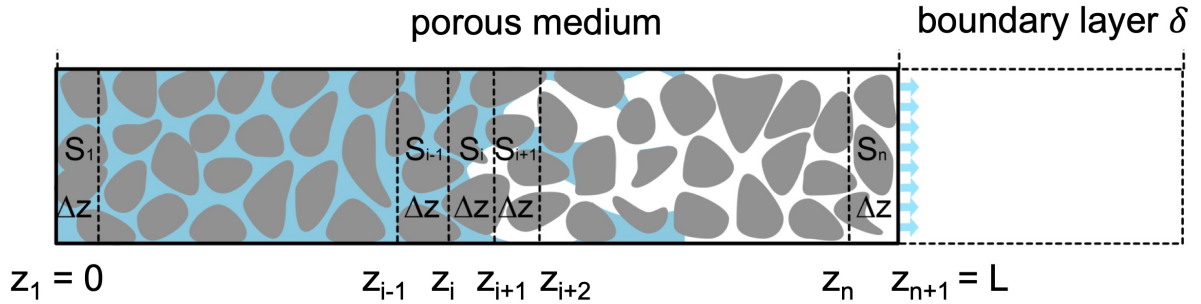


Figure 5.4: Representation of the discretization scheme used to solve the continuum model.

The balance equation (Eq. 5.2) is integrated over an arbitrary control volume:

$$\int_{z=i}^{z=i+1} \varepsilon \frac{dS_i}{dt} dz = \int_{z=i}^{z=i+1} \frac{d}{dz} \left( D(S_i) \frac{dS_i}{dz} \right) dz. \quad (5.16)$$

Terms in Eq. 5.16 are evaluated separately using the proper profile assumptions (Fig. 5.5). For the accumulation term (left-hand side term in Eq. 5.16) the Leibniz integral rule is applied and a piecewise constant profile (which means the saturation is uniformly distributed in each finite volume) is assumed:

$$\int_{z=i}^{z=i+1} \varepsilon \frac{dS_i}{dt} dz = \varepsilon \frac{d}{dt} \int_{z=i}^{z=i+1} S_i dz = \varepsilon \frac{d}{dt} \left( S_i \int_{z=i}^{z=i+1} dz \right) = \varepsilon \frac{d}{dt} (S_i \Delta z). \quad (5.17)$$

The diffusion term (right-hand side of Eq. 5.16) is calculated to

$$\int_{z=i}^{z=i+1} \frac{d}{dz} \left( D(S_i) \frac{dS_i}{dz} \right) dz = D(S_i) \frac{dS_i}{dz} \Big|_i^{i+1}. \quad (5.18)$$

By piecewise linear approximation, one gets:

$$D(S_i) \frac{dS_i}{dz} \Big|_i^{i+1} = D(S_i) \Big|_{z=z_{i+1,t}} \frac{S_{i+1} - S_i}{\Delta z} - D(S_i) \Big|_{z=z_{i,t}} \frac{S_i - S_{i-1}}{\Delta z}. \quad (5.19)$$

The spatially discretized equation for  $i^{th}$  element is thus obtained by:

$$\varepsilon \frac{d}{dt} (S_i \Delta z) = D(S_i) \Big|_{z=z_{i+1,t}} \frac{S_{i+1} - S_i}{\Delta z} - D(S_i) \Big|_{z=z_{i,t}} \frac{S_i - S_{i-1}}{\Delta z}. \quad (5.20)$$

The boundary conditions of this CM should be specified separately for the first (left side) element and the last element (right side). The left-hand side is blocked for liquid transport, which makes the term of  $D(S_1) \Big|_{z=z_{1,t}}$  equal to zero. As a result, we get the moisture transport equation for the first finite volume element of the porous medium as:

$$\varepsilon \frac{d}{dt} (S_1 \Delta z) = D(S_1) \Big|_{z=z_2} \frac{S_2 - S_1}{\Delta z}. \quad (5.21)$$

The right-hand side boundary is at the drying front (DF), the position of which depends on the drying history. In the first drying period, the drying front is at the surface, and  $S_{DF}$  is equal to  $S_n$ . Assuming that there is no accumulation at the surface, which means same moisture flux at both sides, one then obtains:

$$D(S_{DF}) \frac{dS_{DF}}{dz} \Big|_{z=DF,t} = -\frac{\dot{m}_v}{\rho_w}. \quad (5.22)$$

In the receding drying front period, the mass balance equation for the volume element at the drying front ( $i = DF$ ) can be written as:

$$\varepsilon \frac{d}{dt} (S_{DF} \Delta z) = -\frac{\dot{m}_v}{\rho_w} - D(S_{DF}) \Big|_{z=z_{DF-1,t}} \frac{S_{DF} - S_{DF-1}}{\Delta z}. \quad (5.23)$$

Consequently, the moisture transport equation (Eq. 5.2) is solved by FVM as:

$$\frac{dS_1}{dt} = D(S_1) \Big|_{z=z_{2,t}} \frac{S_2 - S_1}{\varepsilon \Delta z^2} \quad \text{for } i = 1, \quad (5.24)$$

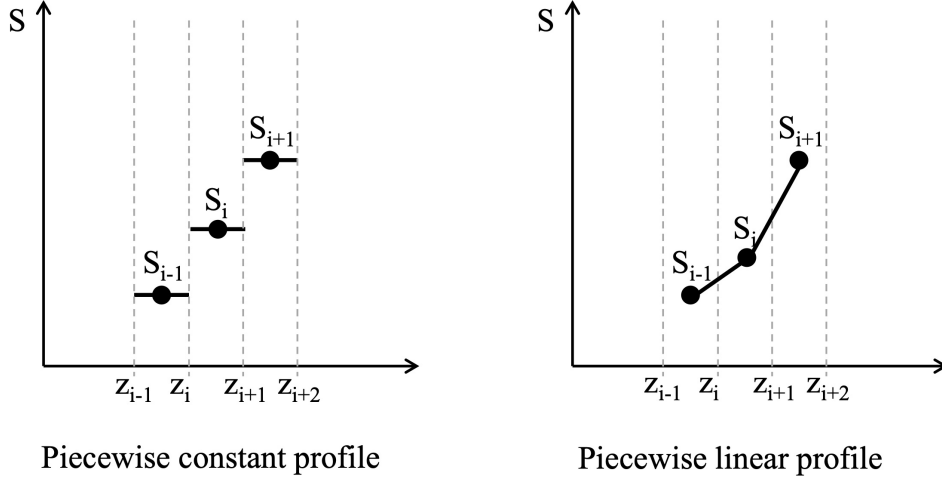


Figure 5.5: The schematic of profile in FVM.

$$\frac{dS_i}{dt} = D(S_i) \Big|_{z=z_{i+1},t} \frac{S_{i+1} - S_i}{\varepsilon \Delta z^2} - D(S_i) \Big|_{z=z_i,t} \frac{S_i - S_{i-1}}{\varepsilon \Delta z^2} \quad \text{for } 1 < i < DF, \quad (5.25)$$

$$\frac{dS_{DF}}{dt} = -\frac{\dot{m}_v}{\varepsilon \Delta z \rho_w} - D(S_{DF}) \Big|_{z=z_{DF-1},t} \frac{S_{DF} - S_{DF-1}}{\varepsilon \Delta z^2} \quad \text{for } i = DF. \quad (5.26)$$

In these ODEs,  $D(S_i) \Big|_{z=z_{i+1},t}$  represents the moisture transport coefficient at length  $z_{i+1}$ , which depends on saturations  $S_i$  and  $S_{i+1}$ . The system of ODEs is solved using the solver `ode15s` in MATLAB. The same method can also be applied to Eqs. 5.6, 5.7 and 5.13, with results which will be presented in Chapter 7.

# Chapter 6

## Determination of the macroscopic parameters of the one-equation continuum model from pore network simulations

*This chapter is partly taken from “Lu, X., Kharaghani, A., Tsotsas, E., (2020). Transport parameters of macroscopic continuum model determined from discrete pore network simulations of drying porous media: Throat-node vs. throat-pore configurations. Chemical Engineering Science 223, 115723”. Another part is taken from “Lu, X., Tsotsas, E., Kharaghani, A., (2021). Drying of capillary porous media simulated by coupling of continuum-scale and microscale models. International Journal of Multiphase Flow 140, 103654”.*

In Chapters 4 and 5 two versions of the one-equation continuum model (CM) have been presented. Both versions of the CM need macroscopic parameters with boundary conditions defined differently. The first model version considers a moving boundary condition and requires the moisture transport coefficient  $D$ , the relative humidity at the surface  $\varphi_{\text{surf}}$  and at the drying front  $\varphi_{\text{DF}}$ . The second model version requires two additional parameters, namely the vapor diffusion coefficient in the dry zone of the porous medium  $D_{v,e}$  and in the gas-side boundary layer  $D_{v,b}$ .

In this chapter, we present the method used to extract these macroscopic parameters from pore network simulations and the respective results. The parameters are functions of local saturation or the local relative humidity, which are hard to determine from classical experiments. With the help of pore network simulations, however, one can capture relevant transport information in the course of drying. The basic idea is that of extracting macroscopic parameters by averaging properties over a particular volume of a pore network. In this work, the averaging volume is a slice containing all horizontal throats/pores of

a certain layer and half of the volume of throats located above and below the middle plane. PNM simulations in this chapter are carried out with the geometrical and physical parameters presented in Tables 3.1 and 3.2.

To reduce randomness of macroscopic parameters, we take several PNM datasets from ten parallel simulations. The averaging method have been introduced in Chapter 3 and is used for averaging all macroscopic parameters in this Chapter.

## 6.1 Moisture transport coefficient

The moisture transport coefficient is an important macroscopic parameter. First, Section 6.1.1 presents the method of evaluation of the moisture transport coefficient from the PNM dataset. Then, the resulting profiles are discussed in Section 6.1.2. It is necessary to note that the network geometry, i.e. throat-node model (TNM) or throat-pore model (TPM), influences the drying kinetics (Chapter 3), suggesting that the moisture transport coefficient could also be impacted by use of one or the other of these two network configurations, which will be discussed here.

### 6.1.1 Computation for extracting the moisture transport coefficient

First the liquid flow rate and the vapor flow rate are computed individually by assorting respectively the vertically connected pores between every two slices. If both pores are filled with liquid, they are attributed to the liquid flow rate. When one of the two pores or both pores are filled with vapor, the vapor flow rate is calculated. In this way, individual transport coefficients for the liquid and for the vapor are obtained. Summing those up, we obtain the compounded moisture transport coefficient and its profile upon saturation.

The liquid and vapor flow rates (in the  $z$ -direction) between slices can be numerically identified by summing the liquid fluxes from liquid pores (or nodes) in the  $n^{\text{th}}$  slice to the  $(n + 1)^{\text{th}}$  slice :

$$\dot{j}_{w,n \rightarrow n+1} = \frac{1}{A} \sum_{i,j} g_{w,ij} (P_{w,i}^n - P_{w,j}^{n+1}), \quad (6.1)$$

and the vapor fluxes between the vapor pores (or nodes) in the  $n^{\text{th}}$  slice and the  $(n + 1)^{\text{th}}$  slice:

$$\dot{j}_{v,n \rightarrow n+1} = \frac{1}{A} \sum_{i,j} g_{v,ij} P \ln \left( \frac{P - P_{v,j}^{n+1}}{P - P_{v,i}^n} \right). \quad (6.2)$$

Moisture transport coefficients are obtained for the liquid phase ( $D_w(S)$ ) and the vapor phase ( $D_v(S)$ ), as:

$$D_w(S) = -\frac{\dot{j}_{w,n \rightarrow n+1}}{\rho_w \frac{S_{n+1} - S_n}{h}}, \quad D_v(S) = -\frac{\dot{j}_{v,n \rightarrow n+1}}{\rho_w \frac{S_{n+1} - S_n}{h}}, \quad (6.3)$$

where  $h$  is the center distance between two pores. They can represent the moisture

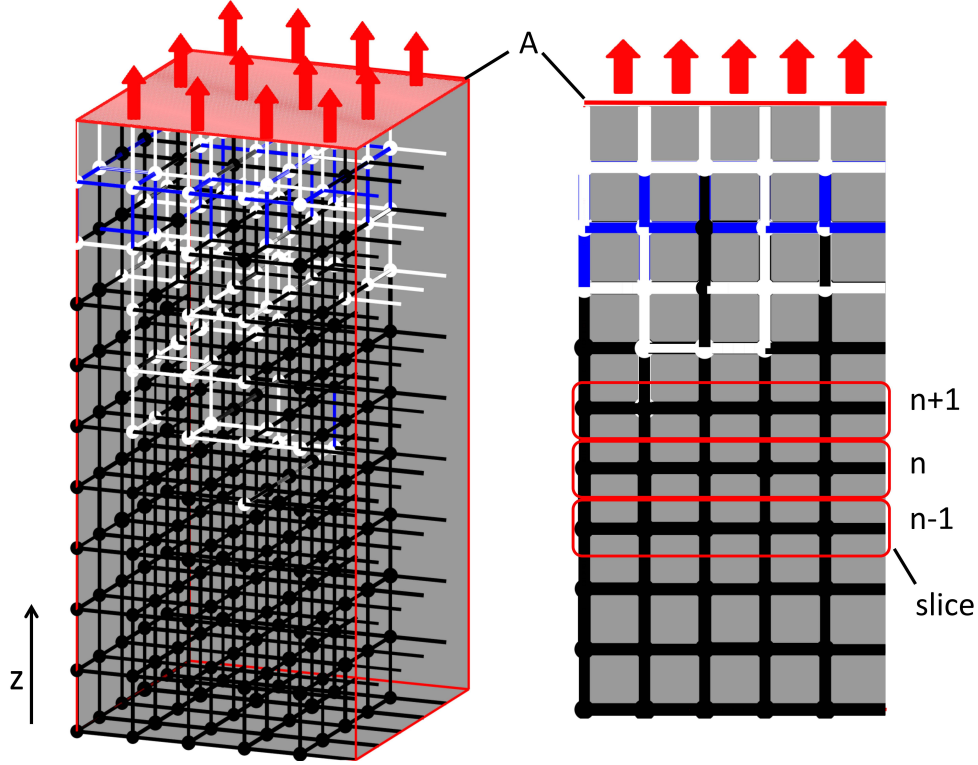


Figure 6.1: (left) A small pore network ( $5 \times 5 \times 10$ ) open to evaporation from the top and (right) its front projection when  $S_{\text{net}} = 0.8$ . A slice contains all throats and pores of one horizontal layer and half of vertical throats. The liquid and vapor throats/pores in the network are shown in black and white, respectively. The blue throats/pores are partially filled with liquid.

transport in the porous medium in simplified way according to Fick's law that is driven by saturation. The overall moisture transport coefficient is

$$D(S) = D_w(S) + D_v(S), \quad (6.4)$$

and, hence, a function of local saturation

$$S = \frac{S_n + S_{n+1}}{2}. \quad (6.5)$$

One has to keep in mind that by means of the above equations we only determine data points along one single line of Fig. 6.2. To obtain the entire moisture transport matrix profile of the drying process, we must apply similar equations to the entire PNM dataset.

### 6.1.2 The moisture transport coefficient

Figure 6.2 shows the moisture transport coefficients  $D(S)$  as a function of local saturation obtained from pore network simulations. Attari Moghaddam et al. (2017b) identified  $D$ - $S$  curves related to the drying process and described three critical points: The limit  $S \approx 1$

at which moisture transport is dominated by the liquid phase; the limit  $S \approx 0$  at which moisture transport is governed by the vapor phase; and the turning point ( $S_T$ ) at which the moisture transport reaches a minimal value. They found moisture transport coefficient profiles to show a clear trend when the local saturation is smaller than  $S_{irr}$ , but failed to identify moisture transport coefficient profiles at high local saturation. In the present work, we noticed another critical saturation point when slices contain the maximum of interfacial area ( $S_{a_s, \max}$ ). The interfacial area of the liquid phase ( $a_s$ ) is defined as the sum of the cross-sectional areas of all menisci in each slice. Based on these four points, we can subdivide the profiles of moisture transport coefficients ( $D$ - $S$  profiles) into three regions: liquid transport dominated region (LTDR), two-phase transport region (TPTR) and vapor transport dominated region (VTDR).

The LTDR is the range from nearly full saturation ( $S \approx 1$ ) to  $S_{a_s, \max}$ , in which moisture transport is fully in the liquid phase. This region can be observed clearly in the ratio of liquid flow rate over total flow rate ( $\zeta$ ) when  $\zeta = 1$  (Fig. 6.4), which means that the whole moisture flow rate is contributed by the liquid. However,  $S_{a_s, \max}$  cannot be clearly seen in Fig. 6.2 due to the coarse time intervals. Figure 6.3 gives the moisture transport coefficient profiles for TPM with smaller  $S_{\text{net}}$  intervals.

The shape of moisture transport coefficient profile in the LTDR depends on the interplay between capillary and viscous forces. In the initial drying period (high  $S_{\text{net}}$ ), the evaporation rate is high, indicating high values of moisture transport coefficient at  $S \approx 1$ , under control by capillary forces. Thus, the moisture transport coefficient depends on the distribution of meniscus radii but not on local saturation. After some time (lower  $S_{\text{net}}$ ), liquid transport starts to suffer of liquid viscosity from the bottom layers. As a result, lower values of moisture transport coefficient are observed in high saturation slices ( $S \approx 1$ ). As the drying process continues, liquid viscosity plays a significant role in the bottom slices but impacts weakly the slices which contain maximum interfacial area ( $S_{a_s, \max}$ ) possessing a high possibility of capillary pumping.

Slices with the maximum interfacial area ( $S_{a_s, \max}$ ) are near to the drying front. The pressure drop caused by liquid viscosity can be calculated as:

$$\Delta P_f = \frac{8\mu\dot{M}_w}{\pi\rho_w} \left( \frac{R_1}{R_1^4} + \frac{L_t}{R_t^4} + \frac{R_2}{R_2^4} \right) \propto \frac{\gamma}{R^4}, \quad (6.6)$$

so that it is related to the distance between the two menisci ( $\gamma$ ). Long distance between two active menisci produces a high value of pressure drop. Therefore, the moisture transport coefficient increases from high saturation slices (in bottom layers with long distance for moisture transport) to slices with  $S_{a_s, \max}$  that have a high probability of capillary pumping with less transport distance between active menisci.

The value of moisture transport coefficient increases when altering the network geometry from TNM to TPM (Fig. 6.2). Moreover, the range of LTDR is extended. Figure 6.7

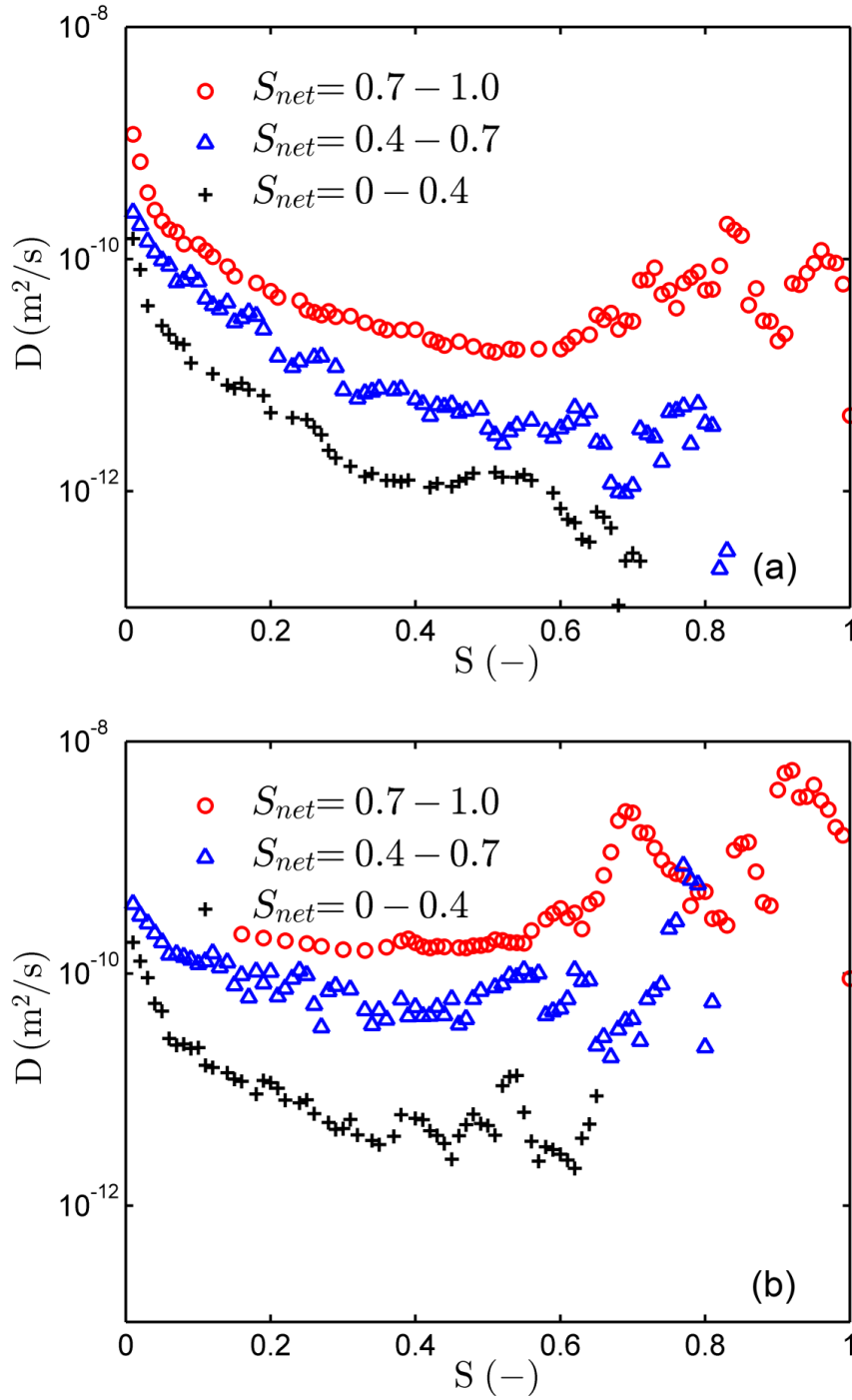


Figure 6.2: The moisture transport coefficient for (a) TNM and (b) TPM network geometry. The values are averaged for ten realizations over local saturation intervals; TNM and TPM from the present work with same time intervals as in Attari Moghaddam et al. (2017b).

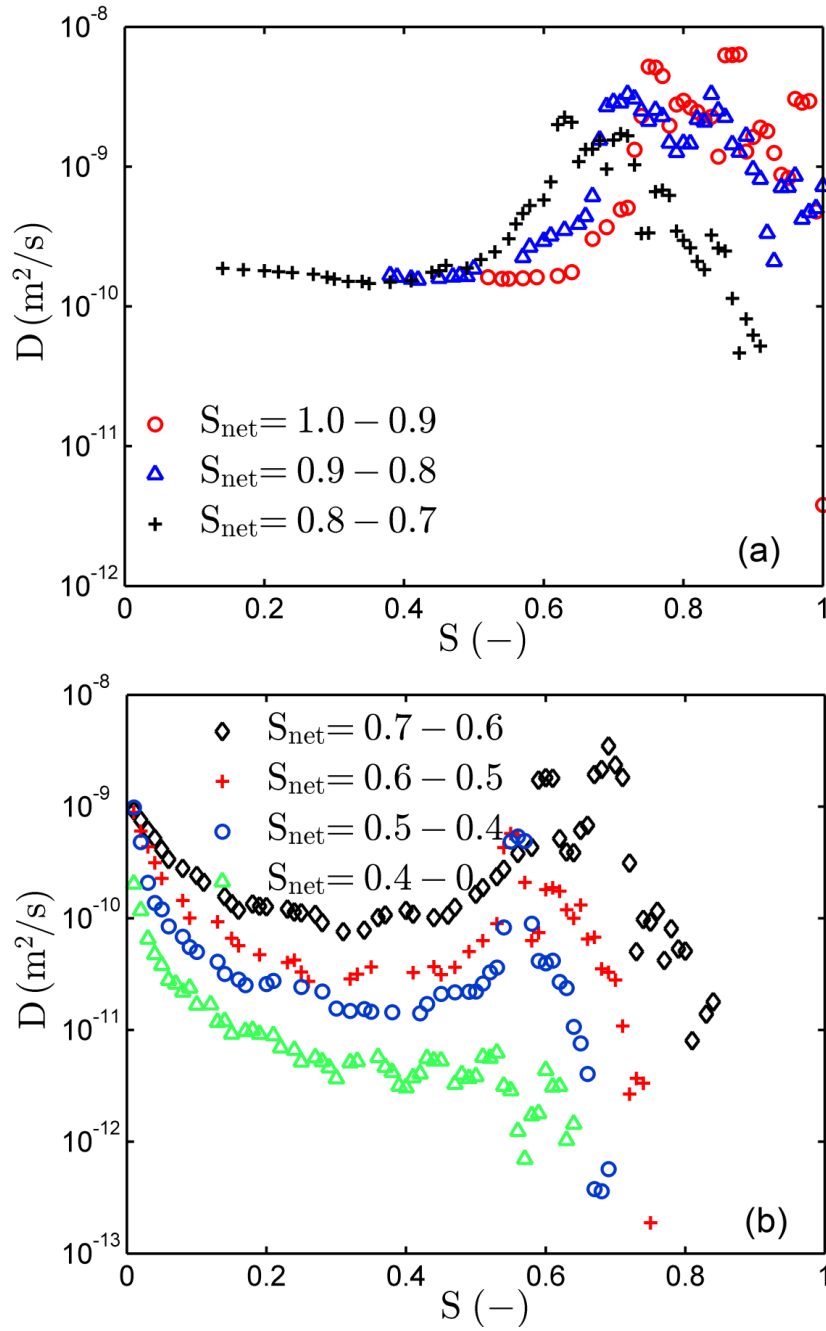


Figure 6.3: The moisture transport coefficient for TPM network geometry obtained from pore network simulations by using smaller time intervals. The values are averaged over ten realizations for intervals of local saturation  $S$ .

shows the liquid-vapor interfacial area as a function of local saturation during the drying process. As can be seen, the interfacial area profile is not unique. Different values  $S_{a_s, \max}$  are observed during the drying process. However,  $S_{a_s, \max}$  is always smaller for a network with TPM geometry. Therefore, the range of LTDR, between  $S \approx 1$  and  $S_{a_s, \max}$ , expands in TPM.

The two-phase transport region (TPTR) is a region in which both the liquid and vapor phases contribute to moisture transport. In this region from  $S_{a_s, \max}$  to  $S_T$  the moisture transport coefficient ( $D$ ) decreases by increasing internal resistance; below  $S_T$  the moisture transport is enhanced again, this is why  $S_T$  is called the turning point.  $S_T$  can be determined according to the ratio of liquid flow rate to total moisture flow rate ( $\zeta$ ) (Fig. 6.4). When  $\zeta = 0.5$  (*i.e.*, same contribution of liquid and vapor phases to the moisture flow), we have observed the minimum value of moisture transport coefficient (Fig. 6.2). In this region, the moisture transport in the vapor phase starts to play a role. The liquid phase is broken into liquid clusters and single menisci (Fig. 3.9). As a result, the moisture transport coefficient decreases from  $S_{a_s, \max}$  to  $S_T$ . The profiles of liquid ratio also depend strongly on the network geometry. The TPTR is shorter for the TNM because the TNM produces more liquid clusters and single menisci (Fig. 3.9). However, liquid phase still has a major contribution in the TPTR for a relatively long saturation range in the TPM (Fig. 6.4). Different values of  $S_T$  are also shown for the entire drying process. When  $S_{\text{net}} = 0.7$ , smaller internal resistance is observed in the TPM (Fig. 3.9), so that liquid can still be pumped to pores near the surface. The ratio  $\zeta$  does not reach the value 0.5 for which vapor and liquid provide the same flux contribution. Hence,  $S_T$  does not appear in Fig. 6.4. As a result, the moisture transport coefficient (Figs. 6.2b and 6.3a) is absent for lower local saturation during this period.

The VTDR is observed for local saturation smaller than  $S_T$  where moisture transport occurs dominantly in the vapor phase. With air invasion, the liquid is broken down into a dispersed phase, forming many single menisci and liquid clusters (Fig. 3.9). Whereas liquid viscosity controls the liquid transport mechanism, the moisture transport in the vapor phase is driven by differences in vapor pressure. The vapor pressure in the two-phase zone is related to the active interfacial areas  $a_s$ . Similar profiles are observed for the TPM and the TNM in the VTDR, because two geometries have the same vapor resistances for the same network. The VTDR shrinks though in the TPM. The range of VTDR is altered along drying time (e.g., no VTDR is observed during the first drying period for the TPM in Fig. 6.3a).

Note that moisture transport coefficients obtained from the PNM dataset have a high degree of scatter. So it is questionable how such scattered data should be implemented into the CM and would affect its predictive performance. These issues will be discussed in Chapter 7.

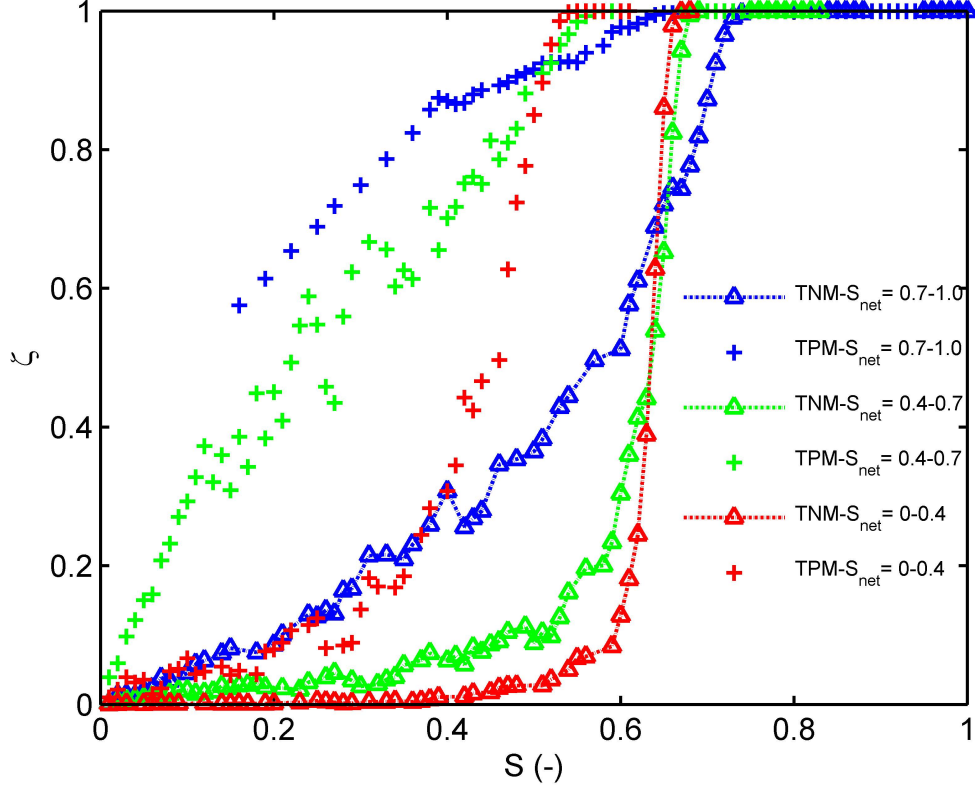


Figure 6.4: Ratio of liquid flow rate to total flow rate predicted by the TNM and the TPM. The values are averaged over ten realizations for small intervals of local saturation  $S$ .

## 6.2 Relative humidity

Relative humidity at the surface and the drying front is used to identify the boundary conditions of the CM. In this part, evaluation of these two parameters from the PNM data and the respective results are discussed.

### 6.2.1 Computation of the relative humidity

From PNM perspective, different vapor pressures exist at the exits of network surface throats (Fig. 6.5). The air is saturated with vapor (dark blue) above the partially filled and completely filled surface throats. In contrast, dry surface throats lead to unknown surface vapor pressure (light blue in Fig. 6.5), which needs to be specified by solution of the system of mass balances. We used the ratio of average vapor pressure at the surface ( $\langle P_v \rangle_{\text{surf}}$ ) from the PNM over the saturated vapor pressure ( $P_v^*$ ) to obtain the surface relative humidity:

$$\varphi_{\text{surf}}(S_{\text{surf}}) = \frac{\langle P_v \rangle_{\text{surf}}}{P_v^*}. \quad (6.7)$$

Moreover, we have calculated surface saturation from the PNM data. Surface saturation,  $S_{\text{surf}}$ , comprises all throats and pores shown in Fig. 6.5: Vertical throats that end at the surface, their underlying layer of pores, and horizontal throats connecting the pores of

this sub-surface layer. Surface saturation,  $S_{\text{surf}}$ , is the volume of liquid in all those pores and throats divided by their total volume.

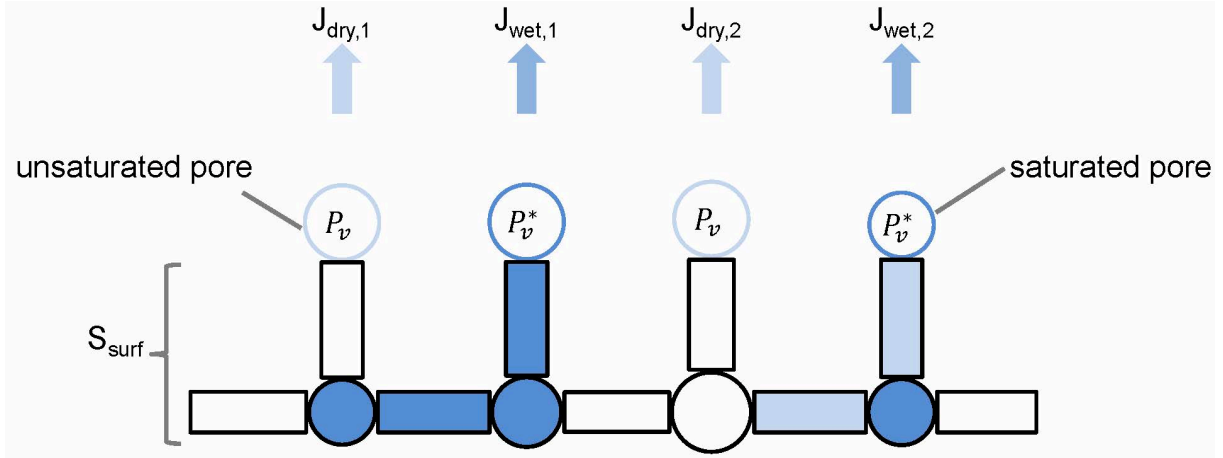


Figure 6.5: Surface parameter estimation from pore network modeling; dark blue: full throat/pore, light blue: partially filled throat/pore, white: dry throat/pore. Saturation vapor pressure above wet patches (full or partially filled throats/pores, dark blue); vapor pressure above dry throats/pores (light blue) is unknown and needs to be determined from the mass balances.

A similar idea is used to calculate the relative humidity at the drying front. However, this profile would be contained in the set of profiles of the relative humidity for the two-phase region. In the two-phase region, the relative humidity should again be determined as a function of local saturation. This can be done by spatially averaging the partial vapor pressure of each vapor pore/node in the considered slice:

$$\varphi(S) = \frac{\langle P_v \rangle_{\text{slice}}}{P_v^*}. \quad (6.8)$$

Here,  $S$  is the average saturation in a slice containing all horizontal throats/pores of a certain layer and half of the volume of throats immediately above or below this layer (Fig. 6.1).

### 6.2.2 Relative humidity profile

Figure 6.6 shows the correlation between surface relative humidity and surface saturation. From the beginning of the drying process, the vapor pressure at the surface deviates from the saturation vapor pressure, which is contradictory to the conventional assumption that the relative humidity at the surface of materials can be determined by the desorption isotherm. Thus, using the desorption isotherm to the CM should be questioned. Attari Moghaddam et al. (2017b) explained the situation in which the vapor pressure on the surface (or in the two-phase zone) deviates from the saturation vapor pressure when slice saturation is smaller than a particular value by non-local equilibrium effects (NLE). This means that

local thermodynamic equilibrium is satisfied at the meniscus surface (where the vapor pressure is thus the saturation vapor pressure) but not at the scale of averaging volume, which is divergent from the CM assumptions. Following this explanation, it is reasonable that the vapor pressure at the surface early deviates from the saturation vapor pressure.

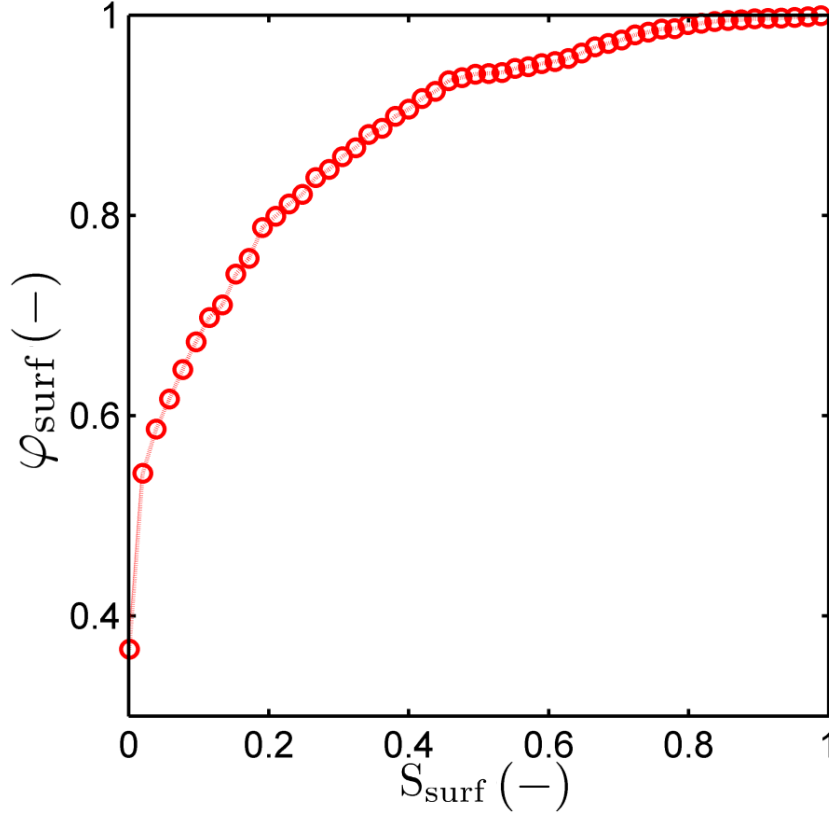


Figure 6.6: The surface vapor pressure-saturation relationship obtained from TPM pore network simulations.

The moisture transport through the vapor phase can be observed in the ratio of vapor pressure to saturation pressure within the network ( $\varphi$ ), since it is induced by vapor pressure differences (Fig. 6.8). Vapor pressure deviations from the saturation vapor pressure (NLE effect) appear after  $S_{a_s, \max}$ . The vapor pressure is related to the interfacial area ( $a_s$ ) (Fig. 6.7). The more interfacial area is formed in a slice, the easier it is to maintain the saturated vapor pressure. Interfacial area as a function of local saturation in the two-phase zone can be presented as: When air invades the network, the interfacial area increases linearly to a maximum.  $S_{a_s, \max}$  is a saturation which corresponds to relatively high moisture transport coefficient, marks the end of the LDTR and denotes the starting point of the NLE effect. After reaching the maximum, the interfacial area drops linearly due to evaporation. The structures of the liquid phase in the two-phase zone are different (Fig. 6.7).

The internal NLE effect is observed in both network geometries but it is slightly more pronounced in the TPM network (Fig. 6.8). Before the network surface dries, similar profiles of vapor pressure are observed. The strong NLE effect lasts longer for the TPM

(smaller value of  $S_{a_s, \max}$ ), because the saturation of the surface slice is sustained for longer time (Fig. 3.10).

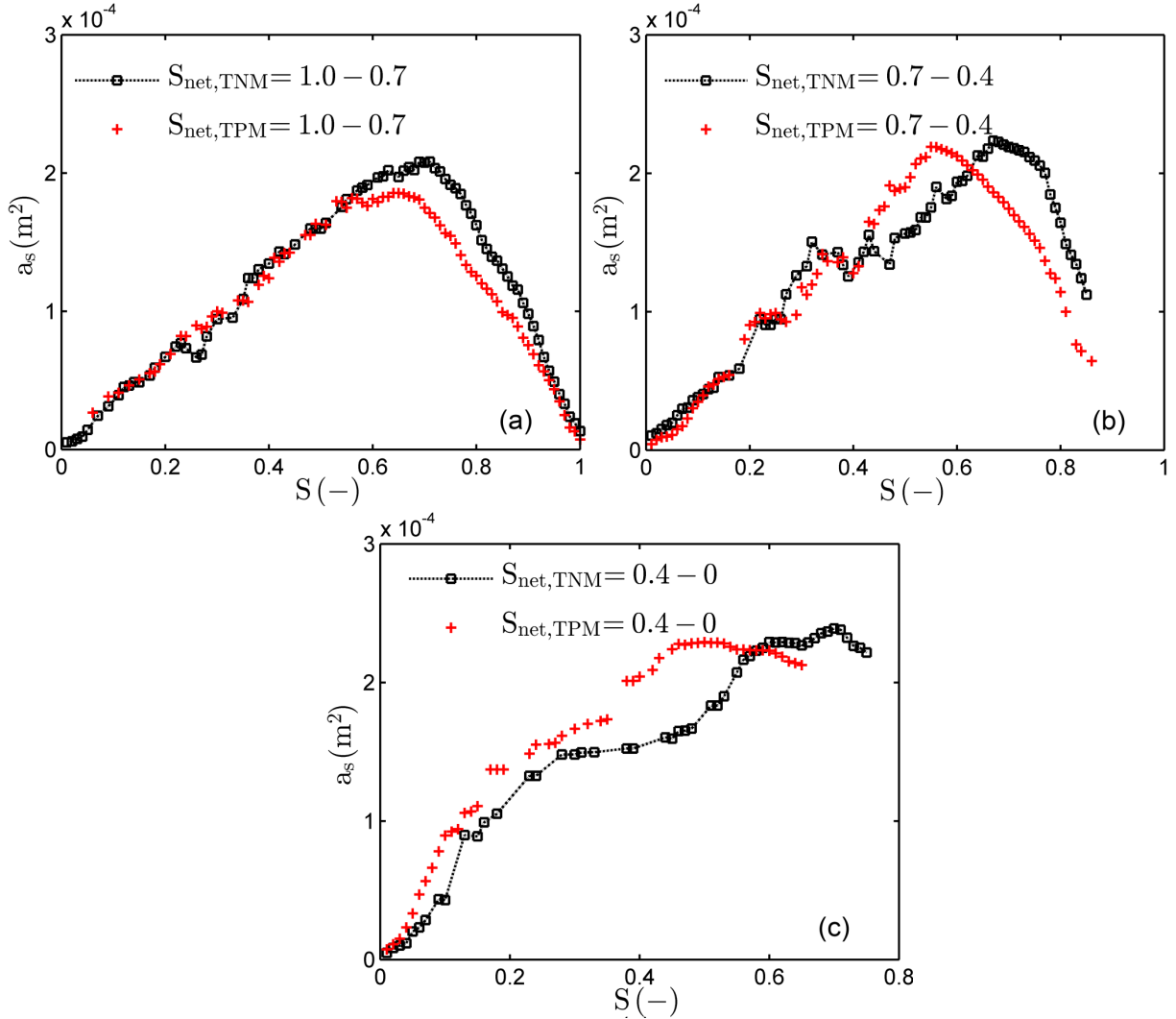


Figure 6.7: Interfacial area as a function of local saturation obtained from drying simulations of TNM and TPM network geometries: (a)  $S_{\text{net}} = 1.0 - 0.7$ , (b)  $S_{\text{net}} = 0.7 - 0.4$ , and (c)  $S_{\text{net}} = 0.4 - 0$ . The values are averaged over ten realizations for small saturation  $S$  intervals.

### 6.3 Vapor transport coefficients

Parameters of the vapor transport are required by the three-transport-zone CM. Comparable with the model in Sec. 6.1, we extended the averaging method of determining the moisture transport coefficient to vapor transport parameters. One major difference here is that the moisture transport coefficient is correlated with the local saturation. In contrast, vapor transport parameters can be linked with the local relative humidity.

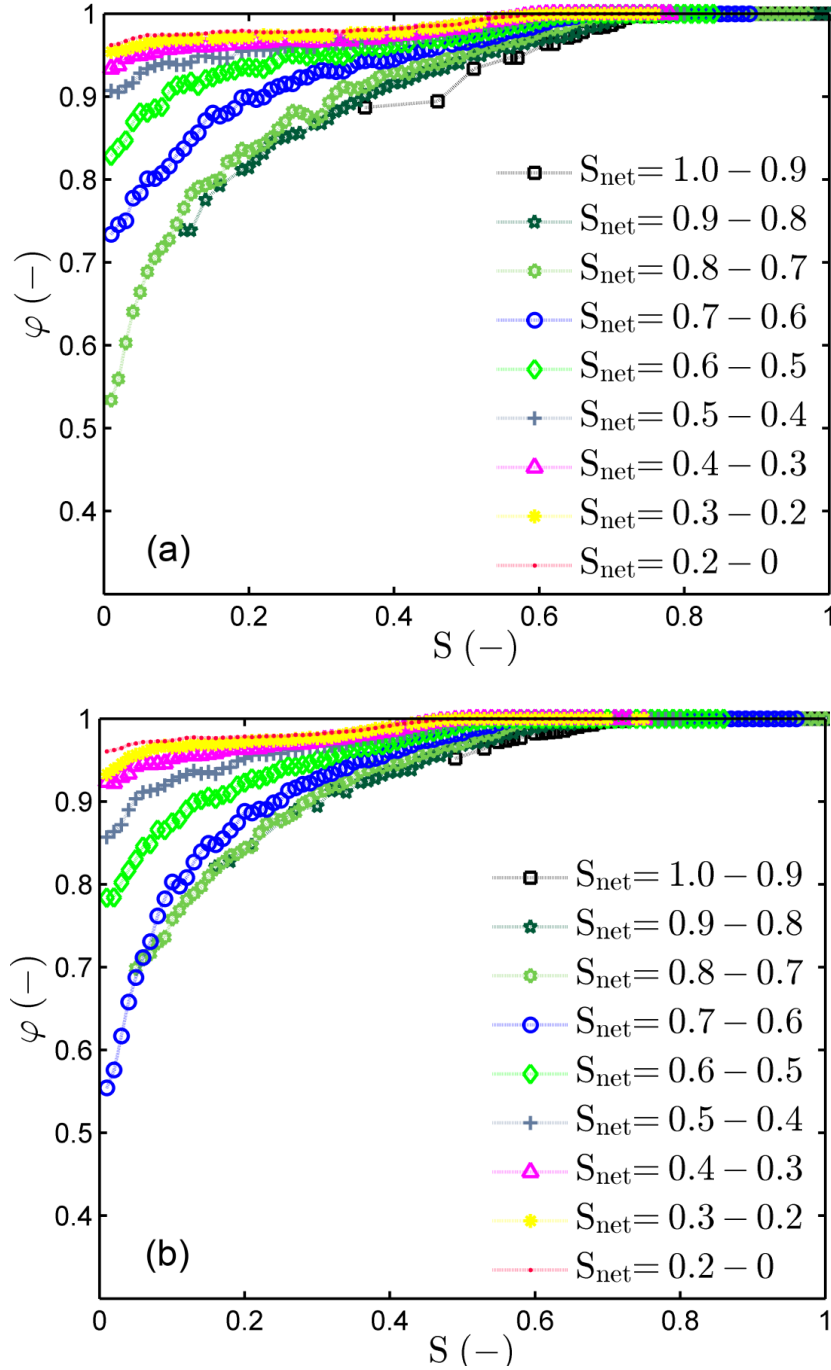


Figure 6.8: Mean values of internal NLE function ( $\varphi$ ) obtained from PNM drying simulations as function of local saturation ( $S$ ) for different network saturation ( $S_{\text{net}}$ ) intervals for: (a) TNM and (b) TPM.

### 6.3.1 Computation of the vapor transport parameters

An exemplary network that can be used to illustrate the computation of vapor transport coefficients is shown in Fig. 6.9.

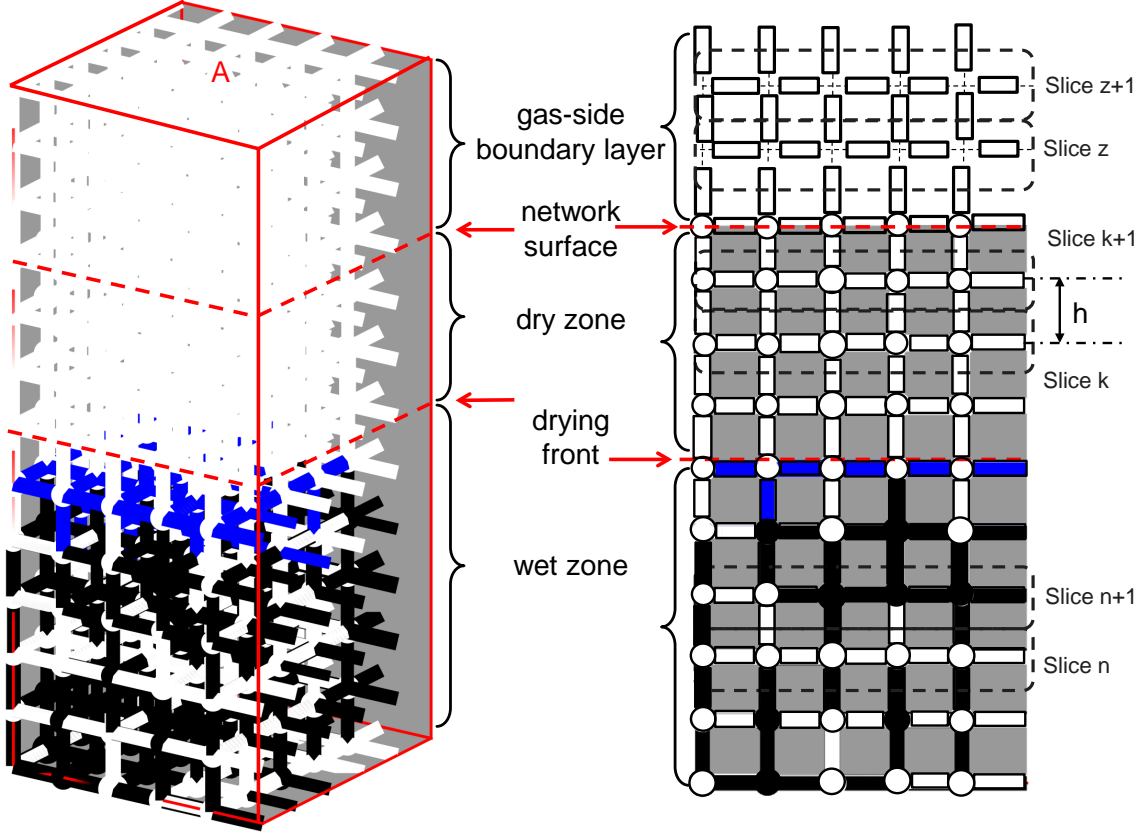


Figure 6.9: (left) A small pore network ( $5 \times 5 \times 10$ ) open to evaporation from the top with gas-side boundary layer ( $5 \times 5 \times 3$ ) and (right) its front projection when  $S_{\text{net}} = 0.6$ . A slice contains all throats and pores of one horizontal layer, and half of the vertical throats. The liquid and vapor throats/pores in the network are shown in dark and white, respectively. The blue throats/pores are partially filled with liquid.

The vapor flow rate (in the  $z$ -direction) between slices can be numerically calculated by summing the vapor fluxes between vapor pores in the  $k^{\text{th}}$  slice and the  $(k+1)^{\text{th}}$  slice in the dry zone (DZ) of the porous medium:

$$j_{v,k \rightarrow k+1,DZ} = \frac{1}{A} \sum_{i,j} g_{v,ij,DZ} P \ln \left( \frac{P - P_{v,j}^{k+1}}{P - P_{v,i}^k} \right), \quad (6.9)$$

where  $i$  is the vapor pore in slice  $k$  and  $j$  represents the vapor pore in slice  $k+1$ ,  $A$  ( $m^2$ )

is the cross-sectional area of the network, and  $g_{v,ij,DZ}$  is the conductance:

$$g_{v,ij,DZ} = \frac{D_{va}\tilde{M}_v}{\tilde{R}T\left(\frac{R_{p,i}}{A_{p,i}} + \frac{L_t}{A_t} + \frac{R_{p,j}}{A_{p,j}}\right)}. \quad (6.10)$$

Here,  $A_{p,i}$ ,  $A_{p,j}$  and  $A_t$  denote the cross-sectional areas of pore  $i$  ( $\pi R_{p,i}^2$ ), pore  $j$  and of the connecting throat ( $\pi R_t^2$ ), respectively.  $L_t$  is the throat length, which depends on the sizes of the two pores located at the throat ends.  $D_{va}$  (m<sup>2</sup>/s) denotes the binary diffusion coefficient of vapor in the air.

Similarly, the equation that holds in the gas-side boundary layer (GB) is:

$$j_{v,z\rightarrow z+1,GB} = \frac{1}{A} \sum_{i,j} g_{v,ij,GB} P \ln \left( \frac{P - P_{v,j}^{z+1}}{P - P_{v,i}^z} \right). \quad (6.11)$$

Here,  $g_{v,ij,GB}$  is considered as:

$$g_{v,ij,GB} = \frac{D_{va}\tilde{M}_v A_{t,GB}}{\tilde{R}Th}. \quad (6.12)$$

Since representation by pores and throats is formally continued in the boundary layer,  $h$  is the center distance between two pores and  $A_{t,GB}$  is the throat cross-sectional area:

$$A_{t,GB} = h^2. \quad (6.13)$$

The vapor diffusion coefficients in the dry zone ( $D_{v,e}(\varphi)$ ) and in the gas-side boundary layer ( $D_{v,b}(\varphi)$ ) are obtained from:

$$D_{v,e}(\varphi) = -\frac{j_{v,k\rightarrow k+1,DZ}}{\frac{\tilde{M}_v P_v^*}{\tilde{R}T} \frac{\varphi_{k+1} - \varphi_k}{h}}, \quad (6.14a)$$

$$D_{v,b}(\varphi) = -\frac{j_{v,z\rightarrow z+1,GB}}{\frac{\tilde{M}_v P_v^*}{\tilde{R}T} \frac{\varphi_{z+1} - \varphi_z}{h}}. \quad (6.14b)$$

Those coefficients can represent the vapor transport in the porous medium in a simplified way according to Fick's law that is driven by vapor concentration. Vapor concentration is here expressed by  $\varphi_{z+1}$  and  $\varphi_z$ , or  $\varphi_{k+1}$  and  $\varphi_k$ , which represent the average values of relative humidity in slices  $z$  and  $z+1$  or  $k$  and  $k+1$ , respectively. The diffusion coefficients are assigned to the arithmetic average of relative humidity between slices:

$$\varphi = \frac{\varphi_{z+1} + \varphi_z}{2} \quad \text{or} \quad \varphi = \frac{\varphi_{k+1} + \varphi_k}{2}. \quad (6.15)$$

## 6.3.2 Profiles of vapor transport parameters

### 6.3.2.1 Vapor diffusion coefficient in the gas-side boundary layer

Figure 6.10 shows the vapor diffusion coefficient in the gas-side boundary layer against relative humidity. It should be noted that the ordinate scale in Fig. 6.10 is very much magnified. This means, that  $D_{v,b}$  is nearly constant and nearly equal to the binary diffusion coefficient ( $2.569 \times 10^{-5}$  m<sup>2</sup>/s at 20°C, shown as dashed line in Fig. 6.10). This verifies PNM computations as well as the derivation of the parameter  $D_{v,b}$ . There is a miniature dependence on  $\varphi$ , which is attributed to Stefan flow. Equation 6.14b does not take Stefan flow into consideration, so that the influence of Stefan flow must be incorporated into the evaluated  $D_{v,b}$ . However, Stefan flow is small for the investigated case of slow drying (20°C), so that dependence on  $\varphi$  and deviation from the binary diffusion coefficient are both very small.

The classical binary diffusivity is considered as a constant value, which is a function of temperature, ambient pressure, and the molecular species involved (Bruce et al., 2001). Acosta et al. (2006) reported the <sup>3</sup>He diffusion coefficient obtained from NMR measurements ( $1/D(^3\text{He})$ ) to be inversely proportional to the helium molar fraction in four different buffer gases (4He, N<sub>2</sub>, Xe, and SF<sub>6</sub>), whereas  $1/D(\text{Xe})$  was directly proportional to xenon molar fraction using He as the buffer gas. The diffusion coefficient depends on the molecular weight of species (diffusing gas and buffer gas). In the vapor-air diffusion process, the water molecular weight (18 g/mol) is smaller than the average molecular weight of air (29 g/mol), which is a similar case as helium diffusion in N<sub>2</sub>, Xe or SF<sub>6</sub> gas, indicating agreement with the correlation of vapor diffusion coefficient with relative humidity ( $\varphi$ ) in simulation results.

The relationship of the vapor diffusion coefficient in the gas-side boundary layer with the relative humidity can also be applied at the surface of the porous medium. Surface humidity can be determined from the surface NLE (Attari Moghaddam et al., 2018). The mass transport mechanism for surface humidity is the same as in the gas-side boundary layer. Thus, the correlation obtained in Fig. 6.10 can be applied to the transport process in the whole region from the surface to the bulk of the surrounding gas phase.

### 6.3.2.2 Vapor diffusion coefficient in the dry zone of the porous medium

Figure 6.11 shows the vapor transport coefficient for the dry zone of the porous medium ( $D_{v,e}$ ) over the relative humidity ( $\varphi$ ). Identified  $D_{v,e}$  is nearly constant over  $\varphi$ , which is again the expected behavior. It verifies PNM computations as well as the derivation of this parameter. The very weak dependence on  $\varphi$  may be due to Stefan flow in the throats (considered in PNM, but not in Eq. 6.14a), similarly as before. With a molecular diffusion coefficient of  $2.569 \times 10^{-5}$  m<sup>2</sup>/s, a significantly lower value of  $D_{v,e}$  is expected.

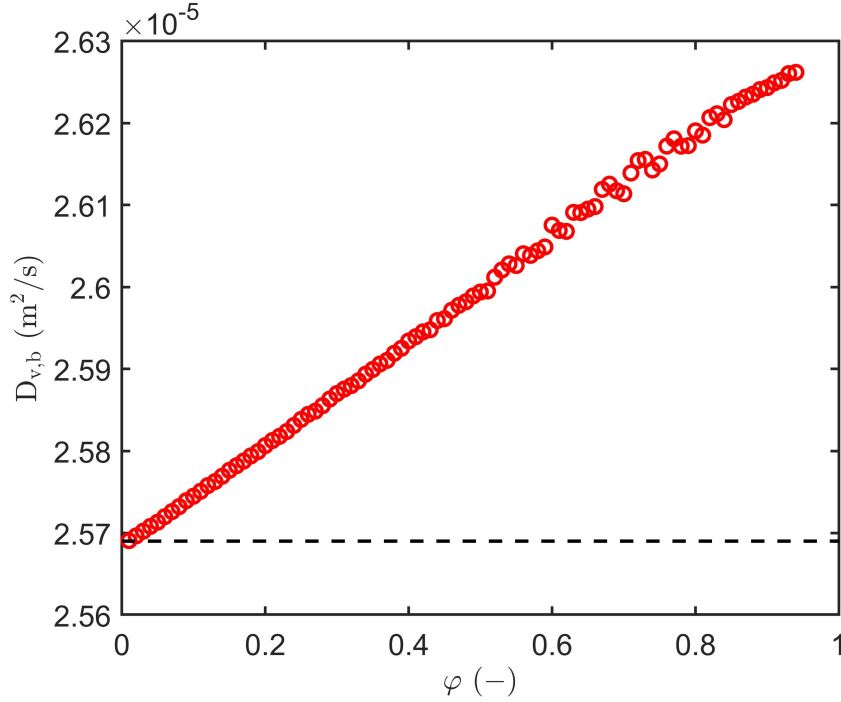


Figure 6.10: Vapor diffusion coefficient in the gas-side boundary layer ( $D_{v,b}$ ) in dependence on the local relative humidity ( $\varphi$ ). The dash line represents the binary diffusion coefficient at 20°C. The values have been averaged over ten realizations for small saturation intervals.

Smaller diffusion coefficients in porous media than in the unconfined gas phase are usually attributed to obstruction (effect proportional to porosity) and tortuosity. With a total porosity of 0.35,  $D_{v,e}$  by obstruction should be  $8.99 \times 10^{-6} \text{ m}^2/\text{s}$ , significantly larger than observed. This would additionally imply a tortuosity of 1.55, much larger than one would expect for a simple cubical lattice (eventually equal to 1).

However, in our synthetic porous medium with large pores at network grid points and smaller throats in between, one should rather expect the throats alone to define the obstruction effect. With 0.26 volume porosity due to the throats,  $D_{v,e}$  of  $6.68 \times 10^{-6} \text{ m}^2/\text{s}$  by obstruction is obtained. Considering cross-sectional porosity by the throats, which is 0.17,  $D_{v,e}$  of  $4.37 \times 10^{-6} \text{ m}^2/\text{s}$  is obtained. Identified  $D_{v,e}$  with approximately  $5.8 \times 10^{-6} \text{ m}^2/\text{s}$  lies between those values, and appears very reasonable. Working with the volume porosity of the throats, the remaining tortuosity effect of  $6.68/5.8 = 1.15$  may well be due to the lateral (means: to the sides) expansion of cross-section from the throats to the pores (which have by definition larger radii).

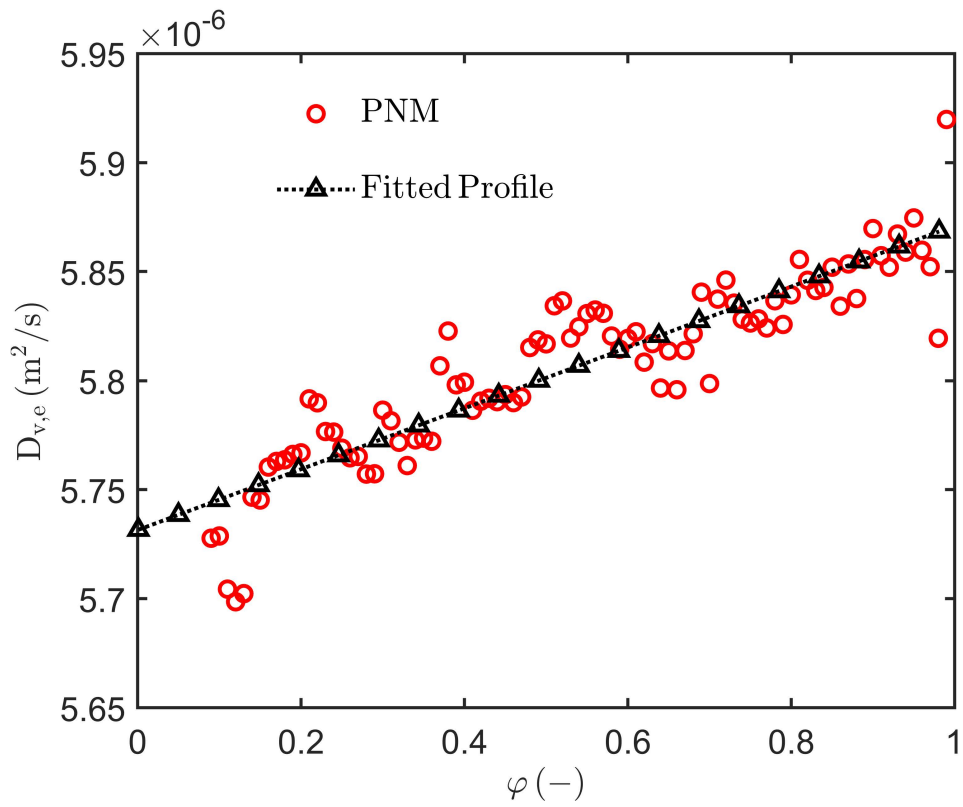


Figure 6.11: Vapor transport coefficient in the dry zone ( $D_{v,e}$ ) against local relative humidity ( $\varphi$ ): The red circles are the volume-averaged original data, whereas the dark triangles denote the fitted profile. The values have been averaged over ten realizations for small saturation intervals.

# Chapter 7

## Feeding the macroscopic parameters into the one-equation continuum model

*This chapter is partly taken from “Lu, X., Kharaghani, A., Tsotsas, E., (2020). Transport parameters of macroscopic continuum model determined from discrete pore network simulations of drying porous media: Throat-node vs. throat-pore configurations. Chemical Engineering Science 223, 115723”. Another part is taken from “Lu, X., Tsotsas, E., Kharaghani, A., (2021). Drying of capillary porous media simulated by coupling of continuum-scale and microscale models. International Journal of Multiphase Flow 140, 103654”.*

In this chapter, we discuss methods for treating macroscopic parameters extracted from the PNM dataset to be fed into the continuum model (CM). Those parameters share the same characteristics: Non-linear, with scatter, process-dependent. To investigate those effects on the CM, we compare the simulation results by introducing different treatments on those macroscopic parameters.

To solve the CM (Chapter 5), we have to know macroscopic parameters in advance. As discussed, there are five such parameters: The moisture transport coefficient  $D(S)$ , the vapor diffusion coefficient in the dry zone  $D_{v,e}(\varphi)$ , the vapor diffusion coefficient in the gas-side boundary layer  $D_{v,b}(\varphi)$ ; Moreover, the non-local equilibrium (NLE) function at the surface  $\varphi_{surf}(S_{surf})$  and at the drying front  $\varphi_{DF}(S_{DF})$ .

As a starting point, the profiles of the moisture transport coefficient  $D(S)$  which have been presented in Fig. 6.3 are used. The moisture transport coefficients were obtained from the PNM by averaging within each total saturation range of  $\Delta S_{net} = 0.10$  for a small local saturation interval ( $S = 0.01$ ), as  $D(S_{net}; S)$ . Three of these curves, namely  $D(S_{net} = 0.40 - 0.30; S)$ ,  $D(S_{net} = 0.30 - 0.20; S)$  and  $D(S_{net} = 0.20 - 0.00; S)$ , had been averaged into one curve in Fig. 6.3. The functions  $D_{v,e}(\varphi)$  and  $D_{v,b}(\varphi)$  have been be

determined are shown in Figs. 6.11 and 6.10.

The NLE functions at the surface  $\varphi_{surf}(S_{surf})$  and at the drying front  $\varphi_{DF}(S_{DF})$  are needed for the boundary conditions. Figure 6.6 shows the profile of relative humidity with surface saturation, which is also used in this chapter.  $\varphi_{DF}$  can be read from the internal NLE functions  $\varphi(S)$  presented in Fig. 6.8 at  $S_{DF}$ . Which function should be used depends on network saturation. Thus, to introduce internal NLE in terms of  $\varphi_{DF}$  into the CM, we have to record the network saturation in CM by:

$$S_{net,CM} = \frac{\sum_{i=1}^{DF} S_i}{n_{CV}}, \quad (7.1)$$

where  $n_{CM}$  denotes the number of control volume in the porous medium. Using  $S_{net,CM}$ , the relative humidity at the drying front can then be determined.

### 7.1 Influence of averaging intervals on the CM solution

Moisture transport coefficients  $D(S_{net}; S)$  play a prominent role among the five macroscopic parameters in the operation of CM because of the dependence of this model parameter on the global state of the drying process (network saturation), the position in the porous medium (local saturation) as well as pore structure. Attari Moghaddam et al. (2017b) determined the  $D(S)$  function by averaging within consecutive intervals of 0.30, 0.30 and 0.40 in network saturation from the PNM dataset. However, Figure 6.3 analyzed moisture transport coefficients averaged over smaller intervals of network saturation, namely  $\Delta S_{net} = 0.10$ . Through averaging over different intervals of network saturation, we have obtained different  $D(S_{net}; S)$  profiles. Thus, the network saturation interval can affect the performance of the CM.

To better understand this aspect, we performed CM computations by using the macroscopic parameters as introduced in Chapter 6, but testing various  $D(S_{net}; S)$  profiles obtained for different averaging intervals from the PNM dataset to predict the local saturation distribution at a high global saturation of  $S_{net} = 0.99$  (Fig. 7.1).  $D(S_{net}; S)$  has been selected for intervals of 0.01, 0.05, and 0.10 network saturation:  $D(S_{net} = 1.00 - 0.99; S)$ ,  $D(S_{net} = 1.00 - 0.95; S)$  and  $D(S_{net} = 1.00 - 0.90; S)$ . Figure 7.1 indicates that  $D(S_{net}; S)$  from the largest time interval fails to predict the saturation distribution at  $S_{net} = 0.99$ . The closest profile to the PNM results is achieved with  $D(S_{net} = 1.00 - 0.99; S)$ . Figure 7.1b also shows the normalized differences of local saturations predicted by the CM from reference values of saturation (directly obtained from PNM) along with the network. Figure 7.1b demonstrates that the highest difference appears at the surface, which might affect the performance of the CM in calculating the evaporation rate. Thus,  $D(S_{net}; S)$  from the smallest interval of network saturation on the PNM dataset could lead to a better prediction by means of the CM. However, it would not be practicable to provide hundreds

of  $D(S_{net}; S)$  profiles for the continuous modeling of drying. Therefore, the interval of network saturation used in PNM to estimate the  $D(S_{net}; S)$  profiles should be at least restrained to network saturations with similar global drying characteristics.

$D(S_{net}; S)$  at high saturation is scattered both in Attari Moghaddam et al. (2017b) and in Fig. 6.3. Such scatter might be caused by the pore structures and amplified by consideration of several network realizations. Though network geometry is generated from the same normal size distribution in this case, the individual throat/pore radii and their spatial distribution are different, which leads to variations of the drying process. Combining those realizations into one representative figure might reduce the scatter in the profile. And, the treatment of  $D(S_{net}; S)$  at high saturation might impact the prediction of the CM.

## 7.2 Influence of different treatment methods on the CM solution

Attari Moghaddam et al. (2017b) processed the scattered data by fitting. In contrast, this work directly used the scattered dataset, but interpolated linearly between each two points. Figure 7.2 shows  $D(S_{net} = 1.00 - 0.90; S)$ , i.e. moisture transport coefficients gained by averaging PNM data for network saturations from 1.00 to 0.90, as well as by averaging over ten realizations.  $D(S_{net} = 1.00 - 0.90; S)$  is scattered when the local saturation is larger than the irreducible saturation,  $S_{irr} = 0.78$ . Figure 7.2 also shows the 90% confidence bound of the moisture transport coefficient from the PNM. The 90% confidence bounds indicate that fitting of the function between these bounds could be reasonable. Thus,  $S(S_{net}; z)$  profiles predicted by using different fitting functions of  $D(S_{net} = 1.00 - 0.90; S)$  could be confined between extremal  $S(S_{net}; z)$  functions simulated by inserting the upper and the lower bound functions into the CM.

Figure 7.3 shows  $S(S_{net}; z)$  profiles predicted by the continuum model by inserting  $D(S_{net} = 1.00 - 0.90; S > 0.78)$  according to either the original averaged data, or the upper bound fitting function, or the lower bound fitting function. In all cases,  $D(S_{net} = 1.00 - 0.90; S < 0.78)$  is the same, and all cases are compared with the same profile from PNM results,  $S_{PNM}(S_{net} = 1.00 - 0.90; z)$ . Figure 7.3 indicates that the saturation distribution which is based on  $D(S_{net} = 1.00 - 0.90; S > 0.78)$  from the averaged data is closer to  $S_{PNM}(S_{net} = 1.00 - 0.90; z)$ , compared with the  $S_{CM}(S_{net} = 1.00 - 0.90; z)$  profiles from the upper and lower bound fitting functions.

Comparison of the normalized error in the prediction of local saturation in the network (Fig. 7.3, down) suggests that the fitting approach in the high saturation range would cause notable differences in saturation prediction, especially at the surface, where the upper bound profile evolves 100% normalized error. The poor prediction of saturation at the surface could, for example, result in the surface of the porous medium being dried earlier than expected. Thus, the relative humidity at the surface might jump out of the correlation according to surface NLE for conditions that would not correspond to PNM

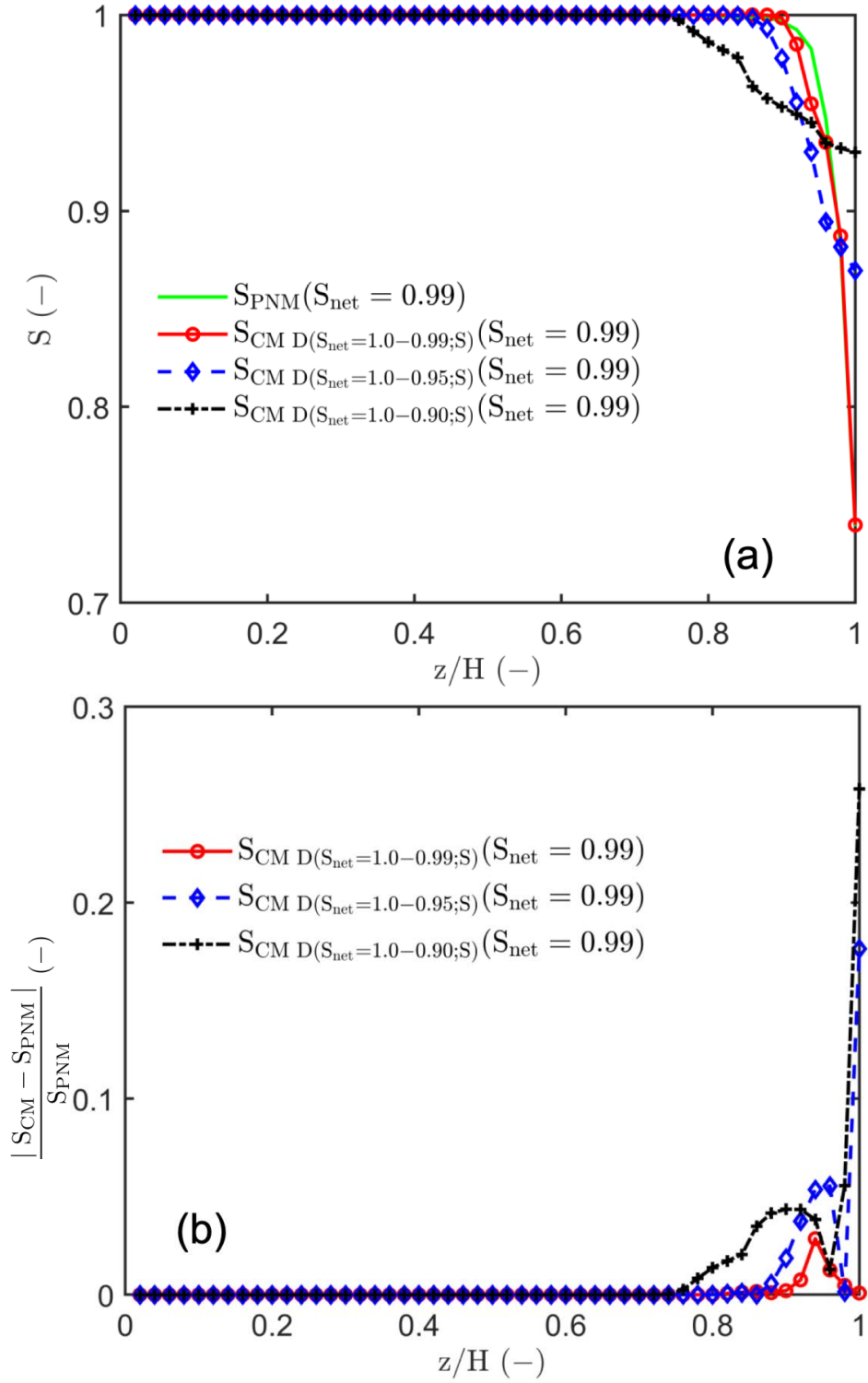


Figure 7.1: (a) Saturation profiles at  $S_{net} = 0.99$  obtained from the PNM and from the continuum model with various  $D(S_{net}; S)$  profiles, as well as (b) the normalized difference between those methods; different averaging intervals of network saturation have been used in the determination of  $D$ , corresponding to:  $D(S_{net} = 1.00 - 0.99; S)$ ,  $D(S_{net} = 1.00 - 0.95; S)$  and  $D(S_{net} = 1.00 - 0.90; S)$ .

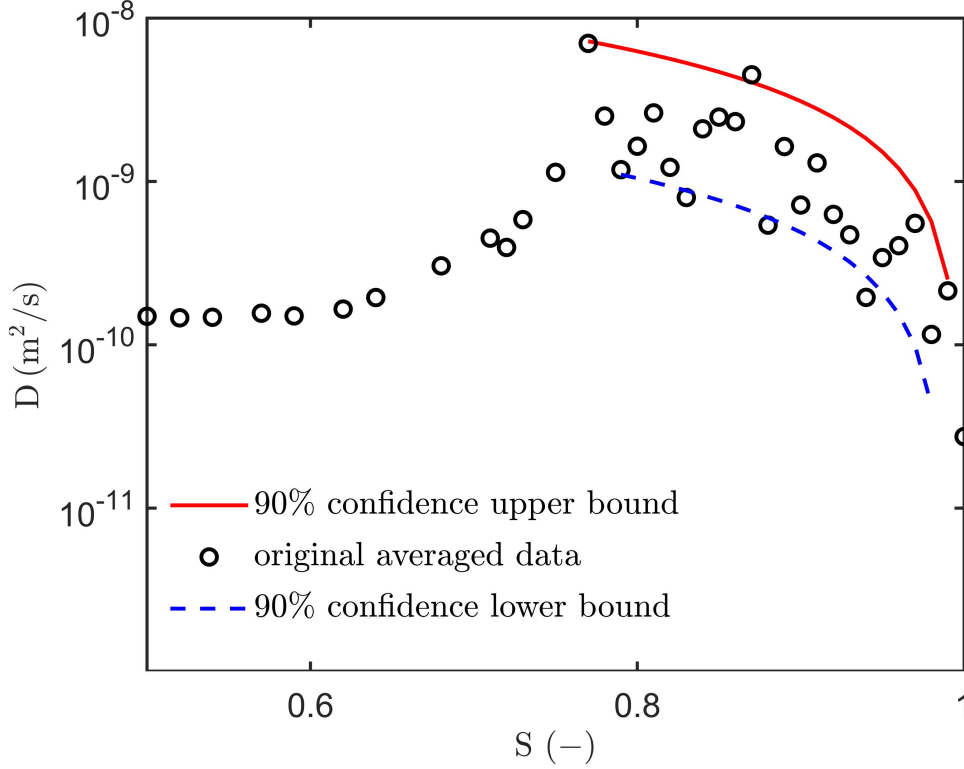


Figure 7.2: The moisture transport coefficient obtained from pore network simulations by averaging over a small time interval of network saturation between  $S_{net} = 1.00$  and  $S_{net} = 0.90$ , and the respective 90% confidence band. The values are averaged over ten realizations for intervals of local saturation  $S$ .

for the given network geometry setting. Such errors may bring troubles in boundary conditions to the CM and eventually terminate the computation, so that they need to be prevented.

### 7.3 Assessment of the CM by PNM simulations

The performance of the CMs can be altered by the methods used to extract parameters from the database created by means of the PNM. Some evidence of this behavior has been discussed in the previous sections. Recently, parameterization of the CM by means of the PNM database has first been attempted by Attari Moghaddam et al. (2017b). They determined the  $D(S)$  function by averaging within consecutive intervals of 0.30, 0.30 and 0.40 in network saturation from the PNM dataset (Fig. 6.2). Besides, they also fitted each profile into non-linear functions.

In contrast, we have identified 10  $D(S)$  profiles in Fig. 6.3. This has been done by defining 10 intervals of global saturation with a width of  $\Delta S_{net} = 0.10$  each. Additionally, PNM data originating from ten parallel realizations have been averaged. To reduce the possibility of termination of the algorithm, the saturation distribution  $S(S_{net}; z)$  obtained from the CM for each network saturation interval of 0.10 has been compared with the reference PNM saturation. If saturation at the surface did not match, some data had to be

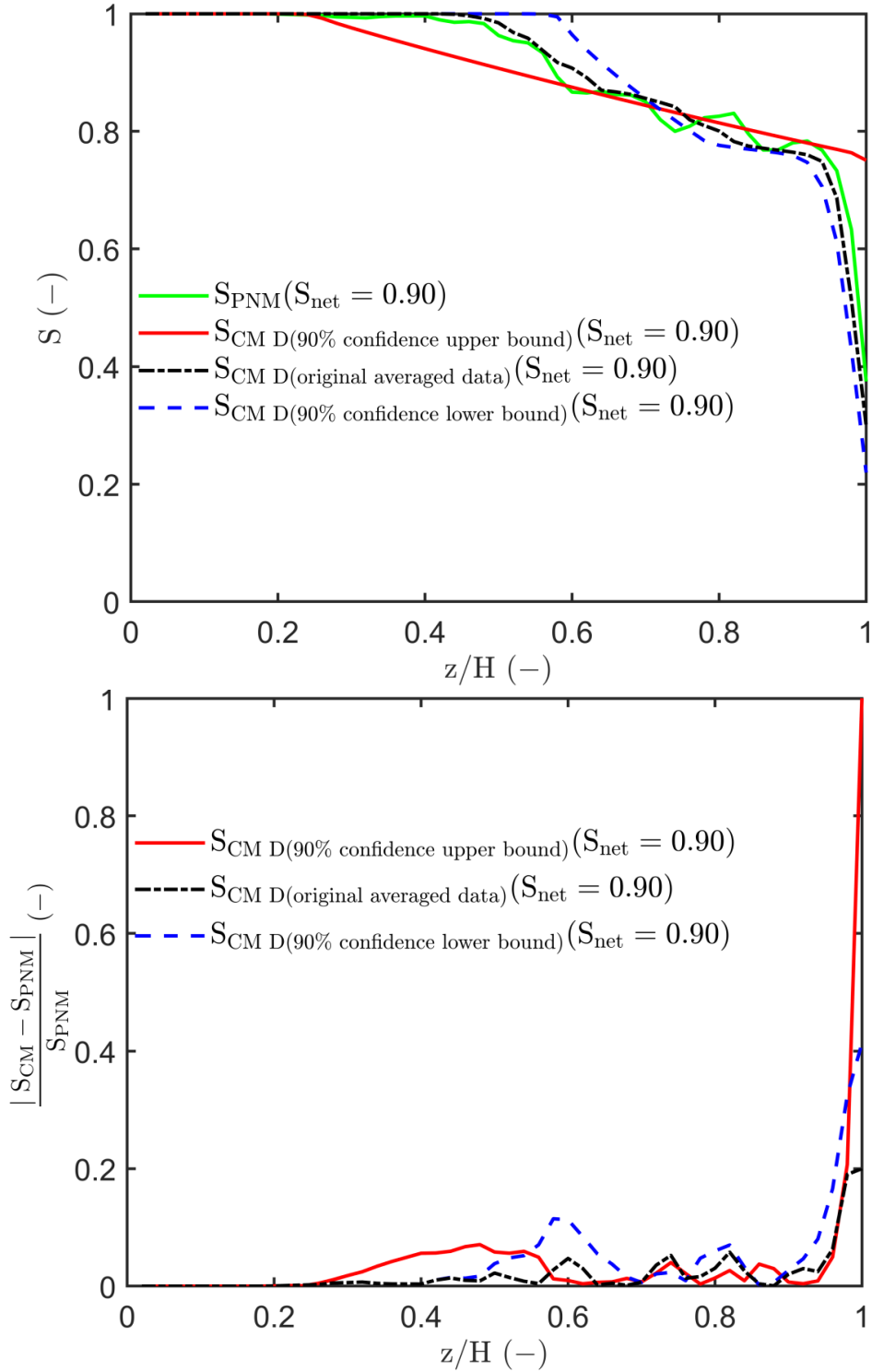


Figure 7.3: The saturation profile at  $S_{net} = 0.90$  obtained from the PNM and the continuum model with  $D(S_{net} = 1.00 - 0.90; S > 0.78)$  according to the original averaged data, the upper bound fitting function, or the lower bound fitting function. Same  $D(S_{net} = 1.00 - 0.90; S < 0.78)$  has been used at lower global saturation. Down: normalized error between PNM and the continuum model.

ruled out in the high saturation region. The principle was that once the surface saturation is lower than expected, which means the liquid in the bottom is hard to transport to the surface, the value of  $D$  has to be increased in the high saturation range, otherwise the value of  $D$  is reduced. First, the total range of local saturation was divided into ten equal intervals, i.e.,  $S = 0.90$  to  $1.00$ . In each interval, the mean value, i.e.  $\bar{D}(S = 0.90 - 1.00)$ , was calculated. Then, reasonable bounds to the  $D(S)$  function were set in that interval, for example by deleting values of  $D$  larger than  $5\bar{D}$  and smaller than  $0.01\bar{D}$ . Linear interpolation between the remaining points was used to calculate  $S(S_{net}; z)$ . The bounds on  $D(S)$  had to be adjusted based on the comparison of  $S(S_{net}; z)$  from the CM and from the PNM. Figure 7.4 shows the saturation profiles obtained from the pore network simulations with TPM configuration (Chapter 3) and the solution of the dynamic CM (Sec. 5.1) obtained by inserting macroscopic parameters from Sec. 6.1 and Sec. 6.2, which is comparable with the treatment by Attari Moghaddam et al. (2017b).

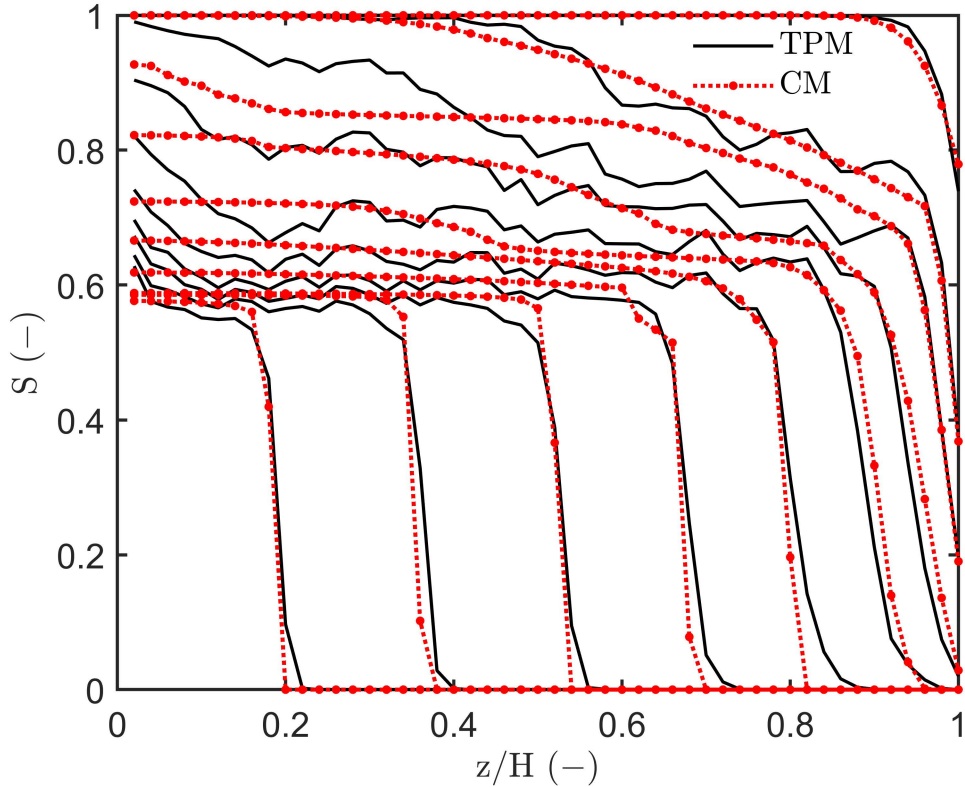


Figure 7.4: Saturation profiles obtained from the dynamic continuum model (red dots) and the pore network simulations for the throat-pore configuration (black lines). TPM saturation profiles are averages over ten realizations. From top the profiles belong to network saturations of 0.99, 0.90, 0.80, 0.70, 0.60, 0.50, 0.40, 0.30, 0.20 and 0.10, respectively.

The CM predicts fairly the saturation profiles, except those profiles at high network saturation where the numerical values of the moisture transport coefficient are scattered (see Fig. 6.3). A fairly good agreement of saturation at the drying front is observed. Attari Moghaddam et al. (2017b) used fitting functions to represent the data for the

moisture transport when  $S_{net} > 0.68$ , which resulted in difficulty of predicting the saturation at the drying front. By comparing their simulation results and our simulation results, we observed that it is still hard to provide a good agreement for the high saturation slices especially at regions near the network bottom ( $z/H = 0$ ). In these slices, the moisture transport coefficient represents the capillary pumping of viscous liquid, which depends on the network structure. Due to the limited number of realizations of PNM, data from these slices is noisy in high local saturation (Fig. 6.3). Hence the extraction of suitable transport coefficients becomes very difficult.

## 7.4 Hybrid method

A classical alternative to the estimation of effective parameters by local (slice) results of the PNM and averaging is the so-called inverse method that pursues the backward path from liquid saturation as a function of time and space to valid parameters. The inverse method was also considered for estimating the parameters of two-phase flow problems (Pel et al. 1995, 1996; Ghaedi et al., 2015; Jabbari et al., 2019). The inverse method could help to avoid the issue of importing scattered parameters into the CM. However, the optimized functions used in the inverse method, for example, applied by Jabbari et al. (2019), may also result in easier breakdown of CM solutions by improper initial guesses or due to the lack of sufficient constraints. Thus, proper initial guesses, for example macroscopic parameters obtained from the PNM, as well as proper learning rates in gradient methods, might help to determine better parameter profiles for use in the CM. Such approaches will be called hybrid methods in the following.

The hybrid method is applied for, first, a very small interval of  $\Delta S_{net} = 0.01$  from  $S_{net} = 1.00$  to 0.99, and then larger intervals of  $\Delta S_{net} = 0.10$  in network saturation (i.e., to  $S_{net} = 0.90, 0.80, 0.70$ , etc.). It generates CM results by importing ten  $D(S)$  profiles (some of which are exemplarily shown in Fig. 7.5) combined with the other four parameters (Sec. 6.2 and Sec. 6.3) into the three-transport-zone CM (Sec. 5.2). For example, to compute the network saturation distribution for  $S_{net} = 0.70$ , the hybrid method imports the  $D_{input}(S_{net} = 0.80 - 0.70; S)$  profile shown in Fig. 7.5b into the CM. On this basis, the distribution of local saturation in the network,  $S_{CM}(S_{net} = 0.80 - 0.70; z_i)$  is predicted. This prediction is then compared with the local saturation distribution from the PNM,  $S_{PNM}(S_{net} = 0.80 - 0.70; z_i)$ , and the comparison is quantified by the objective function ( $E$ ):

$$E = \frac{1}{2} \sum_i (S_{CM}(S_{net}; z_i) - S_{PNM}(S_{net}; z_i))^2. \quad (7.2)$$

The purpose of the hybrid method is to reduce the value of the objective function. The hybrid method examines the discrepancy of the saturation for each control volume (CV) in the CM. For example, the accumulation of moisture in the  $i^{th}$  CV is controlled by the value of the moisture transport coefficient at input and output.  $S_{CM}(S_{net}; z_i) > S_{PNM}(S_{net}; z_i)$

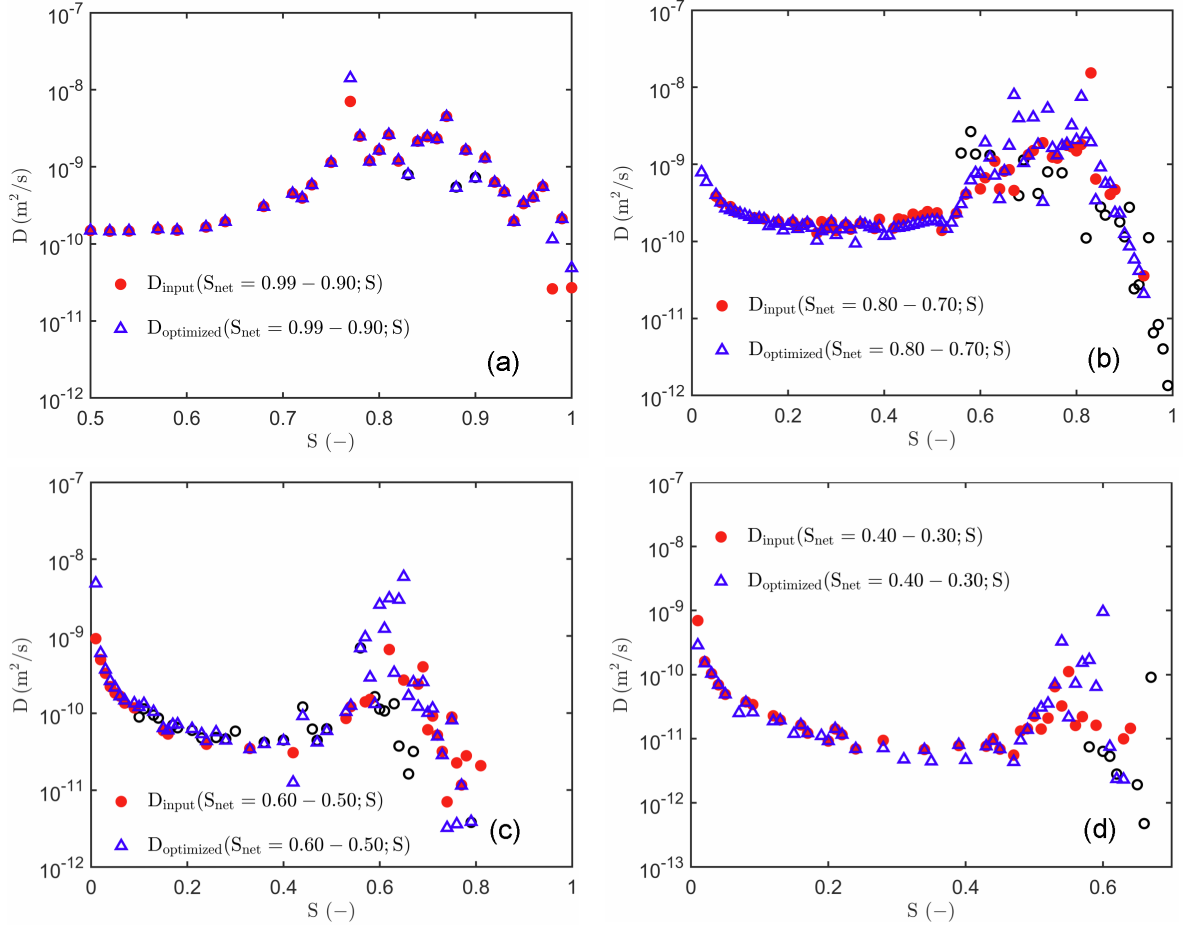


Figure 7.5: Moisture transport coefficients for four exemplarily shown datasets: (a)  $D(S_{net} = 0.99 - 0.90; S)$ , (b)  $D(S_{net} = 0.80 - 0.70; S)$ , (c)  $D(S_{net} = 0.60 - 0.50; S)$ , and (d)  $D(S_{net} = 0.40 - 0.30; S)$ ;  $\bullet$ : data used as input,  $\triangle$ : data optimized by the hybrid method,  $\circ$ : data previously deleted from the datasets.

means that the saturation of the  $i^{th}$  CV is overestimated by the CM. To reduce the saturation at  $z_i$ , we could increase the value of  $D$  at saturation  $(S_{CM}(z_i) + S_{CM}(z_i + 1))/2$  (output flow) and reduce  $D$  at saturation  $(S_{CM}(z_i) + S_{CM}(z_i - 1))/2$  (input flow) by a small quantity (i.e., to  $(1.00 \pm 0.01)D$ ). The situation of  $S_{CM}(S_{net}; z_i) < S_{PNM}(S_{net}; z_i)$  is treated inversely. It should be pointed out that the first CV only considers  $D(S_{net}; z_i = 2)$  at the output side, whereas the CV at the drying front alters the  $D(S_{net}; z_i = DF - 1)$  at the input side. Then, the adjusted  $D(S_{net}; z_i)$  is an input parameter to solve the CM again. The simulation result of, for example,  $S_{CM}(S_{net} = 0.80 - 0.70; z_i)$  has to be compared with  $S_{PNM}(S_{net} = 0.80 - 0.70; z_i)$  by recalculating the objective function, Eq. 7.2. The procedure will be repeated until the value of the objective function has reached a certain tolerance, i.e. 0.05. The whole process will be repeated until the network saturation  $S_{net} = 0.10$ . Finally, ten optimized datasets  $D_{optimized}(S_{net}; S)$  are obtained, and four of them are exemplarily shown in Fig. 7.5 (denoted by the blue triangles). Datasets presented in Fig. 7.5 are  $D(S_{net} = 0.99 - 0.90; S)$ ,  $D(S_{net} = 0.80 - 0.70; S)$ ,  $D(S_{net} = 0.60 - 0.50;$

$S$ ), and  $D(S_{net} = 0.40 - 0.30; S)$ . It should be noted that  $D(S_{net} = 1.00 - 0.99; S)$  has been averaged with  $D(S_{net} = 0.99 - 0.90; S)$ , as well as  $D(S_{net} = 0.40 - 0.30; S)$ ,  $D(S_{net} = 0.30 - 0.20; S)$  and  $D(S_{net} = 0.20 - 0.10; S)$  have been averaged into, respectively, one profile in Fig. 6.3. Figure 7.5 also shows the moisture transport coefficients (denoted by red cycles) which have been used as input values for the hybrid method. In the four plots also points that have previously been deleted from the dataset are appearing as empty cycles. Not shown profiles (the other six profiles) are similar. The optimized  $D(S_{net}; S)$  indicate high values of the moisture transport coefficient at specific local saturations, which correspond to slices that contain maximum interfacial area. For example, the maximum of the dataset  $D(S_{net} = 0.80 - 0.70; S)$  is found at approximately  $S = 0.70$ . This value would not be easy to recognize by averaging over  $S_{net}$ . The trend agrees with the theory of governing liquid transport in the capillary-viscous regime that has been discussed in Chapter 6.

Figure 7.6 shows the saturation profiles and drying kinetics by the three-transport-zone CM (Chapter 5) combined with  $D(S_{net}; S)$  from the hybrid method, as well as compared with the results obtained from the PNM. As can be seen, the macroscopic CM is capable of reproducing the drying characteristics of capillary porous media.

The agreement between the adequately parameterized three-transport-zone CM and the PNM is strong, especially after a drying front has started receding into the medium. Although the drying kinetics and the saturation profile for the first drying period can be easily accessed by the CM Pel et al. (1996), literature methods to predict the second drying period rely on empirical parameters (Pel et al., 2002; Pel and Landman, 2004). This work presents, for the first time, the coupling of the CM and PNM with the local macroscopic parameters. The saturation profiles obtained from the CM demonstrate: The edge effect that appears in the initial drying period (Or et al., 2013); fluctuations in the saturation distribution which are caused by the random pore size distribution; and, the viscosity effect that holds the liquid in the bottom of the porous medium (Fig. 7.6). These effects are missed by the classical approach (Pel et al., 2002; Pel and Landman, 2004).

Saturation profiles obtained in more classical way (dynamic CM without hybrid adaption) are shown in Fig. 7.4. Their discrepancy from the PNM is shown in Fig. 7.7, and it is compared to the respective discrepancy of three-transport-zone CM from Fig. 7.6b. This is done in two ways: (a) calculating the performance errors by summing the discrepancy for the entire drying period along the length of the network; (b) identifying the performance errors by summing the discrepancy over the entire length of the network for each of 0.10 network saturation.

Figure 7.7 indicates that CM associated with optimized  $D(S_{net}; S)$  from the hybrid method provides a better prediction not only at the surface but also among the bottom slices. Additionally, the CM, coupled with the hybrid method, shows a strong agreement with the PNM along the whole drying period (Fig. 7.7b). The highest improvement

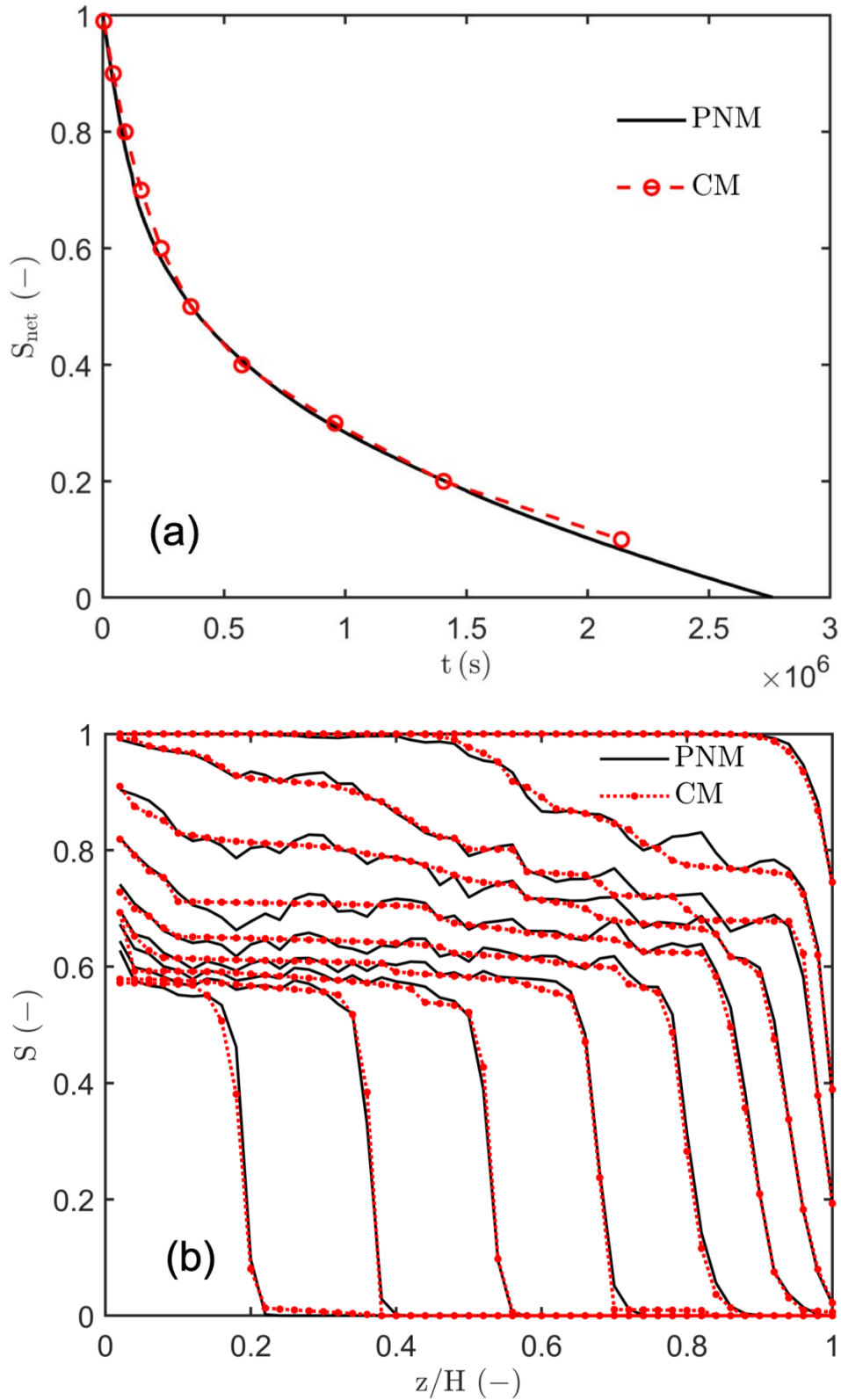


Figure 7.6: (a) Drying kinetics and (b) saturation profiles obtained from the three-transport-zone CM and the PNM simulations. The saturation profiles of the PNM are averages over ten realizations. From top the profiles belong to network saturations of 0.99, 0.90, 0.80, 0.70, 0.60, 0.50, 0.40, 0.30, 0.20 and 0.10, respectively

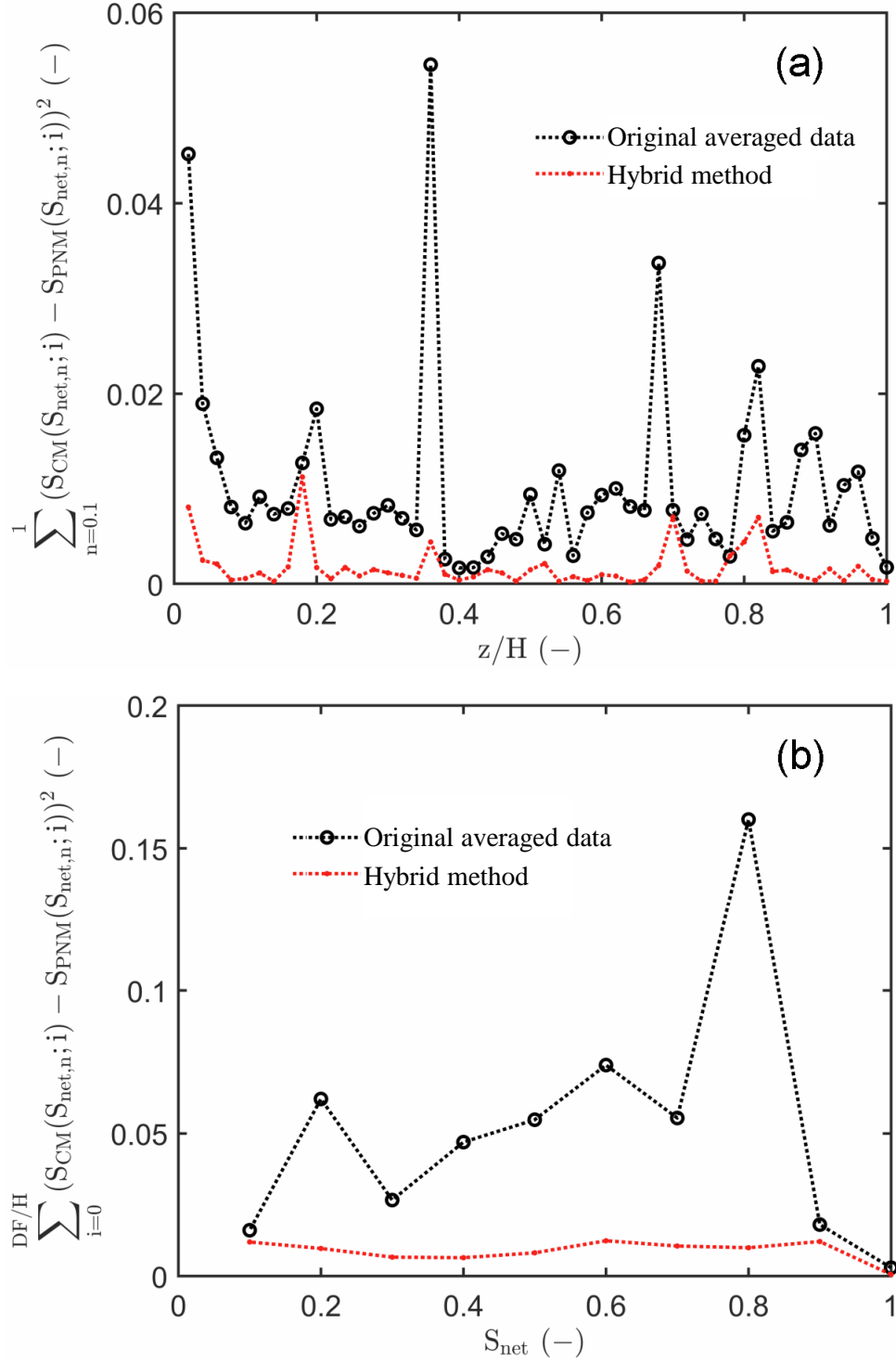


Figure 7.7: Deviation from PNM results of predictions of three-transport-zone CM using the hybrid method vs. original averaged data according to Fig. 6.3: (a) performance errors by summing the discrepancy over the entire drying period along the length of the network; (b) performance errors by summing the discrepancy over the entire length of the network for each 0.10 of network saturation.

has been seen for the network saturation profile at  $S_{net} = 0.80$ . However, some errors in saturation prediction using the hybrid method can still be observed in Fig. 7.7. One reason may be that the amount by which the moisture transport coefficient is changed within each step is arbitrary and fixed in the hybrid method, i.e., 0.01 of the previous value of  $D$  is assumed in the current work.

Nevertheless, it can be seen that the dataset from the hybrid method preserves much of the transport information from the primary dataset (created by PNM) when used in the frame of the CM. Since the saturation profile reflects the complex interplay of capillary and viscous forces and the structural impact, it can be said that these interactions are preserved by the scattered values of moisture transport coefficient that the hybrid method provides. Contrary, such information is at least partially destroyed by the fitting approach to moisture transport coefficients, i.e. when extensively averaged and smooth functions are used to approximate this parameter.

## 7.5 Comparison between the two versions of the continuum model

In this work, we introduced two versions of the CM, and both of them could be used to predict the saturation profiles (Fig. 7.4 vs. Fig. 7.6). Figure 7.4 used the moving front boundary condition CM with original data from PNM. In contrast, profiles shown in Fig. 7.6 were obtained by introducing the optimized moisture transport coefficient profiles by the hybrid method into the three-transport-zone CM. The comparison in Fig. 7.7 could not point out fundamental differences between the two versions of the CM in regard of the saturation profiles. To further test those two CMs, we introduce the original moisture transport coefficients from Fig. 6.3 and the rest of the macroscopic parameters are discussed in Chapter 6 into both CMs. The moving front boundary condition CM and the three-transport-zone CM make use of the same moisture transport coefficient profiles, as well as the same functions of relative humidity at the surface and the drying front. Two other parameters, the vapor transport coefficient in the dry zone and in the external layer, are used only in the three-transport-zone CM. Figure 7.8a shows the drying time and Fig. 7.8b shows drying kinetics obtained from those two models and compares them with the reference result from the PNM. It is clearly indicated that the moving front boundary condition CM fails to predict the drying time, especially for the receding front period ( $S < 0.50$ ) since the drying kinetics is overestimated. In contrast, the drying time and drying kinetics obtained from the three-transport-zone CM is close to the drying time predicted by the PNM. The reason behind this behavior is the vapor transport coefficient at low local saturation slices in the moving front boundary condition CM. In the moving front boundary condition CM, the dry zone is treated by adding this zone to the gas-side diffusion layer. The boundary condition is then placed at the drying front by introducing a Stefan law evaporation rate. This implicitly assumes that the vapor diffusion coefficient in the dry zone would be equal to the diffusion coefficient in the boundary layer. However,

this assumption is contradictory to the vapor diffusion coefficients obtained from the PNM in Fig. 6.11, suggesting a smaller vapor diffusion coefficient in the drying zone. Thus, the moving front boundary condition CM attributes much lower obstacles to vapor diffusion and, consequently, results in much short drying time. One method to adjust the moving front boundary condition CM would be to correspondingly expand the drying zone when assigning this zone to the gas-side boundary layer.

Additionally, the NLE effect plays a vital role in the three-transport-zone CM. Figure 7.9a shows the drying time obtained from the CM without NLE and from the PNM simulations. Figure 7.9b presents the saturation profiles obtained from the CM without NLE. The CM without considering NLE assumes the saturation vapor pressure at the surface and at the drying front. The moisture transport coefficient is that of the optimized dataset calculated using the hybrid method (Fig. 7.5); vapor transport parameters are presented in Sec. 6.3.2. As can be seen in Fig. 7.9a the drying time predicted by the CM is longer compared to that predicted by PNM. The reason is that the moisture transport coefficient at the bottom of the network is smaller than that at the top of the network, suggesting that the liquid cannot easily be transported to the surface by capillary forces. This is evident in the saturation profiles. From these profiles one can see that the liquid saturation in the bottom is high when the saturation front starts to recede (after  $S_{net} < 0.90$ ).

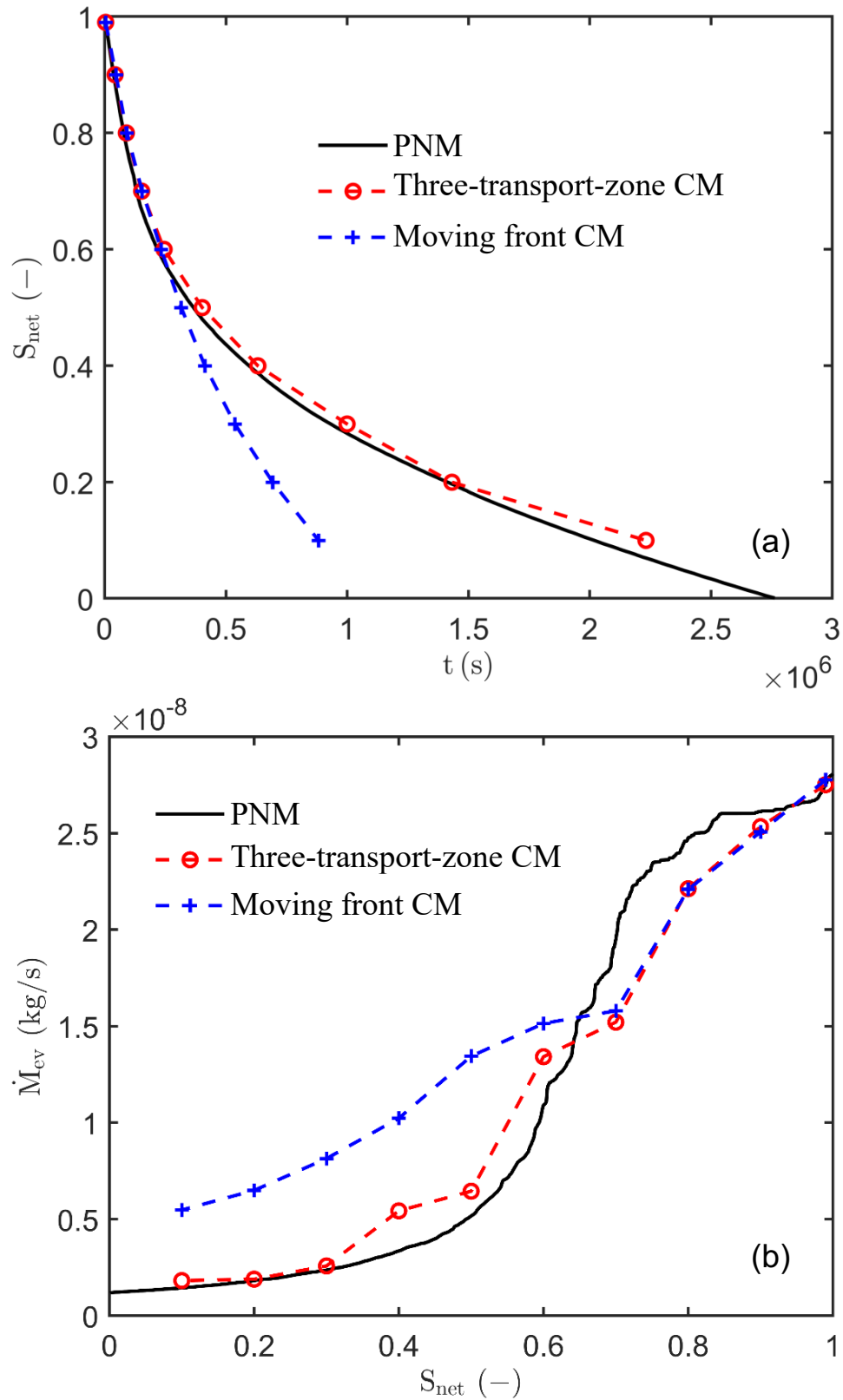


Figure 7.8: Drying time (a) and drying kinetics (b) predicted by the pore network model (PNM) and the two continuum models (CM): moving front CM and three-transport-zone CM. The values of PNM is averages over ten realizations.

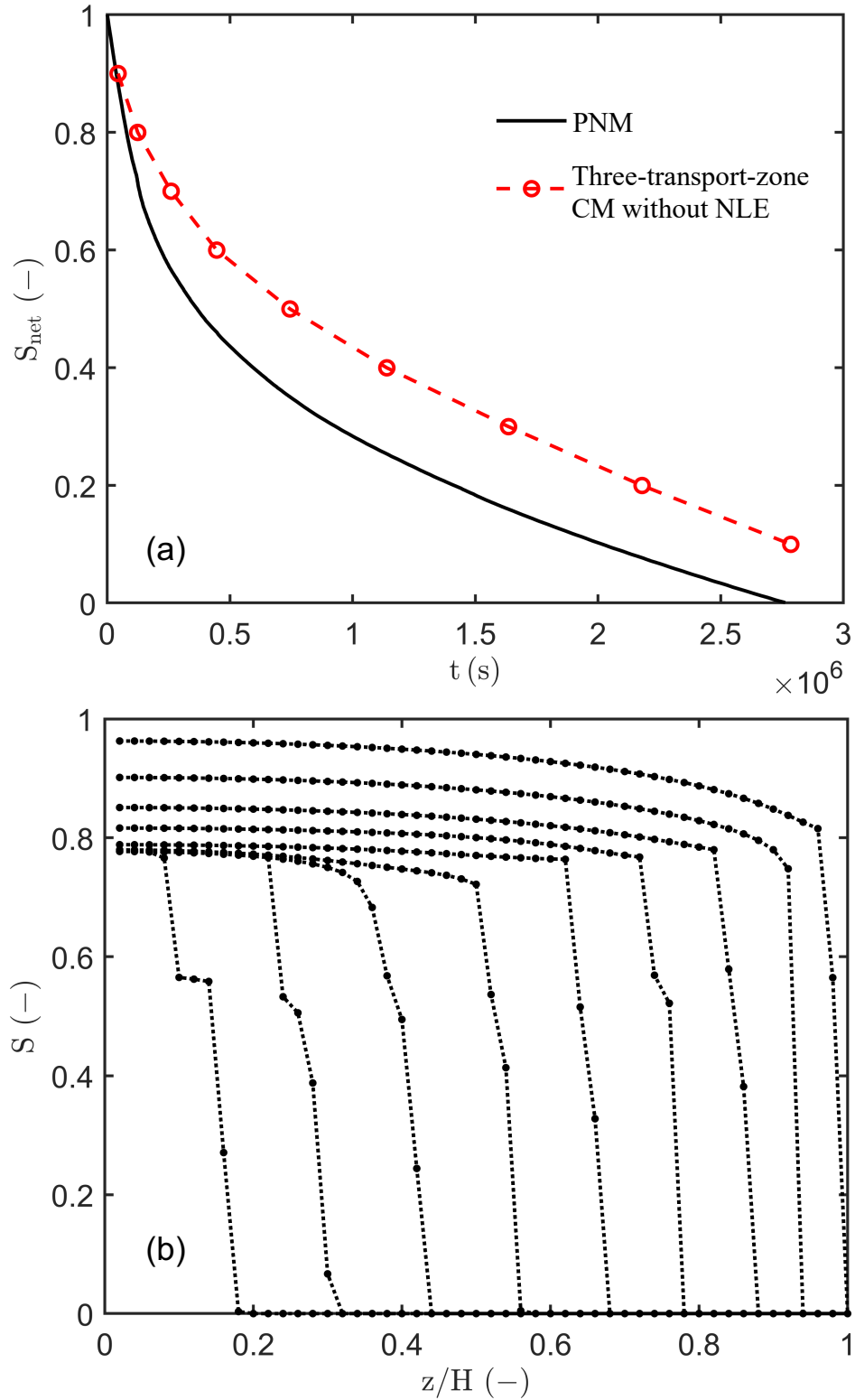


Figure 7.9: (a) Drying kinetics obtained from the three-transport-zone CM without NLE and the PNM simulations and (b) saturation profiles obtained from the three-transport-zone CM without NLE. The saturation profiles of the PNM are averages over ten realizations. From top the profiles belong to network saturations of 0.90, 0.80, 0.70, 0.60, 0.50, 0.40, 0.30, 0.20 and 0.10, respectively.

# Chapter 8

## Evaporation from the surface of capillary porous media

*Part of this chapter has been published in “Lu, X., Tsotsas, E., Kharaghani, A., (2021), Insights into evaporation from the surface of capillary porous media gained by discrete pore network simulations. International Journal of Heat and Mass Transfer, 168, 120877”.*

Reliable prediction of the drying rate from the surface of a porous medium remains a scientific challenge due to complex interactions between the gas-side boundary layer and porous medium structure. One way to tackle this issue is to opt for a microscale pore network model (Chapter 2). Two parameter functions (surface vapor pressure-surface saturation, surface vapor transport coefficient-surface vapor concentration relationship) are assessed from the pore network modeling (PNM), which can be used in the frame of a continuum model (CM) to couple the porous medium with the boundary layer (Chapters 4 and 5). The vapor pressure-surface saturation relationship has been discussed in Chapter 6. In this chapter, we focus on the surface vapor transport coefficient.

Surface parameters can be used to avoid the assumption of saturation pressure at the surface of the drying material in the one-equation CM, taking into account that surface saturation is controlled by the moisture transport within the porous medium as well as by diffusion in the boundary layer. Correspondingly, a surface diffusion coefficient and a vapor pressure-saturation relationship appear in the CM. In this context, Attari Moghaddam et al. (2017b, 2018) linked the surface saturation with the surface vapor pressure and redefined their relationship as a non-local equilibrium (NLE) effect. At the same time, Attari Moghaddam et al. (2018) indicated the way towards two-equation models by stressing that two kinds of pores exist at the surface (Fig. 8.1), and by evaluating the relative contribution of dry and wet surface regions to the total mass transfer rate. Such contributions were though correlated with surface wetness: A quantity which is hard to apply to macroscale CM, and may differ from surface saturation. Differences between surface wetness and surface saturation will be stressed in this chapter, keeping in mind

that a direct link of the mass transfer rate with the surface saturation or the surface vapor pressure would be preferable, because those are the state variables that usually appear in CMs.

In this chapter, both approaches which are illustrated in Fig. 8.1 to treat the drying surface in respective CMs will be addressed. The first method (Fig. 8.1a) corresponds to the one-equation CM and considers the drying surface as a uniform slice that is affected by the wet and dry surface regions. Surface saturation influences the surface vapor concentration, which in turn sets the driving force for mass transfer into the external transfer region. Latter corresponds to a vapor transport coefficient that can be assessed from PNM data. The second method (Fig. 8.1b) treats the drying surface as two separate regions - the wet and the dry region. In the respective two-equation CM, vapor flux from the dry region to the diffusive boundary layer could be balanced with the internal vapor flux to the surface of the drying material. Since this is straightforward, it will not be discussed here. Contrary, we will focus on the more intricate part of defining the evaporation flux from the wet area and developing practicable tools for its estimation.

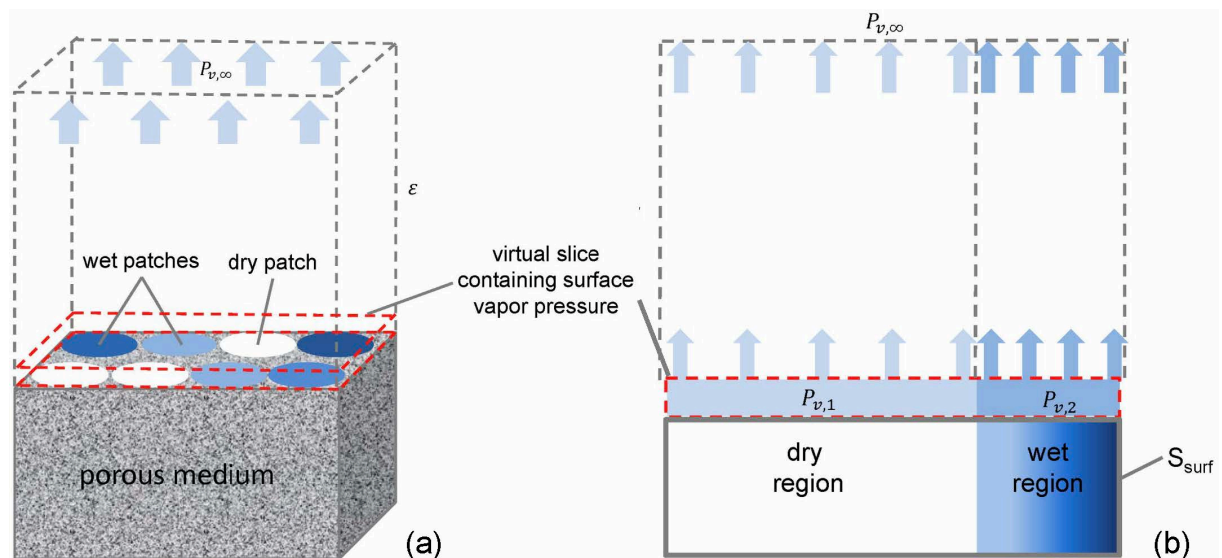


Figure 8.1: Presentation of drying surface for one-equation and two-equation CMs, respectively: a) Wet patches (dark blue from fully filled surface throats, light blue from partially filled surface throats) and dry patches (white, from empty surface throats) exist on the surface of the drying medium, but surface vapor pressure is averaged in a virtual slice placed at the porous surface. b) Wet patches and dry patches are combined into two separate regions, and each region (the wet and the dry one) contributes separately to the total evaporation rate.

Moreover, emendation factors are introduced to link the normalized evaporation rate from the wet part of the porous medium surface with the surface wetness or surface saturation. Their evaluation shows that the normalized evaporation rate contributed from wet patches tends to surface saturation with increasing intensity of drying, whereas a

similar but weaker trend can be observed with surface wetness. This correlation provides, especially in case of enhanced and non-isothermal drying processes, a simple method for coupling the wet surface region with the gas-side boundary layer in a two-equation CM. Besides, we evaluate the evaporation rate from the wet surface region by inserting PNM data into a modified version of Schlünder's model.

### 8.1 Pore network setting and surface parameter estimation

The underground PNM of this scheme is defined on a regular three-dimensional lattice of spherical pores and cylindrical throats (Chapter 2). Details of the algorithm have been described in Chapter 3. In the PNM,  $25 \times 25$  pores are considered in every of in total 51 cross-sections of the porous medium. This cubical grid of pores and throats between them, with 1 mm lattice spacing (center-to-center pore distance) is also extended beyond the evaporating surface of the medium to simulate external mass transfer by diffusion in the adjoining gas-side boundary layer. Extension is by 10 layers in the standard case, reduced to 3 layers for mimicking conditions of faster drying in Sec. 8.4. The bottom of the PNM is adiabatic, whereas periodic boundary conditions are applied to the side faces. Throat and pore radii are randomly sampled from the same normal distribution with a mean of  $250 \mu m$  and a standard deviation of  $25 \mu m$ . However, pore radii are chosen to be larger (or at least equally large) than the largest radius of neighbor throats. Ambient pressure and room temperature ( $20 \text{ }^\circ\text{C}$ ) are assumed to prevail. Material properties are set for water and air (or the combination thereof) at this temperature. Specifically, the binary vapor diffusivity has been obtained according to Schirmer (1938):

$$D_{v,a} = 22.6 \times 10^{-6} \left( \frac{T}{273} \right)^{1.81}, \quad (8.1)$$

where  $T$  is Kelvin temperature, to  $D_{v,a} = 2.57 \times 10^{-5} \text{ m}^2/\text{s}$ .

Surface conditions can be evaluated from PNM simulation results in the way that is illustrated in Fig. 8.2. On one hand, individual values of surface vapor pressure can be averaged in a virtual slice placed at the top of the porous medium. The resulting average surface vapor pressure is affected by the existence of dry and wet regions, and thus, is related to the surface moisture content (Chapter 6.2). Latter can be expressed by means of surface saturation or surface wetness, as will be seen in Sec. 8.4. Using the surface saturation and correlating with the (also average) relative humidity  $\varphi_{surf}$ , a non-local equilibrium (NLE) relationship can be obtained (Attari Moghaddam et al., 2017b). NLE means that thermodynamic equilibrium is satisfied at the menisci but not at the scale of a slice, so that neither free water saturation conditions nor desorption isotherms are applicable to the surface of the drying medium. Contrary, the surface NLE function must be determined and used for computation in the frame of an one-equation CM.

On the other hand, wet and dry surface throats can be distinguished, breaking path for

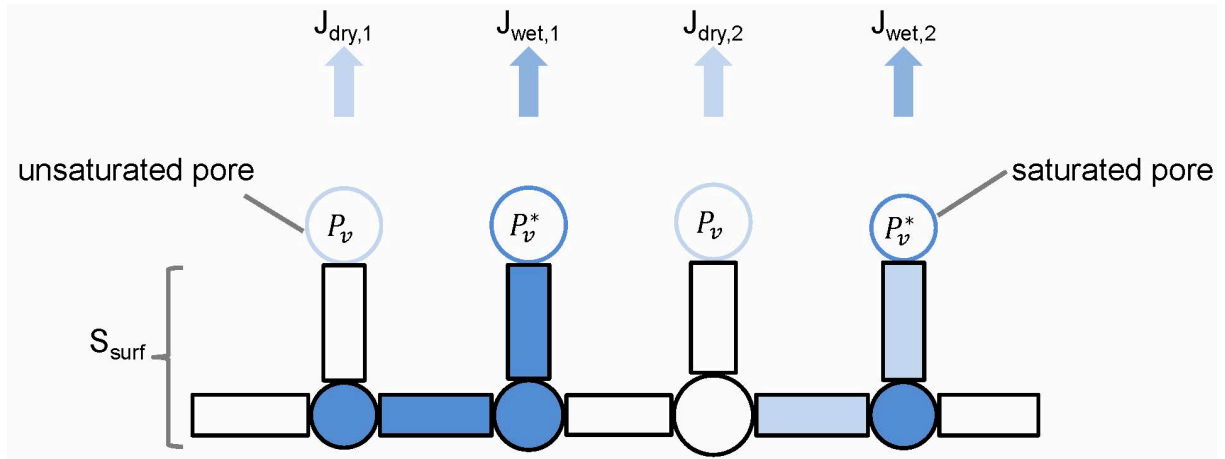


Figure 8.2: Surface parameter estimation from pore network modeling; dark blue: full throat/pore, light blue: partially filled throat/pore, white: dry throat/pore. Saturation vapor pressure above wet patches (full or partially filled throats/pores, dark blue); vapor pressure above dry throats/pores (light blue) is unknown and needs to be determined from the mass balances.

the derivation of parameters which would be relevant for two-equation CMs. For example, evaporation rates from wet ( $J_{wet,i}$ ) and dry ( $J_{dry,i}$ ) surface throats can be evaluated individually, and they can be added to total contributions from either the wet or the dry part of the surface of the drying medium. Assigning those contributions to Fick's law and reversing the respective expression, values of an effective vapor diffusivity can be obtained separately for the wet region and for the dry region of the surface. Summing those up, it is possible to return to the one-equation approach with a global effective vapor diffusivity ( $D_v$ ), which in case of slow drying should be close to the molecular diffusivity from Eq. 8.1.

## 8.2 Surface parameters from pore network data

Surface parameters evaluated from PNM data are the surface NLE function, as well as wet, dry and total effective surface vapor diffusivity. The surface NLE function has been introduced in Chapter 6. Thus, in this part, we evaluate the surface vapor diffusivity. Results will be discussed in the following.

Surface saturation,  $S_{surf}$ , comprises all throats and pores shown in Fig. 8.2: Vertical throats that end at the surface, their underlying layer of pores, and horizontal throats connecting the pores of this sub-surface layer. Surface saturation,  $S_{surf}$ , is the volume of liquid in all those pores and throats divided by their total volume.

The surface contains two kinds of vertical throat ends (virtual surface pores), and they all contribute to the evaporation rate (Fig. 8.3). By consideration of Stefan flow, the

evaporation flow rate from wet pore  $i$  is

$$J_{wet,i} = A_{wet,i} \frac{D_{v,a} \widetilde{M}_v P}{\widetilde{R} T h} \ln \left( \frac{P - P_{v,j}}{P - P_v^*} \right), \quad (8.2)$$

and from dry pore  $i$  is

$$J_{dry,i} = A_{dry,i} \frac{D_{v,a} \widetilde{M}_v P}{\widetilde{R} T h} \ln \left( \frac{P - P_{v,j}}{P - P_{v,i}} \right). \quad (8.3)$$

Here,  $j$  is the next vapor pore in vertical direction to the surface (grid node in the gas region) adjacent to pore  $i$ , whereas  $h$  is the spacing of the grid (isotropic and uniformly equidistant in both, the pore network and the gas boundary layer).  $P_{v,j}$  is the vapor pressure at  $j$ . Vapor pressure at  $i$  is saturation vapor pressure  $P_v^*$  in case of a wet pore; in case of a dry pore, it is  $P_{v,i}$  and has to be obtained from the PNM.  $P$  denotes the total pressure (here atmospheric).  $A_{wet,i}$  and  $A_{dry,i}$  are the cross-sectional areas that correspond to wet or dry pore  $i$ , respectively. With equidistant Cartesian tessellation of the surface, those are equal to  $h^2$ , i.e. they comprise the whole surface tile and not just the circular throat end in it (Fig. 8.1). It should be noted that usage of saturation pressure  $P_v^*$  over the whole square tile in case of a wet core means that CRP conditions are assumed for this unit element of the surface, in accordance with Schlünder's CRP concept.

The vapor flow rate from the whole wet region ( $J_{v,wet}$ ) can be obtained by summing over all wet surface pores:

$$J_{v,wet} = \sum_{i=1}^{N_{wet}} J_{wet,i}. \quad (8.4)$$

Similarly, the vapor flow rate from the dry region ( $J_{v,dry}$ ) is:

$$J_{v,dry} = \sum_{i=1}^{N_{dry}} J_{dry,i}, \quad (8.5)$$

where  $N_{wet}$  and  $N_{dry}$  denote the number of wet pores and dry pores at the surface, respectively.

After having calculated the vapor flow rate for each region, two values of effective surface vapor diffusivity can be defined and calculated for the wet and for the dry region, respectively, by reversing Eq. 1.12, i.e. by applying the reversed Fick's law over the whole thickness of the gas boundary layer:

$$D_{v,wet} = \frac{\frac{J_{v,wet}}{A_{surf}}}{\frac{\widetilde{M}_v P_v^*}{\widetilde{R} T} \left( \frac{\varphi_{surf} - \varphi_\infty}{\varepsilon} \right)}, \quad (8.6)$$

and

$$D_{v,dry} = \frac{\frac{J_{v,dry}}{A_{surf}}}{\frac{\widetilde{M}_v P_v^*}{\widetilde{R}T} \left( \frac{\varphi_{surf} - \varphi_\infty}{\varepsilon} \right)}. \quad (8.7)$$

Here,  $\varphi_\infty$  is the relative humidity at the distance  $\varepsilon$  from the medium surface, assumed to be zero in the present work.

Figure 8.3 shows the effective surface vapor diffusivity contributed from the wet and the dry region as a function of surface saturation. The effective surface vapor diffusivity from the wet region dominates at high surface saturation, since the surface throats and pores are almost full with liquid. However, the surface pore pressure deviates from the saturation vapor pressure in the course of the drying process. The dry region starts to play a role. Correspondingly, the effective surface vapor diffusivity from the dry region increases during the drying process and becomes even dominating in the low saturation period. Figure 8.3 suggests that the contribution of each part of the surface is dynamic within a certain range of values.

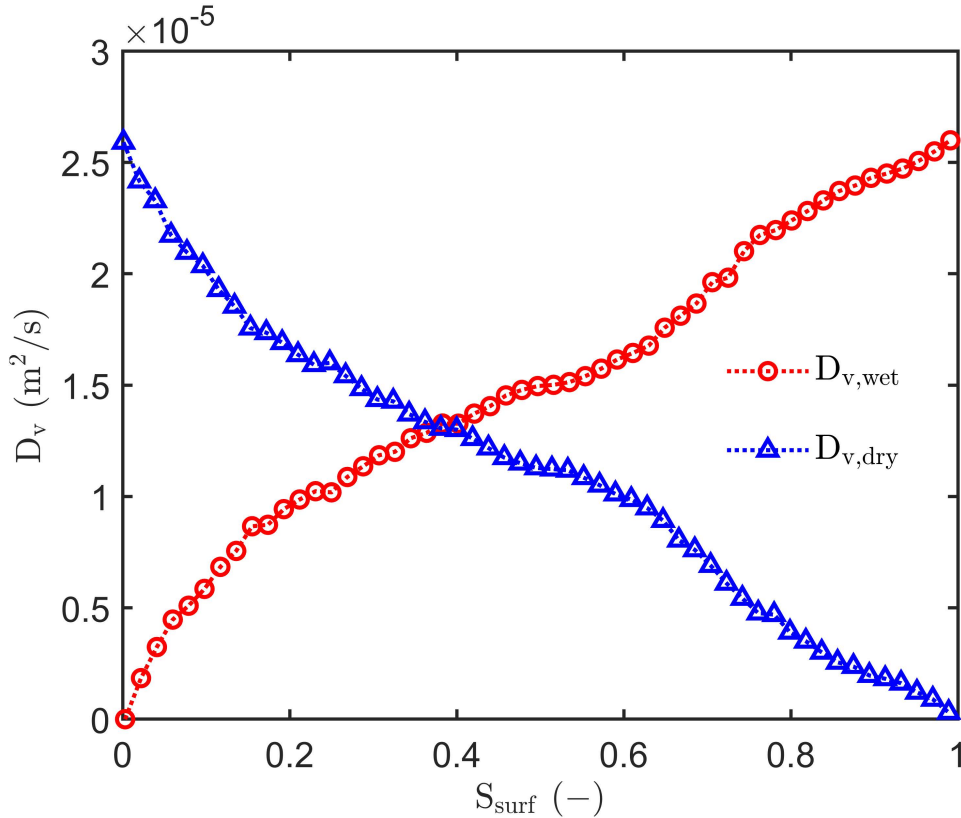


Figure 8.3: Effective vapor diffusivity above the wet region and the dry region of the surface of the pore network as a function of surface saturation. The results are averaged over 20 realizations.

Since the total surface area  $A_{surf}$  is used in both Eqs. 8.6 and 8.7, the overall effective vapor diffusivity,  $D_v$ , can be determined simply by the sum of the diffusivities from the

wet and dry regions:

$$D_v = D_{v,wet} + D_{v,dry}. \quad (8.8)$$

The overall effective vapor diffusivity in the boundary layer is plotted against surface network saturation,  $S_{surf}$ , as well as over relative humidity at the surface,  $\varphi_{surf}$ , in Fig. 8.4. Both plots show that the effective parameter ( $D_v$ ) is very close to the respective physical parameter that has been used in the PNM, namely the binary molecular diffusivity of water vapor in air of  $D_{v,a} = 2.57 \times 10^{-5} \text{ m}^2/\text{s}$  according to Eq. 8.1. This is the expected behavior and a verification for the correctness of PNM computations in the boundary layer as well as of PNM data evaluation.

However, one can also see in Fig. 8.4 that  $D_v$  is not exactly equal to  $D_{v,a}$ , but somewhat larger. The reason is that Stefan's law has been used for gas-phase vapor transport in PNM (within the network as well as in the boundary layer, Eqs. 8.2 and 8.3), whereas the inverse identification of effective boundary layer diffusivities has been conducted by Fick's law (Eqs. 8.6, 8.7). Fick's law is based on equimolar diffusion and linear, whereas Stefan's law takes one-side diffusion with a logarithmic driving force into account. The difference is miniature when the temperature of the evaporating liquid is much smaller than the boiling temperature of the liquid at the imposed pressure, which is fulfilled for our slow drying case at 20 °C and 1 *bar*.

Deviation of  $D_v$  from  $D_{v,a}$  would though increase at higher temperatures, and when opting for Fick's law for the external mass transfer in model equations the effective parameter should be used in such cases, including the dependence of  $D_v$  on  $S_{surf}$  or  $\varphi_{surf}$  that has been illustrated in Fig. 8.4. At this end, correlation of  $D_v$  with  $S_{surf}$  may appear reasonable by analogy to the correlation of internal moisture transport coefficients of drying porous media with local saturation, e.g. Pel et al. (1993). However, this relationship is shown to be strongly non-linear in Fig. 8.4, whereas the relationship of  $D_v$  with  $\varphi_{surf}$  has the advantage of being nearly linear (Fig. 8.4).

### 8.3 Wet surface region evaporation rates

We have seen in Sec. 8.2 that an one-equation CM can be used to describe the drying process at the macroscale, but this model requires heavy fitting of the internal transport parameters (Attari Moghaddam et al., 2017b) as well as use of an appropriate NLE function at the surface of the drying medium, like that of Fig. 6.6, in order to properly work. At the same time, we have seen that two regions (wet and dry) can naturally be distinguished at the surface, which is also true inside the drying medium. Such findings motivate the development and use of two-equation models, related with the expectation that the explicit consideration of a wet and a dry part in such models will reduce the necessity and arbitrariness of fitting compared to the one-equation CM.

However, in a two-equation CM the boundary condition needs to be defined separately

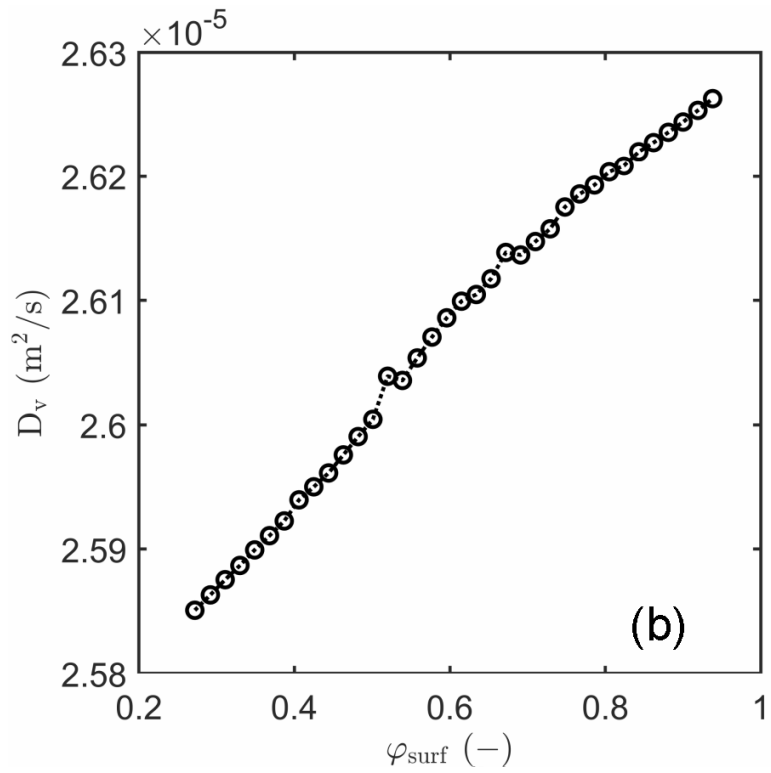
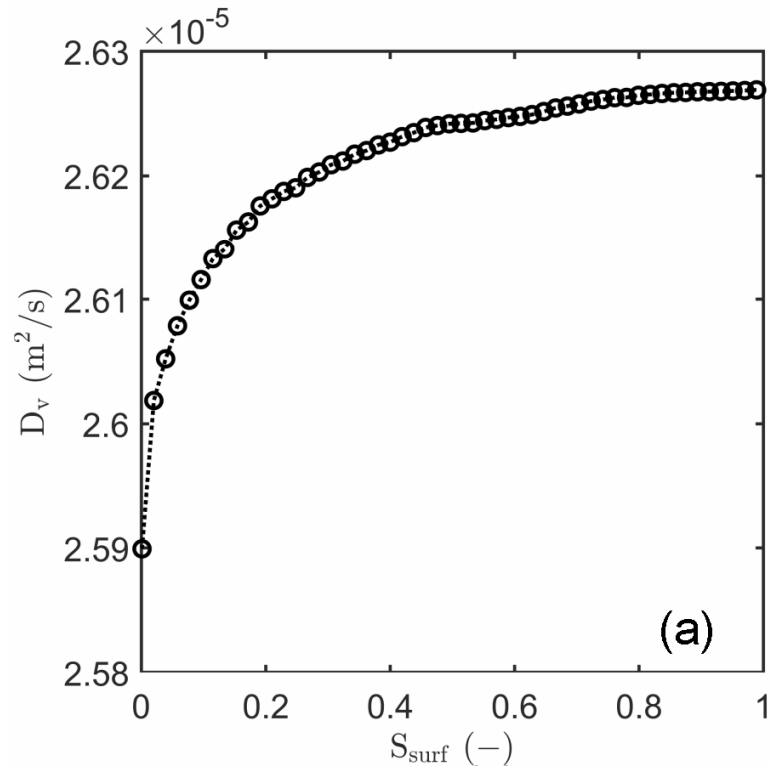


Figure 8.4: Overall effective vapor diffusivity in the boundary layer against (a) surface saturation, (b) surface relative humidity. The results are averaged over 20 realizations.

for the dry and the wet region of the surface. The dry region could be handled by switching from the effective vapor diffusivity of the porous medium to molecular (or effective) vapor diffusivity in the gas-side boundary layer, because the vapor is a continuous phase in the entire considered domain and there is no phase transition at the boundary. In this frame, one could, for example, set equal fluxes at the two sides of the dry part of the surface through Fickian expressions with different diffusivities.

Contrary, liquid transport takes place on one and vapor diffusion on the other side of the wet region of drying medium's surface, so that setting the boundary condition is there more challenging and will be treated in the following. To start with, it is noted that evaporation rate in the CRP (first, gas-side controlled drying period), denoted by  $J_{v,I}$ , can easily be predicted from Eq. 1.12: Obtaining boundary layer thickness  $\delta$  from external flow correlations or computations, using  $P_v^*$  instead of  $P_{v,surf}$ , and multiplying with total surface area  $A_{surf}$  to transform flux  $j$  into a flow rate. It is evident that evaporation flow rate from the wet part of the surface should be smaller than  $J_{v,I}$ , so that instead of analyzing  $J_{v,wet}$ , the ratio  $J_{v,wet}/J_{v,I}$  may be considered, which is similar to the normalized drying rate used in various empirical approaches to drying kinetics (Tsotsas, 1994). Building on that, it would be natural to assume  $J_{v,wet}/J_{v,I}$  being directly proportional to surface saturation  $S_{surf}$ . However, this is probably also simplistic, so that we are expanding the linearity by introducing a correction, which will be called emendation factor and denoted by  $F_1$ :

$$\frac{J_{v,wet}}{J_{v,I}} = F_1 S_{surf}. \quad (8.9)$$

However, proportionality to surface saturation  $S_{surf}$  is not evident. For example, surface wetness  $\psi_{surf}$  might be used as well, as in Schlünder's model (Eq. 1.10). In that case, Eq. 8.9 is rearranged upon the new variable, with  $F_2$  as the corresponding emendation factor:

$$\frac{J_{v,wet}}{J_{v,I}} = F_2 \psi_{surf}. \quad (8.10)$$

Especially Eq. 8.9 would be a very elegant definition of the boundary condition for the liquid phase in a two-equation CM, but the emendation factor should be known in advance. Use of the PNM provides unique opportunities in this sense to find out: How the normalized evaporation rate from the wet surface region correlates with  $S_{surf}$  or  $\psi_{surf}$ ; how far such correlations are from direct proportionality; which emendation factors are obtained from PNM data.

The assessment of Eq. 8.9 by means of PNM data is shown in Fig. 8.5 in terms of the dependence of  $J_{v,wet}/J_{v,I}$  on  $S_{surf}$ , and in Fig. 8.6 by means of the respective emendation factor  $F_1$ . Data points are not far away from the diagonal in Fig. 8.5 (which would mean  $F_1 = 1$ ), but there are measurable differences, so that the emendation factor deviates significantly from unity as can be seen in Fig. 8.6.

Figure 8.6 suggests that the emendation factor depends on the drying process. When the surface is filled with liquid, the normalized evaporation rate for the wet region equals the surface saturation, so that the emendation factor is close to unity for  $S_{surf} > 0.5$ . The emendation factor starts to play a role when the air invades into the porous medium. The emendation factor is larger than unity after  $S_{surf} < 0.5$ , which means that the normalized evaporation rate for the wet region is larger than the surface saturation. A reason for this might be that the liquid phase is structured due to the random pore size distribution in the PNM.

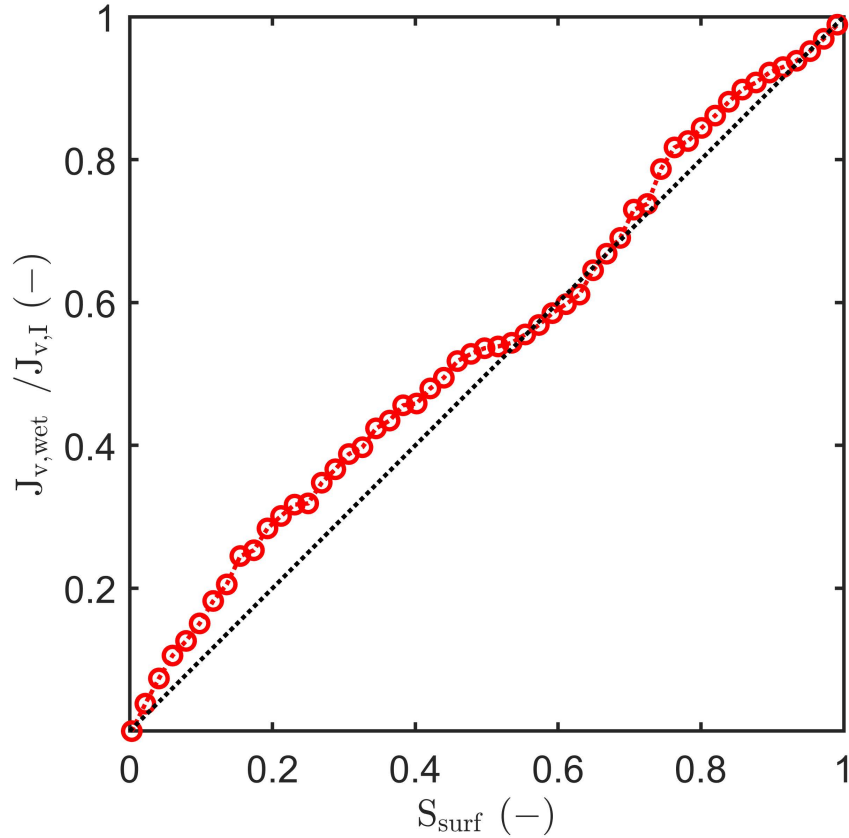


Figure 8.5: Normalized evaporation rate from the wet region over surface saturation from PNM data.

The interrelation between surface wetness  $\psi_{surf}$  and surface saturation  $S_{surf}$  according to the PNM is depicted in Fig. 8.7. As explained in Sec. 8.2, PNM surface saturation  $S_{surf}$  is obtained by consideration of all structural elements shown in Fig. 8.2, namely vertical throats to the surface as well as pores and horizontal throats of the layer directly below the surface. Contrary, every tile that contains the end of a totally or partially saturated vertical throat is considered to be fully wet in the evaluation of surface wetness, all others being dry. With equidistant Cartesian tessellation of the surface, this means that surface wetness  $\psi_{surf}$  is simply equal to the number of wet tiles  $N_{wet}$  to the total

number of square surface elements  $N_{tot}$ :

$$\psi_{surf} = \frac{N_{wet}}{N_{tot}}. \quad (8.11)$$

Figure 8.7 shows  $\psi_{surf}$  to be tentatively smaller than  $S_{surf}$ . The surface wetness  $\psi_{surf}$  is only associated with the vertical throats to the surface. Therefore, the emendation factor  $F_2$  of Eq. 8.10, shown in Fig. 8.8, is larger than the emendation factor  $F_1$  from Fig. 8.6, with otherwise similar behavior. There would be appealing aspects in the use of surface wetness as the variable with which the normalized evaporation rate from the wet region might be correlated, because of possibilities for the direct experimental determination of this quantity by, for example, near infrared spectroscopy. On the other hand, it might be argued that in reality surface saturation is measured by such methods at the macro-scale, the difference to surface wetness being an artifact that arises because  $S_{surf}$  is determined for a very small volume in the PNM. Measured data that would distinguish between 2D saturation (surface wetness) and 3D saturation in a thin surface slice (surface saturation) is nonexistent to our knowledge, so that this issue cannot be fully resolved. However, the present results clearly indicate that use of surface wetness  $\psi_{surf}$  is rather disadvantageous (the deviation of the emendation factor from unity is larger), so that surface saturation  $S_{surf}$  should be preferred.

Irrespective of the definition upon  $\psi_{surf}$  or  $S_{surf}$ , emendation factors differ significantly from unity in the previous evaluation, which, though, has been conducted for a very slow drying process. In order to estimate the influence of drying intensity while still preserving the isothermal character of the simulations, thickness of the boundary layer was reduced from the reference value of  $\delta = 10h$  in the previous simulations to  $\delta = 3h$ . Comparison of the data of Fig. 8.9a with those of Fig. 8.5 shows that the normalized evaporation rate  $J_{v,wet}/J_{v,I}$  comes thus closer to  $S_{surf}$  (i.e., to the diagonal of the plot). At the same time, the relationship between  $\psi_{surf}$  and  $S_{surf}$  (cf. Fig. 8.9b with Fig. 8.7) does not seem to change dramatically. Emendation factors defined for  $S_{surf}$  and  $\psi_{surf}$  are plotted in Figs. 8.10a and b, respectively, for both boundary layer thicknesses. Figure 8.10b shows emendation factors that decrease significantly with increasing global drying rate when defined on the basis of  $\psi_{surf}$ . Defined for  $S_{surf}$ , the emendation factor  $F_1$  is essentially equal to unity at  $\delta = 3h$ . In case of the faster process, surface menisci dry immediately after having been activated by liquid evaporation. The drying surface and the underneath region become more uniform, and the growth of cavities to an empty structure below dried surface areas is reduced.

In total, the results indicate that setting the normalized evaporation rate  $J_{v,wet}/J_{v,I}$  equal to surface saturation  $S_{surf}$  can be expected to be a good approximation for relatively fast drying processes in practice, which means that Eq. 8.9 with  $F_1 = 1$  would be an appropriate boundary condition to the wet part of two-equation continuous models.

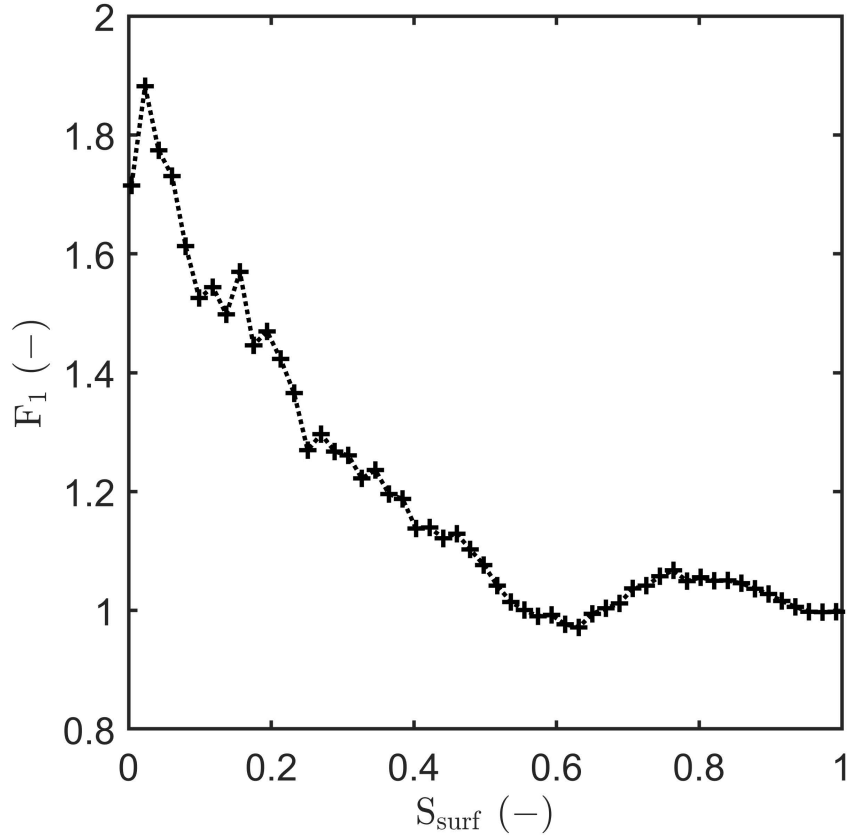


Figure 8.6: Emendation factor ( $F_1$ ) as a function of surface saturation calculated from the PNM data of Fig. 8.5.

#### 8.4 Schlünder's formula for the wet surface region

The previous evaluation has shown that the emendation factor approaches unity with increasing intensity of the drying process, especially when using surface saturation in order to capture the decrease in evaporation rate from the wet surface region in the course of drying. This provides a reasonable and easily implementable boundary condition for the wet region in two-equation models. However, the question arises whether approaches like Schlünder's model might possibly contribute to a still better solution, especially at low global drying rates. As discussed, Schlünder's formula has been derived for explaining the existence of the first drying period. It does not recognize the gradual appearance of completely dried patches on the surface and is, thus, inadequate for quantitative calculation of the evaporation rate, especially when the surface has already been depleted from most of the originally contained liquid. Its application to the wet part of the surface might though be favorable and has not been investigated before.

To facilitate this investigation, we modify the original derivation which considered square surface elements with circular wet spots in them and resulted in Eqs. 1.10 and 1.11. Instead, we consider only the circular wet spots as representatives of completely or partially filled cylindrical surface throats of the PNM. One such cylindrical surface

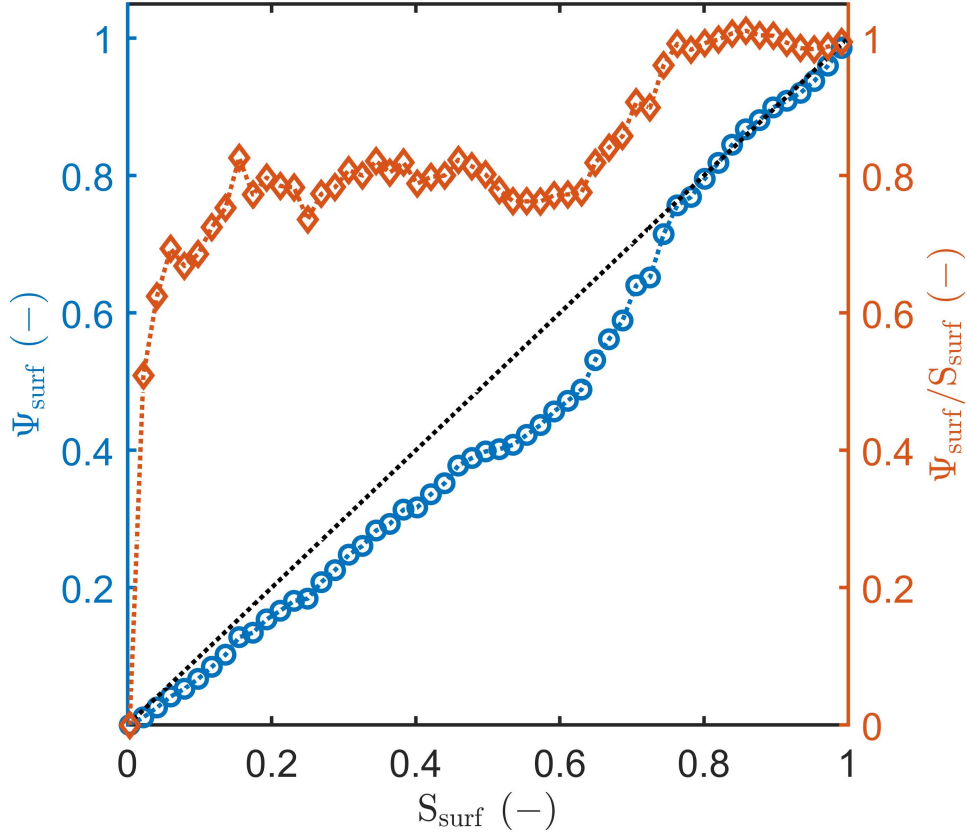


Figure 8.7: Correlation of surface wetness  $\psi_{surf}$  with surface saturation  $S_{surf}$  from the PNM data.

tube with radius  $r_t$  is shown in Fig. 8.11. The tube is initially filled with liquid up to  $r_t$ . However, the liquid-filled part of the tube shrinks to a cylinder of smaller radius  $r_p$  when the saturation of the tube with liquid is reduced. This means that surface throats which are emptying by retreating menisci in the PNM are represented by shrinking tubes in the modification of Schlünder's model. Due to geometry, surface throat saturation and surface wetness are the same and related to  $r_p$  as:

$$S = \psi = \left(\frac{r_p}{r_t}\right)^2. \quad (8.12)$$

Schlünder's concept in Fig. 8.11 is that water vapor first diffuses from  $r_p$  at saturation pressure  $P_v^*$  to  $r_t$  at partial vapor pressure  $P_v^0$ , and then over the thickness  $\varepsilon$  of the boundary layer from  $P_v^0$  to ambient partial vapor pressure  $P_{v,\infty}$  (assumed zero). If the first step were quick and short in comparison to the second one, then the whole basis area in light blue appears as if it were at saturation pressure  $P_v^*$ .

In total, instead of Eq. 1.10 the modified model for surface throat  $i$  results in:

$$\frac{J_{v,i}}{J_{v,I}} = \frac{1}{1 + \Phi_i}, \quad (8.13)$$

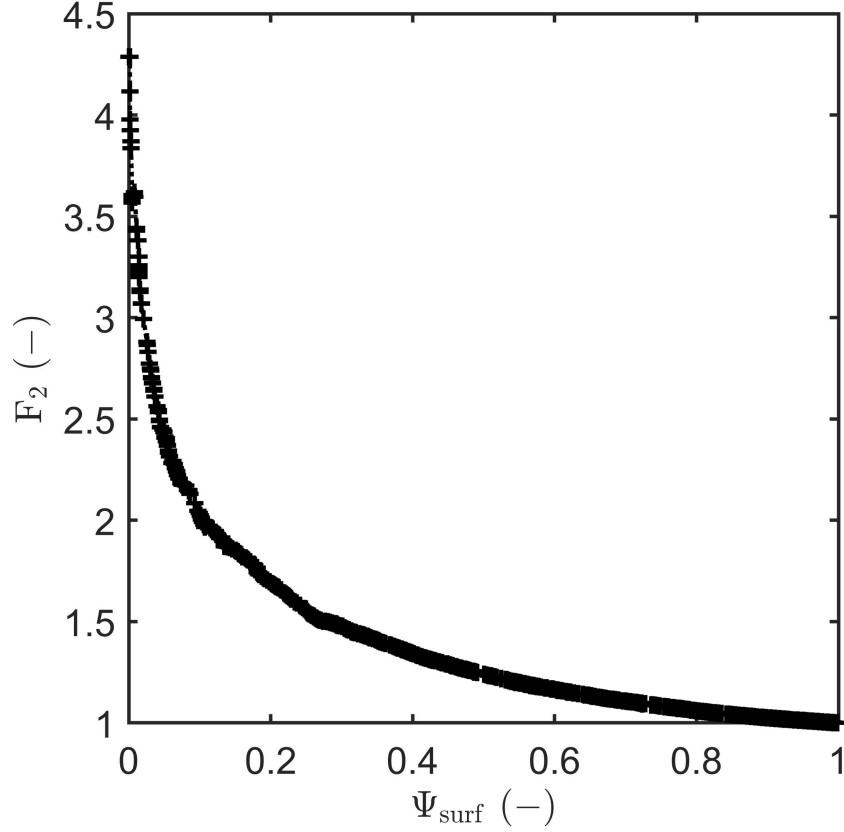


Figure 8.8: Emendation factor ( $F_2$ ) as a function of surface wetness calculated from PNM data.

and

$$\Phi_i = \frac{r_{t,i}}{2\delta} \left( \sqrt{\frac{1}{S_i}} - 1 \right). \quad (8.14)$$

In Eqs. 8.13 and 8.14, the ratio of the evaporation rate from the considered wet surface throat ( $J_{v,i}$ ) to the initial evaporation rate ( $J_{v,I}$ ) is correlated with the parameter  $\psi_i$ , which might be understood as a resistance for vapor diffusion in lateral direction.

Transition from Eq. 8.13 to the whole evaporative surface is achieved by calculating  $\psi_i$  from Eq. 8.14 for each individual wet surface throat with its specific radius and saturation (from PNM results), weighing with the individual cross-sectional area  $A_i$ , summing over the total number of wet surface throats  $N_{wet}$ , and dividing by the total surface area of the porous medium  $A_{surf}$  to obtain:

$$\frac{J_{v,wet}}{J_{v,I}} = \frac{1}{A_{surf}} \sum_i^{N_{wet}} A_i \frac{1}{1 + \Phi_i}. \quad (8.15)$$

Use of Eq. 8.15 means that individual data and the modified version of Schlünder's formula are used at every wet surface spot, so that the heterogeneity of the surface is accounted for. Comparison of normalized evaporation rates  $J_{v,wet}/J_{v,I}$  from Eq. 8.15 with the already shown values of  $J_{v,wet}/J_{v,I}$  obtained directly from the PNM is presented

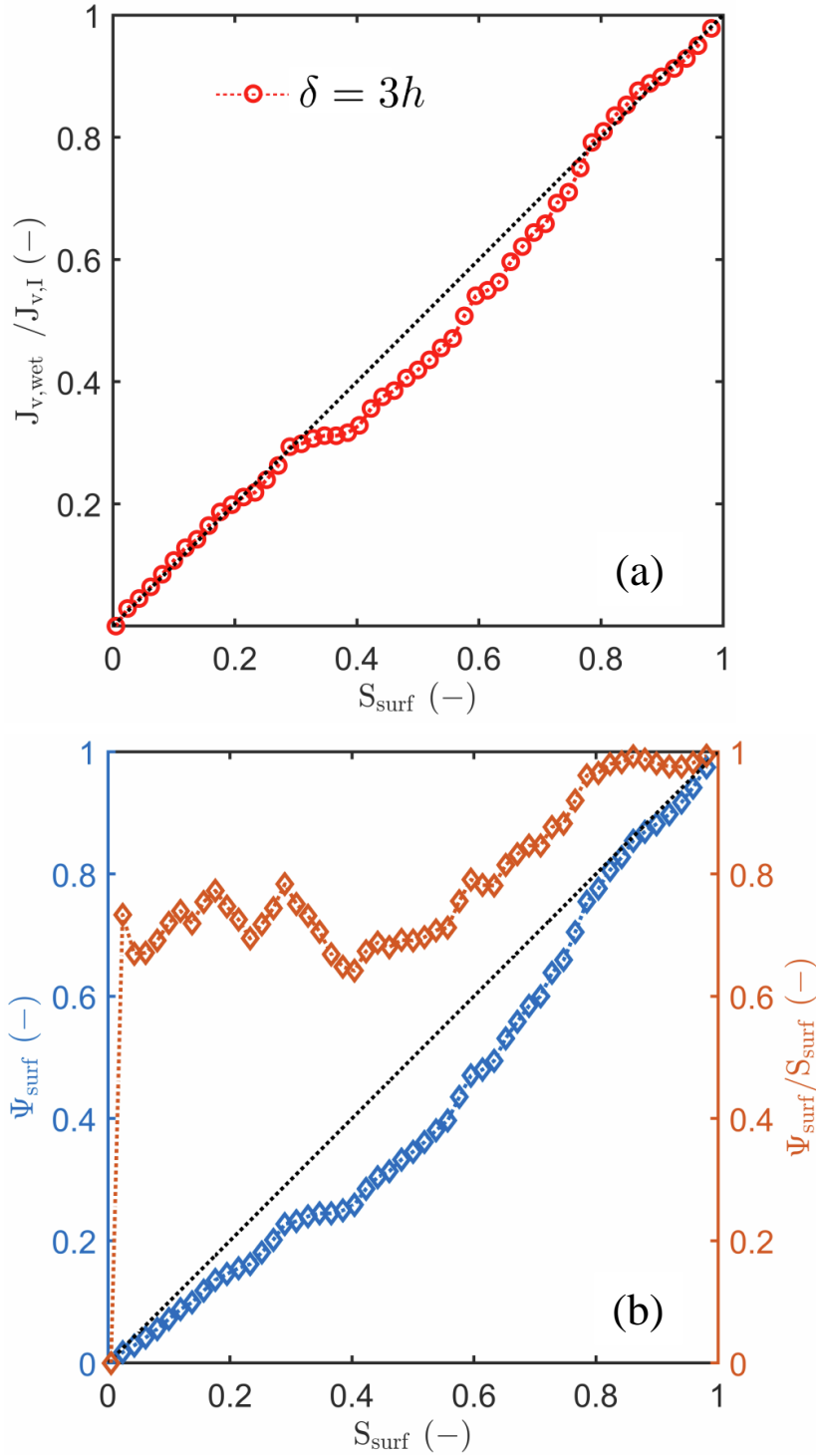


Figure 8.9: (a) Normalized evaporation rate of the wet region from the PNM with  $\delta = 3h$ ; (b) surface wetness as a function of surface saturation from the PNM with  $\delta = 3h$ .

in Fig. 8.12a for very slow ( $\delta = 10h$ ) and in Fig. 8.12b for enhanced ( $\delta = 3h$ ) drying. Agreement can be seen in some regions (very large  $S_{surf}$  for  $\delta = 10h$ , very large as well as small  $S_{surf}$  for  $\delta = 3h$ ), but there is also significant overestimation or underestimation compared with the results obtained from the PNM in other regions. It should be noted

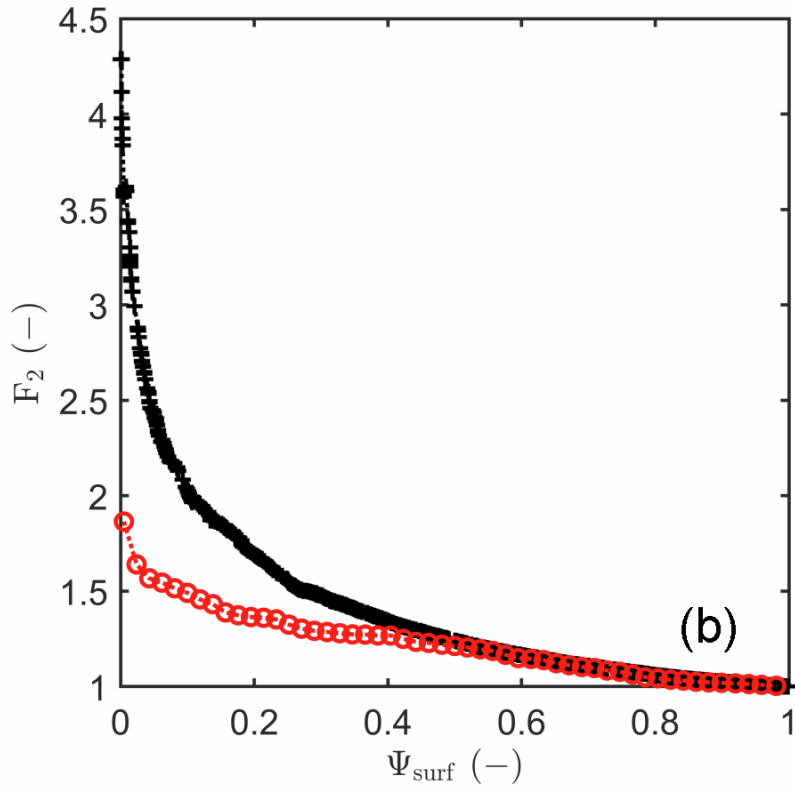
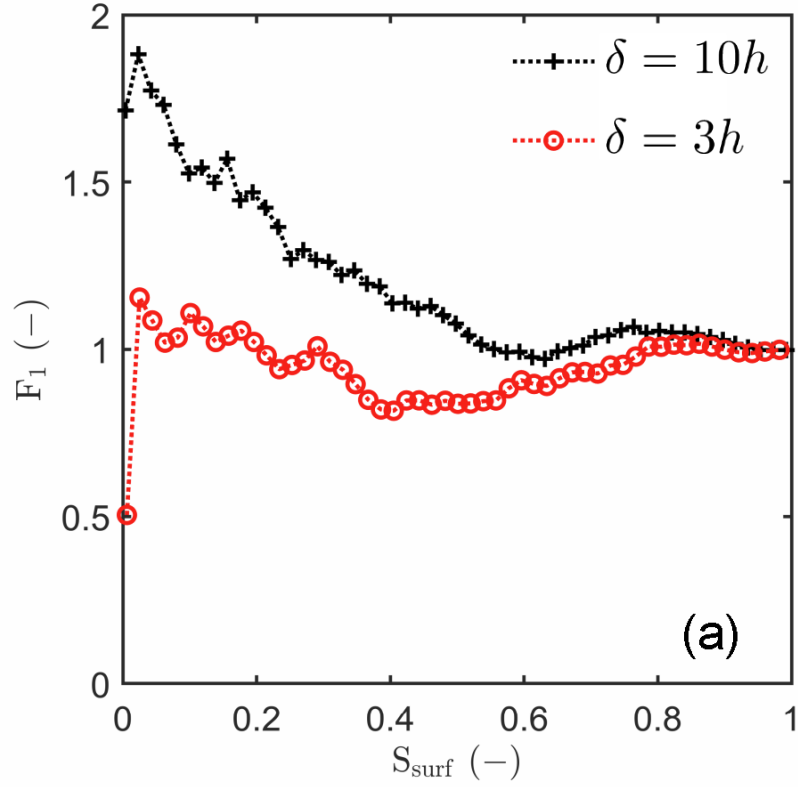


Figure 8.10: Influence of drying intensity, modified by variation of boundary layer thickness from  $\delta = 10h$  (reference case) to  $\delta = 3h$  on: (a) Emendation factor  $F_1$  for correlations with surface saturation  $S_{surf}$ ; (b) emendation factor  $F_2$  for correlations with surface wetness  $\psi_{surf}$ .

that only surface throats have been considered in Eq. 8.15, whereas surface saturation  $S_{surf}$  takes into account also the horizontal throats and pores located immediately below the surface. These parts of the surface slice also play a role in the surface pore pressure in the PNM, but not in Schlünder's formula. Additionally, the pressure of surface pores is affected by the liquid structure in the surface slice, including the liquid underneath of the surface, which could help to hold the pressure of vapor pores at saturation. Contrary, only surface wetness is considered in Schlünder's formula, which does not seem to be enough to express the interrelation of liquid content with the evaporation rate. In total, application of Schlünder's equation does not seem to improve our ability to correlate the normalized evaporation rate with surface saturation, so that use in the boundary condition for the wet part of the porous medium in a two-equation CM does not appear to be reasonable.

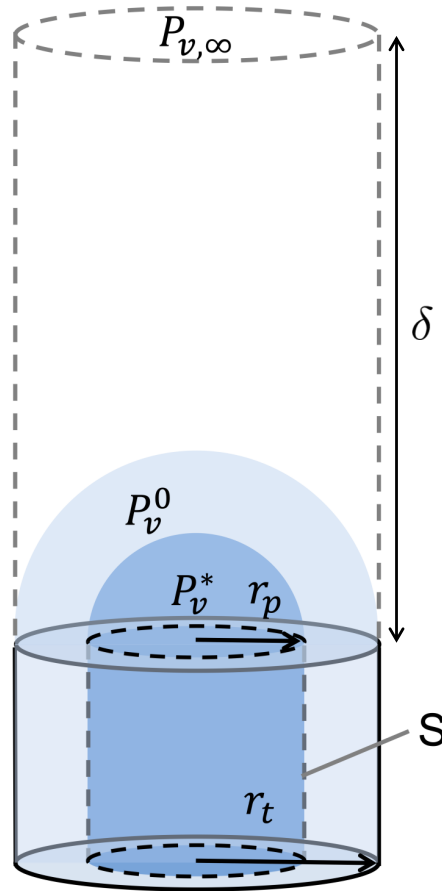


Figure 8.11: Schematic of single wet surface throat for the revised Schlünder's formula: Initially, the whole cylinder with radius  $r_t$  is filled with liquid; then, the liquid retreats with decreasing throat saturation  $S$  to a cylinder of radius  $r_p$ .

Even in case of agreement of  $J_{v,wet}/J_{v,I}$  obtained from the Schlünder formula and directly from the PNM, this does not mean that the Schlünder formula could predict  $F > 1$ . It should be clear that the Schlünder formula only includes the relationship between the saturation of vertical throats and the surface wetness in Eq. 8.15, whereas the surface saturation  $S_{surf}$  takes into account also the horizontal throats and pores located beneath

the surface. In other words, the profile of  $\psi$  with  $S$  in Schlünder's formula differs from the profile of  $\psi_{surf}$  with  $S_{surf}$  in Fig. 8.7. Thus, the evaluated emendation factors  $F_1$  or  $F_2$  in Fig. 8.10 make much more sense from the point of view of close representation of PNM results.

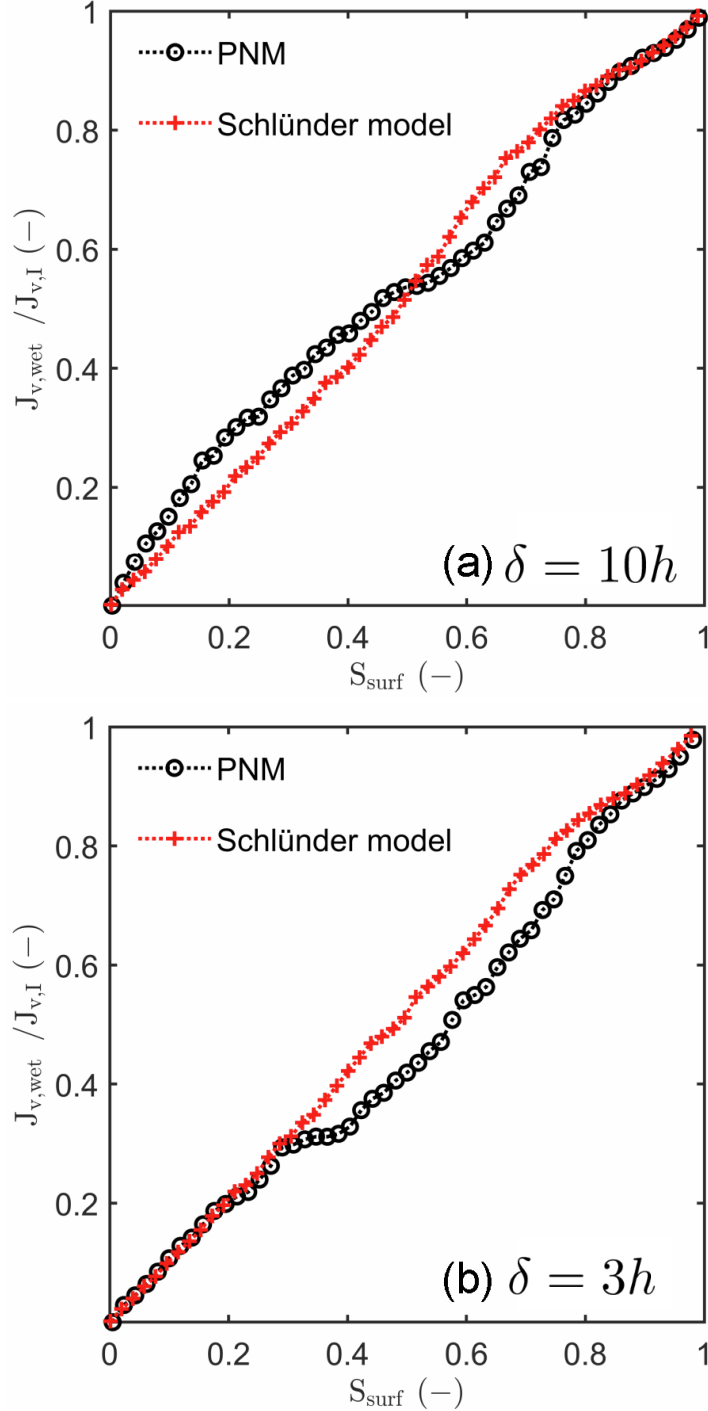


Figure 8.12: Normalized evaporation rates of the wet surface region obtained from Eq. 8.15 (denoted by Schlünder model) as well as directly from the pore network model for two different values of boundary layer thickness (a)  $\delta = 10h$ , (b)  $\delta = 3h$ .

# Chapter 9

## Macroscopic parameters dependence on the pore network heterogeneity

*Part of this chapter will be published as “Lu, X., Tsotsas, E., Kharaghani, A., The dependence of continuum model parameters on the spatially correlated pore structure studied by pore-network drying simulations”.*

Based on the analysis of the influence of macroscopic parameters on the continuum model (CM), two parameters, the moisture transport coefficient as well as the relative humidity, take the primary responsibility in reproducing the drying characteristics of the porous media. In this chapter, we show the effect that features of pore structure (monomodal pore size distribution (PSD) with variable mean throat radius and standard deviation of throat/pore radius, bimodal PSD) have on those two macroscopic parameters.

In this chapter, we employ the throat-pore model introduced in Chapter 2 as a framework to investigate the influence of pore structure on the macroscopic parameters discussed in Chapter 6. Default parameters of the pore network model are listed in Tables 3.1 and 3.2. The network size remains at  $25 \times 25 \times 51$  with gas-side boundary layer thickness at  $25 \times 25 \times 10$ . It should be noted that the pore radii are larger than or at least equal to the largest radius of neighbor throats (Fig. 2.4). Initial standard deviations of pores/throats are set equal. After the adjustment, the mean pore radius is larger than the initial setting value and the standard deviation of pore radius is smaller. The mean radius and standard deviation of pores are derived quantities. Thus, in this section, we focus on the impact of the radius distribution of throats on parameters relevant for the drying process. For each network, we extract the moisture transport coefficient profiles and profiles of the relative humidity from the pore network data. To reduce randomness of macroscopic parameters, we take several PNM datasets from ten parallel simulations. The averaging method has been introduced in Chapter 3 and is used for averaging all macroscopic parameters also in this chapter.

## 9.1 Influence of mean throat radius

Three values of mean throat radius,  $\bar{R}_t = 50 \mu m$ ,  $\bar{R}_t = 150 \mu m$  and  $\bar{R}_t = 250 \mu m$ , with the same standard deviation of throat radii,  $\sigma_{0,t} = 5 \mu m$ , are separately used to perform simulations with the throat-pore model (Fig. 9.1). The radii of throats are sampled from said distributions; the radii of pores are altered corresponding to the explained rules. These settings result in differences in the void space of the porous medium, altering the porosity (Table 9.1).

Table 9.1: Characteristics of pore structures used for drying simulations.

Parameters			
Network size	$25 \times 25 \times 51$	$25 \times 25 \times 51$	$25 \times 25 \times 51$
Boundary layer size	$25 \times 25 \times 10$	$25 \times 25 \times 10$	$25 \times 25 \times 10$
Mean throat radius ( $\mu m$ )	50	150	250
Mean pore radius ( $\mu m$ )	57	156	256
Standard deviation of throat radius ( $\mu m$ )	5	5	5
Center distance between two pores ( $mm$ )	1.0	1.0	1.0
Liquid volume ( $m^3$ )	$6.8 \times 10^{-7}$	$5.1 \times 10^{-6}$	$1.1 \times 10^{-5}$
Network porosity	0.022	0.162	0.358

Figure 9.2 shows the moisture transport coefficient profiles calculated based on the method that has been proposed in Chapter 6 for the pore networks with different mean value of throat radius. The moisture transport coefficient increases with increasing mean throat radius. This is attributed to the fact that resistance to mass transport decreases at higher porosities that result from the mean throat radius increase.

However, two characteristic saturations, the saturation when slices contain the maximum of interfacial area ( $S_{a_s, max}$ ) and the turning point ( $S_T$ ) at which the moisture transport reaches a minimal value, remain nearly unchanged. To explore the reason, we determined the profiles of the interfacial area and the ratio of liquid flow rate over the total flow rate.

The saturation at which slices contain the maximum of interfacial area ( $S_{a_s, max}$ ) is identified by summing of the cross-sectional areas of all menisci in each slice. However, the cumulative interface area in a slice is not comparable among samples with different mean throat radius. Therefore, it is made dimensionless by dividing by the void area in the slice, obtained from the void volume in the slice  $V_s$  over slice thickness  $h$ . In this way, a relative interfacial area is obtained as

$$\tau = \frac{a_s}{(V_s/h)}. \quad (9.1)$$

Figure 9.3 shows the alteration of the relative interfacial area for different network structures. The peak value occurs when the slice has the maximum of interfacial area.

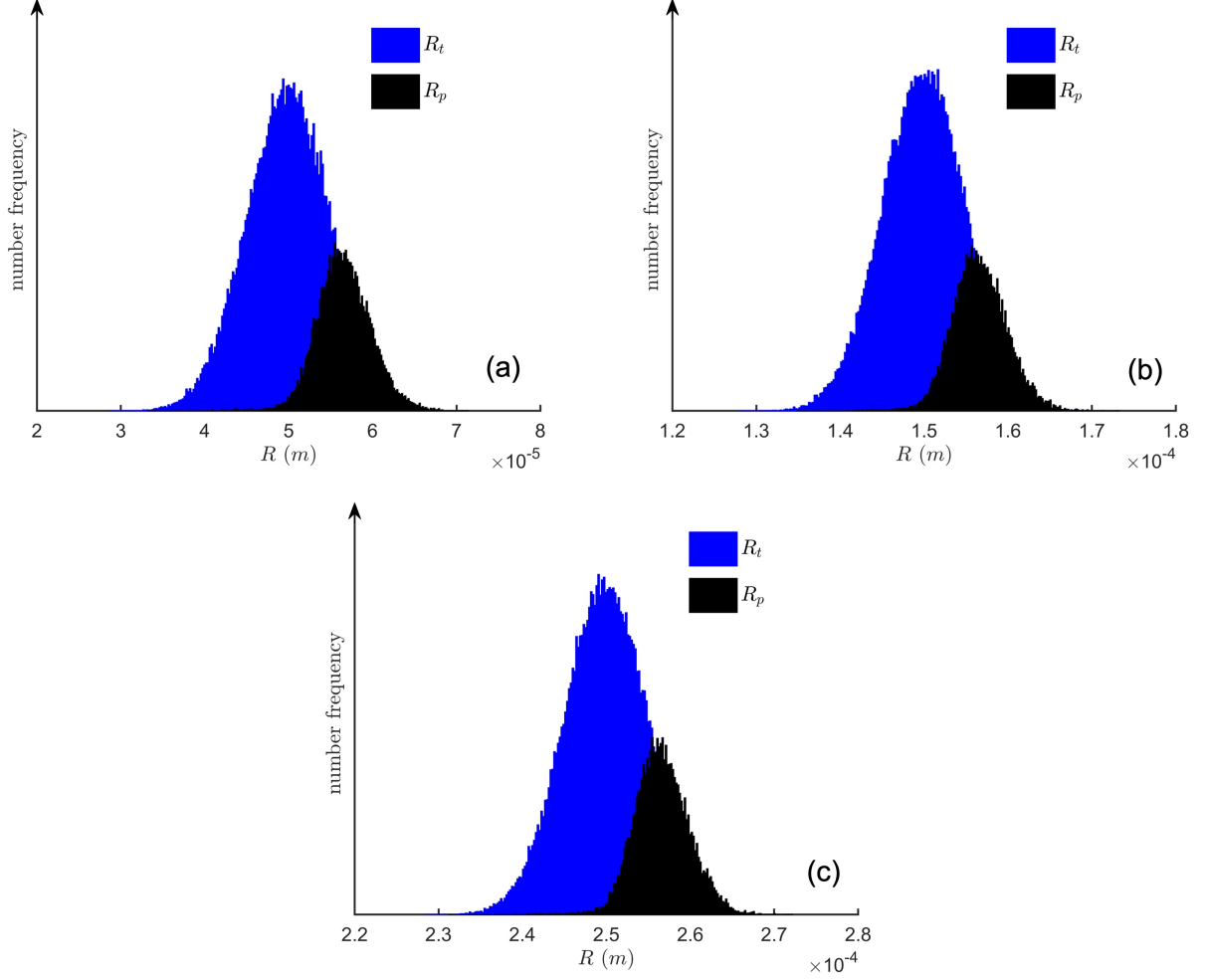


Figure 9.1: The final radii of throats and pores of three types of networks with identical standard deviation of throat radius,  $\sigma_{0,t} = 5 \mu m$ : (a)  $\bar{R}_t = 50 \mu m$ , (b)  $\bar{R}_t = 150 \mu m$ , (c)  $\bar{R}_t = 250 \mu m$ .

The peaks of relative interface area occur for all three networks, and irrespectively of the stage of the drying process, almost at the same saturation.

Additionally, turning point saturation ( $S_T$ ) is achieved at the moment when the liquid flow rate contributes 50% to the total flow rate. According to the simulation results presented in Fig. 9.4, equality in the contributions of the liquid phase and the vapor phase is reached almost at the same saturation for the networks with different mean throat radius. A reason for this behavior might be that the capillary effect is unaltered with expanding the mean throat radius while keeping the same standard deviation. Assuming the same liquid viscosity, the difference in capillary pressure, as the driving force, is controlled by the discrepancy between two active menisci,

$$\Delta P_c = 2\sigma \left( \frac{1}{R_1} - \frac{1}{R_2} \right) = \frac{2\sigma (R_2 - R_1)}{R_1 R_2}. \quad (9.2)$$

Here,  $R_1$  and  $R_2$  denote the radii of two active menisci, respectively. This means that the

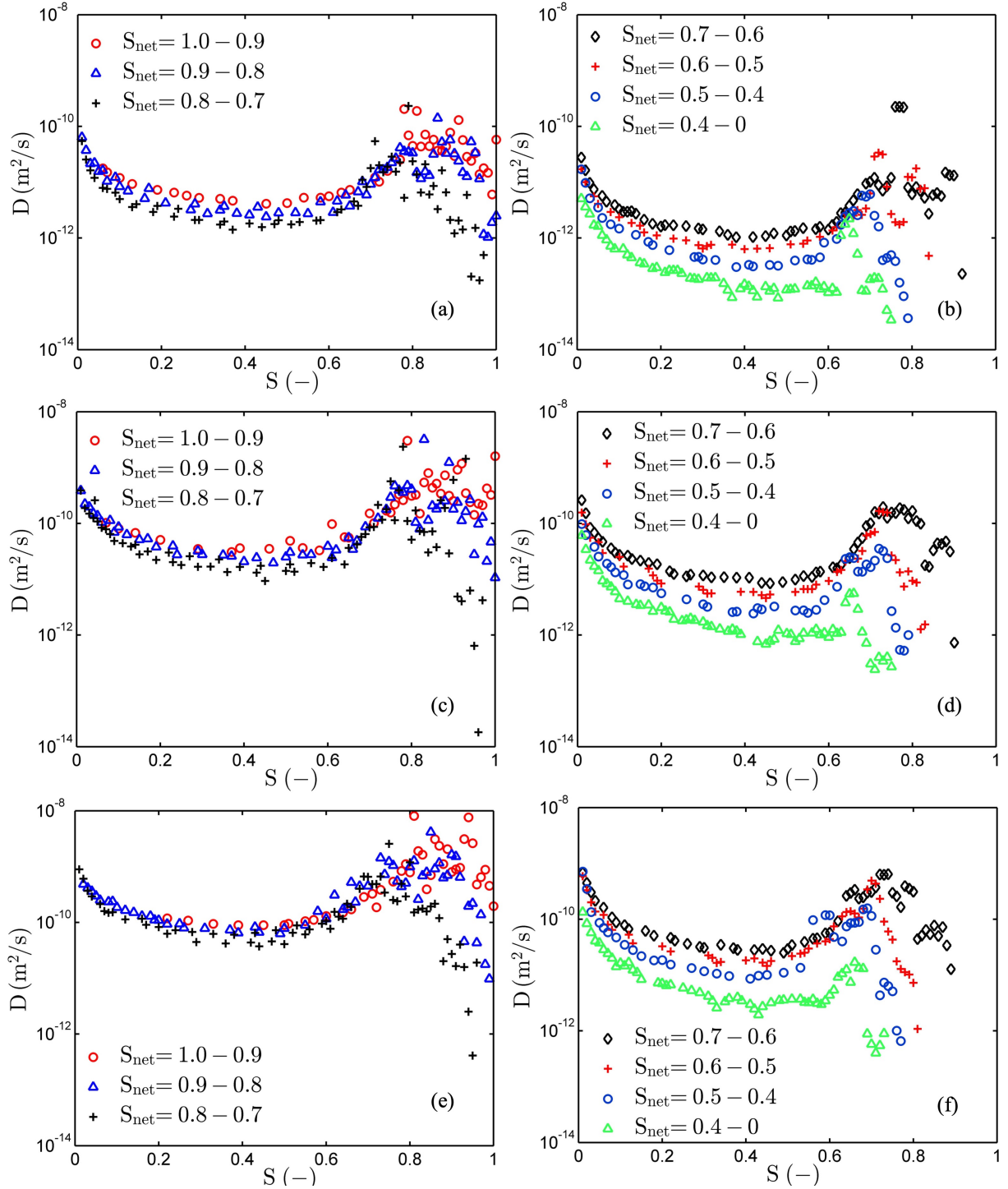


Figure 9.2: Moisture transport coefficient profiles obtained from the pore network drying simulations for three different values of the mean throat radius  $\bar{R}_t = 50 \mu\text{m}$  (a, b),  $\bar{R}_t = 150 \mu\text{m}$  (c, d) and  $\bar{R}_t = 250 \mu\text{m}$  (e, f). The values are averaged over ten realizations for local saturation  $S$  intervals.

driving force is not a function of the mean throat radius. Therefore, the similar values of  $S_{a_s, \max}$  and  $S_T$  demonstrate that the three regions that can be distinguished in regard of moisture transport, namely liquid transport dominated region (LTDR), two-phase transport region (TPTR) and vapor transport dominated region (VTDR), compare with

Chapter 6, are not shifted.

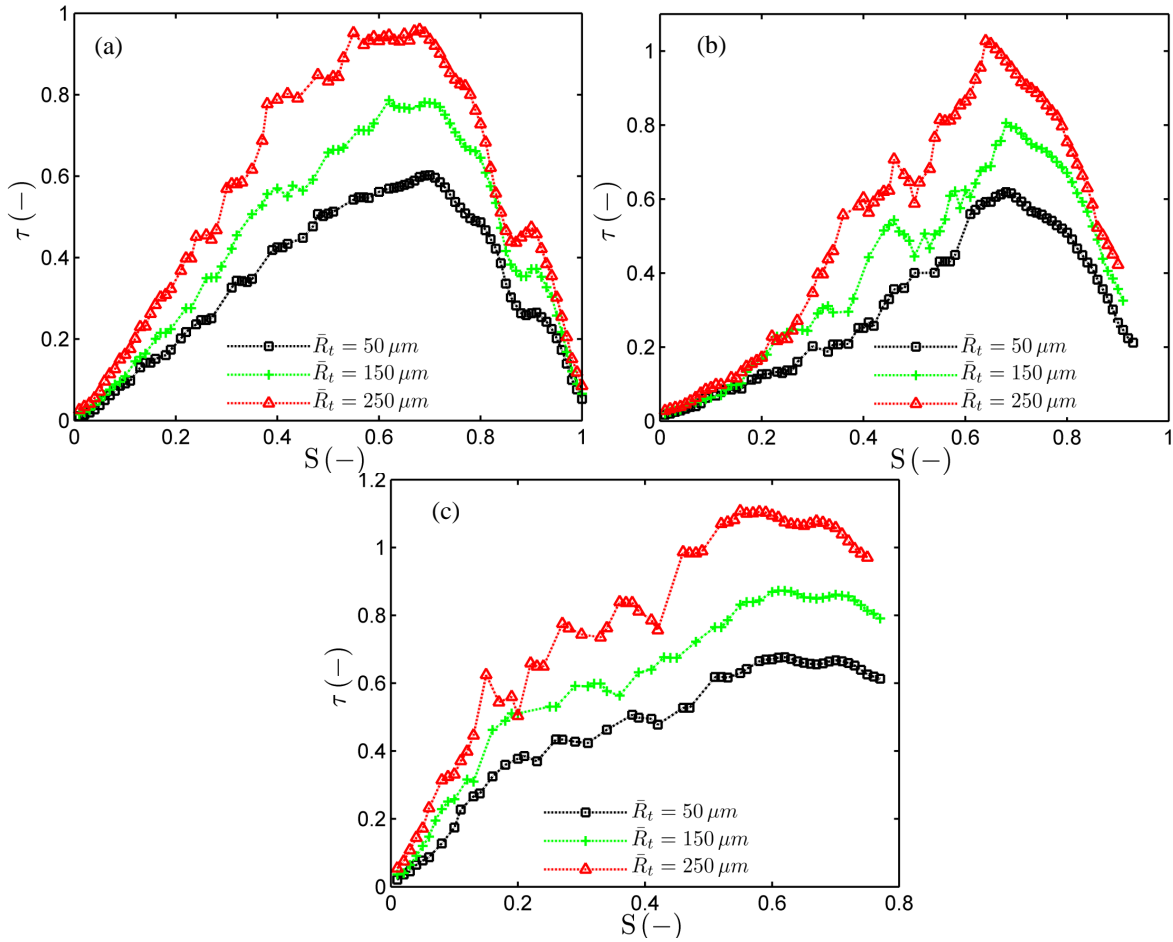


Figure 9.3: The relative interfacial area as a function of local saturation, obtained from PNM simulations for network saturations from (a) 1 to 0.7, (b) 0.7 to 0.4 and (c) 0.4 to 0. The values are averaged over ten realizations for intervals of local saturation  $S$ .

The relative humidity of the two-phase region has also been determined (Fig. 9.5). The non-local equilibrium effect (NLE) is increased by reducing the mean throat radius. This could be due to stronger resistance for the liquid transport that results in a more uniform drying front, preventing either air invasion or liquid transport from the bottom of the porous medium to the front, which may strengthen the unevenness of the vapor pressure distribution in the two-phase region. This explanation can be proved by profiles of the relative surface area of the liquid phase (Fig. 9.3). The relative interfacial area is, indeed, increased with increasing the mean throat radius. In other words, the vapor pressure is more easily held at high values when the porous medium contains more interfacial area.

The surface relative humidity of the three networks is shown in Fig. 9.6. The surface NLE is very distinct for the network with a smaller value of mean throat radius. Substantial flow resistance preventing the transport of liquid leads to shrinkage of wet surface area appearing at very early stage of the drying process, which causes the sharp decrease in

surface relative humidity. Such behavior of the relative humidity appears to be similar to a desorption isotherm, but has nothing to do with solid-moisture interactions.

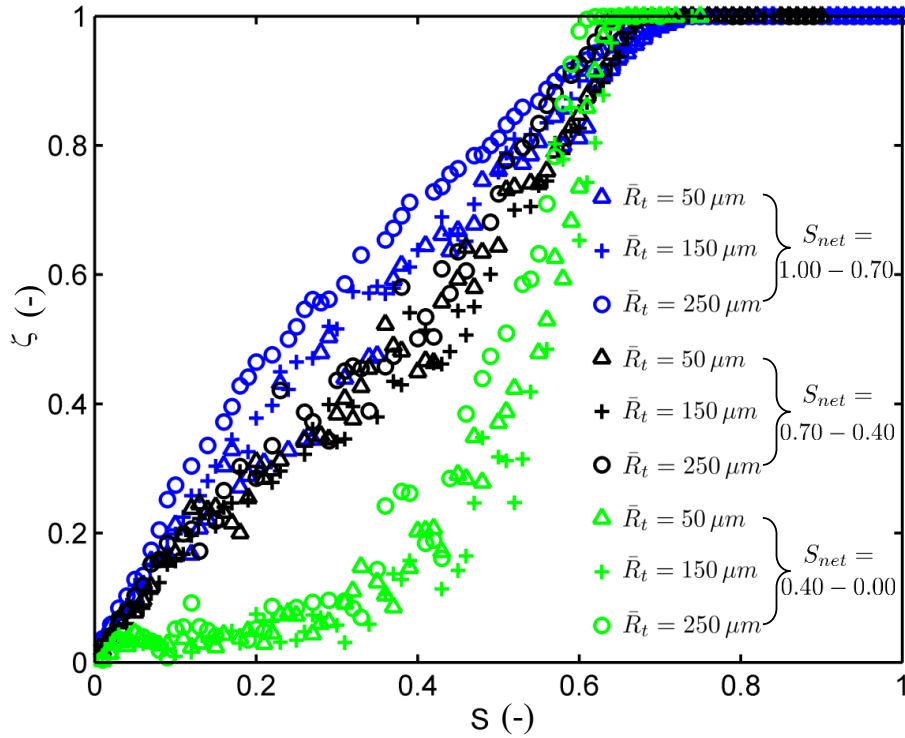


Figure 9.4: The ratio of the liquid flux over the total flux during drying of different pore networks obtained in different intervals of network saturation  $S_{net}$ . The networks had mean throat radii of  $50 \mu\text{m}$ ,  $150 \mu\text{m}$  and  $250 \mu\text{m}$ . The values have been averaged over ten realizations for small intervals of local saturation  $S$ .

## 9.2 Influence of the standard deviation of throat radius

Equation 9.2 indicates that the difference in capillary pressure is affected by the discrepancy between the radii of hydraulically connected pairs of active menisci. Thus, the value of the standard deviation of throat radius is expected to shift the values of  $S_{a_s, max}$  and  $S_T$ . Figure 9.7 shows the moisture transport coefficient profiles from drying simulations of three networks with different values of the standard deviation of throat radius,  $\sigma_{0,t} = 5 \mu\text{m}$ ,  $25 \mu\text{m}$  and  $50 \mu\text{m}$ , but with the same mean throat radius,  $\bar{R}_t = 250 \mu\text{m}$  (Table 9.2). The porosity of the network, on the other hand, is not changed in those three geometry settings. As the porosity remains the same, resistance in those networks can coarsely be considered the same, leading to a similar range in the magnitude of identified moisture transport coefficients (Fig. 9.7). However, the three transport regions mentioned in Chapter 6 are altered. Thus, we explore the profiles of the relative interface area of the liquid phase (Fig. 9.8) and relative liquid flow rate (Fig. 9.9), for better visualization.

$S_{a_s, max}$  is reached when the surface area of the liquid phase is maximum. Figure 9.8b shows that  $S_{a_s, max}$  moves to lower values with increasing standard deviation of radii. This

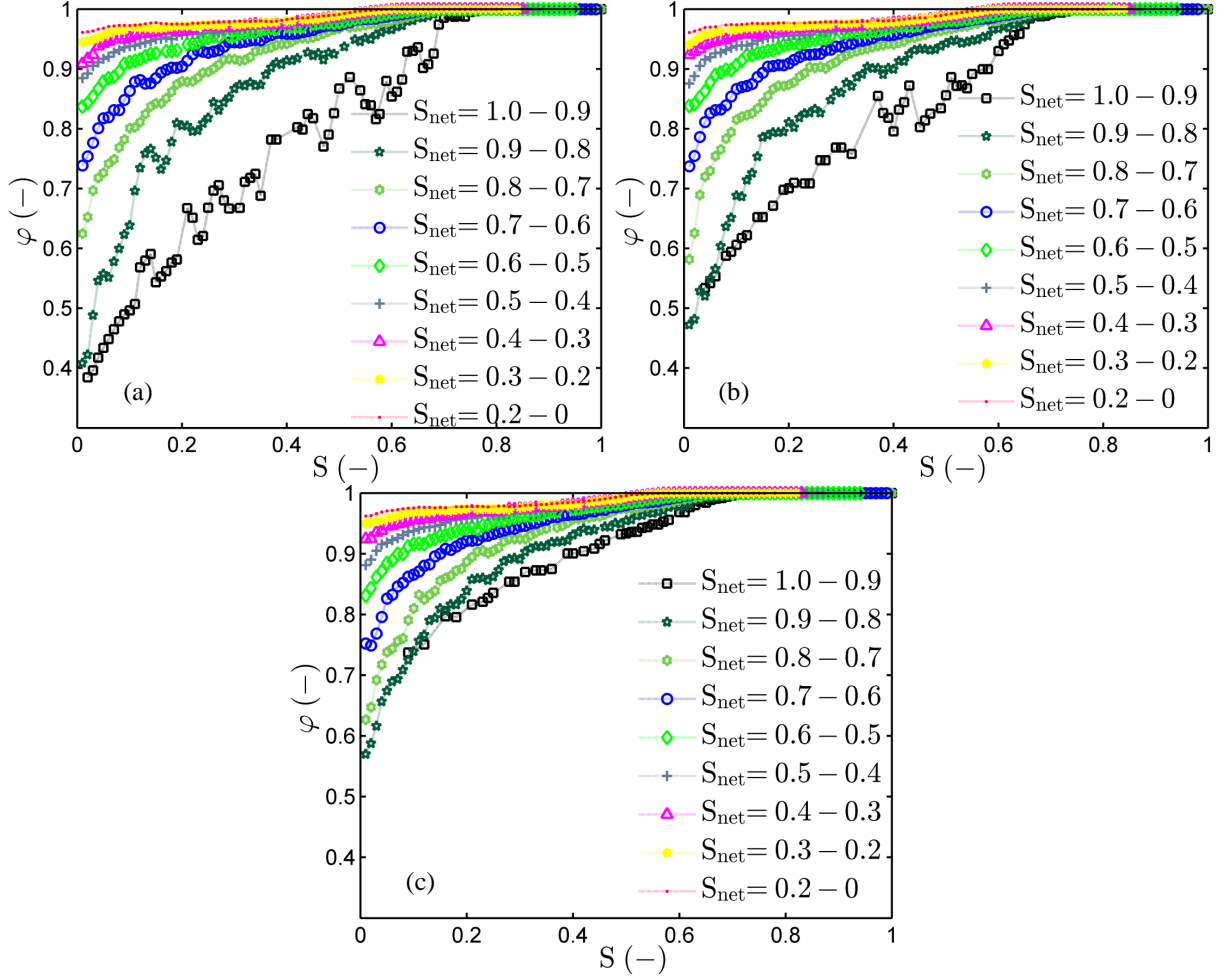


Figure 9.5: Internal NLE functions obtained from PNM drying simulations (ten realizations each) for different mean throat radii of  $50 \mu m$  (a),  $150 \mu m$  (b) and  $250 \mu m$  (c).

means that the liquid transport dominated region is expanded. This is also correlated with Fig. 9.9, which shows that the period with full contribution from the liquid phase is extended in the network with large value of standard deviation. One reason probably is the enhanced driving force by larger discrepancy in the capillary pressure.

Figure 9.9 can also be used to read the alteration of the turning point  $S_T$ , i.e. the saturation when the liquid flow rate over the total flow rate is 0.5. It can be seen that the turning point  $S_T$  also moves to lower saturation with wider throat size distribution. The shifted  $S_T$  means that the vapor transport dominated region becomes smaller. It can be seen from Fig. 9.9 that  $S_T$  is not even reached for the networks with a standard deviation of  $\sigma_{0,t} = 25 \mu m$  and  $50 \mu m$  when  $S_{net} = 1.0 - 0.7$ .

Vapor-dominated moisture transport is related to the relative humidity in the two-phase region (Fig. 9.10). A large slope of the relative humidity is the driving force for high vapor transport. Although the maximum deviation of the vapor pressure from the saturated vapor pressure is similar in all three networks,  $S_{a_{s,max}}$  moves to lower saturation for wider standard deviation (Figs. 9.8 and 9.9), suggesting that the NLE effect first appears for

Table 9.2: Characteristics of pore structures used for drying simulations.

Parameters			
Network size	$25 \times 25 \times 51$	$25 \times 25 \times 51$	$25 \times 25 \times 51$
Boundary layer size	$25 \times 25 \times 10$	$25 \times 25 \times 10$	$25 \times 25 \times 10$
Mean throat radius ( $\mu m$ )	250	250	250
Mean pore radius ( $\mu m$ )	256	283	317
Standard deviation of throat radius ( $\mu m$ )	5	25	50
Center distance between two pores ( $mm$ )	1.0	1.0	1.0
Liquid volume ( $m^3$ )	$1.11 \times 10^{-5}$	$1.10 \times 10^{-5}$	$1.19 \times 10^{-5}$
Network porosity	0.357	0.353	0.358

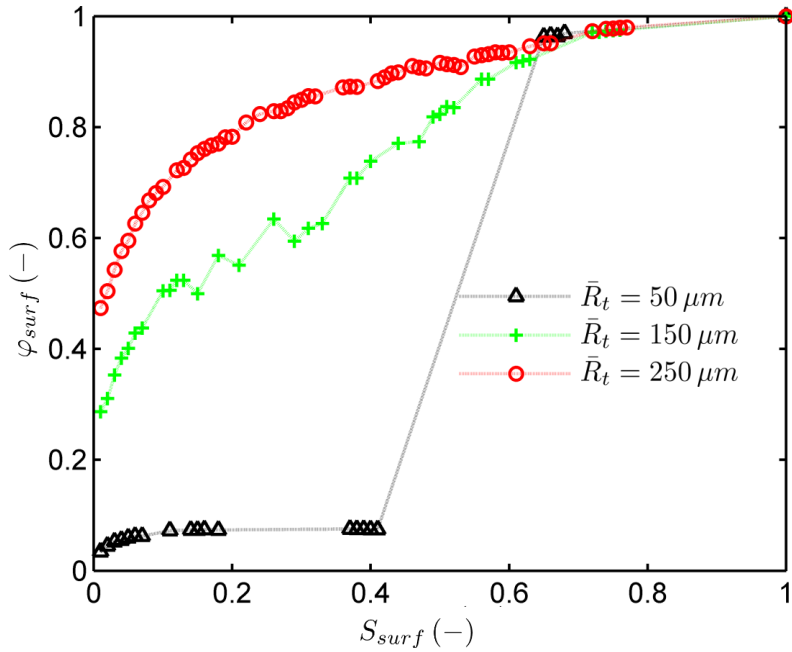


Figure 9.6: Mean value of surface NLE ( $\varphi_{surf}$ ) obtained from PNM drying simulations as a function of surface saturation ( $S_{surf}$ ) for networks with different mean throat radius.

the network with narrower pore size distribution.

Figure 9.10 also shows that the NLE effect in the two-phase region is reduced with decreasing network saturation in all three networks, though with different rate. For example, the minimum value of relative humidity is reached at the very beginning of the drying process ( $S_{net} = 0.9 - 0.8$ ) for the network with  $\sigma_{0,t} = 5 \mu m$ . In contrast, for the network with  $\sigma_{0,t} = 50 \mu m$  this minimum value occurs when the network saturation is in the range of  $0.6 - 0.5$ . Interestingly, the slope of the profiles that give the maximum deviation of the average partial vapor pressure from the saturated vapor pressure, i.e. the strongest NLE effect, demonstrates the largest gradient of vapor pressure in the two-phase region, implying the highest driving force for the vapor transport. This gradient becomes

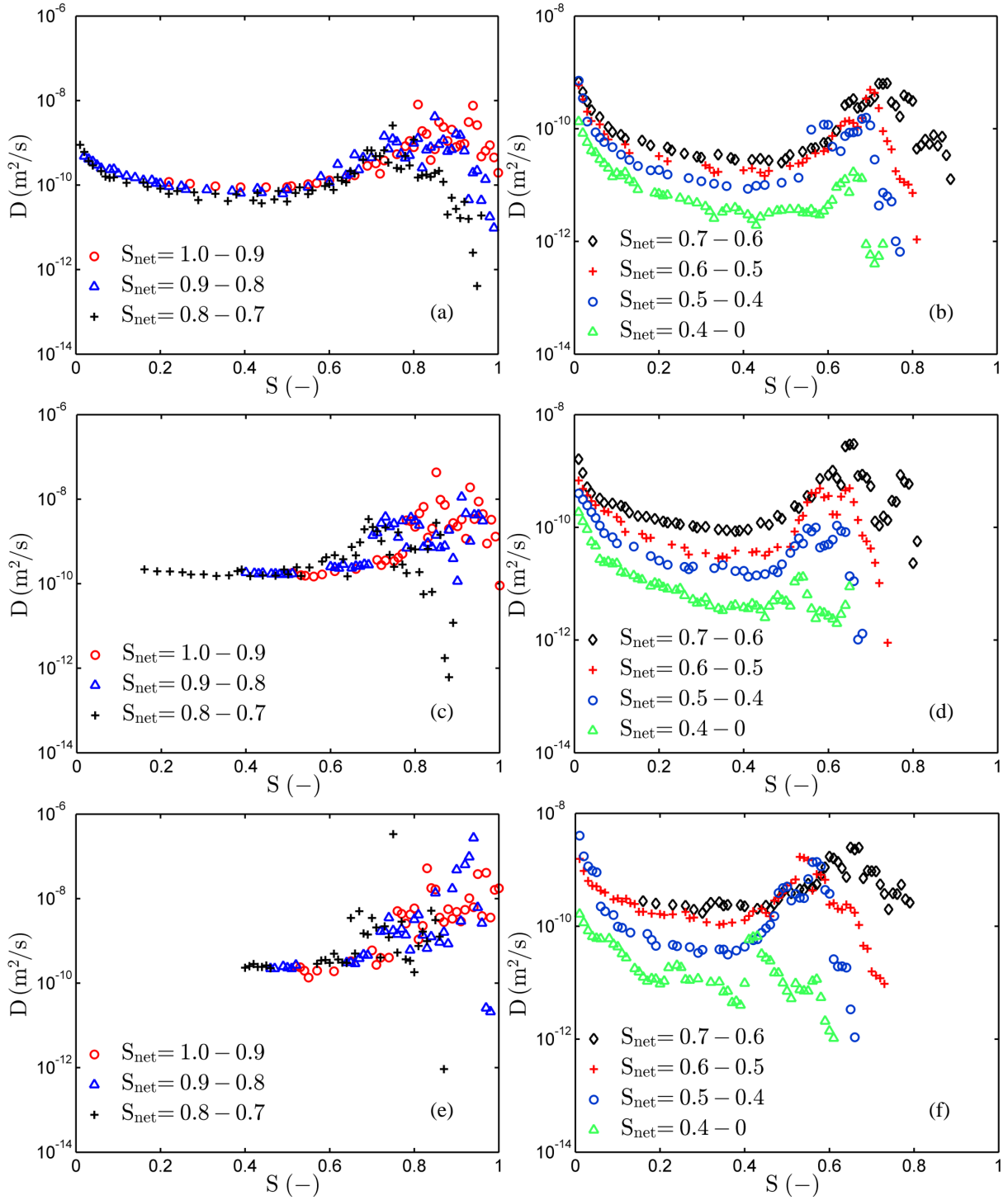


Figure 9.7: Moisture transport coefficient profiles obtained from PNM drying simulations (ten drying simulations each) for different standard deviations of the radii of throats:  $\sigma_{0,t} = 5 \mu\text{m}$  (a, b),  $\sigma_{0,t} = 25 \mu\text{m}$  (c, d) and  $\sigma_{0,t} = 50 \mu\text{m}$  (e, f).

however flatter in the two-phase region during the later stages of the drying process. Vapor transport with the largest gradient lasts longer for the network with the widest distribution of throat radii. This finding indicates that the vapor transport in the two-phase region becomes more important in the networks with wider pore size distribution.

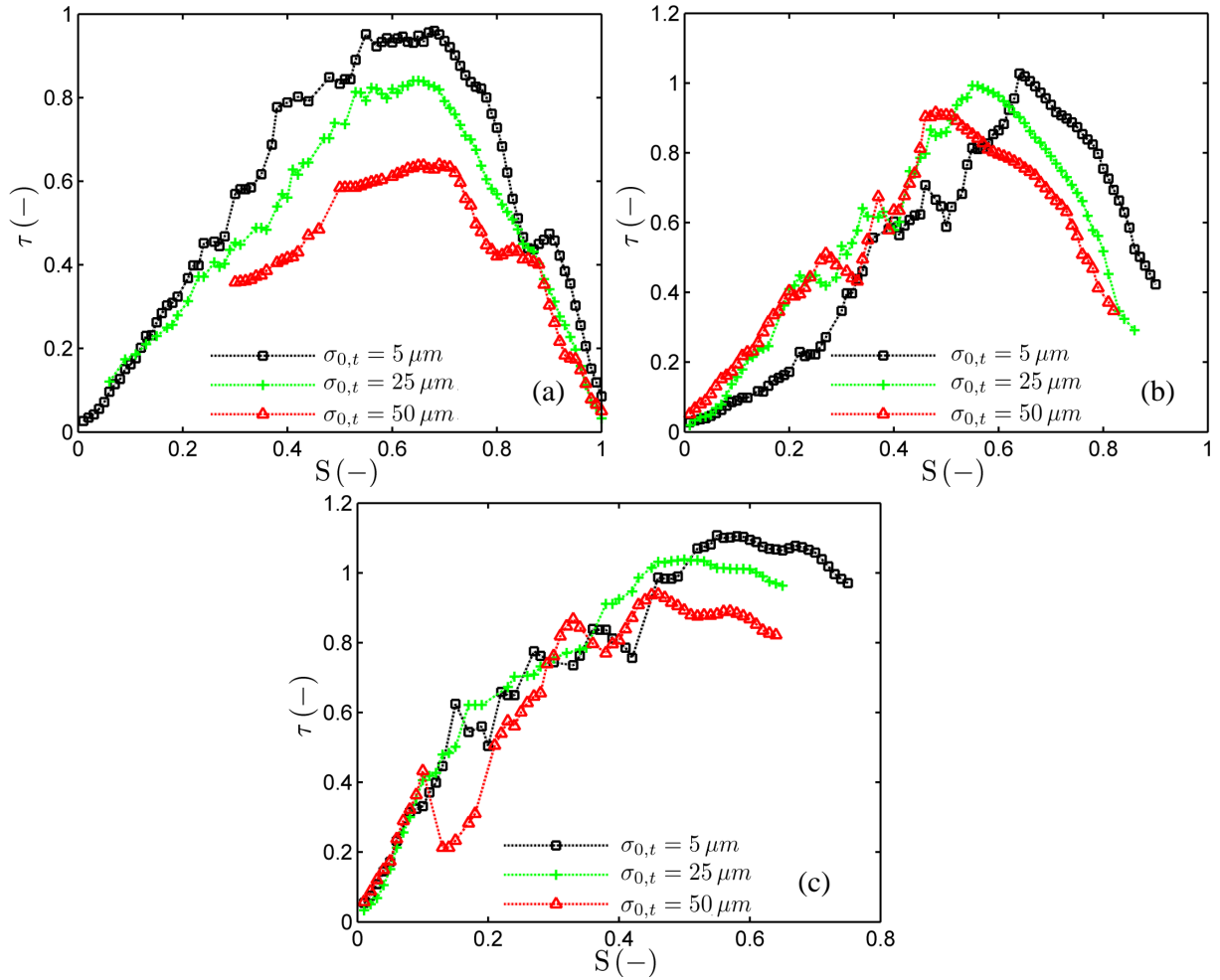


Figure 9.8: Relative interfacial area between liquid and gas as a function of local saturation obtained for networks with different values of standard deviation of throat radii. The three figures represent the drying process when network saturation is between (a) 1 and 0.7, (b) 0.7 and 0.4 and (c) 0.4 and 0. The values have been averaged over ten realizations for small intervals of local saturation  $S$ .

However, the surface NLE does not appear to significantly depend on the standard deviation of radii. The three networks with different values of standard deviation show similar profiles of the relative humidity in Fig. 9.11. A reason for this might be that the overall liquid transport is not influenced by the alteration of the standard deviation. The surface behavior is the result of interactions among many factors, i.e. capillary pressure, liquid viscosity, etc.

### 9.3 Bimodal pore size distribution

A pore structure with bimodal size distribution is generated as follows. Five macro-channels are placed vertically in perpendicular direction to the network surface in each column of the network. There, micro-channels are replaced. Otherwise, micro-channels constitute the throats and pores of the network, similarly as before. Radii of micro-channels (narrow

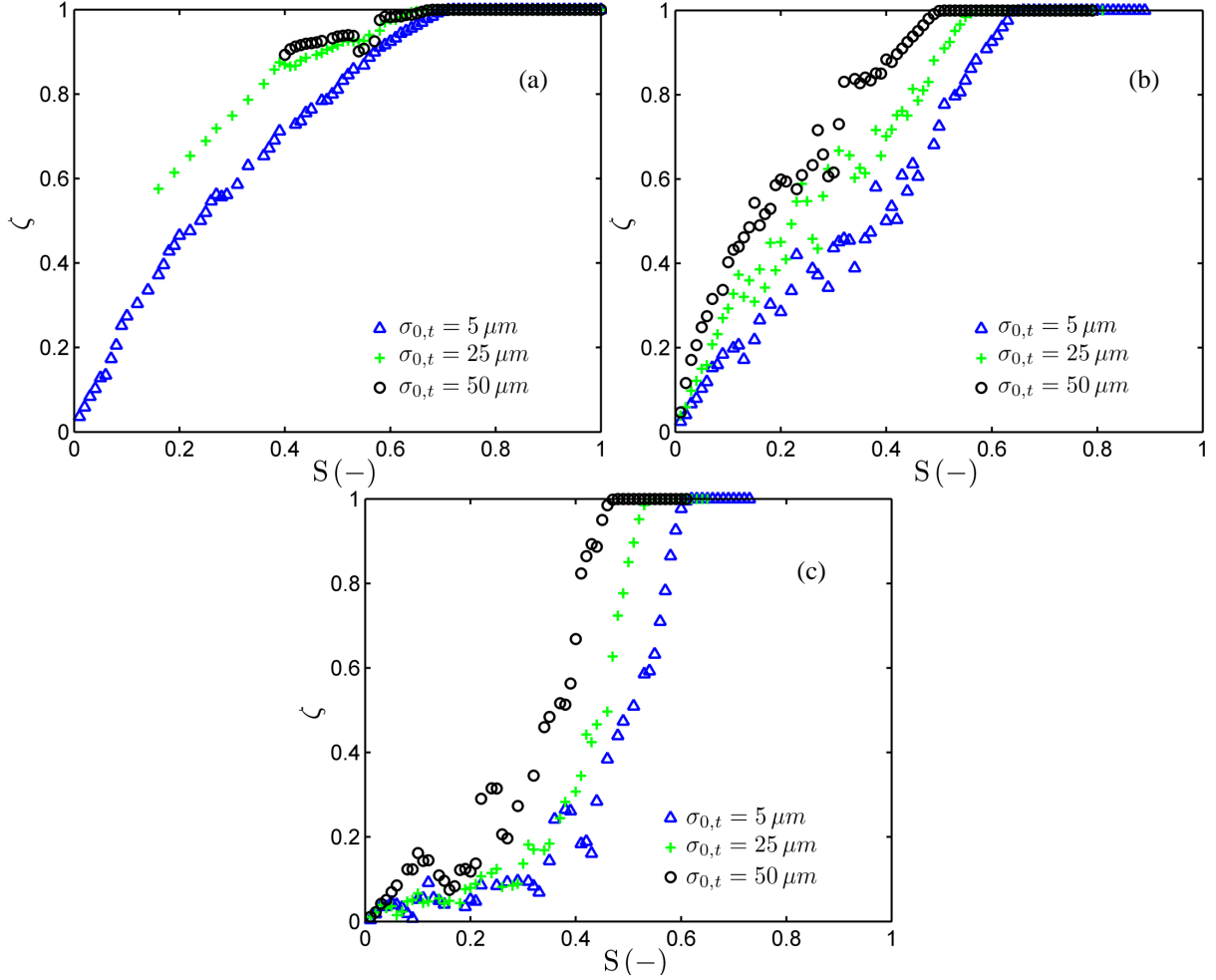


Figure 9.9: The ratio of liquid flux over total flux during drying for networks with different values of standard deviation of radii (values averaged over ten realizations): (a)  $S_{net} = 1.0 - 0.7$ , (b)  $S_{net} = 0.7 - 0.4$  and (c)  $S_{net} = 0.4 - 0$ .

throats and pores) are sampled from a distribution with  $200 \pm 25 \mu\text{m}$  (Table 9.3). For macro-channels (wide throats and pores) a distribution with  $350 \pm 25 \mu\text{m}$  is used. It should be noted that the radius of pore is assumed to be larger than or equal to the radii of neighbor throats. This shifts the values of pore mean radius and standard deviation (Fig. 9.12). Other parameters of the PNM are the same as before. The moisture transport coefficient profiles obtained for the bimodal network are shown in Fig. 9.13.

Table 9.3: Characteristics of pore structures used for drying simulations.

Parameters		
Mean throat radius ( $\mu\text{m}$ )	200	350
Mean pore radius ( $\mu\text{m}$ )	233	361
Standard deviation of throat radius ( $\mu\text{m}$ )	25	25
Center distance between two pores ( $\text{mm}$ )	1.0	1.0

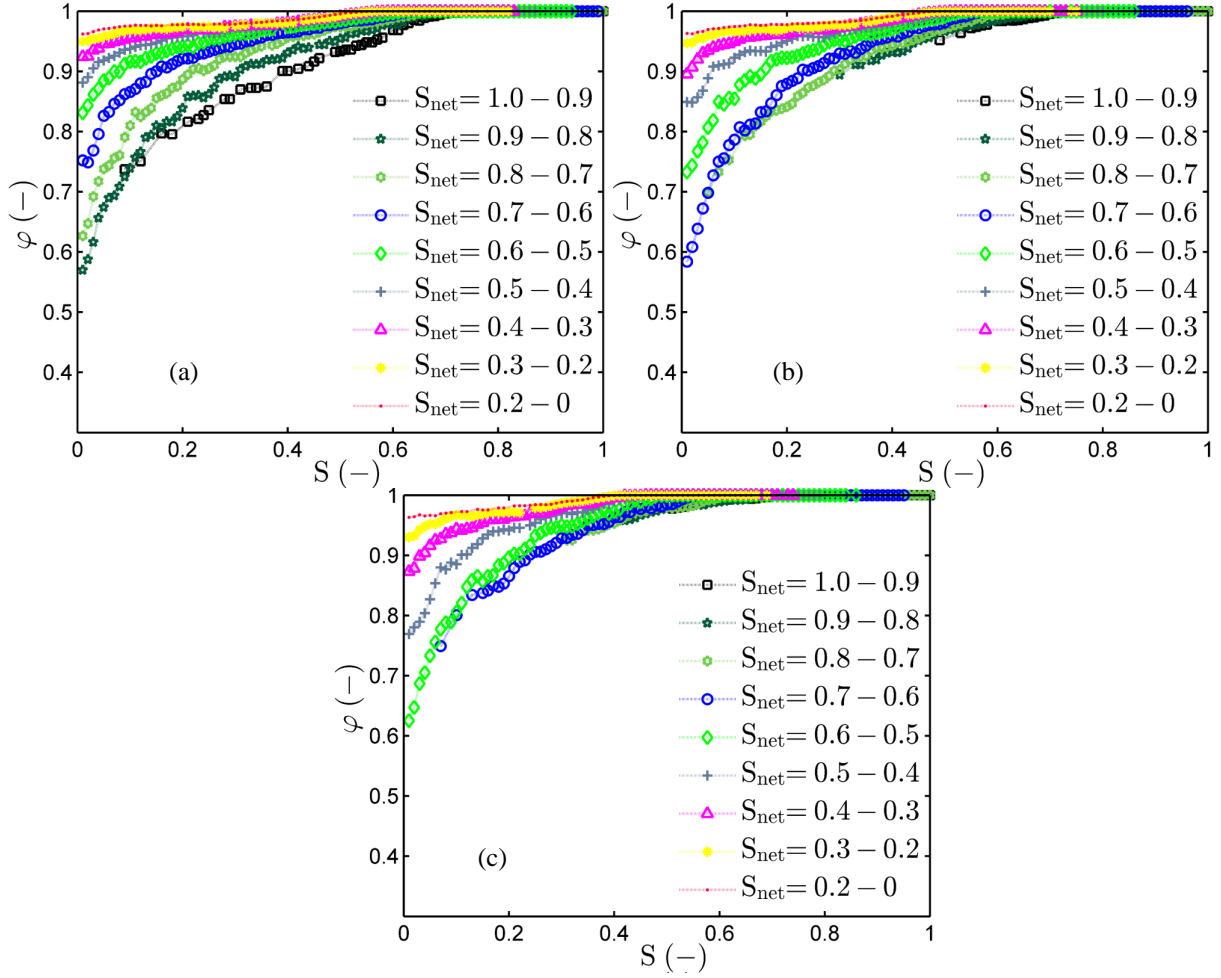


Figure 9.10: Internal NLE functions obtained from PNM drying simulations (ten realizations each) for networks with different standard deviations of throat radii: (a)  $\sigma_{0,t} = 5 \mu\text{m}$ , (b)  $\sigma_{0,t} = 25 \mu\text{m}$  and (c)  $\sigma_{0,t} = 50 \mu\text{m}$ .

Figure 9.13 demonstrates that the LTDR prevails during almost the entire drying process, and the VTDR only appears after network saturations smaller than 0.4. Additionally, relative liquid surface area shows that  $S_{a_s, max}$  is reached when the network saturation is around 0.4 (Fig. 9.14a), as well as  $S_T$  appears after  $S_{net} = 0.4$  (Fig. 9.14b). Such behavior can be explained by the fact that the vertical macro-channels enhance the discrepancy of capillary pressure, which is considered as the major mechanism for liquid transport. The introduced vertical macro-channels control the movement of liquid: The liquid in macro-channels is first drained completely, then followed by draining of the micro-channels (Metzger and Tsotsas, 2008). This type of invasion sustains the liquid transport dominated region over an extended period. Thus,  $S_{a_s, max}$  and  $S_T$  appear very late during the drying process.

The moisture transport coefficient of the bimodal network in the VTDR is similar to profiles for the monomodal networks (Fig. 9.7). It seems that introduced macro-channels play little role in vapor transport. In the receding drying period, phase transition happens

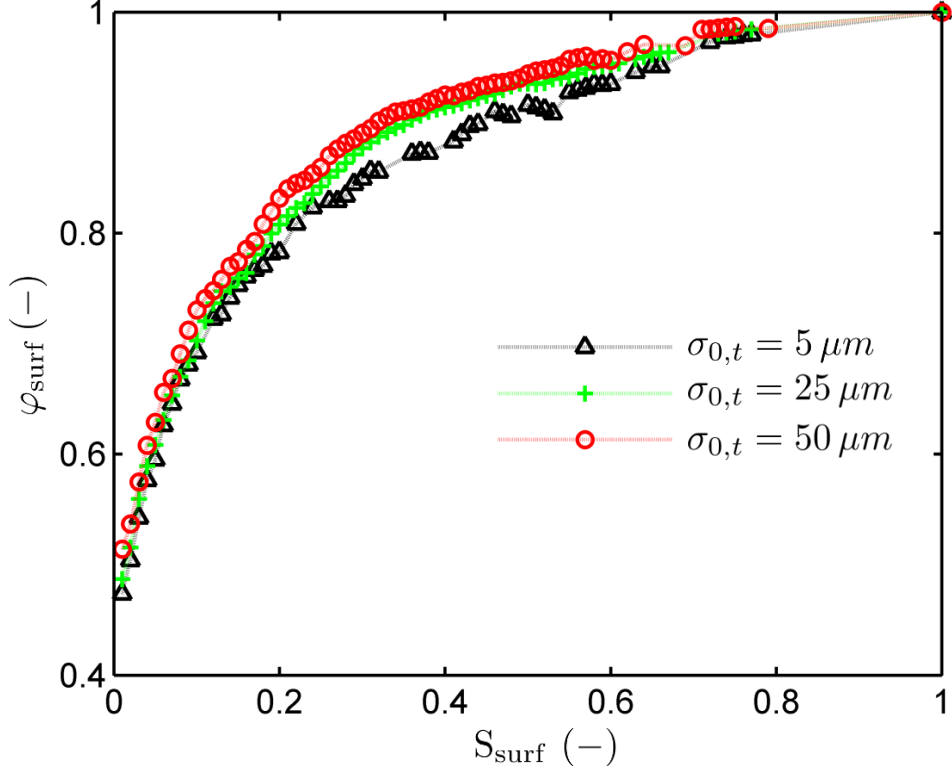


Figure 9.11: Surface NLE functions obtained from PNM drying simulations for networks with different width of the throat radius distribution.

in the micro-channels, which is the same situation as for the monomodal distribution of radii. However, the NLE effect is less pronounced for the bimodal network structure (Fig. 9.15). Corresponding to the above analysis, the NLE effect only appears when the network saturation becomes smaller than 0.6. This means prior to this instant, the vapor pressure in the two-phase region is at saturation pressure.

The surface NLE of the bimodal network is compared with the monomodal network in Fig. 9.16. The monomodal network generated with a mean throat radius of  $\bar{R}_t = 250 \mu\text{m}$  and standard deviation of  $\sigma_{0,t} = 25 \mu\text{m}$  was taken as a reference. The presence of macro-channels does not influence dramatically the surface relative humidity. A similar profile of relative humidity is observed in the case when the local saturation is larger than 0.6. Afterward, the relative humidity of the bimodal network becomes lower than the reference case. A reason might be that the reference case is set with mean throat radius  $\bar{R}_t = 250 \mu\text{m}$ , but the micro-channels of the bimodal network have a mean throat radius of merely  $\bar{R}_t = 200 \mu\text{m}$ . Such behavior is matched with the case of monomodal distributions having different mean throat radius (Fig. 9.6).

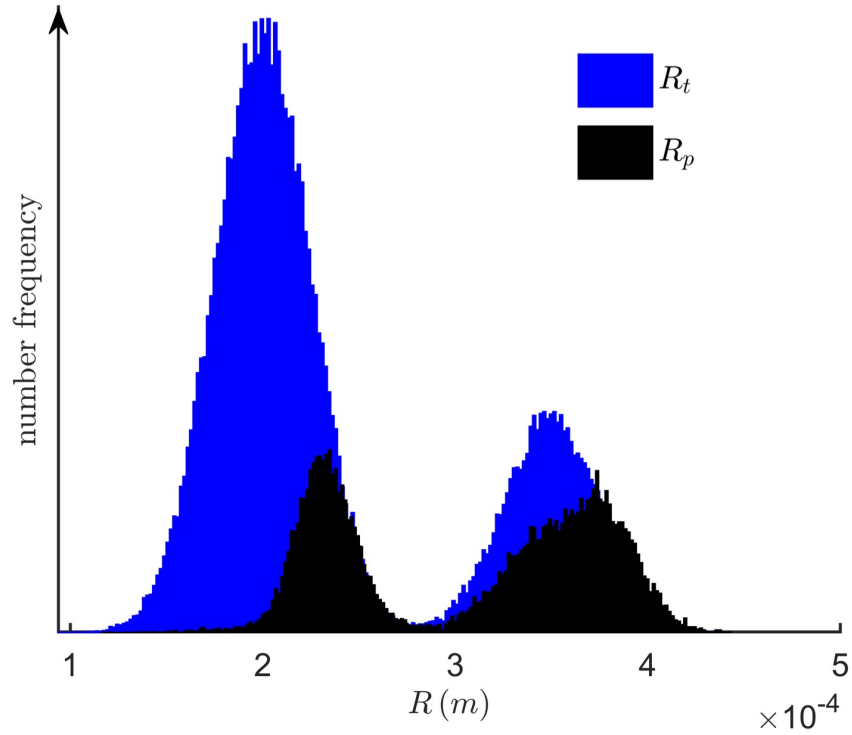


Figure 9.12: Distributions of throat radius (blue) and pore radius (black) from which bimodal networks with macro-channels (wide throats and pores),  $350 \pm 25 \mu\text{m}$ , and micro-channels (narrow throats and pores),  $200 \pm 25 \mu\text{m}$ , have been generated.

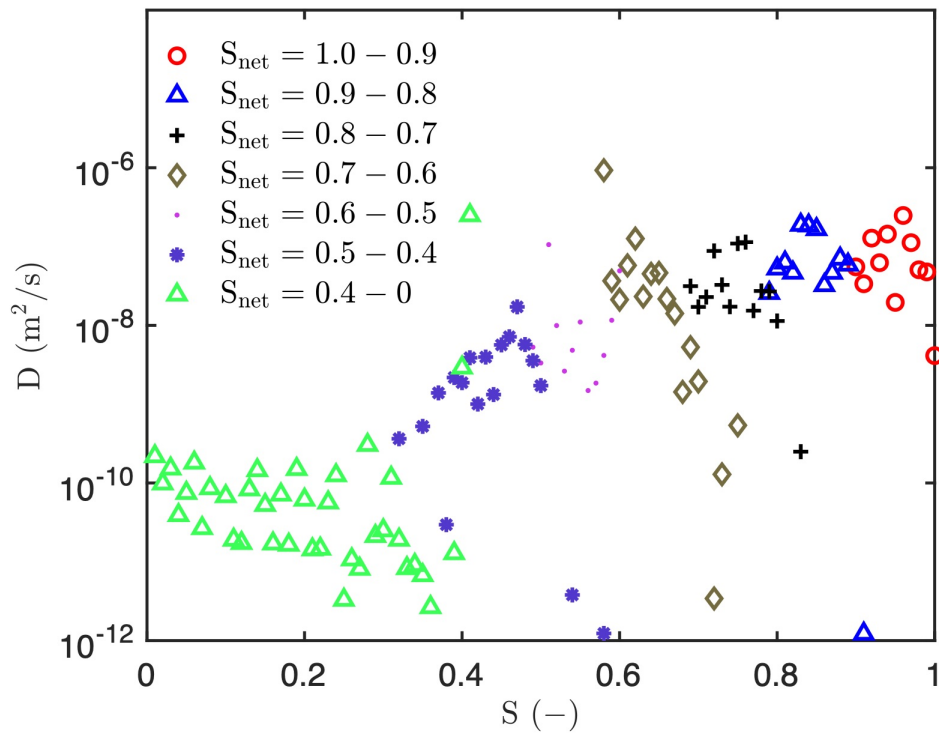


Figure 9.13: Moisture transport coefficient profiles obtained from PNM drying simulations conducted with the bimodal network (ten realizations).

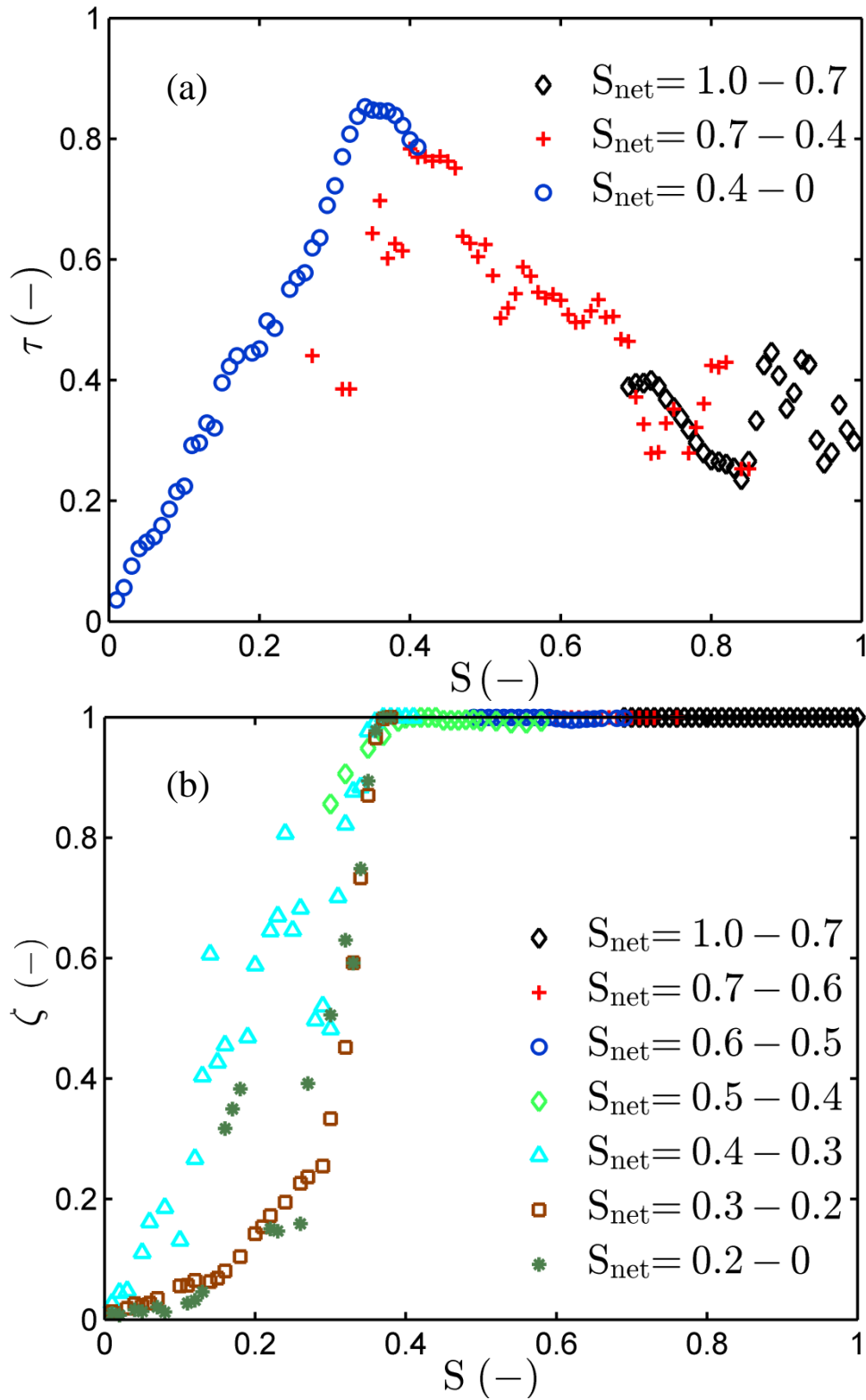


Figure 9.14: Relative interfacial area between liquid and gas (a) and the ratio of liquid flux over total flux during drying (b) obtained from PNM drying simulations with the bimodal PSD (the values are averaged over ten realizations for small intervals of local saturation  $S$ ).

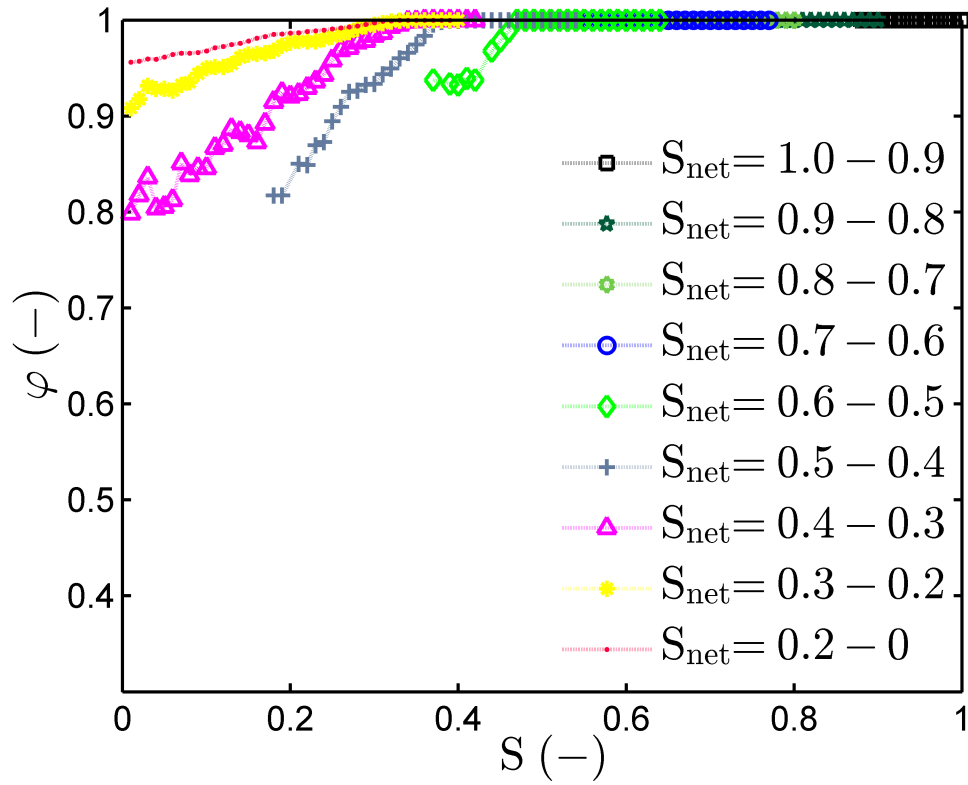


Figure 9.15: The vapor pressure-saturation relationships obtained for pore structures with bimodal network. The values are averaged over ten realizations for local saturation  $S$  intervals.

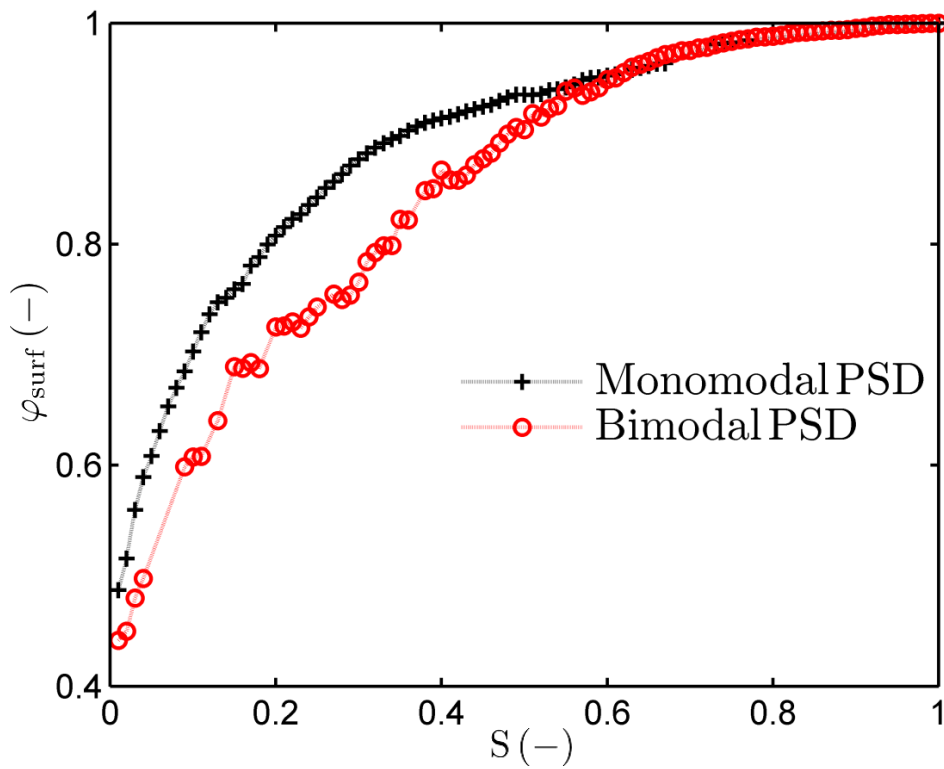


Figure 9.16: Surface NLE of the bimodal network, compared with the reference case of monomodal network ( $\bar{R}_t = 250 \pm 25 \mu\text{m}$ ).

# Chapter 10

## Parameters in the Brooks and Corey capillary pressure model

*Part of this chapter is taken from “Lu, X.; Kharaghani, A.; Adloo, H.; Tsotsas, E. The Brooks and Corey capillary pressure model revisited from pore network simulations of capillarity-controlled invasion percolation process. Processes 2020, 8, 1318”.*

In the previous chapters, liquid viscosity was seen as one of the major factors in liquid transport. Here, however, we return to the more fundamental principle of a capillary-controlled invasion percolation (IP). By applying the throat and pore network model, we examine the macroscopic properties as functions of matrix saturation and network structure. We directly obtain the relationship of capillary pressure with effective saturation from the pore network simulations. The pore network model (PNM) in this chapter is quite different from the algorithm presented in Chapter 2. The present PNM is static. This means the fluid configuration is only dependent on capillary pressure. Based on PNM results, we identify parameters in the Brooks and Corey capillary pressure model (wetting phase residual saturation, entry pressure, size distribution index) and revisit their association with microstructure.

### 10.1 Model description

One major task in this chapter is to generate networks with different pore structure. As geometry parameters we vary the mean throat radius  $\bar{R}_t$ , the mean pore radius  $\bar{R}_p$ , the mean radius of network  $\bar{R}$ , the mean throat length  $\bar{L}_t$ , the standard deviation of network  $\sigma_0$  and the pore connectivity  $Z$ . The network size is  $25 \times 25 \times 25$ . The standard case is constructed on a regular three-dimensional grid of spherical pores connected by cylindrical throats. Next, we describe the IP algorithm. Finally, we present results obtained from IP simulations.

### 10.1.1 Network structure

The radii of throats and pores are sampled from a normal distribution with given mean radius and standard deviation but ensuring that the pore radii are larger than the neighbor throat radii (same as before). This shifts the mean radius of the pores. Two examples are given for radii distributions of throats and pores for networks with  $\bar{R}_t = 250 \mu m$  and  $\sigma_{0,t} = 5 \mu m$  in Fig. 10.1a and  $\bar{R}_t = 250 \mu m$  and  $\sigma_{0,t} = 50 \mu m$  in Fig. 10.1b.

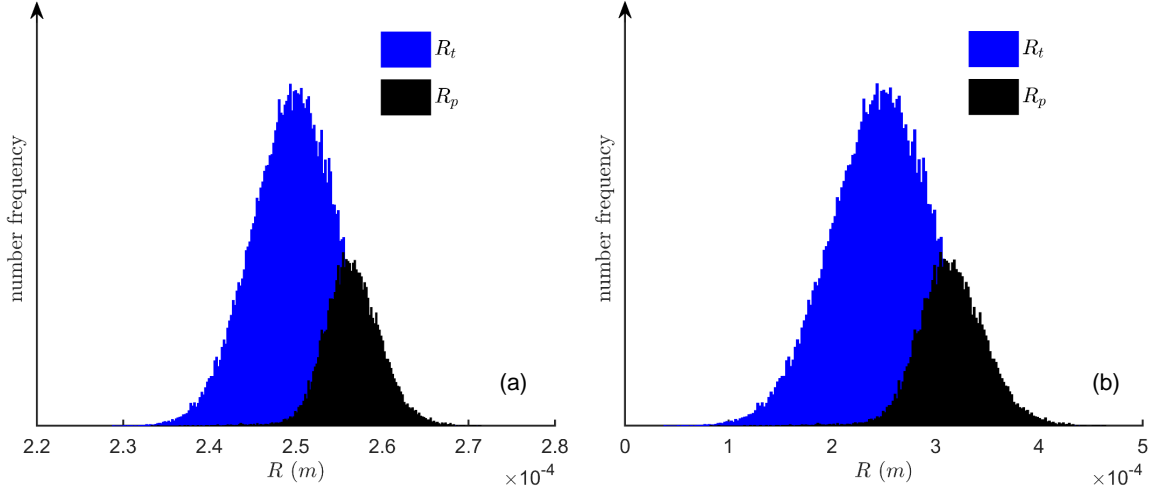


Figure 10.1: Distributions of pore radius and throat radius with mean throat radius  $250 \mu m$  and standard deviation of throat radii  $5 \mu m$  (a) and mean throat radius  $250 \mu m$  and standard deviation of throat radii  $50 \mu m$  (b).

The network geometry parameters,  $\bar{R}_t$ ,  $\bar{R}_p$ ,  $\bar{R}$ ,  $\bar{L}_t$  and  $\sigma_0$ , are determined as follows: The mean throat radius  $\bar{R}_t$  and the mean pore radius  $\bar{R}_p$  are calculated by taking the averages of generated throat radius and pore radius distributions, respectively. The mean radius of the network  $\bar{R}$  is calculated by summing up of all pore radii ( $R_{p,i}$ ) and throat radii ( $R_{t,ij}$ ) in the network then divided to the total numbers of throats ( $N_t$ ) and pores ( $N_p$ ):

$$\bar{R} = \frac{\sum_{i=1}^{N_p} R_{p,i} + \sum_{ij=1}^{N_t} R_{t,ij}}{N_p + N_t}. \quad (10.1)$$

The standard deviation of the network  $\sigma_0$  is calculated as

$$\sigma_0 = \sqrt{\frac{1}{N_t + N_p - 1} \left( \sum_{i=1}^{N_p} (R_{p,i} - \bar{R})^2 + \sum_{ij=1}^{N_t} (R_{t,ij} - \bar{R})^2 \right)}. \quad (10.2)$$

In this chapter, we generate networks with pore structures presented in Tables 10.1, 10.2, 10.3 and 10.4. The center distance between two pores in the network is constant,  $h = 1000 \mu m$ . The throat length is calculated same as before,  $L_{t,ij} = h - R_i - R_j$ . The mean throat

length  $\bar{L}_t$  is determined by averaging over the length of all throats in the network,

$$\bar{L}_t = \frac{\sum_{ij=1}^{N_t} L_{t,ij}}{N_t}. \quad (10.3)$$

The network geometry parameters with connectivity  $Z = 6$  are listed in Table 10.1.

Moreover, we alter the connectivity of the pores in the network,  $Z = 3, 4, 5, 6$  and  $8$ . The networks with connectivity from  $3$  to  $6$  are generated from cubic networks where one pore is connected with  $6$  pores. The standard case is  $Z = 6$ . For example, to change the connectivity of the network from  $6$  to  $3$ , we remove  $3$  throats attached to one pore. Then, we update the data structures for throats and pores (see Chapter 2). Finally, we construct the network with  $Z = 3$ . A similar method is used to construct the networks with  $Z = 4, 5$ . It should be noted that the surface of the network only contains vertical throats (see Chapter 2). To sustain the liquid connectivity in the network, the pores under the network surface must contain vertical throats. However, the network with  $Z = 8$  is built on an octahedral grid, in which one pore connects with  $8$  pores. The center distance between two pores is, again, assumed as  $1000 \mu\text{m}$ . In this network each surface pore is connected with  $4$  throats. The geometry parameters of networks generated with different connectivity are listed in Table 10.2.

Table 10.1: Geometry parameters of the networks generated with connectivity  $Z = 6$ .

	$\bar{R}_t$ ( $\mu\text{m}$ )		$\bar{R}_p$ ( $\mu\text{m}$ )	$\sigma_0$ ( $\mu\text{m}$ )		$\sigma_0/\bar{R}$ ( $\mu\text{m}/\mu\text{m}$ )		$\bar{L}_t$ ( $\mu\text{m}$ )	$\bar{R}_p/\bar{L}_t$ ( $\mu\text{m}/\mu\text{m}$ )
	input	output	output	input	output	input	output	output	output
case 1	10	10	11.3	1	1	1/10	1/10	977	0.01
case 2	10	10	12.6	2	2	2/10	2/10	975	0.01
case 3	10	10	16.7	5	5.2	5/10	5.2/11.8	966	0.02
case 4	10	11.6	23	10	9.1	10/10	9.1/14.6	953	0.02
case 5	100	100	113	10	10	10/100	10/100	773	0.15
case 6	200	200	226	20	22	20/200	22/207	550	0.41
case 7	250	250	256	5	5	5/250	5/251	488	0.52
case 8	250	250	283	25	27	25/250	27/259	432	0.66
case 9	250	250	317	50	55	50/250	55/267	365	0.87

### 10.1.2 Static PNM algorithm

It is assumed that all throats and pores are initially filled with free capillary water. A gas reservoir is located at the top of the network (inlet). At the bottom, the network is connected to a water reservoir (outlet) (Fig. 10.2 as one example). Air invades from the top of the network according to an IP algorithm. Periodic boundary conditions are

Table 10.2: Geometry parameters of networks generated with different connectivity  $Z$  with identical value of mean throat radius,  $\bar{R}_t = 250 \mu m$ .

	$Z$	$\bar{R}_p$	$\sigma_0$		$\sigma_0/\bar{R}$		$\varepsilon$	$\bar{L}_t$	$\bar{R}_p/\bar{L}_t$
	(-)	( $\mu m$ )	( $\mu m$ )		( $\mu m/\mu m$ )		(-)	( $\mu m$ )	( $\mu m/\mu m$ )
	input	output	input	output	input	output	output	output	output
case 10	3	275	25	25	25/250	25/260	0.227	447	0.62
case 11	4	277	25	26	25/250	26/259	0.268	442	0.63
case 12	5	280	25	27	25/250	27/259	0.312	437	0.64
case 13	6	283	25	27	25/250	27/259	0.353	432	0.66
case 14	8	287	25	28	25/250	28/258	0.437	426	0.67

applied to the lateral faces of the network. The effects of gravity and liquid viscosity are neglected. Thus, capillary forces completely control the fluid configurations.

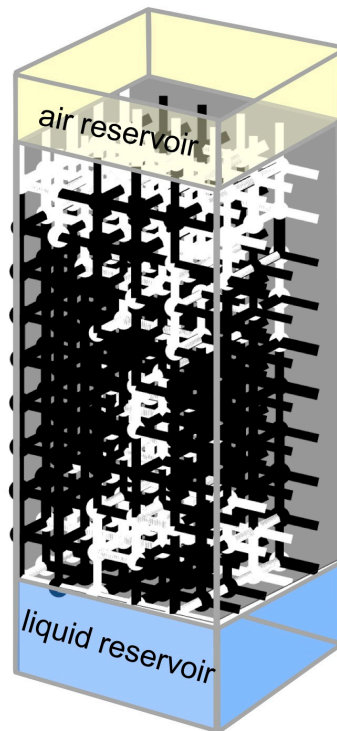


Figure 10.2: Schematic of the pore network used for capillary-controlled IP simulations. The pore network is connected to air reservoir at the top and liquid reservoir at the bottom. Throats/pores filled with liquid are shown in black, whereas gas throats/pores are shown in white.

Network representation by the throat-pore model means that the invasion process happens at menisci throats and pores. Only the invasion process at throats is however considered in the throat-node model, usually assuming perfect wetting condition (contact angle  $\theta$  of  $0^\circ$ ) (Cieplak and Robbins, 1990; Prat, 1993; Metzger et al., 2007a). The liquid transition between pore and throat is neglected. Once a throat meniscus reaches the entrance of a pore, a fully developed meniscus forms in the pore. This is because

Tsakiroglou and Payatakes (1991) illustrated that mercury menisci could reach equilibrium not only at the entrance to a throat but also at the entrance to the pore. Here, we assumed that the pore radius is larger (or equal) than the radii of the neighbor throats, leading to smaller capillary pressure required for the air to invade into the pore.

The capillary-controlled IP algorithm implemented here follows the original invasion percolation procedure proposed by Wilkinson and Willemsen (1983):

1. Initially, all the pores and throats are completely filled with water. Neglecting pressure difference due to liquid head, the liquid pressure in the network and the liquid reservoir are set to zero for simplicity, without affecting the final capillary-pressure relationship. The air pressure necessary for any of the interior throats to be displaced with air is computed. We use Young-Laplace equation to find the pressure difference between air and water necessary for a meniscus to penetrate the throat:

$$P_c = P_g - P_l = \frac{2\sigma\cos\theta}{r}, \quad (10.4)$$

where  $P_c$  is the capillary pressure,  $P_g$  is the gas pressure and  $P_l$  denotes the liquid pressure. Without considering the liquid pressure ( $P_l = 0$ ), the capillary pressure is equal to the gas pressure.

The pores at the interface between the air reservoir and the network do not contain liquid (Fig. 10.2). Thus, the network, initially, has a meniscus in a throat with radius equal to the radius of that throat ( $\theta = 0^\circ$ ). Once a single throat gets unfilled of water, a meniscus pore is formed. The radius of the meniscus in the pore is considered as the radius of this pore due to the assumed pore body shape. Therefore, if a throat is unfilled of water, the adjacent downstream pore is also emptied completely at the same time, creating new menisci at the other throat entrances (filled with water) attached to that pore body. Accordingly, the water phase in the attached throats becomes disintegrated at that pore.

2. For the menisci which have been formed in the previous step, the capillary threshold is calculated by Eq. 10.4. The meniscus throats with the smallest capillary thresholds are detected.
3. The air pressure is increased to the smallest capillary threshold calculated in step 2 (called entry pressure  $P_e$ ) to invade accessible throats with that threshold and create meniscus throats.
4. Once a meniscus pore is invaded, it forms the active capillary thresholds at neighbor throats which still contain liquid. When a meniscus throat is invaded, it forms a new active meniscus pore. Hence, the newly formed menisci (meniscus throats/pores) are identified, along with calculating their capillary threshold pressures.

5. The network saturation is calculated by integrating over all residual liquid volume in the network and dividing it by the total void space volume. The smallest capillary threshold pressure is then assigned to the gas pressure. This is one data point in the capillary pressure-saturation curve.
6. Due to the random radius distribution of throats/pores, the initially backbone liquid cluster may be divided into several liquid clusters (may be isolated from the bottom reservoir). We account for the number of liquid clusters by a variant of the Hoshen-Kopelman algorithm (Metzger et al., 2006). The invasion percolation happens simultaneously in each cluster which is still connected to the liquid reservoir according to step 3. If the invading pressure is greater than the capillary threshold of any of them, they are also invaded.
7. This algorithm is repeated from step 2 to 6 until the clusters get isolated from the liquid reservoir which is connected to the network bottom. This means all the pores at the bottom layer are unfilled of water. The remaining liquid in the network is considered as the irreducible saturation

Monte Carlo method with 40 realizations is used to reduce the uncertainty of the reported parameters.

## 10.2 Wetting phase residual saturation

The wetting phase residual saturation shares the physical characteristics of mercury entrapment, which indicate that the mercury entrapment varies with the width of the pore size distribution as well as with the connectivity of the network (Portsmouth and Gladden, 1991). With this background, we performed IP simulations with different values of the mean radius of the network, with various widths of the pore size distribution as well as different averaged connectivity of pores (Table 10.1). Figure 10.3 shows the wetting phase residual saturation as function of structural characteristics of the pore network undergoing the capillary-controlled invasion percolation (IP) process.

A similar level of  $S_{irr}$  is observed in Fig. 10.3a for the networks with an identical value of  $\sigma_0/\bar{R} = 0.1$  ( $\mu\text{m}$ ) (cases 1 and 5 in Table 10.1). The mean throat radius of the network in case 5,  $\bar{R} = 100 \mu\text{m}$ , is larger than that in case 1,  $\bar{R} = 10 \mu\text{m}$ . This may infer that  $S_{irr}$  is independent of the pore size. By contrast, different morphologies at  $\sigma_0/\bar{R} \approx 0.1$  (cases 1, 5, 6 and 8) show that  $S_{irr}$  decreases with increase in the ratio of  $\bar{R}_p/\bar{L}_t$  (Fig. 10.3a); the ratio  $\bar{R}_p/\bar{L}_t$  indicates the role of spherical pore volume in the capillary invasion process, corresponding to the ratio of the spherical pore volume over the volume of the cylindrical throat:

$$\frac{V_p}{V_t} = \frac{2R_p^3}{3R_t^2L_t} \propto \frac{R_p}{L_t} \quad \text{as} \quad R_p = R_t. \quad (10.5)$$

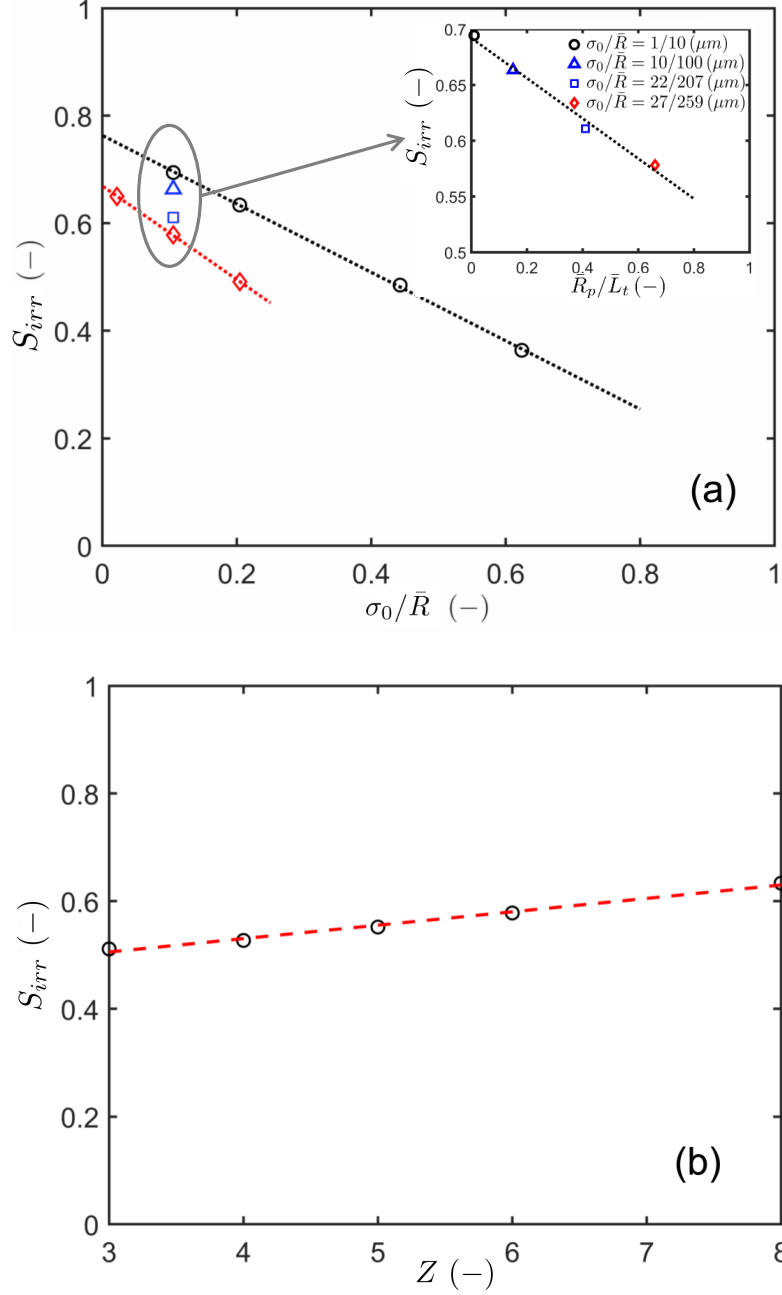


Figure 10.3: (a) Residual saturation as a function of ratio of the standard deviation to the mean radius of the network ( $\sigma_0/\bar{R}$ ). Data denoted by (' $\bullet$ ') have been obtained for the networks with  $\sigma_0/\bar{R} = 1/10$  ( $\mu\text{m}$ ) (case 1),  $2/10$  ( $\mu\text{m}$ ) (case 2),  $5.2/11.8$  ( $\mu\text{m}$ ) (case 3) and  $9.1/14.6$  ( $\mu\text{m}$ ) (case 4). Other data have been recorded ' $\triangle$ ' with  $\sigma_0/\bar{R} = 10/100$  ( $\mu\text{m}$ ) (case 5), ' $\square$ ' with  $\sigma_0/\bar{R} = 22/207$  ( $\mu\text{m}$ ) (case 6) and ' $\diamond$ ' with  $\sigma_0/\bar{R} = 5/251$  ( $\mu\text{m}$ ) (case 7),  $27/259$  ( $\mu\text{m}$ ) (case 8),  $55/267$  ( $\mu\text{m}$ ) (case 9). The center distance between two pores was  $h = 1000$   $\mu\text{m}$ .  $\bar{R}_p$  is the mean radius of pores in the network, and  $\bar{L}_t$  is the mean throat length. The connectivity ( $Z$ ) was 6; Parameters for cases 1 – 9 are listed in Table 10.1. (b) Residual saturation as a function of connectivity (cases 10 – 14 in Table 10.2). The simulation values are averaged over 40 realizations.

Figure 10.3 shows that  $S_{irr}$  decreases with increasing  $\sigma_0/\bar{R}$ . This result is contradictory with the results obtained by Portsmouth and Gladden (1991), who reported that mercury entrapment increases when expanding the standard deviation of network. One should keep in mind that  $S_{irr}$  in the current work corresponds to that of a drying process that takes place under capillary-controlled IP. When gas invades the network, the liquid phase splits up into several regions with different sizes, the so-called liquid clusters that consist of at least one nonempty throat connected to one nonempty pore, or even forms single liquid throats/pores surrounded by air, namely single menisci. The isolated clusters and single menisci, which are separated from the bottom reservoir, cannot be drained to the bottom reservoir by invasion percolation. The remaining liquid in these isolated clusters and single menisci could be removed by evaporation when a vapor pressure gradient is present in the porous medium. However, in the capillary-controlled period of drying, the porous medium is all saturated with vapor, which leads to the liquid in isolated clusters and single menisci being trapped in the porous medium. Thus, the isolated menisci clusters and single menisci are not of interest in current work.

Figure 10.4 depicts the volume distributions of liquid-filled throats and pores in a network at the initial stage ( $S = 1$ ) and at the final stage ( $S = S_{irr}$ ) with different  $\bar{R}_p/\bar{L}_t$ . At  $\bar{R}_p/\bar{L}_t = 0.01$ , the pores contain a very small amount of liquid that can be neglected when compared with liquid stored in the throats (Fig. 10.4a). The spherical pore volume contribution increases with increasing pore radius (from Fig. 10.4a to 10.4d). By comparing the liquid-filled volumes before and after the invasion, the fraction of invaded pores is seen to be larger than that of invaded throats. This could demonstrate that the pores play a significant role when they store a large fraction of liquid volume in the porous medium. The effect of throat length has been reported by Sok et al. (2002) based on stochastically generated networks with coordination number  $Z = 4$  specified from Fontainebleau sandstone sample, showing that increasing the throat length leads to a contrary effect on the residual saturation.

Comparing the liquid before and after invasion in Fig. 10.4, it can be seen that the majority of remaining liquid is trapped in throats with radii smaller than the mean radius. The mercury extrusion algorithm is different from the IP algorithm that can partially describe the drying process since the trapped mercury could be reshaped by refilling the neighboring throats/pores, meeting the demands of the Laplace/Washburn equation (Portsmouth and Gladden, 1991). Trapped mercury in the porous medium could express the shielding effect, being surrounded by the smallest throats in the network. The pore radius is assumed larger than the radius of neighbor throats, so that the pore could be trapped by the smaller throats. Therefore, the probability of mercury entrapment is enhanced by expanding the size distribution. This might explain why values of  $S_{irr}$  simulated for the capillary-controlled IP are contradictory with observations on the mercury entrapment from porosimetry. Regarding drying, Lai et al. (2018) tested the irreducible

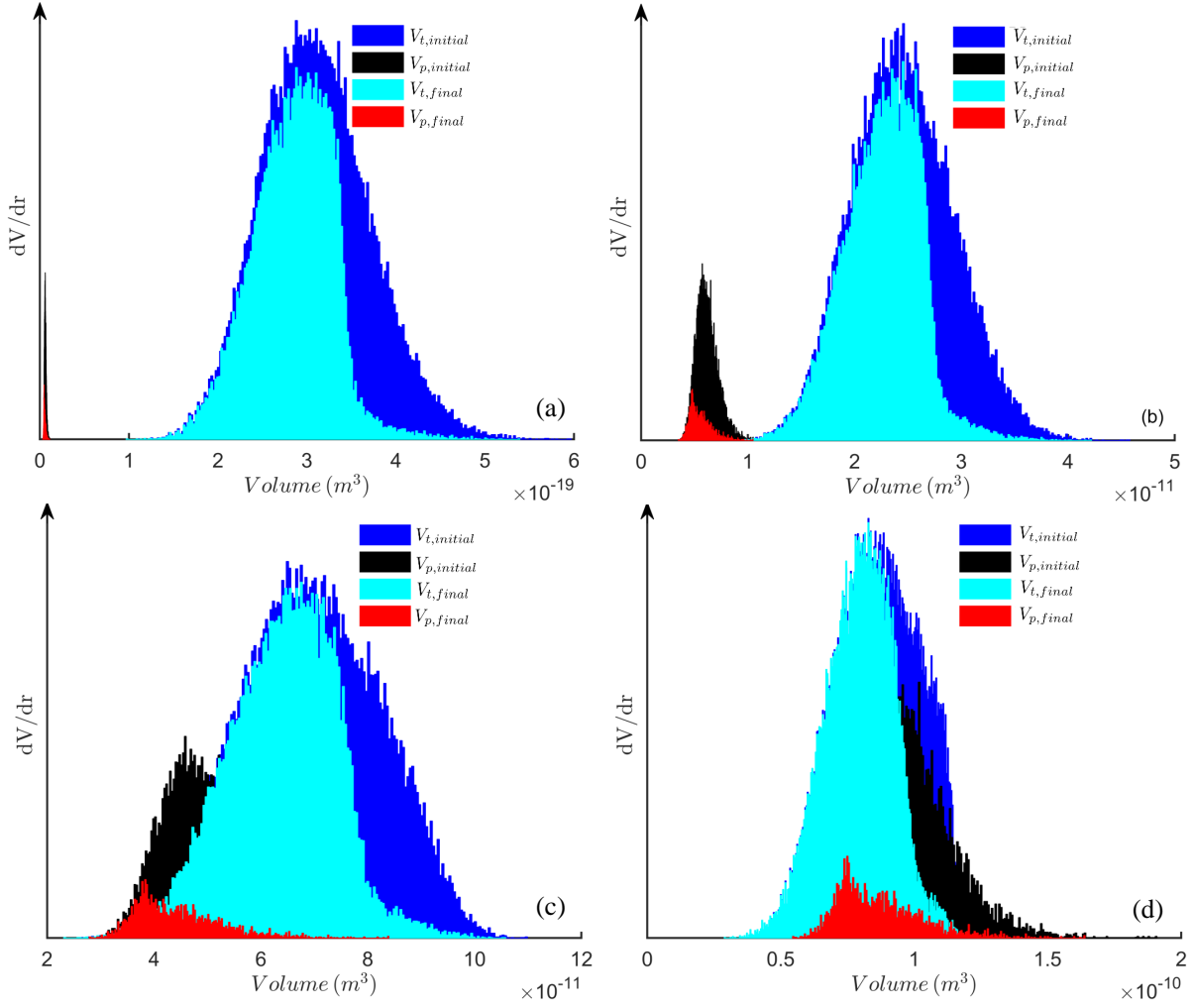


Figure 10.4: The volume distribution of liquid-filled throats and pores in the network at the beginning of the capillary-controlled IP process and at  $S_{irr}$  for a single simulation: (a) case 1, (b) case 5, (c) case 6, (d) case 8 in Table 10.1. The network connectivity is 6.

saturation for six rock samples, showing that it decreases with increasing spread of size distribution. Their observation validates indirectly our pore network simulations.

The wetting phase residual saturation shows a positive linear correlation with the averaged pore connectivity in the network (Fig. 10.3b). The pore connectivity affects the porosity of the network, as the porosity increases when plugging more throats onto a pore, which means that the void space increases during this procedure (Table 10.2). Thus, normalized wetting phase residual saturation is proposed as the ratio of the wetting phase residual saturation on the unity of the porous porosity ( $S_{irr}/\varepsilon$ ) and its correlation with connectivity is shown in Fig 10.5. Figure 10.5 shows that the normalized wetting phase residual saturation decreases with connectivity, which agrees with experimental observations by Ojha et al. (2018). Increasing pore connectivity provides more pathways for the liquid to be expelled from the network. With increased pore connectivity, more throat menisci are formed in the network once one liquid pore has completely been invaded.

As a result, it enhances the IP in that more throat menisci provide more options for air invasion. Such observations can be supported by the percolation theory (see, e.g., Hunt, 2005; Stauffer and Aharony, 2018).

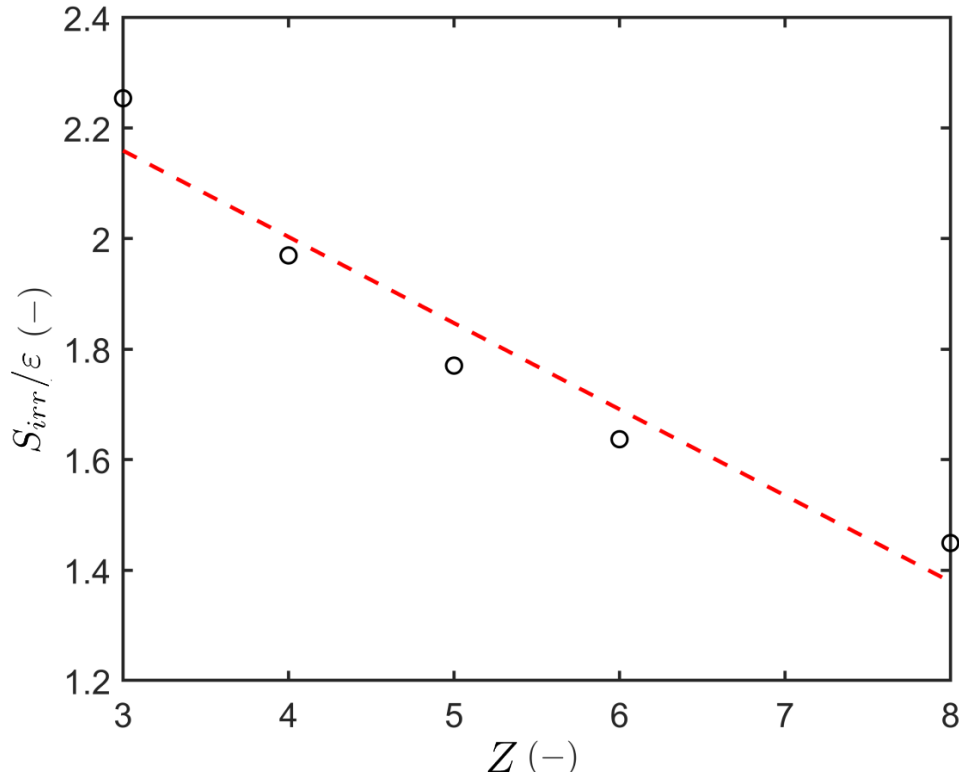


Figure 10.5: The function  $S_{irr}/\varepsilon$  against pore connectivity according to the case 10 to case 14 in Table 10.2. Simulated values have been averaged over 40 realizations.

The residual saturation reported in the current work might be questioned for higher values than those reported by Sok et al. (2002). This discrepancy can partly be due to the fact that the present work does not account for the film effect. In fact, liquid films play a crucial role in the wetting phase residual saturation, because they reduce the resistance for liquid transport and thereby enhance the liquid hydraulic connectivity (Prat, 2002). Another reason might be that the spread of size distributions in the present network simulations is smaller than in real porous media. Sok et al. (2002) reported a pore volume range from  $1 \times 10^{-5} \text{ mm}^3$  to  $1 \times 10^{-2} \text{ mm}^3$  based on the structure of Fontainebleau sandstone. The enlarged  $\sigma_0/\bar{R}$  of network radii could decrease the irreducible saturation (see Fig. 10.3a).

### 10.3 Entry pressure

Figure 10.6 shows the relation of entry pressure  $P_e$  and mean capillary pressure  $P_{c,mean}$  with the porous medium properties. The entry pressure is computed using the algorithm described in Sec. 10.1. The mean capillary pressure is calculated by the Young-Laplace

equation (Eq. 1.3) with the mean radius of network,  $\bar{R}$ . Here, the mean capillary pressure  $P_{c,mean}$  is a reference capillary pressure.

The networks in Fig. 10.6a are generated for a constant standard deviation of the network ( $\sigma_0 = 5 \mu m$ ) and six different mean values of the network (Table 10.3). As can be seen,  $P_e$  is close to  $P_{c,mean}$  when the ratio  $1/\bar{R}$  is small. A small value of  $\sigma_0/\bar{R}$  means that the standard deviation has a weak impact on the radius distribution so that the network can be viewed as morphologically uniform. Figure 10.6b clearly indicates that the entry pressure decreases with increasing the standard deviation (for geometry parameters see Table 10.4). Networks with a wider distribution are easier to be invaded by the air since the probability of having a larger meniscus at the interface is higher. Figure 10.6c shows that the entry pressure is not related to the connectivity for network coordination numbers smaller than 6 (geometry parameters are given in Table 10.2). The entry pressure increases with connectivity slightly up to  $Z = 6$ , but decreases drastically at  $Z = 8$ . As presented earlier in this chapter, the network structure is completely altered from cubic ( $Z = 3$  to 6) to octahedral ( $Z = 8$ ). For the cubic based networks ( $Z = 3$  to 6), the vertical surface throats are not altered and surface pores are connected with only one throat. However, three throats are connected with each surface pore for the octahedral network. As a result, the air invades more easily into the octahedral network, leading to a lower value of entry pressure. As a final remark in this section one can note that the mean capillary pressure varies linearly with the ratio  $1/\bar{R}$  but it remains almost constant for various values of  $\sigma_0$  and  $Z$ .

Table 10.3: Geometry parameters of the networks generated with  $Z = 6$  and  $\sigma_0 = 5 \mu m$ .

	$\bar{R}_t$ ( $\mu m$ )		$\bar{R}_p$ ( $\mu m$ )	$\sigma_0/\bar{R}$ ( $\mu m/\mu m$ )		$\bar{L}_t$ ( $\mu m$ )	$\bar{R}_p/\bar{L}_t$ ( $\mu m/\mu m$ )
	input	output	output	input	output	output	output
case 15	50	50	57	5/50	5/51	886	0.06
case 16	100	100	107	5/100	5/101	786	0.14
case 17	150	150	156	5/150	5/151	688	0.23
case 18	200	200	207	5/200	5/201	586	0.35
case 19	250	250	256	5/250	5/251	488	0.52
case 20	300	300	307	5/300	5/301	386	0.80

#### 10.4 Capillary pressure-effective saturation

Figures 10.7 and 10.8 show the variations of capillary pressure-effective saturation at various morphologies, obtained from the pore network modeling (Sec. 10.1). The effective saturation ( $S_e$ ) is determined according to Eq. 1.15 using  $S_{irr}$  from Sec. 10.2. Three microstructural parameters of the network are discussed: (1) mean radius of network ( $\bar{R}$ ) (Fig. 10.7), (2) standard deviation of network ( $\sigma_0$ ) (Fig. 10.8), (3) pore connectivity ( $Z$ )

Table 10.4: Geometry parameters of the networks generated with  $Z = 6$  and with  $\bar{R}_t = 250 \mu m$ .

	$\bar{R}_p$	$\sigma_0$		$\sigma_0/\bar{R}$		$\bar{L}_t$	$\bar{R}_p/\bar{L}_t$
	( $\mu m$ )	input	output	input	output	( $\mu m$ )	( $\mu m/\mu m$ )
case 21	256	5	5	5/250	5/251	486	0.35
case 22	270	15	16	15/250	16/255	460	0.59
case 23	283	25	27	25/250	27/259	432	0.66
case 24	297	35	38	35/250	25/262	405	0.73
case 25	310	45	49	45/250	49/266	380	0.82

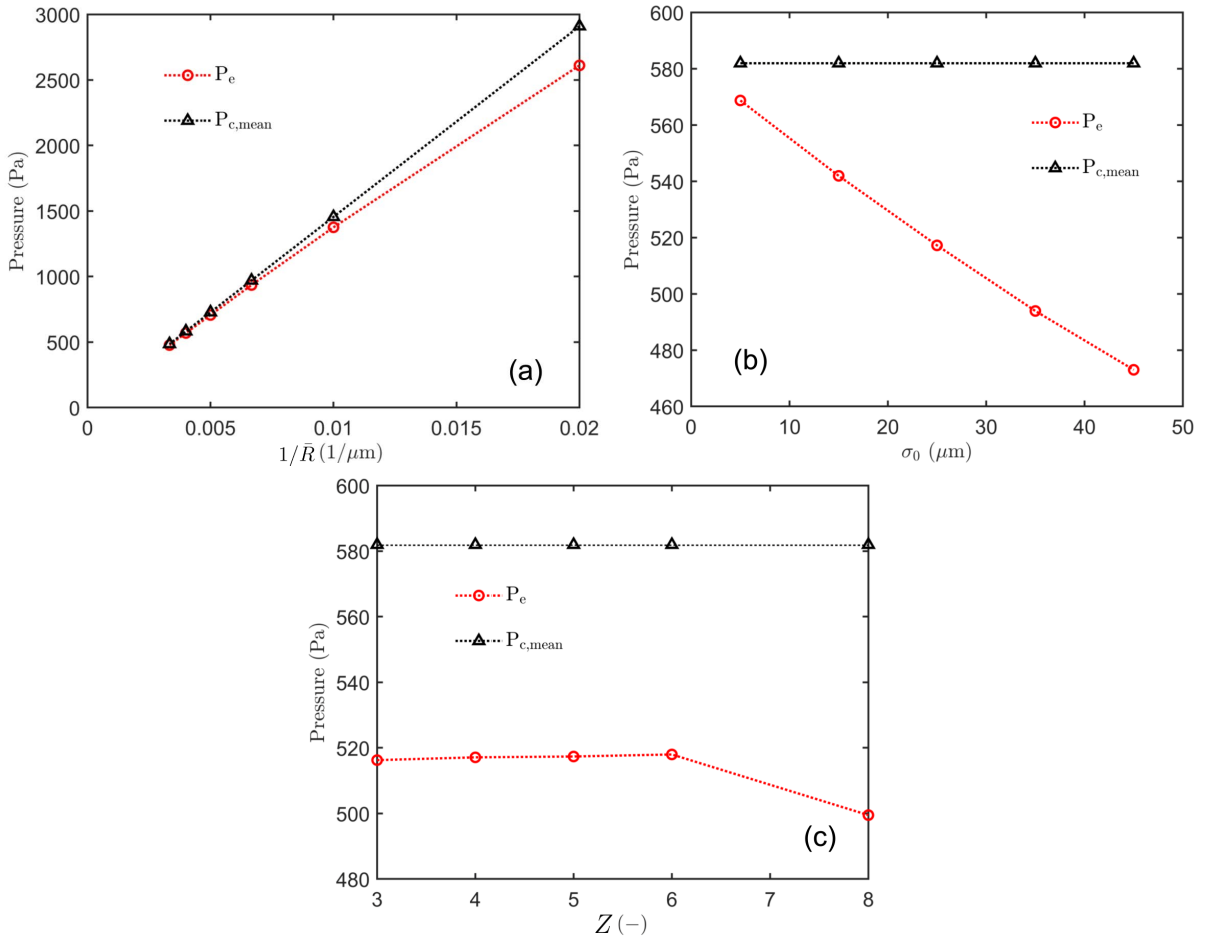


Figure 10.6: Relationship of entry pressure ( $P_e$ ) and mean capillary pressure ( $P_{c,mean}$ ) with specific properties of the porous medium: (a) Influence of mean radius of network ( $\bar{R}$ ) with identical standard deviation ( $5 \mu m$ ) and a connectivity of 6 (case 10 to case 20 in Table 10.3); (b) influence of standard deviation with constant mean radius of network ( $250 \mu m$ ) and a connectivity of 6 (case 21 to case 25 in Table 10.4); (c) influence of connectivity (case 10 to case 14 in Table 10.2). Simulation results have been averaged over 40 realizations.

(Fig. 10.8). They all affect the capillary-saturation profile of a porous medium in the capillary-controlled IP.

As can be seen in Fig. 10.7, the capillary pressure strongly depends on the mean radius of network. With increasing mean radius the value of capillary pressure decreases. This behavior is expected as the capillary pressure is inversely proportional to the mean radius according to the Young-Laplace equation (Eq. 1.3). The overall behavior of the capillary pressure-effective saturation profiles obtained in Fig. 10.7 agrees with the experimental measurements by Hilpert and Miller (2001) and simulation observations by Sweijen et al. (2017).

The role of the two other structural parameters in the behavior of capillary pressure-saturation is presented in Figure 10.8. As shown, the capillary pressure is almost stable against the effective saturation for the network with a narrow pore size distribution (10.8a). This might have the reason that narrow pore size distribution confines the radii in a small range. It can also be seen that the capillary pressure decreases with increasing the standard deviation. Figure 10.8b shows that the entry pressure (the minimum value of  $dP_c/dS_e$  when  $S_e = 1$ ) is almost the same for the networks with connectivity from 3 to 6. The capillary pressure decreases with increasing pore connectivity. The reason is that a pore connected with more throats offers more selections for air invasion, allowing the capillary pressure to decline.

## 10.5 Pore size distribution index

As we could obtain the capillary pressure-saturation profile, the irreducible saturation, and the entry pressure from the pore network simulations, we can evaluate the pore size distribution ( $\lambda$ ) index (for definition of  $\lambda$ , see Chapter 1) by revisiting the Brooks and Corey capillary pressure model (Eq. 1.14).

Figure 10.9 shows that this evaluation results in a nonlinear profile rather than in a specific value. This infers that the pore size distribution index  $\lambda$  depends on the progress of the process (or the effective saturation). Now, it might be questioned whether the profile has a physical meaning. To address this question, first it should be noted that the pore size distribution index  $\lambda$  is a fitting parameter in the Brooks and Corey capillary pressure model. A specific value of this parameter is classically determined by fitting to experimental data of capillary pressure for minimal statistical deviation. Brooks and Corey used this value to express the heterogeneity of a porous medium. However, the primary factor in controlling the capillary pressure is menisci radii distribution. The distribution of the radii of the menisci in throats and pores becomes narrower during, for example, a drying process that follows invasion percolation rules. Additionally, the Brooks and Corey model correlates the capillary pressure with effective saturation. Effective saturation should though be understood as that saturation which is controlled by the capillary pressure. In other words, effective saturation in the current work should only

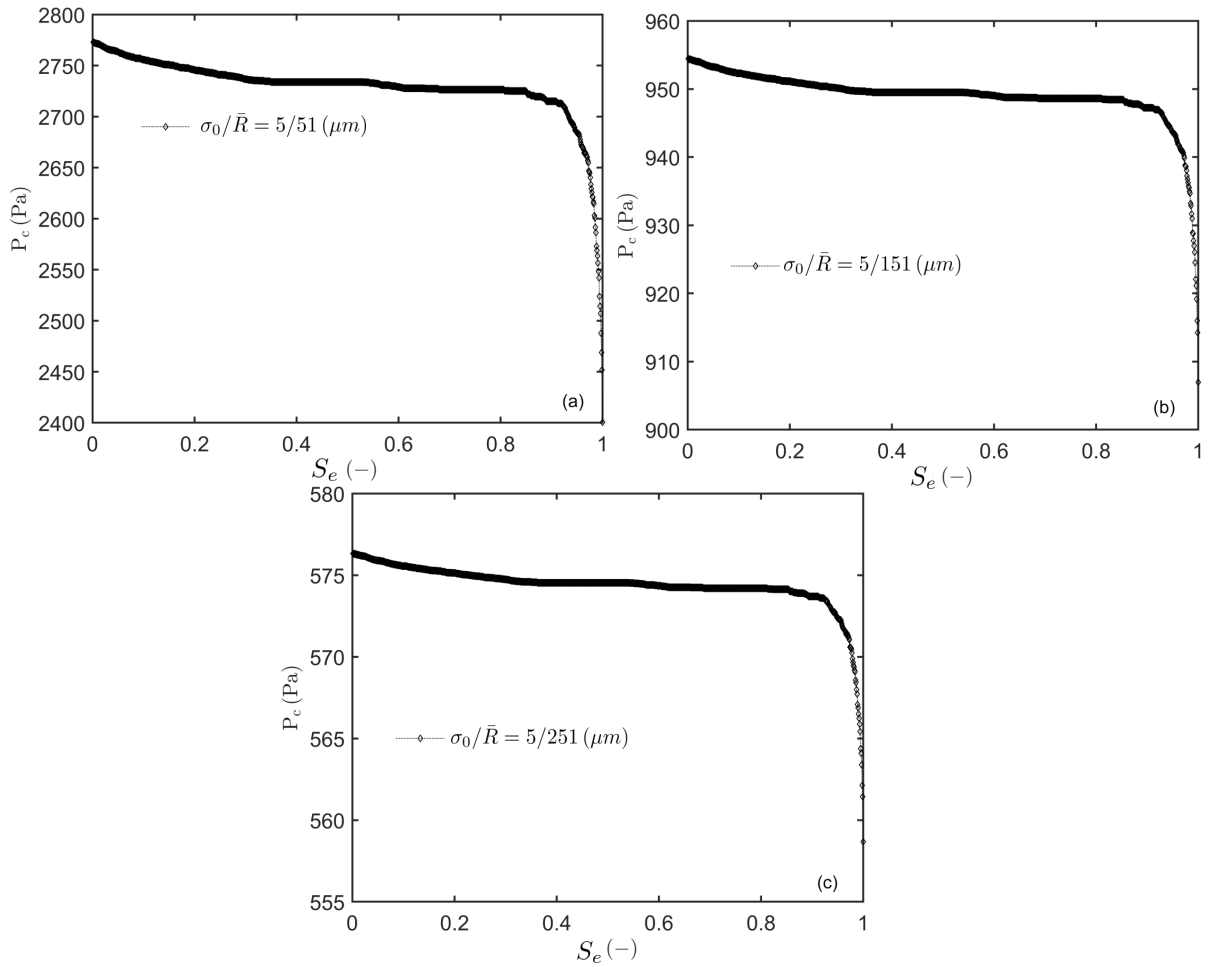


Figure 10.7: Influence of the mean radius of network ( $\bar{R}$ ) on capillary pressure profile  $P_c$  with effective saturation ( $S_e$ ): (a)  $\sigma_0/\bar{R} = 5/51$  ( $\mu\text{m}$ ) (case 15), (b)  $\sigma_0/\bar{R} = 5/151$  ( $\mu\text{m}$ ) (case 17) and (c)  $\sigma_0/\bar{R} = 5/251$  ( $\mu\text{m}$ ) (case 19). The network connectivity is 6. The simulation values are averaged over 40 realizations.

indicate saturation in the major clusters which are connected with the bottom reservoir. The isolated clusters and the single menisci should thus not be included in the Brooks and Corey capillary pressure model. However, the smallest radius among throats and pores tends to be located in isolated clusters and single menisci (Fig. 10.4). This means that the pore size distribution index of the entire network might not be a reasonable quantity for correlating the effective saturation with the capillary pressure.

Since the capillary pressure relies on the radii of menisci which are still active at a certain effective saturation, an index that would represent the distribution of such menisci would be more accurate for the Brooks and Corey capillary pressure model. Figure 10.10 is one example of the spread of the meniscus size distribution (the normalized spread of the meniscus size distribution) during the invasion process. At the initial moment, the standard deviation of menisci equals the standard deviation as assumed for the whole network. The standard deviation of the menisci drops dramatically as the large throats

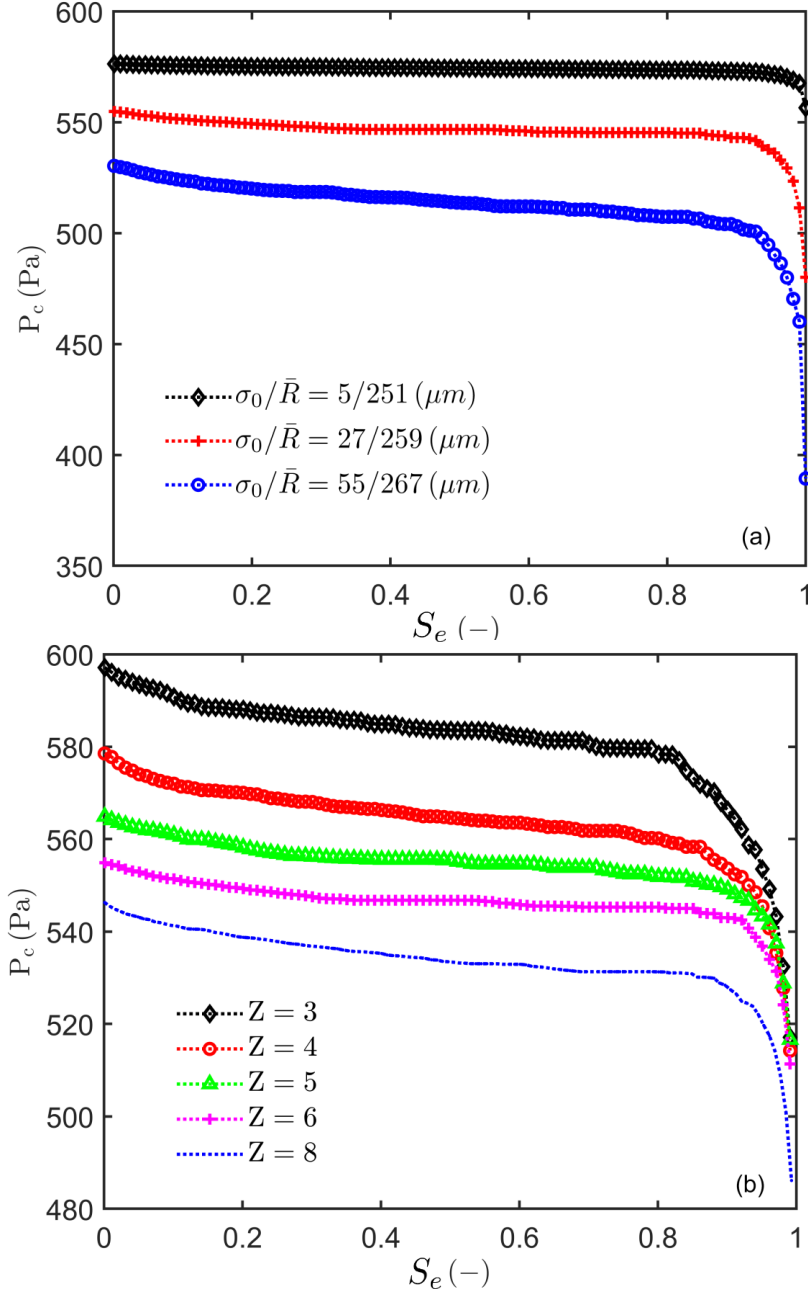


Figure 10.8: The capillary pressure profile  $P_c$  with effective saturation  $S_e$ , influenced by (a) the ratio  $\sigma_0/\bar{R}$  at constant pore connectivity ( $Z = 6$ ) (cases 7, 8 and 9 in Table 10.1) and (b) the pore connectivity (cases 10 to 14 in Table 10.2). The simulation values are averaged over 40 realizations.

are easily invaded, which corresponds to the strong rise of the capillary pressure in the high saturation range ( $S_e \sim 1$ ). Then, the menisci size distribution becomes gradually narrower with decreasing effective saturation along the invasion process. Finally, a sharp decline in the spread of the meniscus size distribution is observed when the effective saturation approaches zero ( $S_e \sim 0$ ). Kewen (2004) found that the pore size distribution index increases with the decline in the fractal dimension (the heterogeneity) of the network. Figure 10.9 shows that the index is close to zero in the high saturation range, where the

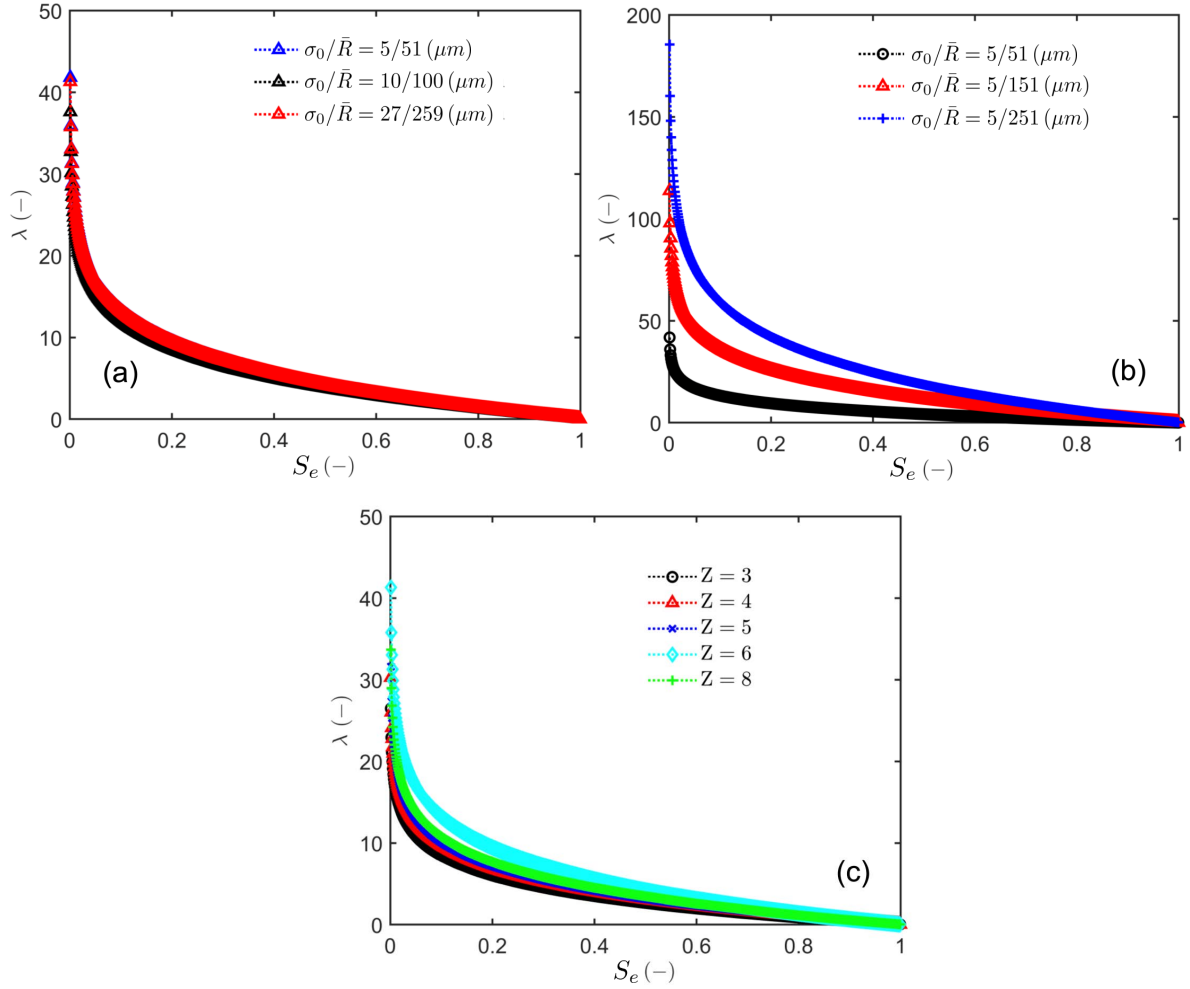


Figure 10.9: The exponent  $\lambda$  related with (a) case 15, case 5 and case 8 & (b) case 15, case 17 and case 19 the ratio of standard deviation over the mean radius of network  $\sigma_0/\bar{R}$  with pore connectivity  $Z = 6$  (see Tables 10.1 and 10.3), and (c) pore connectivity (case 10 to case 14 in Table 10.2). The values are averaged over 40 realizations.

heterogeneity of the menisci is maximum. With ongoing invasion, the distribution of menisci becomes narrower, leading to a decline of the heterogeneity of the menisci. Thus, the index increases slowly during this period. The menisci radii are almost the same when  $S_e \sim 0$ , meaning that the heterogeneity of the menisci is then minimum. Figure 10.9 also demonstrates the index to soar at the lower limit of effective saturation. Therefore, it would be more reasonable to consider the index as a meniscus size distribution index in the Brooks and Corey capillary pressure model.

Figure 10.9 reveals the correlation of the conventionally defined meniscus size distribution index with the structural properties of the porous medium. The meniscus size distribution index is a function of the ratio  $\sigma_0/\bar{R}$  and pore connectivity. Figure 10.9a shows that almost the same profiles are observed for networks with identical  $\sigma_0/\bar{R}$  and the same connectivity. The index  $\lambda$  escalates with the decline of  $\sigma_0/\bar{R}$  (Fig. 10.9b) which also agrees with Kewen

(2004). The index  $\lambda$  is not sensitive upon pore connectivity. It increases when increasing the pore connectivity from  $Z = 3$  to  $Z = 6$ , but drops again for a pore connectivity of 8. This is similar to the behavior of entry pressure shown in Fig. 10.6.

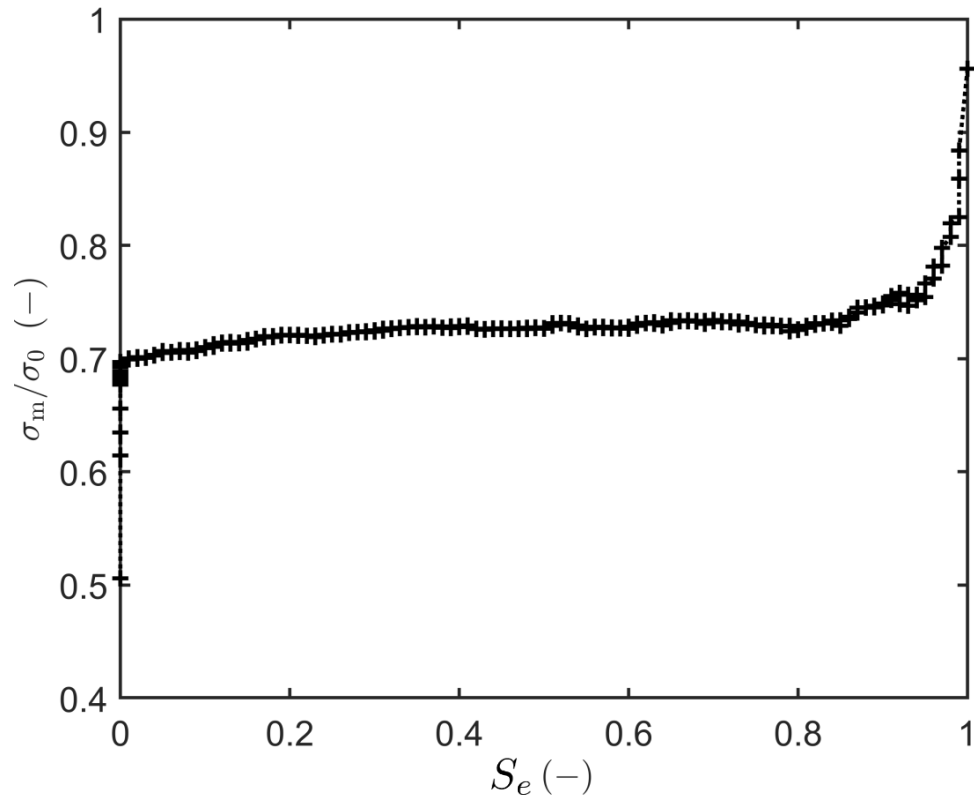


Figure 10.10: The ratio of standard deviation of the distribution of meniscus radii in throats and pores ( $\sigma_m$ ) to the given standard deviation of the network ( $\sigma_0$ ) changes with effective network saturation for case 15.

# Chapter 11

## Summary and Outlook

### 11.1 Summary

This thesis aimed primarily at generating pore scale resolved data for drying porous media by pore network modeling (PNM), and then computing from such data macroscopic parameters that can be fed into continuum models (CMs). Scope and goals of the thesis were presented in Chapter 1, and related to relevant literature.

In Chapter 2, we proposed a representation of the void space by using cylindrical tubes as throats and spherical bodies as pores, called throat-pore model (TPM). This model consists of three main parts: Labeling of throats and pores, generation of throats and pores by assignment of specific radii, and drying algorithm in the capillary-viscous regime.

In contrast to the more classical throat-node model (TNM), the new TPM avoids the overestimation of the void space. Simulations conducted with both geometrical configurations, i.e. TNM and TPM, were compared in Chapter 3. We also compared the vapor conductance of the TPM over the TNM by identifying the relative vapor conductance. The profile of the relative vapor conductance against the ratio of pore radius over throat radius indicates that the volume of spherical pores should not be neglected when increasing the pore radius. A similar procedure was applied to compute the liquid conductance. Comparison of the profiles for relative vapor and liquid conductances shows that the liquid conductance is more sensitive to the alteration of pore radius. Additionally, the drying characteristics of TNM and TPM, i.e. drying kinetics and saturation profiles, were compared. The invasion profile was introduced to compare the drying process of these two network geometries. The similarity of invasion steps in the bottom slices between the two network geometries during the receding front period is contradictory to the obtained differences in simulated saturation profiles. This difference proves that the overestimation of the void space at TNM junctions cannot be neglected and that the TPM is more favorable for pore network simulations of drying porous media.

Chapter 4 focuses on the derivation of the one-equation continuum model (CM). The one-equation CM was derived from mass balances written for the two separated phases (the vapor and liquid phase) and then combined for the total moisture transport. Within

this framework, we proposed two versions of the CM in Chapter 5: The moving boundary condition CM and the three-transport-zone CM that leads to three separate governing equations. The moving boundary condition CM sets the boundary condition alongside with the development of the drying front. In contrast, the three-transport-zone CM includes three sectionally applicable transport equations to reproduce the drying characteristics of capillary porous media. To couple the three transport equations of the model, we introduced flux boundary conditions at the drying front and at the medium surface.

Parameters included in these CMs are evaluated and discussed in Chapter 6. These are the moisture transport coefficient, the relative humidity at the surface and at the drying front, and the vapor transport coefficients. The algorithm for determining parameters from the PNM datasets is in three steps. First, we cut slices virtually from the PNM. One slice comprises all throats and pores in the respective horizontal layer plus half the up and down vertical throats. Then, we calculate the mass flow rate between those slices. Finally, we determine parameters from Fick's law based on flux between slices.

The moisture transport coefficient profiles are divided into three regions by the limits of full and zero saturation and by two critical points. From full saturation ( $S = 1$ ) to the saturation of maximum interfacial area ( $S_{a_s,max}$ ) the liquid transport dominated region (LTDR) is located, in which moisture transport takes place by the liquid phase. From  $S_{a_s,max}$  to  $S_T$  (saturation when  $\zeta = 0.5$ ) is the two-phase transport region (TPTR), in which the moisture transport occurs through the liquid and vapor phases, resisted by liquid clusters and single menisci. From  $S_T$  to the empty slice ( $S = 0$ ) is the vapor transport dominated region (VTDR) where the vapor phase plays a dominant role in moisture transport. When altering the network structure from TNM to TPM, capillary pumping increases, which influences the moisture transport in the LTDR and TPTR. Similar profiles of moisture transport coefficient in the VTDR are observed, but the range of VTDR is narrowed.

Results on the vapor partial pressure to saturation vapor pressure relationship within the network ( $\varphi$ ) showed a non-local equilibrium effect (NLE) that appeared for both network geometries after  $S_{a_s,max}$ . However, the NLE at the surface ( $\varphi_{surf}$ ) appears at the beginning of drying process. This NLE effect is more pronounced in the TPM. The vapor pressure to saturation pressure ratio at the surface ( $\varphi_{surf}$ ) is slightly affected by change in network geometry from TNM to TPM. The interfacial area provides a new aspect to understand liquid structures which indicate capillary pumping (as the driving force for liquid transport) and influence the vapor pressure in the two-phase zone.

The vapor transport parameters in the dry zone and the gas-side boundary layer have been calculated from the pore network model and shown to be nearly constant with relative humidity. The weak dependence of the vapor transport parameters on the relative humidity has been attributed to Stefan flow, which has not been taken into account in the derivation of these model parameters from PNM results. However, the influence of

Stefan flow is small for the investigated case of slow drying. Smaller diffusion coefficient in the porous medium than in the unconfined gas phase (gas-side boundary layer) could be explained reasonably well by obstruction (effect proportional to porosity) and tortuosity.

Effective overall vapor diffusivity has also been derived from pore network results to show that it is equal to the molecular diffusivity of water vapor in the boundary layer. Very small deviations have been observed by evaluating for equimolar diffusion pore network simulations in which the Stefan effect (one-side diffusion) has been considered. It is shown that profiles of the effective overall vapor diffusivity obtained in this way are non-linear with surface saturation but linear with relative humidity.

In Chapter 7, the purpose is to feed the macroscopic parameters into the CM. One should be aware of issues resulting from the fact that the parameter functions are highly associated with the process history and the microstructures. The averaging interval used to obtain macroscopic parameters from the PNM plays a significant role in the performance of the CM. Therefore, averaging should be done only within periods with similar drying behavior. The direct usage of moisture transport coefficients extracted from the PNM shows a better performance of the CM than using the fitting approach to transfer the dataset from the PNM into the CM. In general, inappropriate values of the moisture transport coefficient may not only reduce the accuracy of CM results, but even cause the termination of the CM algorithm.

To solve the issue of the CM being highly sensitive to the moisture transport coefficient, we have introduced a hybrid method to control the performance of the CM by altering this macroscopic parameter locally within a limited range. In this way, a stronger agreement between the continuum and the discrete model is observed in terms of both drying kinetics and saturation profiles. The saturation profiles predicted by the proposed CM using the macroscopic parameters from PNM indicate that the effect of the random pore size distribution, the influence of liquid viscosity, and the edge effect are properly captured. This is hardly possible to achieve by means of classical approaches to the modeling of drying processes.

Chapter 8 focused on the surface of capillary porous media. Surface parameters are determined for the one-equation CM. However, two-equation CMs, which include two mass balances separately for liquid and vapor phases, could be more flexible in representing the drying process. In such models, the boundary condition for the vapor phase balance equation could be treated by equal fluxes at the two sides of the outer surface of the drying medium, since the vapor phase is a continuous phase. Regarding the trickier boundary condition for the liquid phase, we have hypothesized that the ratio of evaporation rate from the wet surface region to the initial evaporation rate can be obtained from either the surface saturation or the surface wetness by multiplication with a quantity that we have called an emendation factor. Emendation factors based on either surface saturation or surface wetness have been evaluated from pore network results and shown to be

process parameters: Higher than unity, dependent on the course of the drying process, and certainly also dependent on the structure of the porous medium, which has though not been varied. Most interestingly, global evaporation rate has been increased in the simulations by reducing the thickness of the gas-side boundary layer and shown to shift both emendation factors towards unity. Especially the emendation factor that has been defined with surface saturation was found to be essentially equal to unity for the faster drying process. This provides a simple and efficient boundary condition to the liquid phase balance of two-equation CMs for practical applications, of an evaporation rate equal to the maximal evaporation rate times surface saturation.

The option of further enhancing this approach by use of a modified version of Schlünder's model has been considered, but was not found to bring real advantages. Quantitative use of Schlünder's model may thus not be recommended either for the whole surface of the drying material or just for the wet part of it, despite of the success of this model in illustrating why partially wet surfaces may nearly reach the evaporation rate of a fully wetted surface.

Since macroscopic parameters could reproduce the drying characteristics of the drying process, in Chapter 9 we discussed the correlation of macroscopic parameters with different pore network structures by means of altering the mean throat radius and the standard deviation of throat radii as well as by placing vertical macro-channels into the grid of micro-channels to create a bimodal network. The two critical saturations in the moisture transport coefficient were discussed for different pore network structures.  $S_{a_s, max}$  and  $S_T$  were not influenced by changing the mean radius of throats, indicating that the three regions in the moisture transport coefficient profile are not altered. Though the values of the moisture transport coefficients decreased when reducing the mean throat radius, they did not change by widening the standard deviation of throats. As a result of variation of the standard deviation of throat size,  $S_{a_s, max}$  and  $S_T$  nevertheless were reduced and thus the LTDR became longer and the VTDR became shorter. In all simulation results, we observe that the moisture transport coefficients are highly associated with the network saturation.

Not only the moisture transport coefficient is impacted by the pore structure, but also the relative humidity at the surface and in the two-phase region is influenced by pore network structure. The relative humidity deviates from unity after the saturation of maximum interface area  $S_{a_s, max}$  has been reached in the two-phase region, but the relative humidity at the surface decreases even at the beginning of the drying process. Decreasing the mean throat radius, lower relative humidity can be observed. The standard deviation of throat radii cannot affect the minimal value of relative humidity but can postpone reaching this minimum.

Additionally, for a bimodal network, we found an extended period of LTDR, suggesting lower values of  $S_{a_s, max}$  and  $S_T$ . However, the moisture transport coefficient of the bimodal

network in VTDR is similar to profiles for the monomodal networks. Moreover, the internal NLE effect is less pronounced for the bimodal structure but the surface NLE effect is not affected by the macro-channels.

In Chapter 10, we explored the influence of the morphology and topology of pore network on the macroscopic parameters (irreducible saturation  $S_{irr}$ , entry pressure  $P_e$ , and the index parameter  $\lambda$ ) of the Brooks and Corey capillary pressure model. For this purpose, pore network simulations were carried out for the limiting case of the capillary-controlled invasion percolation process. This limiting case is relevant in processes such as drainage or slow early-stage drying. According to our pore network simulation results, the irreducible saturation  $S_{irr}$  is not a function of the mean radius of network ( $\bar{R}$ ) but depends on the ratio standard deviation/mean radius of network ( $\sigma_0/\bar{R}$ ), the ratio of the mean pore radius over the mean throat length ( $\bar{R}_p/\bar{L}_t$ ), and the pore connectivity ( $Z$ ). The entry pressure  $P_e$  depends on the largest meniscus radius in the network. It is close to the mean capillary pressure for a network with narrow size distribution, and constant for a constant value of  $\sigma_0/\bar{R}$ . The entry pressure decreases with increasing  $\sigma_0$ , as well as at pore connectivity above six. The pore size distribution index  $\lambda$  is easier to correlate with the meniscus size distribution profile, which depends on the invasion process and the structural properties. Profiles of the distribution index  $\lambda$  are related to the ratio  $\sigma_0/\bar{R}$ : They are the same for networks with the same  $\sigma_0/\bar{R}$  and are shifted upwards with the decline of  $\sigma_0/\bar{R}$ . Pore connectivity plays a minor role in the distribution index.

## 11.2 Outlook

### 11.2.1 Pore network modeling

In this thesis, the thickness of the diffusion boundary layer was assumed to be known. With gas-side mass transfer coefficient from correlations, boundary layer thickness can easily be calculated in practice. However, in some situations it may be necessary to compute external flow and mass transfer. Coupling of PNM with, e.g., the Navier-Stokes equations is still an ongoing topic.

A further restriction of the present derivation concerns the isothermal character of the pore network model used. In some cases, temperature distributions that arise in porous media during drying may cause condensation in their top slice. The thermal effect has already been implemented into 3D PNM (Surasani et al., 2008). However, macroscopic parameters subjected to the thermal effect would be very interesting to derive for implementation in more comprehensive, non-isothermal and non-isotropic versions of the CM.

Moreover, apart from the primary capillary structures considered here, so-called secondary capillary structures may also exist, for example thin liquid films in non-cylindrical capillaries of hydrophilic porous media. Secondary capillary structures can reduce the

moisture transport resistance to the evaporative surface, so that surface saturation can be replenished more easily by liquid from the bottom (Yiotis et al., 2004; Prat, 2007; Vorhauer et al., 2015). Vorhauer et al. (2015) proposed a 2D PNM that accounted for the capillary ring effect, motivated by experimental observations, and considered it by attributing additional volume at the conjunction of throats in the throat-node model. This treatment might, though, further overestimate the void space in the porous medium. In contrast, the throat-pore model underestimates to a certain extent the liquid volume in the corners of throat and pore conjunctions. Those neglected void volumes could be locations with significant capillary ring effect.

As the PNM model becomes more sophisticated by including more mechanisms, the major issue of simulation cost becomes more crucial. Accelerating the performance of PNM is, thus, a further task. The here presented PNM for drying is calculated by CPUs in the platform of Matlab. However, Matlab performs computations in a serial order. It should, therefore, be possible to accelerate the drying algorithm by parallelization.

In Chapter 2, we discussed the bottleneck in the algorithm. Calculating the liquid pressure for each cluster takes a large percentage of simulation time (Fig. 2.10). The size of this loop depends on the number of active meniscus throats. The algorithm in Fig. 2.10 determines the final liquid pressure by shifting the static menisci into the status of active menisci one by one. Such a slow process could be carried out in parallel by making a series of assumptions for the active and static menisci in advance, then calculating the liquid pressure under each assumption. After that, we only have to check the calculated liquid pressure, whether it meets the balance condition of menisci. The result would be selected from the first assumption for which the calculated liquid pressure meets the requirement. Additionally, the current algorithm determines the liquid pressure for each cluster in a series. The liquid pressure in each cluster is though independent, suggesting that a parallel treatment could be applied among clusters. One possible platform would be the GPU calculation, for example, the NVIDIA CUDA toolbox.

Furthermore, the formation of single menisci poses a serious issue for fast computation, since the number of simulation steps to be performed is amplified by taking single menisci into account. It is possible to neglect the role of single menisci in liquid pressure determination but focus on the invasion process in the clusters. Therefore, the role of the single menisci in the drying process should be further investigated and clarified.

### 11.2.2 Two-equations continuum model

In Chapter 5 of this thesis, we proposed a new way to solve the CM. We identified three transport zones as regards the mass transport process, namely, the wet zone (saturated or two-phase flow zone) in the porous medium, the dry zone with the vapor diffusivity of the porous medium (formed after the liquid has receded from the surface), and the gas-side boundary layer with, this time, unconfined vapor diffusion, leading to three separate

governing equations. However, the description of the moisture transport even within the wet zone of the porous medium is conducted by the one-equation CM. In other words, the transport processes of the liquid and vapor phase are combined into the global behavior of the moisture as a whole. In contrast, a two-equation CM, which uses two balance equations to describe the transport processes in the liquid and vapor phases separately, might be more accurate and flexible. Based on the two-equation CM, Chapter 8 discussed the boundary condition for the liquid phase, while the coupling condition for the vapor phase is straightforward by switching from the effective vapor diffusivity of the porous medium to molecular (or effective) vapor diffusivity in the gas-side boundary layer. It would also be interesting to account for the thermal effect in the two-equation CM.

### 11.2.3 Macroscopic parameters

Macroscopic parameters, the moisture transport coefficient, relative humidity, vapor transport parameters, etc., have been obtained under the isothermal drying condition. Besides, in our simple PNM (neglecting some essential physical effects, e.g., the film effect), we only simulated a relatively small network size ( $25 \times 25 \times 51$ ). Since the heat transfer, secondary capillary pressure, and network scale could also play roles in the macroscopic parameters, changes in macroscopic parameters by these factors would deserve to be explored.

Moreover, in Chapter 10 the heterogeneity of parameters correlated with the capillary pressure was pointed out. The capillary pressure curve can further be linked to the transport properties of two-phase flow, i.e., the relative permeability by Darcy's law. Srikiatden and Roberts (2007) and Joekar-Niasar and Hassanizadeh (2011) pointed out that the nonlinear properties, i.e. capillary pressure-saturation function and permeability-saturation function, are critical for realistic modeling of two (or multi)-phase flow in porous media. Thus, evaluating the transition from parameters of the capillary pressure-effective saturation profile to the profile of relative permeability over effective saturation could be a future research direction.

# Bibliography

- Acosta, R. H., Agulles-Pedrós, L., Komin, S., Sebastiani, D., Spiess, H. W., and Blümmler, P. (2006). Diffusion in binary gas mixtures studied by nmr of hyperpolarized gases and molecular dynamics simulations. *Physical Chemistry Chemical Physics*, 8(36):4182–4188.
- Attari Moghaddam, A., Kharaghani, A., Tsotsas, E., and Prat, M. (2017a). Kinematics in a slowly drying porous medium: Reconciliation of pore network simulations and continuum modeling. *Physics of Fluids*, 29(2):022102.
- Attari Moghaddam, A., Kharaghani, A., Tsotsas, E., and Prat, M. (2018). A pore network study of evaporation from the surface of a drying non-hygroscopic porous medium. *AIChE Journal*, 64(4):1435–1447.
- Attari Moghaddam, A., Prat, M., Tsotsas, E., and Kharaghani, A. (2017b). Evaporation in capillary porous media at the perfect piston-like invasion limit: Evidence of nonlocal equilibrium effects. *Water Resources Research*, 53(12):10433–10449.
- Barrett, R., Berry, M., Chan, T. F., Demmel, J., Donato, J., Dongarra, J., Eijkhout, V., Pozo, R., Romine, C., and van der Vorst, H. (1994). *Templates for the solution of linear systems: Building blocks for iterative methods*. Society for Industrial and Applied Mathematics.
- Brace, W. F. (1980). Permeability of crystalline and argillaceous rocks. *International Journal of Rock Mechanics and Mining Sciences & Geomechanics Abstracts*, 17(5):241–251.
- Brooks, R. H. (1966). Properties of porous media affecting fluid flow. *Journal of the Irrigation and Drainage Division, Proceedings of the American Society of Civil Engineers*, 92(2):61–88.
- Bruce, E. P., John, M. P., and John, P. O. (2001). *Properties of Gases and Liquids, Fifth Edition*. McGraw-Hill Education, New York.
- Brunauer, S. (1944). *The Adsorption of Gases and Vapors*. Princeton University press; London, H. Milford, Oxford University Press, New York.

- Carmeliet, J., Hens, H., Roels, S., Adan, O., Brocken, H., Cerny, R., Pavlik, Z., Hall, C., Kumaran, K., and Pel, L. (2004). Determination of the liquid water diffusivity from transient moisture transfer experiments. *Journal of Thermal Envelope and Building Science*, 27(4):277–305.
- Chandler, R., Koplik, J., Lerman, K., and Willemsen, J. F. (1982). Capillary displacement and percolation in porous media. *Journal of Fluid Mechanics*, 119:249–267.
- Cieplak, M. and Robbins, M. O. (1990). Influence of contact angle on quasistatic fluid invasion of porous media. *Physical Review B, Condensed Matter*, 41(16):11508–11521.
- Conner, W. C., Blanco, C., Coyne, K., Neil, J., and Pajares, J. (1987). Analysis of the morphology of high surface area solids: Studies of agglomeration and the determination of shape. *Journal of Catalysis*, 106(1):202–209.
- Conner, W. C. and Lane, A. M. (1984). Measurement of the morphology of high surface area solids: Effect of network structure on the simulation of porosimetry. *Journal of Catalysis*, 89(2):217–225.
- Defraeye, T., Blocken, B., Derome, D., Nicolai, B., and Carmeliet, J. (2012). Convective heat and mass transfer modelling at air porous material interfaces: Overview of existing methods and relevance. *Chemical Engineering Science*, 74:49–58.
- Ferrari, A. and Lunati, I. (2013). Direct numerical simulations of interface dynamics to link capillary pressure and total surface energy. *Advances in Water Resources*, 57:19–31.
- Geoffroy, S. and Prat, M. (2014). *A Review of Drying Theory and Modelling Approaches*, pages 145–173. Springer International Publishing, Cham.
- Ghaedi, M., Heinemann, Z. E., Masihi, M., and Ghazanfari, M. H. (2015). An efficient method for determining capillary pressure and relative permeability curves from spontaneous imbibition data. *Iranian Journal of Oil & Gas Science and Technology*, 4(3):1–17.
- Gupta, S., Huinink, H. P., Prat, M., Pel, L., and Kopinga, K. (2014). Paradoxical drying of a fired-clay brick due to salt crystallization. *Chemical Engineering Science*, 109:204–2011.
- Gómez, I., Sala, J. M., and Millán, J. A. (2007). Characterization of moisture transport properties for lightened clay brick: Comparison between two manufacturers. *Journal of Building Physics*, 31(2):179–194.
- Haghighi, E., Shahraeeni, E., Lehmann, P., and Or, D. (2013). Evaporation rates across a convective air boundary layer are dominated by diffusion. *Water Resources Research*, 49(3):1602–1610.

- Hilpert, M. and Miller, C. T. (2001). Pore-morphology-based simulation of drainage in totally wetting porous media. *Advances in Water Resources*, 24(3):243–255.
- Hunt, A. G. (2005). Pressure Saturation Curves and the Critical Volume Fraction for Percolation. In Hunt, A. G., editor, *Percolation Theory for Flow in Porous Media*, pages 121–143. Springer Berlin Heidelberg, Berlin.
- Jabbari, Y., Tsotsas, E., Kirsch, C., and Kharaghani, A. (2019). Determination of the moisture transport coefficient from pore network simulations of spontaneous imbibition in capillary porous media. *Chemical Engineering Science*, 207:600–610.
- Joekar-Niasar, V. and Hassanizadeh, S. M. (2011). Specific interfacial area: The missing state variable in two-phase flow equations? *Water Resources Research*, 47(5).
- Keita, E., Faure, P., Rodts, S., and Coussot, P. (2013). MRI evidence for a receding-front effect in drying porous media. *Physical Review E, Statistical, Nonlinear, and Soft Matter Physics*, 87:062303.
- Kewen, L. (2004). Theoretical development of the Brooks-Corey capillary pressure model from fractal modeling of porous media. In *SPE/DOE Symposium on Improved Oil Recovery*, pages 6–17. Tulsa, Oklahoma.
- Kharaghani, A. (2020). *Drying and wetting of capillary porous materials: Insights from imaging and physics-based modeling*. Habilitation thesis, Fakultät für Verfahrens- und Systemtechnik, Otto-von-Guericke-Universität Magdeburg.
- Kjosavik, A., Ringen, J. K., and Skjaeveland, S. M. (2002). Relative permeability correlation for mixed-wet reservoirs. *SPE Journal*, 7(01):49–58.
- Knackstedt, M. A., Sheppard, A. P., and Sahimi, M. (2001). Pore network modelling of two-phase flow in porous rock: The effect of correlated heterogeneity. *Advances in Water Resources*, 24(3):257–277.
- Lai, F., Li, Z., Zhang, W., Dong, H., Kong, F., and Jiang, Z. (2018). Investigation of pore characteristics and irreducible water saturation of tight reservoir using experimental and theoretical methods. *Energy & Fuels*, 32(3):3368–3379.
- Le, K. H., Kharaghani, A., Kirsch, C., and Tsotsas, E. (2016). Pore network simulations of heat and mass transfer inside an unsaturated capillary porous wick in the dry-out regime. *Transport in Porous Media*, 114(3):623–648.
- Le, K. H., Kharaghani, A., Kirsch, C., and Tsotsas, E. (2017). Discrete pore network modeling of superheated steam drying. *Drying Technology*, 35(13):1584–1601.

- Lehmann, P. and Or, D. (2013). Effect of wetness patchiness on evaporation dynamics from drying porous surfaces. *Water Resources Research*, 49(12):8250–8262.
- Lockington, D. A., Parlange, J. Y., Barry, D. A., and Leech, C. A. (2003). Drying of porous building materials: Hydraulic diffusivity and front propagation. *Materials and Structures*, 36(7):448–452.
- Marchand, R. G. and Kumaran, M. K. (1994). Moisture diffusivity of cellulose insulation. *Journal of Thermal Insulation and Building Envelopes*, 17(4):362–377.
- Mason, G. and Mellor, D. W. (1995). Simulation of drainage and imbibition in a random packing of equal spheres. *Journal of Colloid and Interface Science*, 176(1):214–225.
- Metzger, T., Irawan, A., and Tsotsas, E. (2006). Remarks on the paper “Extension of Hoshen-Kopelman algorithm to non-lattice environments” by A. Al-Futaisi and T.W. Patzek, *Physica A* 321 (2003) 665-678. *Physica A, Statistical Mechanics and Its Applications*, 363(2):558–560.
- Metzger, T., Irawan, A., and Tsotsas, E. (2007a). Influence of pore structure on drying kinetics: A pore network study. *AIChE Journal*, 53(12):3029–3041.
- Metzger, T., Irawan, A., and Tsotsas, E. (2007b). Isothermal drying of pore networks: Influence of friction for different pore structures. *Drying Technology*, 25(1):49–57.
- Metzger, T. and Tsotsas, E. (2008). Viscous stabilization of drying front: Three-dimensional pore network simulations. *Chemical Engineering Research & Design*, 86(7A):739–744.
- Metzger, T., Tsotsas, E., and Prat, M. (2007c). Pore-network models: A powerful tool to study drying at the pore level and understand the influence of structure on drying kinetics. In Tsotsas, E. and Mujumdar, A. S., editors, *Modern Drying Technology*, pages 57–102. Wiley-VCH Verlag GmbH & Co. KGaA, Weinheim.
- Moebius, F. and Or, D. (2014). Inertial forces affect fluid front displacement dynamics in a pore-throat network model. *Physical Review E*, 90(2):023019.
- Moseley, W. A. and Dhir, V. K. (1996). Capillary pressure-saturation relations in porous media including the effect of wettability. *Journal of Hydrology*, 178(1):33–53.
- Mosthaf, K., Helmig, R., and Or, D. (2014). Modeling and analysis of evaporation processes from porous media on the rev scale. *Water Resources Research*, 50(2):1059–1079.
- Ojha, S. P., Misra, S., Tinni, A., Sondergeld, C. H., and Rai, C. (2018). Estimation of pore-network characteristics and irreducible saturations in wolfcamp and eagle ford shales using low-pressure-nitrogen-adsorption/desorption-isotherm measurements. *SPE Reservoir Evaluation and Engineering*, 21(02):373–391.

- Or, D., Lehmann, P., Shahraeeni, E., and Shokri, N. (2013). Advances in soil evaporation physics: A review. *Vadose Zone Journal*, 12(4):1–16.
- Pel, L., Brocken, H., and Kopinga, K. (1996). Determination of moisture diffusivity in porous media using moisture concentration profiles. *International Journal of Heat and Mass Transfer*, 39(6):1273–1280.
- Pel, L., Ketelaars, A. A. J., Adan, O. C. G., and van Well, A. A. (1993). Determination of moisture diffusivity in porous media using scanning neutron radiography. *International Journal of Heat and Mass Transfer*, 36(5):1261–1267.
- Pel, L., Kopinga, K., Bertram, G., and Lang, G. (1995). Water absorption in a fired-clay brick observed by nmr scanning. *Journal of Physics D, Applied Physics*, 28(4):675–680.
- Pel, L. and Landman, K. A. (2004). A sharp drying front model. *Drying Technology*, 22(4):637–647.
- Pel, L., Landman, K. A., and Kaasschieter, E. F. (2002). Analytic solution for the non-linear drying problem. *International Journal of Heat and Mass Transfer*, 45(15):3173–3180.
- Philip, J. R. and de Vries, D. A. (1957). Moisture movement in porous materials under temperature gradients. *Eos, Transactions American Geophysical Union*, 38(2):222–232.
- Portsmouth, R. and Gladden, L. (1991). Determination of pore connectivity by mercury porosimetry. *Chemical Engineering Science*, 46(12):3023–3036.
- Prat, M. (1993). Percolation model of drying under isothermal conditions in porous media. *International Journal of Multiphase Flow*, 19(4):691–704.
- Prat, M. (1998). Discrete models of liquid-vapour phase change phenomena in porous media. *Revue Générale de Thermique*, 37(11):954–961.
- Prat, M. (2002). Recent advances in pore-scale models for drying of porous media. *Chemical Engineering Journal*, 86(1):153–164.
- Prat, M. (2007). On the influence of pore shape, contact angle and film flows on drying of capillary porous media. *International Journal of Heat and Mass Transfer*, 50(7):1455–1468.
- Rabbani, H. S., Joekar-Niasar, V., and Shokri, N. (2016). Effects of intermediate wettability on entry capillary pressure in angular pores. *Journal of Colloid and Interface Science*, 473:34–43.
- Raeini, A. Q., Blunt, M. J., and Bijeljic, B. (2012). Modelling two-phase flow in porous media at the pore scale using the volume-of-fluid method. *Journal of Computational Physics*, 231(17):5653–5668.

- Schirmer, R. (1938). *Die Diffusionszahl von Wasserdampf-Luft-Gemischen und die Verdampfungsgeschwindigkeit*. PhD thesis, VDI-Verlag.
- Schlünder, E. (1988). On the mechanism of the constant drying rate period and its relevance to diffusion controlled catalytic gas phase reactions. *Chemical Engineering Science*, 43(10):2685–2688.
- Shahraeeni, E., Lehmann, P., and Or, D. (2012). Coupling of evaporative fluxes from drying porous surfaces with air boundary layer: Characteristics of evaporation from discrete pores. *Water Resources Research*, 48(9):9525–9540.
- Shokri, N., Lehmann, P., Vontobel, P., and Or, D. (2008). Drying front and water content dynamics during evaporation from sand delineated by neutron radiography. *Water Resources Research*, 44(6):6418–6429.
- Sok, R. M., Knackstedt, M. A., Sheppard, A. P., Pinczewski, W. V., Lindquist, W. B., Venkatarangan, A., and Paterson, L. (2002). Direct and stochastic generation of network models from tomographic images; effect of topology on residual saturations. *Transport in Porous Media*, 46(2):345–371.
- Srikiatden, J. and Roberts, J. S. (2007). Moisture transfer in solid food materials: A review of mechanisms, models, and measurements. *International Journal of Food Properties*, 10(4):739–777.
- Stauffer, D. and Aharony, A. (2018). *Introduction to percolation theory*. CRC press, London.
- Sun, Y., Kharaghani, A., and Tsotsas, E. (2016). Micro-model experiments and pore network simulations of liquid imbibition in porous media. *Chemical Engineering Science*, 150:41–53.
- Surasani, V. K., Metzger, T., and Tsotsas, E. (2008). Consideration of heat transfer in pore network modelling of convective drying. *International Journal of Heat and Mass Transfer*, 51(9):2506–2518.
- Sweijen, T., Aslannejad, H., and Hassanizadeh, S. M. (2017). Capillary pressure–saturation relationships for porous granular materials: Pore morphology method vs. pore unit assembly method. *Advances in Water Resources*, 107:22–31.
- Talbi, M. and Prat, M. (2019). About Schlünder’s model: A numerical study of evaporation from partially wet surfaces. *Drying Technology*, 37(5):513–524.
- Tsakiroglou, C. D. and Payatakes, A. C. (1991). Effects of pore-size correlations on mercury porosimetry curves. *Journal of Colloid and Interface Science*, 146(2):479–494.

- Tsotsas, E. (1994). From single particle to fluid bed drying kinetics. *Drying Technology*, 12(6):1401–1426.
- Vorhauer, N., Wang, Y. J., Kharaghani, A., Tsotsas, E., and Prat, M. (2015). Drying with formation of capillary rings in a model porous medium. *Transport in Porous Media*, 110(2):197–223.
- Wang, Y., Kharaghani, A., Metzger, T., and Tsotsas, E. (2012). Pore network drying model for particle aggregates: Assessment by x-ray microtomography. *Drying Technology*, 30(15):1800–1809.
- Weishaupt, K., Joekar-Niasar, V., and Helmig, R. (2019). An efficient coupling of free flow and porous media flow using the pore-network modeling approach. *Journal of Computational Physics: X*, 1:100011.
- Whitaker, S. (1977). Simultaneous heat, mass, and momentum transfer in porous media: A theory of drying. *Advances in Heat Transfer*, 13:119–203.
- White, N. F., Duke, H. R., Sunada, D. K., and Corey, A. T. (1970). Physics of desaturation in porous materials. *Journal of the Irrigation and Drainage Division*, 96(2):165–191.
- Wilkinson, D. and Willemsen, J. F. (1983). Invasion percolation: A new form of percolation theory. *Journal of Physics A: Mathematical and General*, 16(14):3365.
- Yiotis, A. G., Boudouvis, A. G., Stubos, A. K., Tsimpanogiannis, I. N., and Yortsos, Y. C. (2004). Effect of liquid films on the drying of porous media. *AIChE Journal*, 50(11):2721–2737.
- Yiotis, A. G., Salin, D., Tajer, E. S., and Yortsos, Y. C. (2012). Drying in porous media with gravity-stabilized fronts: Experimental results. *Physical Review E*, 86(2):026310.
- Yiotis, A. G., Salin, D., and Yortsos, Y. C. (2015). Pore network modeling of drying processes in macroporous materials: Effects of gravity, mass boundary layer and pore microstructure. *Transport in Porous Media*, 110(2):175–196.
- Yiotis, A. G., Stubos, A. K., Boudouvis, A. G., and Yortsos, Y. C. (2001). A 2D pore-network model of the drying of single-component liquids in porous media. *Advances in Water Resources*, 24(3):439–460.

# Publications list

2016.10 - 2021.06

---

## Journal publications

1. Lu X., Kharaghani A., Tsotsas E., (2020). Transport parameters of macroscopic continuum model determined from discrete pore network simulations of drying porous media: Throat-node vs. throat-pore configurations. *Chemical Engineering Science* 223, 115723.
2. Lu X., Kharaghani A., Adloo H., Tsotsas E., (2020). The Brooks and Corey capillary pressure model revisited from pore network simulations of capillarity-controlled invasion percolation process. *Processes*, 8, 1318.
3. Lu X., Tsotsas E., Kharaghani A., (2021). Insights into evaporation from the surface of capillary porous media gained by discrete pore network simulations. *International Journal of Heat and Mass Transfer*, 168, 120877.
4. Lu X., Tsotsas E., Kharaghani A., (2021). Drying of capillary porous media simulated by coupling of continuum-scale and micro-scale models, *International Journal of Multiphase Flow*, 140, 103654.

## Proceedings

1. Lu X., Kharaghani A., Tsotsas E., (2018). Dependency of continuum model parameters on the spatially correlated pore structure studied by pore-network drying simulations. *IDS 2018. 21st International Drying Symposium Proceedings. Editorial Universitat Politècnica de València*. 307-314.

## Oral presentations

1. Lu X., Kharaghani A., Tsotsas E., (2018). A bottom-up approach to obtain continuum model parameters from pore network drying simulations. *10th International Conference on Porous Media & Annual Meeting (Interpore)*, 14.-17. May 2018, New Orleans, USA.

2. Lu X., Kharaghani A., Tsotsas E., (2019). Insights into evaporation from the surface of capillary porous media gained by discrete pore network simulations, *11th International Conference on Porous Media & Annual Meeting (Interpore)*, 6.-10. May 2019, Valencia/Spain.
3. Lu, X., Tsotsas, E., Kharaghani, A.: Coupling of macroscopic continuum and microscopic pore network models of drying, *ProcessNet-Jahrestreffen der Fachgruppen "Hochdruckverfahrenstechnik" und "Trocknungstechnik"*, Online, 15.-16. March 2021.
4. Lu, X., Tsotsas, E., Kharaghani, A.: Drying of capillary porous media simulated by coupling of continuum model and pore network model, *13th International Conference on Porous Media and Annual Meeting (Interpore)*, Online, 31. May - 4. Juni 2021.

### Poster presentations

1. Lu X., Kharaghani A., Tsotsas E., (2018). Influence of pore structure on continuum model parameters investigated by pore network drying simulations, *ProcessNet-Jahrestreffen der Fachgruppen "Mechanische Flüssigkeitsabtrennung", "Trocknung" und "Grenzflächenbestimmte Systeme und Prozesse"*, 26.- 28. February 2018, Merseburg.
2. Lu X., Kharaghani A., Tsotsas E., (2018). Dependency of continuum model parameters on the spatially correlated pore structure studied by pore-network drying simulations, *21th International Drying Symposium (IDS2018)*, 11.-14. September 2018, Valencia/Spain.
3. Lu, X., Tsotsas, E., Kharaghani, A.: First steps towards pore network modeling of single particle calcination, *ProcessNet-Jahrestreffen der Fachgruppen "Fluidverfahrenstechnik" und "Wärme- und Stoffübertragung"*, Online, 24.-26. February 2021.

# Supervised student work

The following MSc. theses have been conducted within the framework of this PhD thesis:

1. Yupeng Leng, A two-equation continuum model for drying of capillary porous media assessed by pore network simulations, Chair of Thermal Process Engineering, Otto-von-Guericke-Universität Magdeburg, May 2019.
2. Zhuo Chen, Optimization of the dynamic pore network modeling algorithm for drying of capillary media, Chair of Thermal Process Engineering, Otto-von-Guericke-Universität Magdeburg, December 2019.
3. Ouqing Yu, Determination of the one-equation continuum model parameters from network simulations: The chemical potential perspective and correlations with pore structures, Chair of Thermal Process Engineering, Otto-von-Guericke-Universität Magdeburg, December 2020.

# Curriculum vitae

Name	<b>Xiang Lu</b>
Date of birth	June 15th, 1992
Place of birth	Anhui, China

## Education

---

Since 2016	<b>PhD</b> candidate at the Chair of Thermal Process Engineering, Otto-von-Guericke-Universität Magdeburg, Germany
2014-2016	<b>MSc.</b> , Otto-von-Guericke-Universität Magdeburg, Germany Major in Chemical and Energy Engineering
2010-2014	<b>BSc.</b> , Nanjing Institution of Technology Major in Polymer Material and Engineering

## Work experience

---

Since 2016	Research assistant Otto-von-Guericke-Universität Magdeburg, Germany
2011-2014	Research assistant Nanjing Institute of Technology, Nanjing, China

---

Magdeburg, February 24, 2022

MSc. Xiang Lu